MATERIALS ENGINEERING

PORTFOLIO

LUCA MONDONICO

Portfolio of projects

Luca Mondonico
+1 (650) 507-9027 | lu.mondonico@gmail.com

ETH
Eidgenössische Technische Hochschule Zürich
Swiss Federal Institute of Technology Zurich

Stanford
University

A solution-processable artificial solid electrolyte interphase for practical lithium metal batteries

Luca Mondonico
19-945-641

Swiss Federal Institute of Technology (ETH) Zürich
Department of Materials

Supervision

Prof. Dr. Zhenan Bao
Prof. Dr. Markus Niederberger

January 2022

Acknowledgements

First of all, I want to thank Prof. Dr. Zhenan Bao for making this master thesis possible in her group at Stanford University. Special thanks go to my mentor Zhiao Yu for his support and guidance through this thesis. He always had time for explaining and sharing his extensive knowledge on lithium batteries with me. Of course, I want to thank Prof. Dr. Markus Niederberger at ETH Zürich for remotely supporting and supervising me during my visit at Stanford.

Further thanks go to Dr. Weilai Yu for performing XPS analysis of my samples, Dr. Jeffrey Tok who introduced me to lab equipment, and Lily Pay who helped me with administrative matters and kept the lab organized. I thank all Bao battery-subgroup members for providing precious suggestions and continuous feedbacks on my project. Big thanks go to all other Bao Group members for answering smaller and bigger questions and for company during coffee and lunch breaks.

Finally, I express my profound gratitude to my family for providing me with support and continuous encouragement throughout my years of study and through the process of researching and writing this thesis. This accomplishment would not have been possible without them.
Thank you.

Abstract

Li metal is regarded as a promising anode for Li batteries owing to its high specific capacity. However, rapid dendrite growth and low reversibility hinder its practical applications. Building an artificial solid electrolyte interphase (ASEI), which can replace the brittle and inhomogeneous native SEI generated by parasitic reactions between Li and liquid electrolyte, is an effective strategy to stabilize a Li metal anode. In this work, we design and synthesize a multifunctional (mechanically strong, Li^+ ion conductive, electrolyte-blocking, and solution processable) ASEI material, LiAl-FBD, for improving Li metal battery performance. The LiAl-FBD crystal structure demonstrates that Al^{3+} ions are bridged by FBD^{2-} ligands to form anion clusters while Li^+ ions are loosely bound at the periphery, enabling a Li^+ ion conductivity of 9.4×10^{-6} S cm^{-1}. The short yet highly fluorinated ligand chains endow LiAl-FBD with hardness and electrolyte-phobicity. The ASEI was found to effectively prevent Li/electrolyte side reactions and extends the cycle life of Li metal electrodes. Ultimately, by pairing LiAl-FBD coated 50μm-thick Li with industrial 3.5 mAh cm^{-2}, NMC811 cathode, and 2.8 μL mAh^{-1} lean electrolyte, the Li metal full cells show superior cycle life than bare ones, achieving 250 cycles at 1 mA cm^{-2}.

Contents

List of Figures

Chapter 1

Introduction

Lithium metal anodes are regarded as some of the most promising negative electrodes in the next generation of batteries [1, 2]. Unfortunately, lithium metal anode's poor cyclability has so far prevented its use in energy storage devices. The issue originates mainly from the unstoppable parasitic reactions between the highly-reactive Li and the electrolyte components, eventually resulting in a poorly-passivating layer called solid-electrolyte-interphase [3, 4].

To address the issues affecting Li metal anodes, artificial SEIs have recently gained attention as an alternative approach, given their potential compatibility with commercial electrolytes [5] and practical manufacturing processes [6]. Researching a novel solution-based processing for ASEIs on the Li metal anode is tremendously important, as it would allow effective ASEIs implementation in the most common industrial coating methods such like spray coating, gravure printing and slot-die coating.

In this work, we design and synthesize a solution-processable, mechanically strong, Li-ion conductive, and electrolyte-blocking ASEI. The artificial SEI is based on a

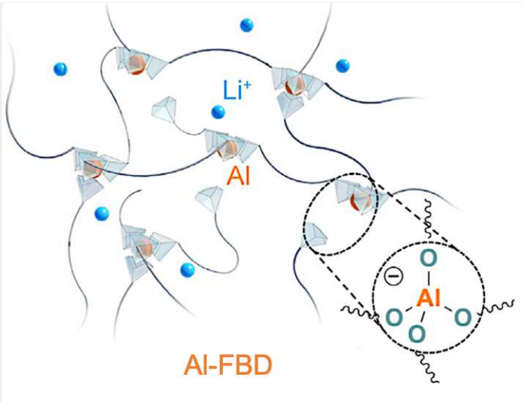

Figure 1.1: Conceptual sketch of polymeric Al-FBD network. Blue spheres, Li+ ions; orange spheres, Al atoms; tetrahedra, anion centers; gray chains, soft ligands.

dynamic polymeric network with high Li^+ single-ion conductivity, whose active centers are tetrahedral $\mathrm{Al}\left(\mathrm{OR}\right)_4^-$ (R = soft fluorinated linker) anions which also act as counter anions to Li^+ ions (Fig. 1.1). With this novel artificial SEI, we demonstrate over 300 stable stripping and plating cycles in Li | Cu cell using commercial carbonate-based electrolyte. Over 90 percent capacity retention for almost 200 cycles in the Li | NMC full battery was achieved using directly-coated thin Li foils and commercial, industry-standard NMC cathode sheets. The design concept of using dynamic single-ion conductor as a stable and scalable artificial SEI is surely promising for practical Li metal batteries.

Chapter 2

Theoretical Background

In recent years, demand for high-density energy storage devices has reached an all-time high [7]. While playing an increasingly significant role in the energy scenario, Li-ion batteries are approaching their theoretical limit [7]. It is therefore essential to develop a new generation of batteries that can meet the increasingly demanding requirements of modern electronic devices such as computers, cell phones and electric cars [8, 9].

Possessing the highest theoretical specific power ($3,860$ mAh g^{-1}) and the lowest electrochemical potential (3.04 V, compared to the standard hydrogen electrode) of any other known negative electrode material, Li metal indeed has the potential to deliver the highest specific energy should it be used as an anode in Li batteries [8, 9].

Despite its great potential, a number of important drawbacks prevent Li metal from being industrially implemented as an anode in Li batteries.
Firstly, Li readily reacts with conventional/commercial carbonate electrolytes to form a so-called solid-electrolyte interface [3, 4], whose typically heterogeneous

nature causes local fluctuations of Li^+ ion flux and current density. The native SEI fails to passivate the Li surface during cycling, thus leading to the creation of dendrites [10]. Secondly, large volume change during Li stripping and plating generates cracks in the mechanically brittle SEI, forms dead Li, and causes further electrolyte consumption [10]. The combined action of the aforementioned effects decreases the Coulombic Efficiency (CE) and compromises the long-term cycle life of Li metal anodes [8].

Several strategies have been proposed to counteract said degradation pathways, including additives and liquid electrolyte engineering [11–14], solid-state electrolytes [4, 15], chemical pretreatment of Li metal [16–18], Li metal hosts [19], or the employment of a shielding cation layer [20]. Nevertheless, obtaining a stable SEI on Li metal is particularly complex [3, 8], thus making the design and fabrication of artificial SEIs a particularly attractive alternative to replace native SEI on Li.

An ideal artificial SEI must possess several essential features. Initially, prior work suggested advantages of having high-modulus coatings on Li [3, 4]; however, Liu at al. observed that in order to achieve macroscopic uniform Li deposition, the SEI needs to readily adapt to the large volume change during Li stripping and plating [10]. This is only possible if the SEI possesses dynamics properties and a certain degree of flowability. Secondly, the artificial SEI should guarantee fast and uniform Li^+ single-ion conductivity as to reduce "hot spots", stabilize the Li metal anode and increase the critical Li deposit size [4, 21].
Lastly, harmful side reactions between lithium and coating or lithium and electrolyte should be minimized; therefore, SEI itself needs to be chemically an electrochemically inert as to mitigate electrolyte penetration in the coating [22].

Nonetheless, only a few SEIs have been implemented that possess all major desirable properties, such as flowability [23], dynamic properties [10], or high ion conductivity [17, 21]. In addition, most of the reported Li metal artificial SEIs, mainly compatible with ether-based electrolytes only, cannot be utilized in current Li-ion batteries due to their incompatibility with commercially used high-voltage and high-energy density lithium nickel manganese copper oxide (NMC) cathodes. It is thus necessary to carefully engineer future artificial SEIs and extend their compatibility to a much broader electrolyte selection.

Despite being challenging, both scientifically and practically, to synergistically incorporate all the ideal properties into one material, it is worth developing a multifunctional ASEI for better protecting Li metal anodes.

Chapter 3

Results and Discussion

3.1 Material Design

Previous work demonstrated the validity of tetrahedral $\mathrm{Al\,(OR)_4^-}$ anions when applied in dynamic polymeric networks for artificial SEIs [24]; therefore, tetrahedral $\mathrm{Al\,(OR)_4^-}$ anions were chosen as dynamic crosslinking centers in our current polymeric architecture. The $\mathrm{Li^+}$ counter ions are introduced as the mobile ions in the network, while relatively soft fluorinated chains (2,2,3,3-tetrafluoro-1,4-butanediol, FBD) are chosen as inert ligands (Fig. 3.1a). Being less chemically reactive and more solvent resistant compared to their non-fluorinated version, 1,4-butanediol (BDO) [24], the FBD chains can potentially mitigate side reactions between Li and the dynamic polymeric network, prevent the dissolution of the network in polar carbonate electrolytes, reduce electrolyte penetration through the ASEI, and guarantee flowability when combined with dynamic $\mathrm{Al\,(OR)_4^-}$ crosslinking sites. Most important, $\mathrm{Li^+}$ ions, which are directly introduced during the polymeric structure synthesis, can transport through the network of fixed $\mathrm{Al\,(OR)_4^-}$ anions, thus making the ASEI a solid-state single-ion conductor [5].

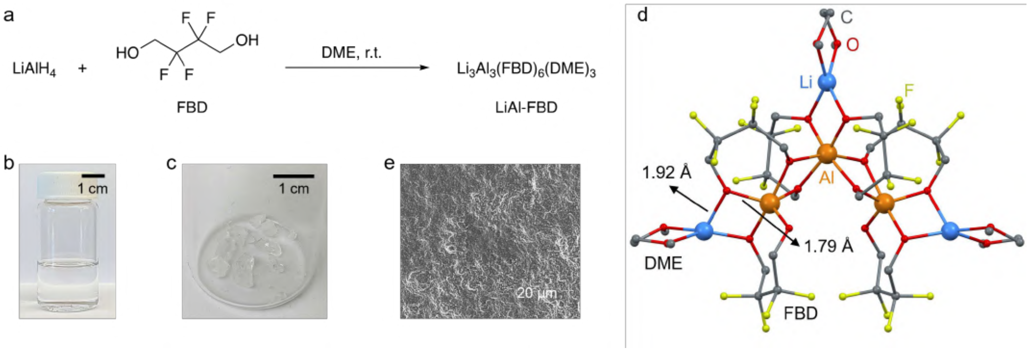

Figure 3.1: (a) Synthesis of LiAl-FBD. (b) Optical image of LiAl-FBD solution. (c,d) Optical image (c) and refined crystal structure (d) of LiAl-FBD. (e) SEM image of coated LiAl-FBD on Li foil.

LiAl-FBD, the key component for the artificial SEI, is derived from the instant reaction between $LiAlH_4$ and FBD in 1,2-dimethoxyethane (DME). After the reaction, which released H_2 as the sole by product, the deprotonation of FBD was confirmed by nuclear magnetic resonance (NMR) spectroscopy. The obtained species, $LiAl(FBD)_2$ in simplified formula, is soluble in DME to form a transparent solution (see Fig. 3.1b), being thus suitable for use in common solution-based coating processes. After evaporating the solvents, crystals are produced (Fig. 3.1c), whose size ranges from centimeters to millimeters; however, it is possible to obtain smaller single crystals upon controlled evaporation of limited amounts of solvent.

By single crystal X-ray diffraction (SCXRD), the crystal structure can be solved and further refined to be $Li_3Al_3\,(FBD)_6\,(DME)_3$ [25]. As shown in Fig. 3.1d, the crystal structure comprises of an anion cluster composed of three Al^{3+} cations as the centers and six deprotonated FBD^{2-} as the bridges/ligands linking those Al^{3+} centers. The ^1H- and ^{19}F-NMR spectra also indicate such a multi-state or clustering feature by showing broadened peaks after the synthesis (Supplementary Figures 5.3, Fig. 5.1, 5.2 and 5.3). It is worth noting the three Li^+ ions are located at the periphery of the cluster, chelated by one DME solvent molecule for each. The longer distance between oxygen atoms on deprotonated FBD^{2-} with Li^+ (1.92Å) compared to Al^{3+} (1.79Å) clearly suggests their loose coordination with Li^+ yet stronger binding with Al^{3+} [25]. As proved by the ASEI high ionic conductivity (up to 9.4×10^{-6} S cm^{-1} at room temperature; see Supplementary Figures 5.3, Fig. 5.5), such an essential feature frees mobile Li^+ ions, and enables reasonably fast ion transport through the ASEI when applied on Li metal surface. In addition, compared to previous research using longer ligands [5], the short yet highly-fluorinated FBD ligand not only prevents Li^+ depletion by providing higher Li^+ concentration (2 w.t.% for LiAl-FBD versus 0.8 w.t.% in the previous report [5]) in the ASEI, but also manifests pivotal electrolyte-blocking properties.

Finally, LiAl-FBD feasibility as a crystalline coating layer was confirmed by scanning electron microscopy (SEM). As shown in Fig. 3.1g and in Supplementary Figures 5.3, Fig. 5.6, a conformal protection layer with a thickness of ~ 500 nm was observed on a thin Li foil. The crystalline nature of LiAl-FBD coating was supported by polarized optical microscope and grazing-incidence wide-angle X-ray scattering (GIWAXS) [25] (Supporting Figures, Fig. 5.11).

It is also worth remarking the LiAl-FBD ASEI was successfully implemented on Li foil using dip-coating method from the solution (5.2.2), thus showing the potential compatibility of our proposed ASEI with solution-based large-scale processing methods.

3.2 Mechanical Properties

It has been previously demonstrated the importance of mechanic properties in improving Li deposition in artificial SEI materials [5, 26].

The strength of crystalline LiAl-FBD was thus assessed via nanoindentation test [27]. As can be seen in Fig. 3.2e and 3.2f, LiAl-FBD displayed a Young's modulus of $\sim 30 - 40$ GPa (in the stable region) and hardness (> 2 GPa (in stable region), both moduli being considerably higher than those of previously reported polymer ASEIs [28, 29]. Previous studies hypothesized a Young's modulus of 4 GPa to be usually effective for a successful suppression of Li dendrites [26, 27], thus making mechanical strength a property of key importance for LiAl-FBD ASEIs to protect Li metal anodes.

3.3 Li-ion Conduction

High Li^+ ion conductivity and high Li transference number (LTN) are notoriously beneficial in artificial SEI to help increase the critical Li nucleate size, render smooth Li deposition, and reduce parasitic reactions of anions with Li metal [4, 21]. A comprehensive understanding of the main Li^+ ion transport mechanism inside ASEI is therefore necessary.

In previous studies [5], molecular dynamics (MD) simulations on polymeric networks similar to LiAl-FBD were performed to better explain the ion transport behavior inside the ASEI. In these cases, the dynamic artificial SEI was simulated as a network of uniformly distributed Li atoms, Al centers, and FTEG (1H,1H,11H,11H-perfluoro-3,6,9-trioxaundecane-1,11-diol, FTEG) polymeric ligand chains. It was hypothesized the presence of two different Li solvation en-

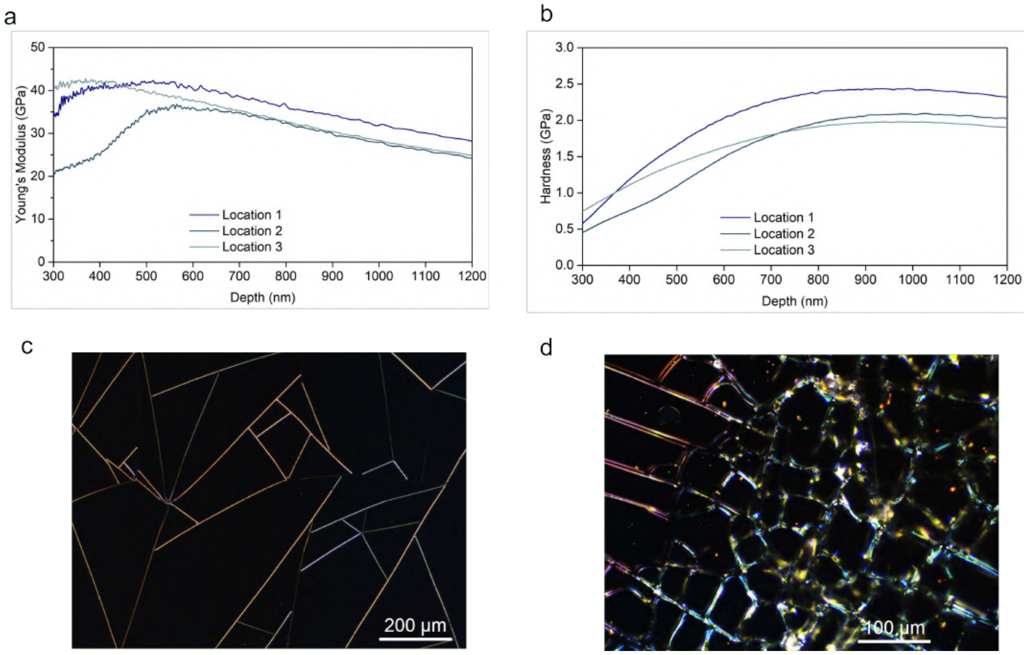

Figure 3.2: (a,b) Nanoindentation measurements showing the Young's modulus (a) and hardness (b) of LiAl-FBD single crystal. (c,d) Polarized optical microscope images showing crystal boundaries of LiAl-FBD coatings on Si wafer.

<u>Note</u>: Clear and straight crystal grain boundaries indicate the crystalline nature of LiAl-FBD coating.

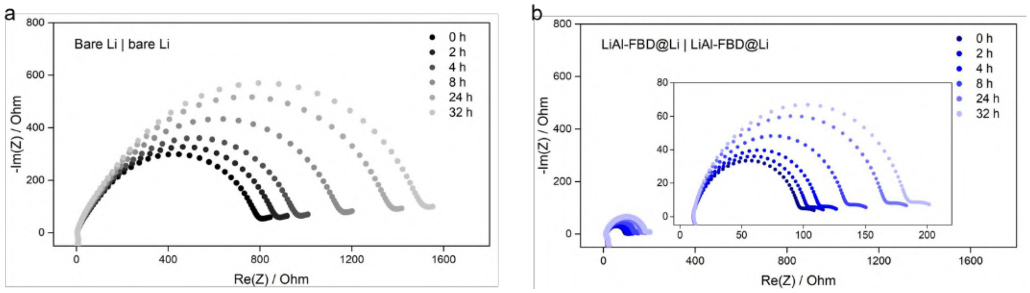

Figure 3.3: Impedance evolution of bare Li | bare Li (a) and LiAl-FBD@Li | LiAl-FBD@Li (b) symmetric cells over time. All the cells used 1M LiPF6 in EC/DMC (LP30) + 2% VC + 10% FEC as the electrolyte.

vironments in the polymeric ASEI: one is from Li^+ ions coordinated close to the $\mathrm{Al}\,(\mathrm{OR})_4^-$ center, and the other is from Li^+ ions coordinated by the ligand chains. Ultimately, it was proved by experimental and simulation results the transport of Li^+ ions in the ASEI is mainly assisted by the fluorinated ligand chains [5]. It is therefore reasonable to assume that Li^+ ion transport through our proposed LiAl-FBD ASEI occurs via FBD-mediated hopping between Al centers.

To further investigate the Li-ion conduction feature of our ASEI, electrochemical impedance spectroscopy (EIS) measurements were performed. LiAl-FBD ASEI impedance is proved by EIS to be much lower compared to bare sample one. As shown by the EIS Nyquist plots (Fig. 3.3a and 3.3b; Supplementary Figures 5.3, Fig. 5.7), the LiAl-FBD protected Li | Li symmetric cell maintained low and stable interfacial impedance over the whole cell resting time, i.e. only increasing from $\sim 100\ \Omega$ to $\sim 180\ \Omega$; by contrast, the bare Li | Li symmetric cell showed continuous and drastic increase in impedance from immediately after the cell assembling ($\sim 800\ \Omega$) to 32 h ($\sim 1,500\ \Omega$). As expected, a consistently high interfacial impedance was generated by the poorly conductive and devastated natural SEI, which originates from continuous electrolyte consumption [3, 8].

3.4 Li metal Deposition and Morphology

To understand more about the protective effect resulting from the LiAl-FBD coating, we conducted X-ray photoelectron spectrometry (XPS) along with SEM analysis to study the ASEI performance, shape and Li deposition morphology, respectively.

3.4.1 XPS results

XPS measurements for the LiAl-FBD ASEI are also performed. To prevent collateral effects from residual salts or LiAl-FBD coating itself, the samples were washed using water and anhydrous DME to expose a fresh surface prior to XPS and SEM testing.

For the bare Li metal, high contents of inorganic electrolyte-derived substances were seen (Fig. 3.4a and 3.4b). For instance, $\mathrm{Li_xPO_yF_z}$ ($\sim$ 687 eV, F1s; $\sim$ 58 eV, Li1s; $\sim$ 535 eV, O1s) and LiF ($\sim$ 56 eV, Li1s) are the decomposition products of $LiPF_6$ salt ($\sim$ 690 eV, F1s), whereas Li_2CO_3 ($\sim$ 533 eV, O1s) and Li_2O are the ones derived from carbonate solvents. Moreover, the species vastly varied with depth profiling, suggesting that such a vertically-nonuniform feature along with the severe electrolyte degradation may be responsible for the poor performance of bare Li. By contrast, XPS spectra of LiAl-FBD@Li revealed distinct patterns showing FBD-based species dominating both F1s and O1s spectra (Fig. 3.4c and 3.4d). Electrolyte-decomposed products were not observed with LiAl-FBD protection, indicating its excellent electrolyte-blocking capability. Although LiF is also present within LiAl-FBD coating Li (Fig. 3.4d), it's uniformly distributed across various levels. Indeed, the LiF species may primarily stem from well-controlled reactions [5] between FBD ligands and Li metal, and such a vertical uniformity

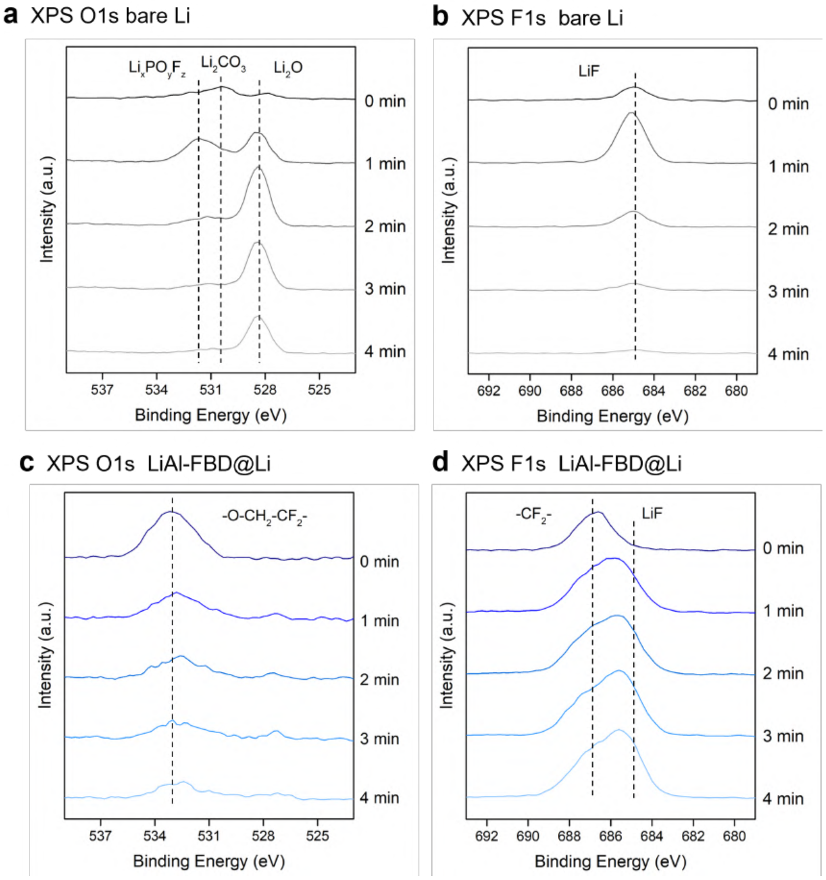

Figure 3.4: (a-d) XPS of bare Li (a,b) and LiAl-FBD coated Li (c,d) soaked in the carbonate electrolyte for four days.

was proved to be beneficial to Li metal cyclability [18, 30]. The XPS of other elements further supported our argument (Supplementary Figures 5.3, Fig. 5.9).

Overall, the previous results clearly indicate that the LiAl-FBD is effective in mitigating the electrolyte penetration and preventing continuous reactions between Li and electrolyte, which typically occur in the uncoated Li.

3.4.2 Li metal deposition

Li deposition morphology is an important factor that determines Li metal stability to ASEI protection. As suggested by previous literature [13], higher Li metal battery performance can be achieved if Li grows on the current collector in a non-dendritic fashion.

In order to better understand the origins of the LiAl-FBD-coated Li metal improved cyclability, we thus performed SEM imaging of Li metal morphology on the Cu current collector. It was noted that the LiAl-FBD protection layer remained nearly intact after 1 mAh cm^{-2} Li deposition, despite being deliberately peeled off to allow cross-sectional SEM analysis (Supplementary Figures 5.3, Fig. 5.10). In order to better study the Li deposition morphology, we then washed off the top protective LiAl-FBD coating.
With the LiAL-FBD protection, the deposited Li at 1 mAh cm^{-2} predominantly showed flat and chunky 2D plate-like structures (Fig. 3.5d, 3.5e and 3.5f); on the other hand, the Li deposits for the bare Cu sample appeared the be needle-like or small particles (Fig. 3.5a, 3.5b and 3.5c), as would be expected with carbonate electrolytes [5]. To clearly show the difference (dendrites versus chunky grains), carbonate electrolyte LP30 + 2% VC + 10% FEC was used here. The samples were prepared by depositing 1 mAh cm^{-2} Li at 0.5 mA cm^{-2} current density on

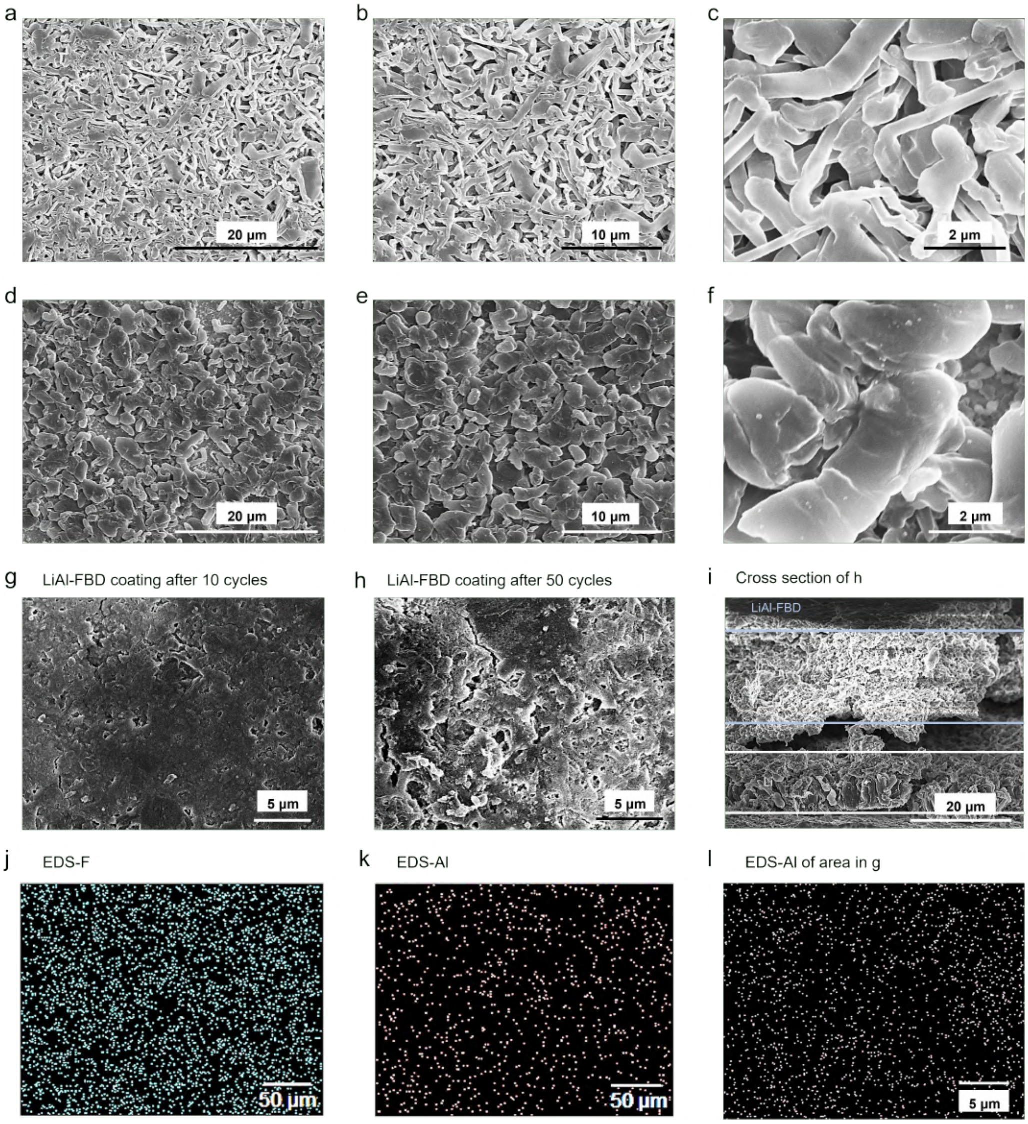

Figure 3.5: (a-c) SEM images of Li deposits on bare Cu at different scales. (d-f) SEM images of Li deposits on LiAl-FBD@Cu (underneath the LiAl-FBD coating) at different scales. (g-i) SEM images of LiAl-FBD@Cu (with Li deposits underneath) after 10 (g) or 50 (h,i) cycles in the Li | Cu half cells. (j,k) EDS images showing F (j) and Al (k) element distribution on the Li surface underneath LiAl-FBD coating. (l) EDS image showing Al element distribution for the area in (g).

either bare Cu or LiAl-FBD@Cu, followed by washing with anhydrous DME solvent to remove residue electrolyte and the coating layer.

The energy-dispersive X-ray (EDS) spectra showed uniformly distributed F and Al elements on the Li metal deposits surface although DME solvent washed most of the LiAl-FBD coating off (Fig. 3.5j and 3.5k). This not only confirms the planarly uniform distribution of LiAl-FBD coating, but also validates the XPS Al2p results by showing good contact between the ASEI and Li metal layer (Supplementary Figures 5.3, Fig. 5.9e).

Although after long cycling the LiAl-FBD coating layer disintegrated and became less conformal, the coating was still found to adhere to the surface of almost each Li deposit, serving as a functional ASEI (Fig. 3.5g, 3.5h and 3.5i; Supplementary Figures 5.3, Fig. 5.10). Particularly, as shown in Fig. 3.5i and Fig. 5.10f, the Li deposits (after 50 cycles) were densely packed underneath the LiAl-FBD layer (top part between the light blue lines and the layer was curled up due to peeling), confirming its protection effect even after long-term cycling.

The least Li | Li interfacial impedance evolution over time (Fig. 3.3b) and the fewest products of parasitic reactions between Li and electrolyte (Fig. 3.4c), further demonstrate the superior Li-surface protection effect of the LiAl-FBD coating is a critical factor for improving the Li deposition morphology. By contrast, the continuous increase observed in Li | Li impedance bare Li (Fig. 3.3a) along with the lack of conformal protection is responsible for its worse Li deposition morphology. These SEM observations are consistent with the Li | Cu cycling results (Fig. 3.7a and 3.7b) and confirm that the efficient design of LiAl-FBD improves Li growth morphology.

3.5 Battery Performance

After verifying its suitability as a conformal ASEI, LiAl-FBD coating was investigated in batteries to confirm its effectiveness in Li metal protection. Conventional carbonate-based electrolyte 1 M $LiPF_6$ in ethylene carbonate (EC) / dimethyl carbonate (DMC) (denoted as LP30) + 2% vinylene carbonate (VC) + 10% fluoroethylene carbonate (FEC) was chosen; therefore, it was possible to examine the effectiveness of LiAl-FBD coating in an electrolyte which is not only commercial, scalable and low-cost, but also not typically compatible with Li metal.

3.5.1 Li | Li symmetric full cells

Firstly, Li | Li symmetric cells were used to examine the electrolyte-blocking feature with LiAl-FBD coating. As already predictable from the EIS evolution over time, the cycling behavior of LiAl-FBD coated Li | Li symmetric cell is far more stable than bare Li one (Fig. 3.6a). The coated cell was cycled for more than 1000 h (500 cycles) without significant polarization or short circuiting, while the bare Li cell experienced severe overpotential increase after cycling for only $\sim$ 300 h, followed by failure at $\sim$ 460 h. In addition, the cycling overpotential value is $\sim$ 25 mV and $\sim$ 100 mV for LiAl-FBD@Li and bare Li, respectively, demonstrating a four-time lower polarization for the protected Li (Fig. 3.6b). These results prove the effectiveness of LiAl-FBD in preventing the Li metal corrosion caused by liquid electrolytes. Combined with the high ionic conductivity of the ASEI, stable impedance and cycling of Li metal anodes can be achieved.

To further confirm the electrolyte-phobic nature of our ASEI, a soaking experiment was conducted: a LiAl-FBD crystal was immersed in either the carbonate (LP30) or ether electrolyte (4M LiFSI/DME 27) used in this work; ^{1}H- and ^{19}F-NMR

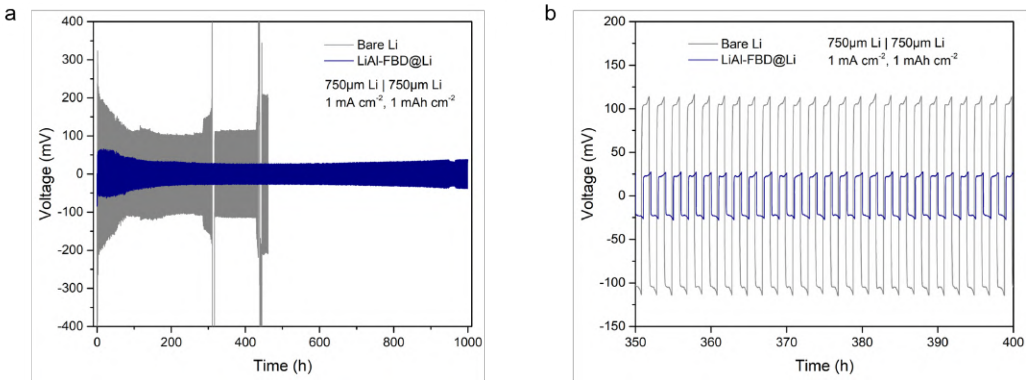

Figure 3.6: (a,b) Cycling performance of bare Li | bare Li and LiAl-FBD@Li | LiAl-FBD@Li symmetric cells; note that figure (b) is a portion of figure (a) as to better visualize the overpotential difference. All the cells used 1M LiPF6 in EC/DMC (LP30) + 2% VC + 10% FEC as the electrolyte.

were performed after 24 h, and they indicated negligible dissolution of LiAl-FBD species (Supplementary Figures 5.3, Fig. 5.8).

3.5.2 Li-Cu half cells

Li | Cu cells were also studied to show the impact of LiAl-FBD coating on cycling stability and Li metal CE. In contrast with the thick Li foils used in Li | Li symmetric cells, the practical, industrial 50-μm-thin Li was here used to assess the practicality of implementing LiAl-FBD coating in realistic battery structures. As suggested by the the voltage curve in Fig. 3.7a, severe fluctuation occurred in the Li | bare-Cu cell, especially during the initial and final stage of cycling; this further confirms the poor passivation capability of native SEI generated by liquid electrolyte. On the contrary, the Li | LiAl-FBD@Cu cell showed a more stable cycling plateau and longer cycle life than the bare Cu one, validating the LiAl-FBD protection for Li metal cycling. As expected, the extracted CEs of two replicated Li | LiAl-FBD@Cu half cells (filled and hollow blue dots in Fig. 3.7b) are consistently high (>97.5%). It can be also noted a slightly higher CE for the

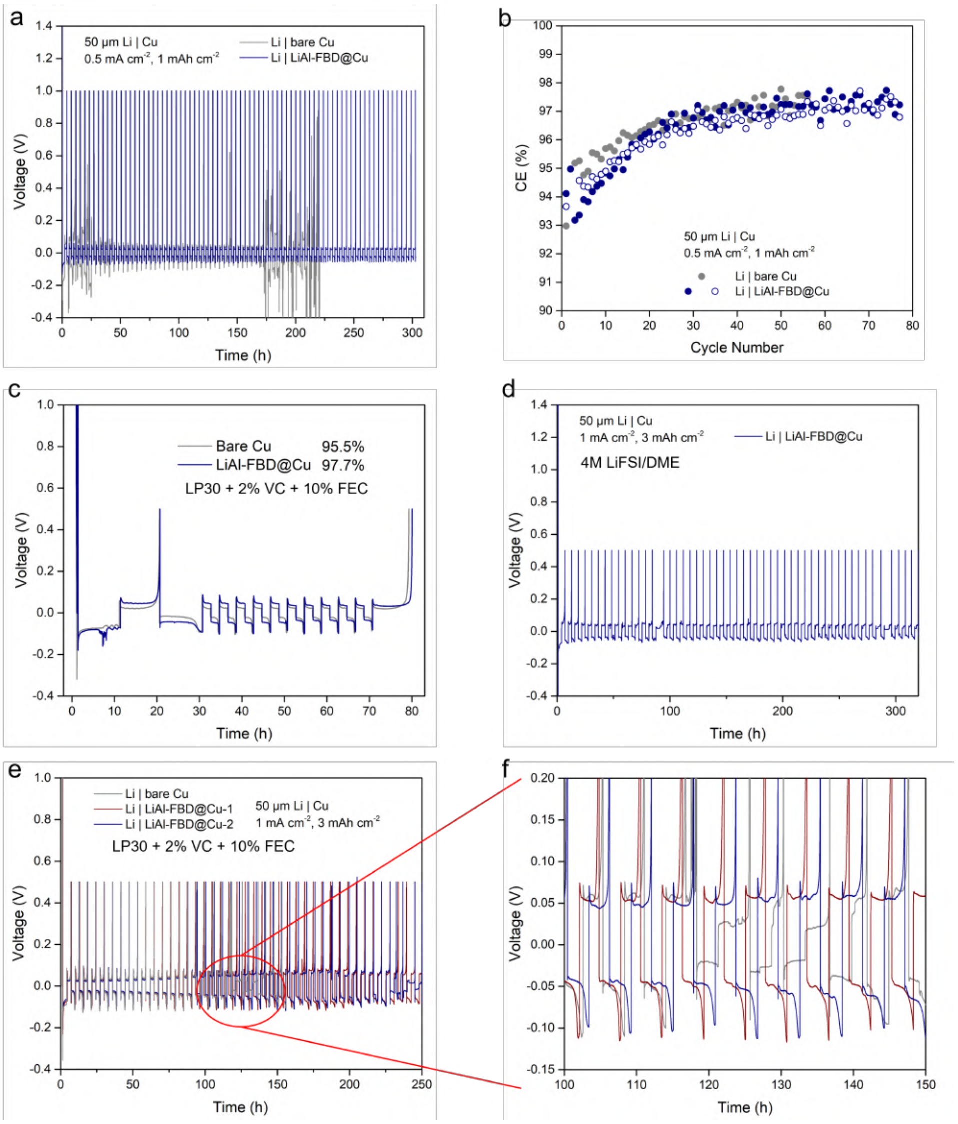

Figure 3.7: (a) Cycling curves of 50-μm-thick Li | bare Cu and 50-μm-thick Li | LiAl-FBD@Cu half cells using 1M LiPF6 in EC/DMC (LP30) + 2% VC + 10% FEC electrolyte. (b) CEs of Li | Cu half cells in (a). Replicated results for LiAl-FBD@Cu are shown in (b). (c) Aurbach protocol [31, 32] test of Li | bare Cu and Li | LiAl-FBD@Cu half cells showing the average CE. (d) Cycling of 50-μm-thick Li | LiAl-FBD@Cu half cell using 4M LiFSI/DME electrolyte at 1 mA cm^{-2} current density and 3 mAh cm^{-2} areal capacity. (e,f) Cycling of 50-μm-thick Li | bare Cu and 50-μm-thick Li | LiAl-FBD@Cu half cells using LP30 + 2% VC + 10% FEC electrolyte at 1 mA cm^{-2} current density and 3 mAh cm^{-2} areal capacity.

Li | bare-Cu cell for the initial ∼ 10 cycles (Fig. 3.7b), probably a consequence of the artifact caused by the voltage fluctuation at the initial cycling stage (Fig. 3.7a). By considering the voltage plateaux noises, the Aurbach CE protocol [31, 32] tests and the Li | Cu half-cell cycling under other conditions (see Fig. 3.7c to 3.7f), the superior performance for LiAl-FBD@Cu over the Li | bare-Cu ones is finally confirmed.

3.5.3 Li-NMC full cells

In order to investigate the effectiveness of LiAl-FBD coating under more realistic conditions, we finally assembled practical Li metal full batteries. Thin Li foil (50 μm thick), commercial lithium nickel manganese cobalt (NMC) oxide cathode sheets with high loadings (2 mAh cm^{-2} NMC532 from commercial source and 3.5 mAh cm^{-2} NMC811 provided by Hyundai Motor Company), lean electrolyte amount (30 or 10 μL/cell, i.e., electrolyte-to-cathode ratio was 15 μL mAh^{-1} for NMC532 and 2.8 μL mAh^{-1} for NMC811), and high cycling current (0.6 mA cm^{-2} for NMC532 cells and 1 mA cm^{-2} for NMC811 ones) were implemented here to faithfully replicate testing conditions.

First, we used a commercial carbonate electrolyte (LP30 + 2% VC + 10% FEC). Figure 3.8a shows that the bare-Li full cell suffered from a sharp decay at ∼100 cycles; this phenomenon was associated with electrolyte depletion [33] resulting from the unstoppable Li/electrolyte parasitic reactions. As plotted in Fig. 3.8b, the LiAl-FBD@Li | NMC532 full cells possessed stable cycle life, and over 60% of original capacity was retained after 200 cycles. No drastic decrease in capacity was observed, thus indicating the LiAl-FBD ASEI effectively protected the Li metal anode by preventing continuous corrosion or electrolyte depletion [33]. It is worth noting that the manifest difference in cycling behavior between the LiAl-FBD@Li cell and the bare one well conforms with the EIS evolution (Fig. 3.3a and 3.3b) and XPS (Fig. 3.4a to 3.4d) results. Consistent with the capacity retention trend, the CE of bare Li | NMC532 full cell experienced severe fluctuations from 100 cycles, while the CE was kept stable ($\sim$100%) throughout the whole cycle life (Fig. 3.8b).

To further push the cycling performance, high-concentration ether-based electrolyte, 4M LiFSI/DME27, was employed. As shown in Fig. 3.8c and 3.8d, the bare Li | NMC811 cell experienced a sudden capacity plunge after $\sim$130 cycles, exactly when the full-cell CE started to significantly fluctuate (Fig. 3.8c and 3.8d). By contrast, the LiAl-FBD@Li | NMC811 cell was stably cycled for $\sim$200 cycles followed by gradual capacity fading until $\sim$250 cycles (Fig. 3.8c). Such a gradual decay is consistent with the LiAl-FBD@Li | NMC532 cell results, and proves once again the protection effect of the LiAl-FBD ASEI. The CE of the LiAl-FBD cell was maintained at $\sim$100% for $>$230 cycles before any fluctuation occurred (Fig. 3.8d). When other electrolyte recipes and cycling conditions were used, the LiAl-FBD@Li cells all showed better performance than bare ones (Supplementary Figures 5.3, Fig. 3.8).

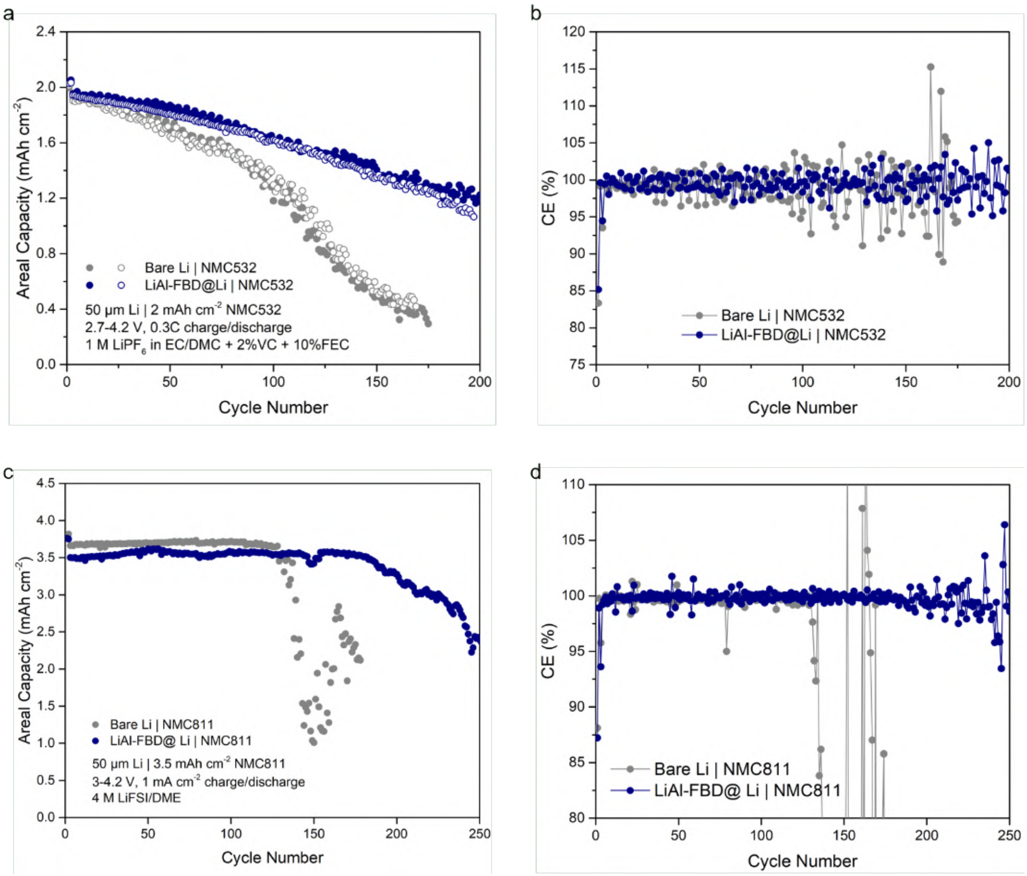

Figure 3.8: (a,b) Full cell performance and corresponding CE evolution using 50-μm-thick Li, commercial NMC532 cathode sheet, and commercial carbonate electrolyte. (c,d) Full cell performance and corresponding CE evolution using 50-μm-thick Li, industrial NMC811 cathode sheet, and high-concentration ether electrolyte. Replicated results for bare Li and LiAl-FBD@Li cells are shown here, in Fig. 3.8 and Supporting Figures, 5.12.

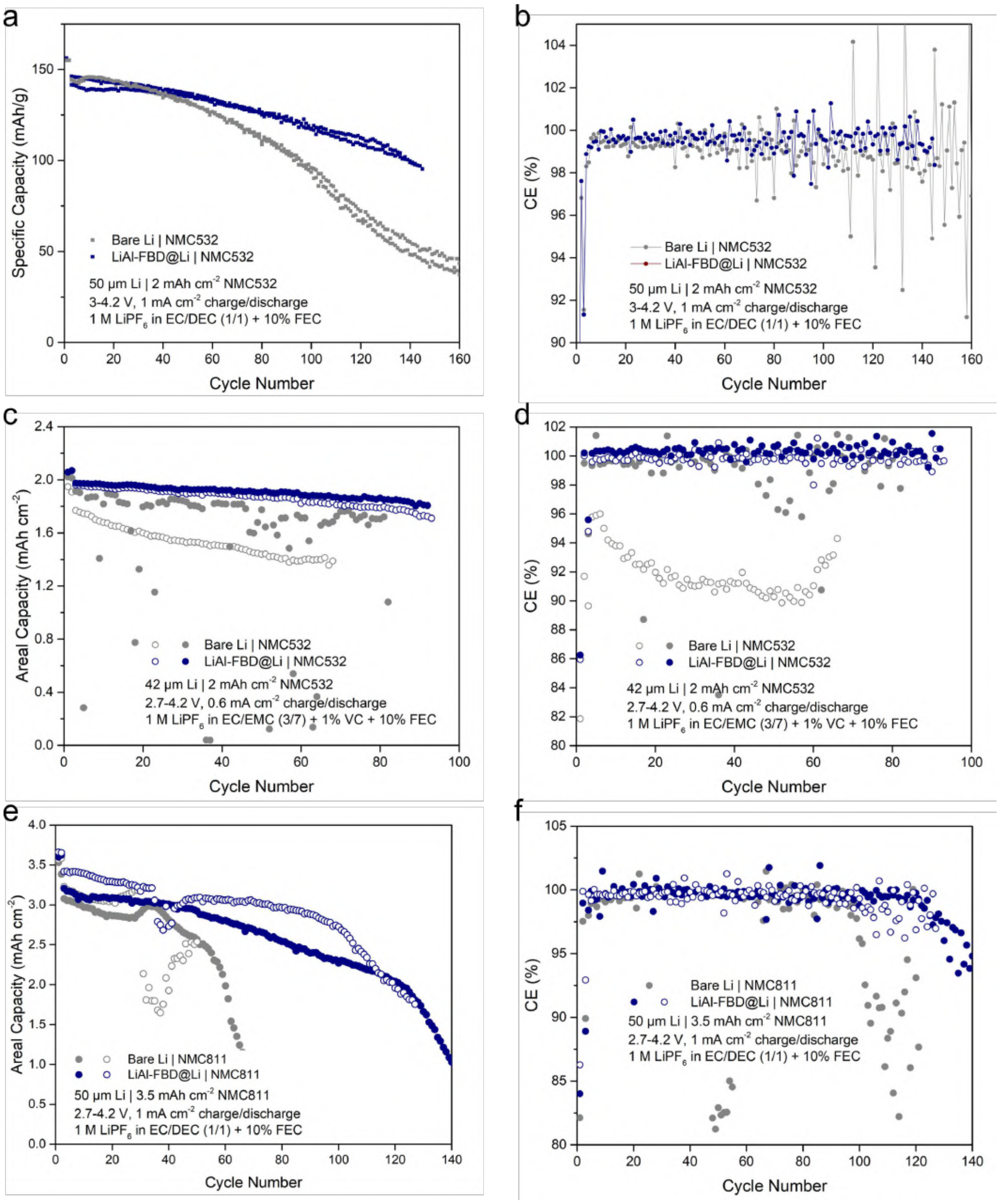
a
Specific Capacity (mAh/g)
Cycle Number
Bare Li | NMC532
LiAl-FBD@Li | NMC532
50 μm Li | 2 mAh cm⁻² NMC532
3-4.2 V, 1 mA cm⁻² charge/discharge
1 M LiPF₆ in EC/DEC (1/1) + 10% FEC
b
CE (%)
Cycle Number
Bare Li | NMC532
LiAl-FBD@Li | NMC532
50 μm Li | 2 mAh cm⁻² NMC532
3-4.2 V, 1 mA cm⁻² charge/discharge
1 M LiPF₆ in EC/DEC (1/1) + 10% FEC
c
Areal Capacity (mAh cm⁻²)
Cycle Number
Bare Li | NMC532
LiAl-FBD@Li | NMC532
42 μm Li | 2 mAh cm⁻² NMC532
2.7-4.2 V, 0.6 mA cm⁻² charge/discharge
1 M LiPF₆ in EC/EMC (3/7) + 1% VC + 10% FEC
d
CE (%)
Cycle Number
Bare Li | NMC532
LiAl-FBD@Li | NMC532
42 μm Li | 2 mAh cm⁻² NMC532
2.7-4.2 V, 0.6 mA cm⁻² charge/discharge
1 M LiPF₆ in EC/EMC (3/7) + 1% VC + 10% FEC
e
Areal Capacity (mAh cm⁻²)
Cycle Number
Bare Li | NMC811
LiAl-FBD@Li | NMC811
50 μm Li | 3.5 mAh cm⁻² NMC811
2.7-4.2 V, 1 mA cm⁻² charge/discharge
1 M LiPF₆ in EC/DEC (1/1) + 10% FEC
f
CE (%)
Cycle Number
Bare Li | NMC811
LiAl-FBD@Li | NMC811
50 μm Li | 3.5 mAh cm⁻² NMC811
2.7-4.2 V, 1 mA cm⁻² charge/discharge
1 M LiPF₆ in EC/DEC (1/1) + 10% FEC

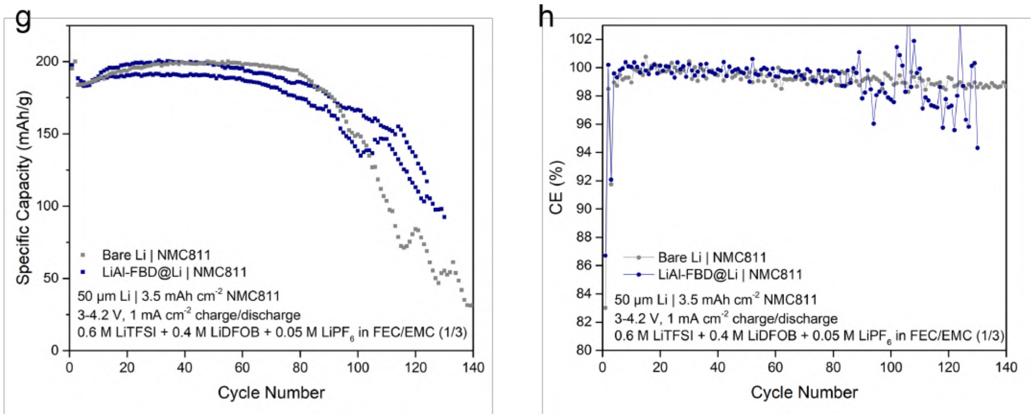

Figure 3.8: Long-term cycling of thin-Li | NMC full cells under different conditions. (a,b) 50-μm-thick Li | 2 mAh cm^{-2} NMC532 using LP40 + 10% FEC under C/2 cycling. (c,d) 42-μm-thick Li | 2 mAh cm^{-2} NMC532 using LP57 + 1% VC + 10% FEC under 0.3C cycling. (e,f) 50-μm-thick Li | 3.5 mAh cm^{-2} NMC811 using LP40 + 10% FEC under 0.3C cycling. (g,h) 50-μm-thick Li | 3.5 mAh cm^{-2} NMC811 using 0.6 M LiTFSI + 0.4 M LiDFOB + 0.05 M LiPF6 in FEC/EMC (3/7) under 0.3C cycling. Replicated cells are shown here.

Chapter 4

Conclusions and Outlook

In summary, we designed and synthesized a mechanically robust artificial solid electrolyte interface (ASEI), LiAl-FBD, that can be solution-processed easily on Li foil. The single crystal structure was solved and demonstrated to be $Li_3Al_3(FBD)_6(DME)_3$, in which Al^{3+} ions were bridged by FBD^{2-} ligands to form the anion-cluster while Li^+ ions were loosely bound and located at the periphery. Such a feature, along with high Li^+ content due to short ligands, enabled fast ion transport. In addition, the highly fluorinated ligands endowed the ASEI with electrolyte-phobicity. Careful characterizations such as nanoindentation, XPS, SEM, EIS, Li | Li symmetric cell cycling and Li metal CE showed that LiAl-FBD is a mechanically-strong, electrolyte-blocking, and ion-conductive coating to well protect the Li metal anode. The Li metal batteries using LiAl-FBD coated thin Li foil, commercial or industrial NMC high-voltage high-loading cathodes, and lean electrolyte condition showed superior cycling performance than bare Li cells, confirming the practicality of using this solution-processable ASEI in realistic Li metal batteries.

Bibliography

[1] Jun Liu et al. “Pathways for practical high-energy long-cycling lithium metal batteries”. In: *Nature Energy* 4.3 (2019), pp. 180–186.

[2] Yuliang Cao et al. “Bridging the academic and industrial metrics for next-generation practical batteries”. In: *Nature nanotechnology* 14.3 (2019), pp. 200–207.

[3] Xin-Bing Cheng et al. “A review of solid electrolyte interphases on lithium metal anode”. In: *Advanced science* 3.3 (2016), p. 1500213.

[4] MD Tikekar et al. *Design principles for electrolytes and interfaces for stable lithium-metal batteries. Nat Energy 1: 16114*. 2016.

[5] Zhiao Yu et al. “A dynamic, electrolyte-blocking, and single-ion-conductive network for stable lithium-metal anodes”. In: *Joule* 3.11 (2019), pp. 2761–2776.

[6] Mun Sek Kim et al. “Langmuir-Blodgett artificial solid-electrolyte interphases for practical lithium metal batteries”. In: *Nature Energy* 3.10 (2018), pp. 889–898.

[7] Kai Liu et al. “Materials for lithium-ion battery safety”. In: *Science advances* 4.6 (2018), p. 9820.

[8] Dingchang Lin, Yayuan Liu, and Yi Cui. “Reviving the lithium metal anode for high-energy batteries”. In: *Nature nanotechnology* 12.3 (2017), pp. 194–206.

[9] Wu Xu et al. “Lithium metal anodes for rechargeable batteries”. In: *Energy & Environmental Science* 7.2 (2014), pp. 513–537.

[10] Kai Liu et al. “Lithium metal anodes with an adaptive “solid-liquid” interfacial protective layer”. In: *Journal of the American Chemical Society* 139.13 (2017), pp. 4815–4820.

[11] Xiulin Fan and Chunsheng Wang. “High-voltage liquid electrolytes for Li batteries: progress and perspectives”. In: *Chemical Society Reviews* (2021).

[12] Benjamin Flamme et al. “Guidelines to design organic electrolytes for lithium-ion batteries: environmental impact, physicochemical and electrochemical properties”. In: *Green Chemistry* 19.8 (2017), pp. 1828–1849.

[13] Shuhong Jiao et al. “Stable cycling of high-voltage lithium metal batteries in ether electrolytes”. In: *Nature Energy* 3.9 (2018), pp. 739–746.

[14] Ziqi Zeng et al. “Non-flammable electrolytes with high salt-to-solvent ratios for Li-ion and Li-metal batteries”. In: *Nature Energy* 3.8 (2018), pp. 674–681.

[15] Jeffrey W Fergus. “Ceramic and polymeric solid electrolytes for lithium-ion batteries”. In: *Journal of Power Sources* 195.15 (2010), pp. 4554–4569.

[16] Junheng Li et al. “Polymers in Lithium-Ion and Lithium Metal Batteries”. In: *Advanced Energy Materials* 11.15 (2021), p. 2003239.

[17] Nian-Wu Li et al. “An artificial solid electrolyte interphase layer for stable lithium metal anodes”. In: *Advanced materials* 28.9 (2016), pp. 1853–1858.

[18] Hao Chen et al. "Uniform high ionic conducting lithium sulfide protection layer for stable lithium metal anode". In: *Advanced Energy Materials* 9.22 (2019), p. 1900858.

[19] Hansen Wang et al. "Lithium metal anode materials design: interphase and host". In: *Electrochemical Energy Reviews* 2.4 (2019), pp. 509–517.

[20] Fei Ding et al. "Dendrite-free lithium deposition via self-healing electrostatic shield mechanism". In: *Journal of the American Chemical Society* 135.11 (2013), pp. 4450–4456.

[21] Quan Pang, Laidong Zhou, and Linda F Nazar. "Elastic and Li-ion–percolating hybrid membrane stabilizes Li metal plating". In: *Proceedings of the National Academy of Sciences* 115.49 (2018), pp. 12389–12394.

[22] Shuya Wei et al. "Electrochemical interphases for high-energy storage using reactive metal anodes". In: *Accounts of chemical research* 51.1 (2018), pp. 80–88.

[23] Guangyuan Zheng et al. "High-performance lithium metal negative electrode with a soft and flowable polymer coating". In: *ACS Energy Letters* 1.6 (2016), pp. 1247–1255.

[24] Sabrina Fischer et al. "A Metal–Organic Framework with Tetrahedral Aluminate Sites as a Single-Ion Li+ Solid Electrolyte". In: *Angewandte Chemie International Edition* 57.51 (2018), pp. 16683–16687.

[25] Zhiao Yu et al. "A solution-processable artificial solid electrolyte interphase for practical lithium metal batteries". In: *Manuscript in preparation* (2022).

[26] Zhiao Yu, Yi Cui, and Zhenan Bao. "Design principles of artificial solid electrolyte interphases for lithium-metal anodes". In: *Cell Reports Physical Science* 1.7 (2020), p. 100119.

[27] Yayuan Liu et al. “An ultrastrong double-layer nanodiamond interface for stable lithium metal anodes”. In: *Joule* 2.8 (2018), pp. 1595–1609.

[28] Yue Gao et al. “Polymer–inorganic solid–electrolyte interphase for stable lithium metal batteries under lean electrolyte conditions”. In: *Nature materials* 18.4 (2019), pp. 384–389.

[29] Yuming Zhao et al. “Stable Li metal anode by a hybrid lithium polysulfidophosphate/polymer cross-linking film”. In: *ACS Energy Letters* 4.6 (2019), pp. 1271–1278.

[30] Zhiao Yu et al. “Molecular design for electrolyte solvents enabling energy-dense and long-cycling lithium metal batteries”. In: *Nature Energy* 5.7 (2020), pp. 526–533.

[31] Doron Aurbach, Yosef Gofer, and Jacob Langzam. “The correlation between surface chemistry, surface morphology, and cycling efficiency of lithium electrodes in a few polar aprotic systems”. In: *Journal of the Electrochemical Society* 136.11 (1989), p. 3198.

[32] Brian D Adams et al. “Accurate determination of Coulombic efficiency for lithium metal anodes and lithium metal batteries”. In: *Advanced Energy Materials* 8.7 (2018), p. 1702097.

[33] Chaojiang Niu et al. “Balancing interfacial reactions to achieve long cycle life in high-energy lithium metal batteries”. In: *Nature Energy* 6.7 (2021), pp. 723–732.

Chapter 5

Appendix

5.1 Materials

2,2,3,3-Tetrafluoro-1,4-butanediol (FBD) was purchased from SynQuest Laboratories and used as received. 1M lithium aluminum hydride in tetrahydrofuran solution (1M $LiAlH_4$/THF), THF (anhydrous, $\geq$99.9%, inhibitor-free), and vinylene carbonate (VC, 99.5%, acid <200 ppm, H_2O <100 ppm) were purchased from Sigma-Aldrich and used as received. 1,2-Dimethoxyethane (anhydrous, 99.5%) was purchased from ACROS Organics and used as received. Other commercial reactants were purchased from Sigma-Aldrich and used without further purification.

5.1.1 Battery Materials

1M $LiPF_6$ in EC/DMC (LP30), 1M $LiPF_6$ in EC/EMC (LP57) and 1M $LiPF_6$ in EC/DEC electrolyte (LP40) were purchased from Gotion. EMC, VC and LiDFOB were purchased from Sigma. FEC was purchased from Guangdong Canrd. LiTFSI was provided by Solvay. One layer of Celgard 2325 (25 μm thick PP/PE/PP) or alumina-coated PE (provided by Hyundai Motor Company) was used as separator. Thick Li foil (750 μm thick) was purchased from Alfa Aesar. Thin Li foil ($\sim$ 50 μm thick) was purchased from China Energy Lithium. Another type of thin Li foil ($\sim$ 42 μm thick) was provided by Hydro-Québec. Copper current collector (25 μm, 99.8% metals basis) was purchased from Alfa Aesar. Single-side coated $LiNi_{0.5}Mn_{0.3}Co_{0.2}O_2$ (NMC532) sheets with $\sim$ 2 mAh cm^{-2} capacity loading were purchased from MTI and $LiNi_{0.8}Mn_{0.1}Co_{0.1}O_2$ (NMC811) sheets with $\sim$ 3.5 mAh cm^{-2} capacity loading were provided by Hyundai Motor Company. Other battery materials, such as 2032-type coin cell cases, springs, and spacers were all purchased from MTI.

5.2 Methods

5.2.1 Synthesis of LiAl-FBD

In an argon-filled glovebox with sub-ppm O_2 (<1 ppm) and H_2O (<0.1 ppm) level (MBRAUN), to an 8 mL vial were added 162 mg FBD and 3 mL DME. Under stirring, 500 μL 1M $LiAlH_4$/THF was added dropwise into the vial. After stirring at room temperature overnight, the yielding solution was filtered through 0.45 μm PTFE filter into 8 mL vial, to obtain $\sim$ 50 mg mL^{-1} LiAl-FBD/DME solution. For single crystals, the LiAl-FBD solution was heated to 80 °C for 6 h to slowly evaporate part of the solvents. After cooling down to room temperature, the crystals were precipitated and transferred into anhydrous hexane for storing.

5.2.2 Fabrication of LiAl-FBD coated Li and Cu

In an argon-filled glovebox with sub-ppm O_2 and H_2O level (Vigor Tech), the coated Cu working electrodes or coated thin Li foils were fabricated with dip-coating method as follows. First, Li foils were punched into 1.0 (for Li | Li and LiCu cells) or 1.98 (for Li | NMC full cells) cm^2 round disks, while Cu foils were punched into 2.1 (for Li | Cu half cells) cm^2. Then they were dipped into $\sim$ 50 mg mL^{-1} LiAl-FBD in DME solution for 1 min and then lifted out. The remaining solution on Li was immediately but gently wiped out with Kimwipes (KIMTECH) until dry yet sticky surface formed.

5.2.3 Nanoindentation tests

For the nanoindentation measurement of Young's modulus and hardness, LiAl-FBD crystal was fixed using epoxy glue onto a Si wafer and the surface was polished finely. The as-prepared Si wafer was later mounted onto an aluminum puck using graphite paste. A Berkovich tip with a dynamic indentation method was used to probe the modulus and hardness of the crystal surface, and the measurement was performed on a Nanomechanics iNano Nanoindenter.

5.2.4 Material Characterizations

^{1}H-, ^{13}C-, and ^{19}F-NMR spectra were recorded on a Varian Mercury 400 MHz NMR spectrometer and ^{7}Li-NMR spectra were recorded on a UI 500 MHz NMR spectrometer at room temperature. A FEI Magellan 400 XHR SEM and a Thermo Fisher Scientific Apreo S LoVac were used for SEM and EDS characterizations. XPS profiles were collected by PHI VersaProbe 1 Scanning XPS Microprobe. The samples were transferred for XPS using a sample transfer vessel that prevented air exposure at any time. Before XPS measurement, the artificial SEIs coated or bare Li was soaked in the electrolyte for 4 days, and then washed with DME for 30 seconds to remove electrolyte and coating layers.

5.2.5 Electrochemical Measurements

All battery components used in this work were commercial large-scale products and electrochemical testing was all carried out in 2032-type coin cell configuration. The EIS measurements were carried out on a Biologic VMP3 system. The cycling tests for half cells and full cells were carried out on an Arbin system. The EIS measurements were taken over a frequency range from 7 MHz to 100 mHz. For Li | Cu half-cell CE cycling tests, ten pre-cycles between 0 and 1 V were initialized to clean Cu electrode surface, and then cycling was done by depositing 1 (or 3) mAh cm^{-2} of Li onto Cu electrode followed by stripping to 1 V. The average CE is calculated by dividing the total stripping capacity by the total deposition capacity after the formation cycle.

For Aurbach CE test, a standard protocol was followed [31, 32]:

(1) perform one initial formation cycle with Li deposition of 5 mAh cm^{-2} on Cu under 0.5 mA cm^{-2} current density and stripping to 1 V;

(2) deposit 5 mAh cm^{-2} Li on Cu under 0.5 mA cm^{-2} current density as Li reservoir;

(3) repeatedly strip/deposit Li with 1 mAh cm^{-2} under 0.5 mA cm^{-2} current density for 10 cycles;

(4) strip all Li to 1 V.

For the Li | NMC full cell study, NMC532 and NMC811 cathode sheets were used and stored in argon-filled glovebox as received. After the first two activation cycles at C/10 charge/discharge, the cells were cycled at different current densities and voltage ranges.

5.3 Supplementary Figures

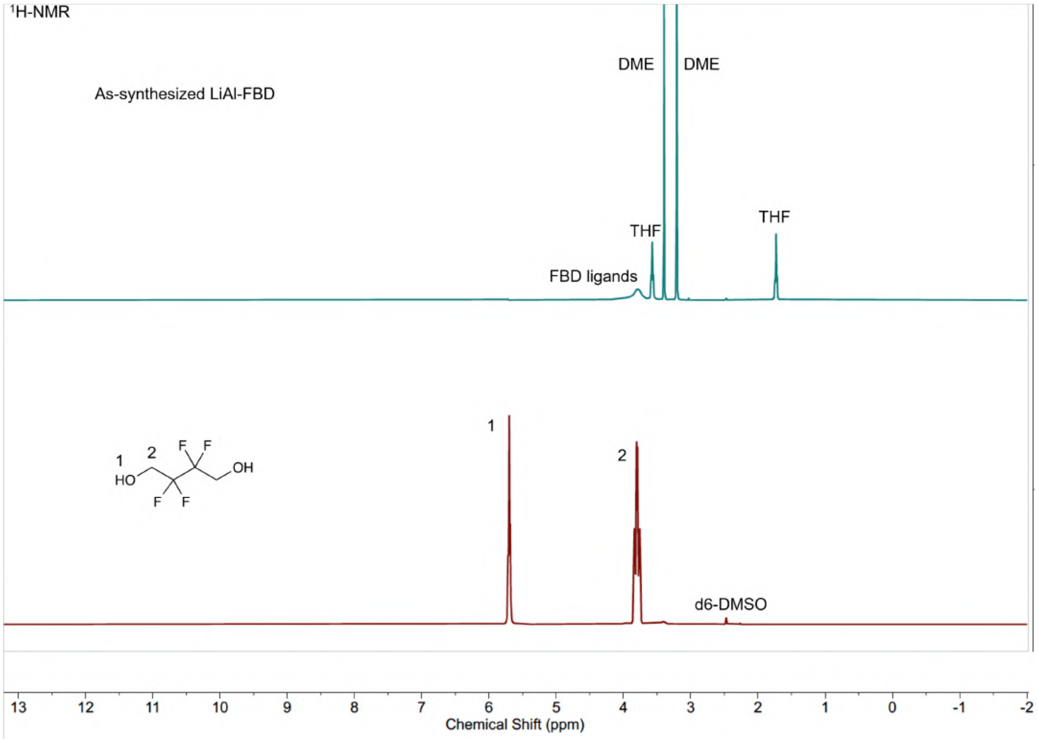

Figure 5.1: ^{1}H-NMR of LiAl-FBD (upper) and FBD (bottom).

<u>Note</u>: After the synthesis, the FBD diol was successfully deprotonated (the disappearance of peak 1) and the peak 2 got broadened. The remaining THF from $LiAlH_4$ solution and the DME solvent were also observed in the LiAl-FBD sample.

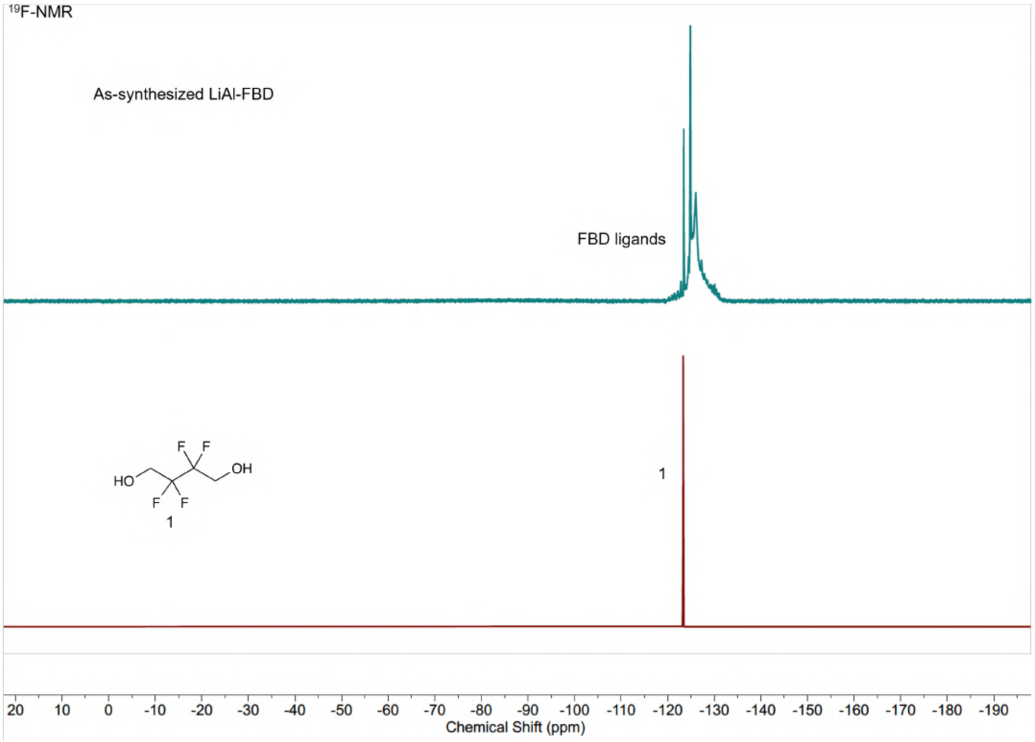

Figure 5.2: ^{19}F-NMR of LiAl-FBD (upper) and FBD (bottom).

Note: After the synthesis, the ^{19}F signal on FBD ligands got broadened, showing different chemical environments in the LiAl-FBD material.

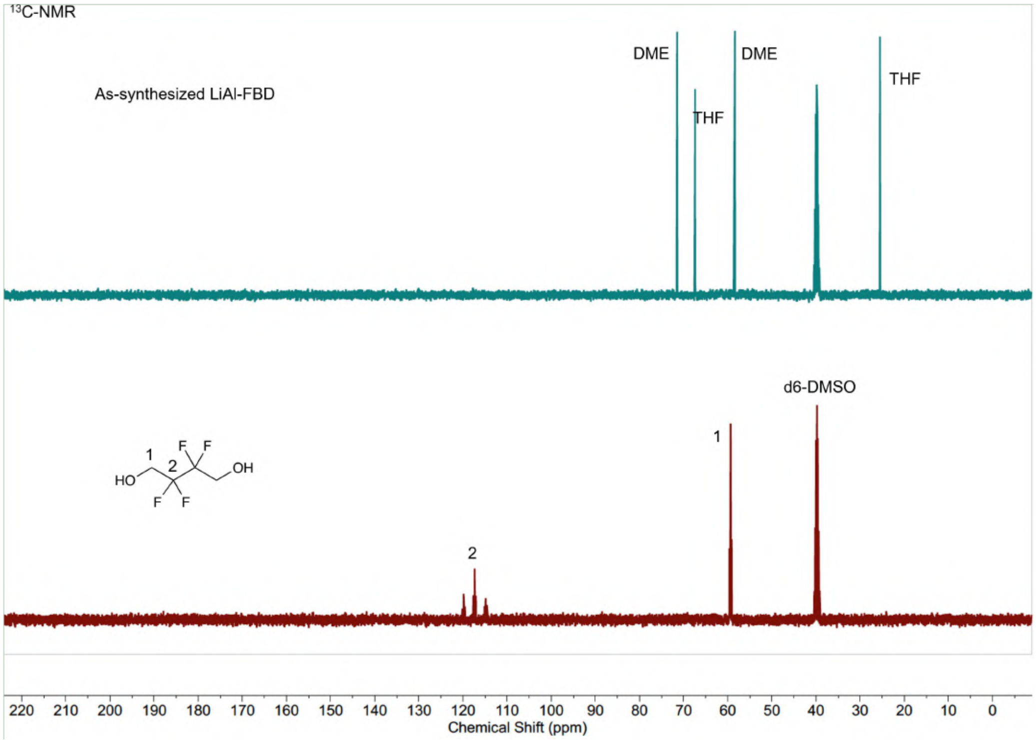

Figure 5.3: ^{13}C-NMR of LiAl-FBD (upper) and FBD (bottom).

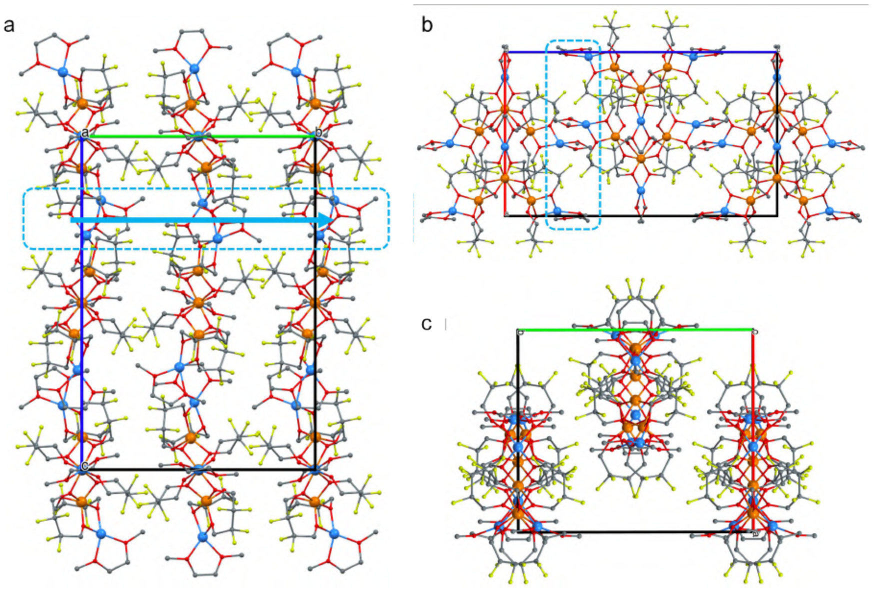

Figure 5.4: Crystal structure of $Li_3Al_3(FBD)_6(DME)_3$ viewing from a- (a), b- (b), and c- (c) axis [25].

Note: The potential Li+ ion transport pathway was labeled in light blue arrow in (a) and (b). Particularly, a sterically favored Li^+ transport channel can be observed from (b). The space is only occupied by a fewer species and Li^+-DME is expected to readily hop.

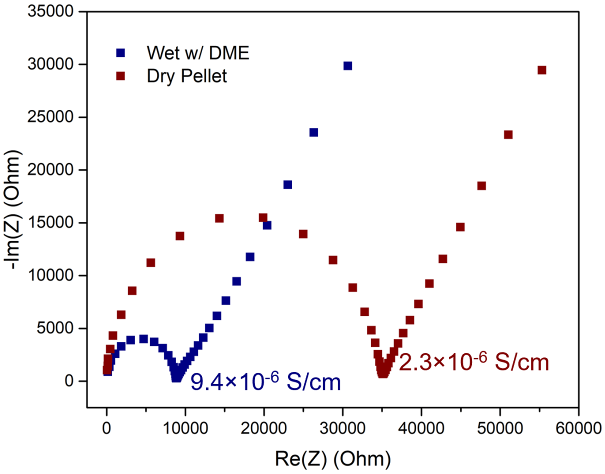

Figure 5.5: Nyquist plot of electrochemical impedance of dry and wet LiAl-FBD pellet. The wet pellet was prepared by adding 10 w.t.% DME solvent as the plasticizer into the dry pellet.

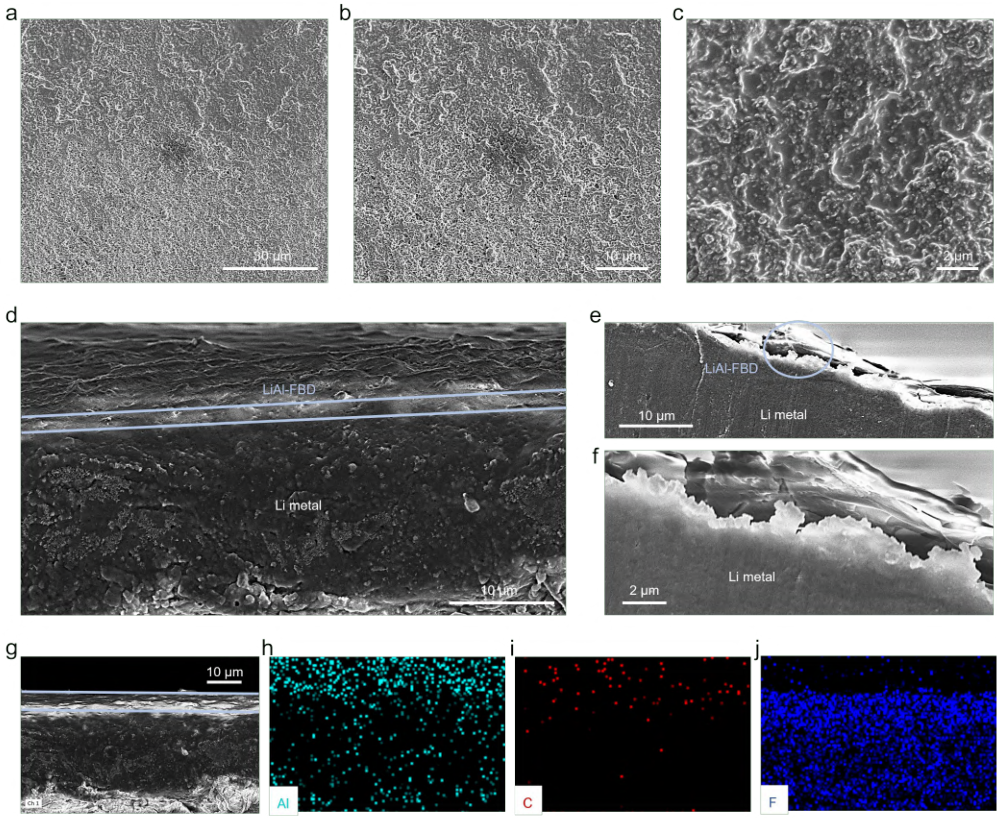

Figure 5.6: (a-c) Top-view SEM images with different scales showing the conformal morphology of LiAl-FBD coating. (d-f) Cross-sectional SEM images showing the thickness (∼500 nm) of LiAl-FBD coating on Li foil. (g-j) EDS of LiAl-FBD coating on 50-μm-thick Li metal foil: Al (h), C (i), and F (j).

Note: The samples used here were Li foils directly dip-coated by LiAl-FBD solution. As shown from the top-view SEM images (a-c), the LiAl-FBD showed conformal coating that covered Li metal surface at all different scales. The cross-sectional SEM images showed that the coating thickness is around 500 nm. The EDS results further confirmed the existence and location of LiAl-FBD: the characteristic elements in LiAl-FBD coating layer such as Al, C and F were concentrated around the coating area. Small amount of signal noise/contamination showed up around the Li metal foil area, which mainly originated from the sample preparation (scissors cutting).

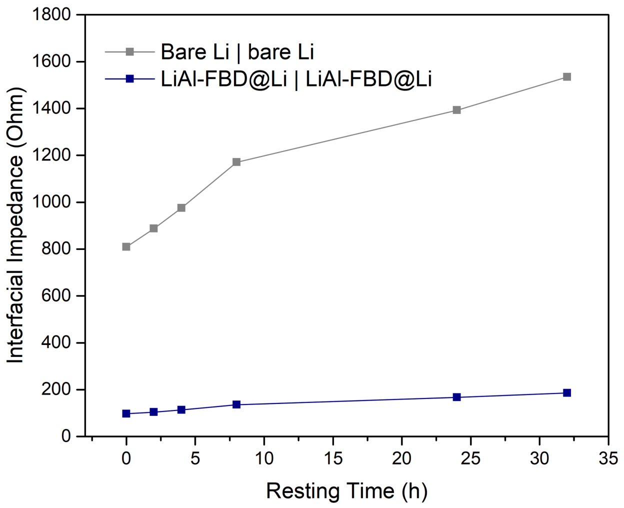

Figure 5.7: Interfacial impedance evolution of bare Li | bare Li and LiAl-FBD@Li | LiAl-FBD@Li symmetric cells over resting time, extracted from Fig. 3.3a and 3.3b.

Note: The absolute values of impedance were much lower for LiAl-FBD coated Li symmetric cell, and the increasing trend of impedance was suppressed as well.

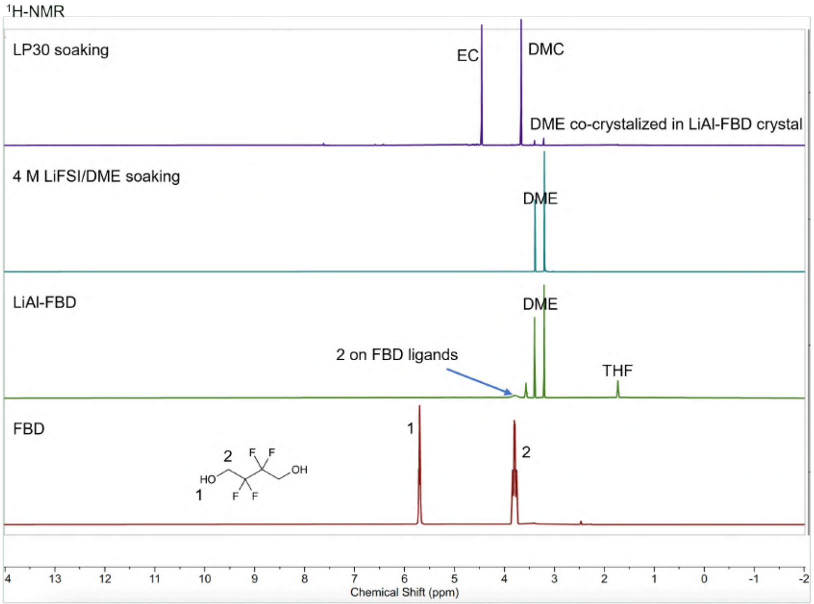
a ^{1}H-NMR

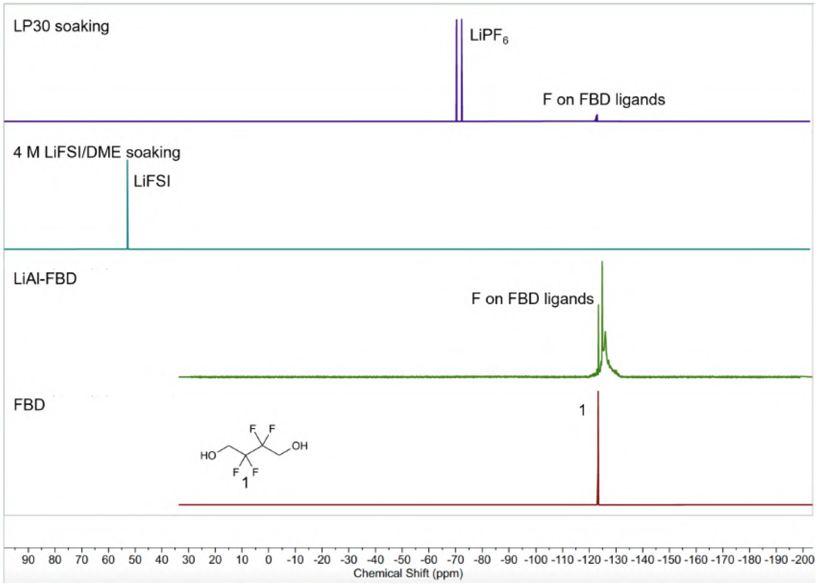
b ^{19}F-NMR

Figure 5.8: ^{1}H- (a) and ^{19}F- (b) NMR of the solutions after LiAl-FBD crystal soaking in LP30 or 4M LiFSI/DME electrolytes for ∼24 h.

Note: Overall, the LiAl-FBD was stable after soaking in the electrolytes we used in this work, with the electrolyte solutions containing few LiAl-FBD species as well.

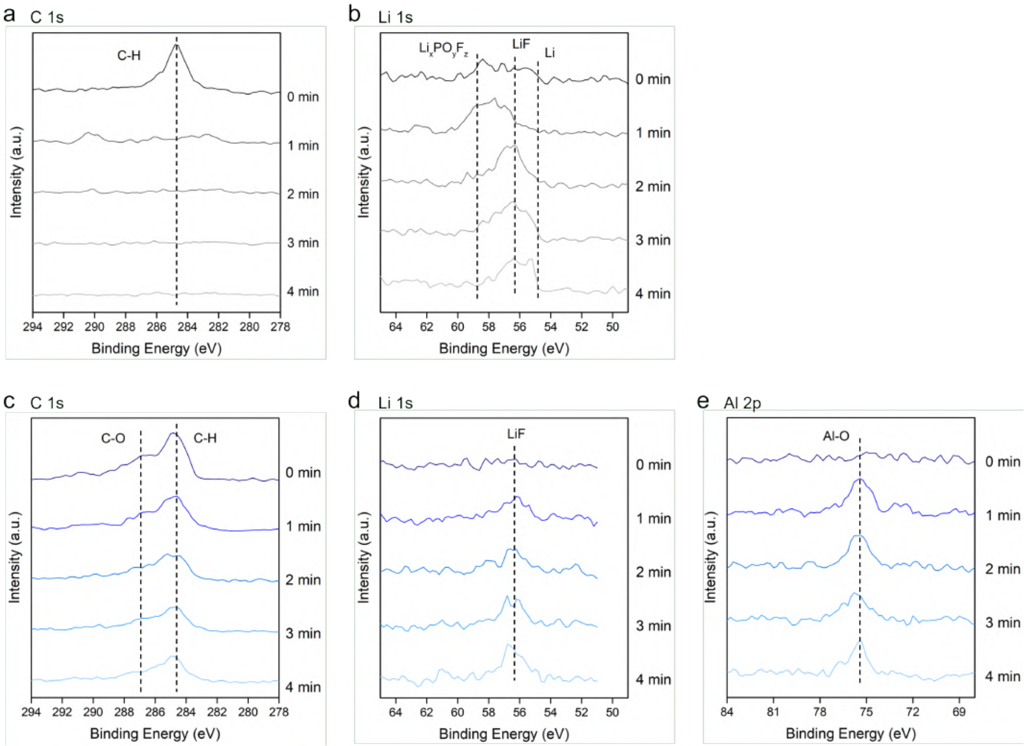

Figure 5.9: (a,b) XPS C1s (a) and Li1s (b) of bare Li. (c-e) XPS C1s (c), Li1s (d) and Al2p (e) of LiAl-FBD@Li.

Note: Compared to the elemental information on bare Li surface, the LiAl-FBD@Li surface showed more C-O in C1s spectra and vertically uniform distribution of LiF species in F1s spectra, both of which are critical features for favorable Li metal protection. The Al2p spectra showed Al-O bonds which derived from LiAl-FBD coating.

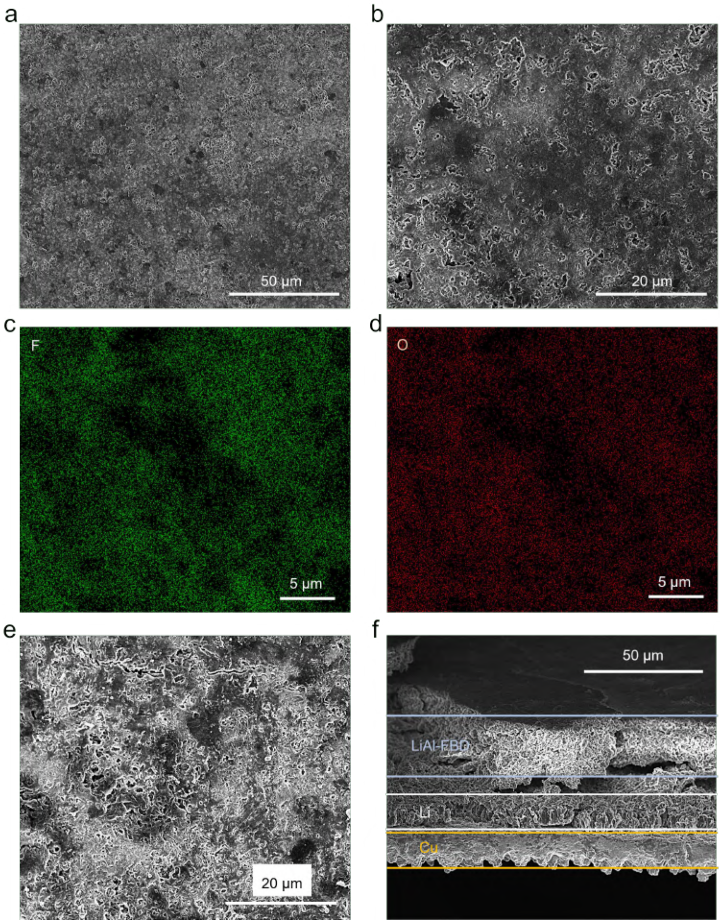

Figure 5.10: (a,b) SEM images of LiAl-FBD@Cu (with Li deposits underneath) after 10 cycles in the Li | Cu half cell. (c,d) EDS mapping of F (c), and O (d) element. (e,f) SEM images (top-view for e and cross-sectional for f) of LiAl-FBD@Cu (with Li deposits underneath) after 50 cycles in the Li | Cu half cell.
Carbonate electrolyte LP30 + 2% VC + 10% FEC was used here. The samples were prepared by cycling 1 mAh cm^{-2} Li at 0.5 mA cm^{-2} current density on either bare Cu or LiAl-FBD@Cu for either 10 or 50 cycles, followed by depositing 1 mAh cm^{-2} Li at 0.5 mA cm^{-2} current density on the Cu substrate (underneath LiAl-FBD coating).

Note: The EDS colors scheme of different elements are different from those used in Fig. 3.5j, 3.5k, 3.5l since different SEM/EDS instruments were used. As shown in (f), the LiAl-FBD coating (top part between the light blue lines) was peeled off (the layer was curled up due to peeling) and the Li deposits (deposited after 50 cycles) were densely packed underneath the LiAl-FBD layer, showing its protection function even after long-term cycling.

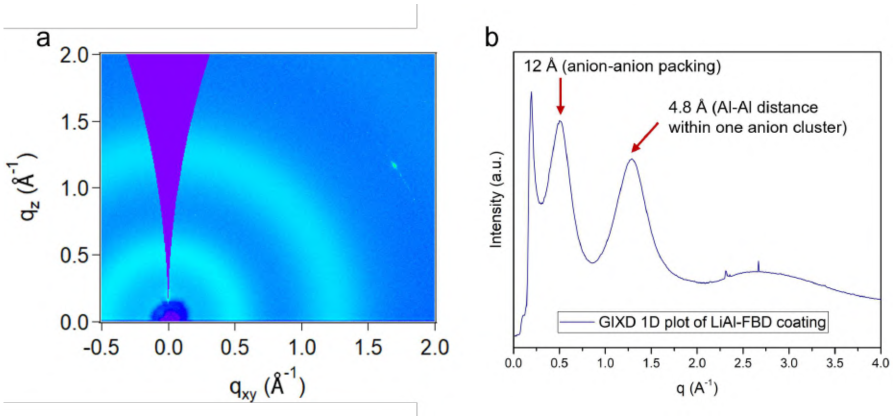

Figure 5.11: (a,b) Grazing-incidence wide-angle X-ray scattering (GIWAXS) results of LiAl-FBD coating on Si wafer [25].

Note: The GIWAXS analysis supports the polarized optical microscope results (Fig. 3.2c and 3.2d) by showing distinguished anion packing peak at ∼12 Å(q ∼0.52 Å^{-1}).

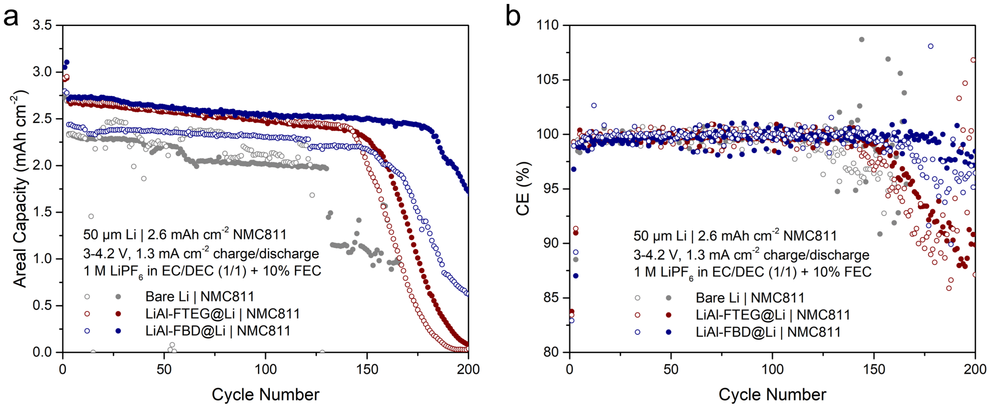

Figure 5.12: Comparison of cycling performance of thin-Li | NMC full cells: bare Li, LiAl-FTEG@Li, and LiAl-FBD@Li. 50-μm-thick Li | 2.6 mAh cm^{-2} NMC811 using LP40 + 10% FEC under 0.5C cycling. Replicated cells are shown here.

Note: Proposed in a previous report [5], LiAl-FTEG is a dynamic, single-ion-conductive and electrolyte-blocking coating material with with low modulus (storage modulus around 1-10 MPa by rheological measurement). LiAl-FBD coating shows slightly better cycling stability than bare control or LiAl-FTEG@Li, which can be attributed to the mechanical strength of LiAl-FBD (Young's modulus around 30-40 GPa by nanoindentation).

ETH
Eidgenössische Technische Hochschule Zürich
Swiss Federal Institute of Technology Zurich

Au NWs/MWCNTs/Au NWs transparent and stretchable current collector for Li-ion batteries

Semester Project I

Luca Mondonico

19-945-641

`lmondonico@student.ethz.ch`

Supervisor: Prof. Markus Niederberger

ETH Zürich

Acknowledgements

I thank...

PROF. DR. MARKUS NIEDERBERGER for having me as part of the multifunctional materials group at ETH Zürich.

TIAN LIU for the precious help and guidance during this research project.

Introduction

As often seen in science fiction films, it is anticipated that futuristic technology will eventually be in the form of portable devices. In recent times, transparent and wearable electronic devices such as smart glasses, electronic maps or flexible screens are gaining tremendous scientific and social attention. However, they still contain a lot of opaque and rigid electronic parts, thus making it hard to truly call them "transparent and wearable" electronics. Therefore, these flexible devices will require electrodes with not only high transparency and electrical conductivity, but also good mechanical compliance. Indeed, during standard operations these devices will undergo different mechanical deformations, ranging from stretching and bending up to twisting and folding. In the last decade, many alternatives to conventional materials have been suggested. For instance, ITO (indium tin oxide) was proposed due to its high transparency and conductivity; however, intrinsic drawbacks of ITO film, such as its brittleness, limited indium resources[3], and high fabrication expense due to high-temperature or vacuum processing[4] limit its use in wearable flexible devices. Carbon nanotubes (CNTs)[5,6], graphene[7,8] and metallic nanowires (NWs)[9-11] have also been introduced. Despite displaying optimal elasticity, flexibility and stretchability, CNTs often suffer from relatively poor electric conductivity (EC), thus low transparency to achieve moderate conductivity. Metallic NWs tend to manifest complementary properties. Metallic NWs, especially Ag NWs (EC $\approx 6.3 \cdot 10^5$ S/cm)[12] and Au NWs (EC $\approx 4.52 \cdot 10^5$ S/cm)[13] have high conductivity because of the high electron density of the constituting metals, but also flexible and elastic. This said, metallic NWs still managed to be used, for instance as transparent electrodes substitutes in the manufacturing of flexible solar cells. Each of these materials has its own strengths and weaknesses, which are inevitably reflected in the performances of the resultant conductor. One of the main objectives of this Semester Project is to combine two different materials in order to account for each material's shortcomings with each other's strength; we attempt to resolve the existing limitations of stretchable electronics by implementing hybrid nanocomposites using a hierarchical transparent structure. The proposed hybrid material is a hierarchical multiscale Au NWs/Multi-walled carbon nanotubes (MWCNTs)/Au NWs nanocomposite percolation network upon a flexible, transparent and hexagonal-structured PDMS membrane, with gold nanowires with relatively smaller dimension (Ø ≈ 3 nm, L ≈ 50−100 μm) and MWCNTs with relatively smaller length but larger dimension (Ø ≈ 11 nm, L ≈ 5−20 μm). In this research, we prepared a Au NWs/MWCNTs/Au NWs hybrid nanocomposite current collector with the enhanced mechanical compliance and optical transparency. The final structure is proved to be conductive (average resistance of 40-50 Ω), transparent (T: 80-85%), highly stretchable (up to 100% strain) with consistent mechanical reliability over long repeated bending/stretching cycles (1000 cycles).

Results and discussion

We report in **Figures 1a**,**1b** and **1c** a simplified 3D scheme of the hierarchical multiscale Au NWs/MWCNTs/Au NWs nanocomposite conductor that was prepared. As suggested by previous research studies[14], the presence of a multilayered structure formed by various materials of different sizes and conductivities may generate and enhance electron transport across different scales[15,16]. For the hybrid conductor, highly conductive Au NWs percolation networks provide backbone electrodes for a fast electron transport, while the quite resistive but elastic MWCNTs carpet guarantees both stretchability and flexibility. In addition to this, the carbon nanotubes can provide local path for electrons which will be further collected by the electron freeway of the Au NWs backbone mesh. A simplified sketch of the multiscale electron transport in our hierarchical nanocomposite is shown in **Figures 1d** and **1e.**

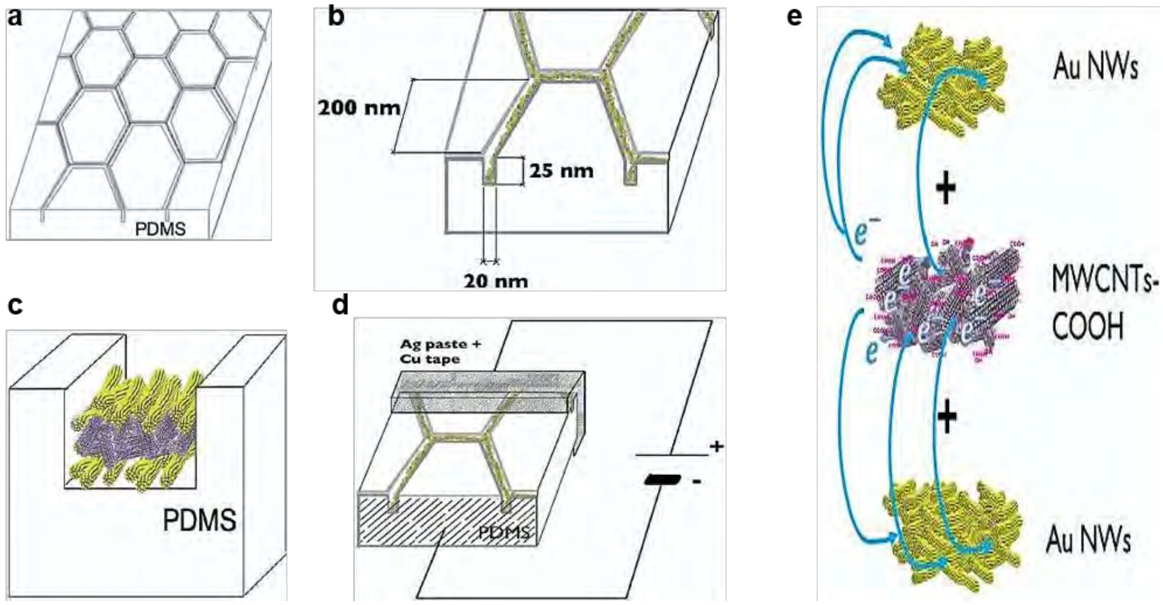

Figure 1. (a) hexagonal grid on the PDMS membrane; (b) size of the channels and characteristic dimensions of the grid; (c) cross-section of a channel on the PDMS substrate; (d) 3D scheme of the hybrid current collector when a certain voltage is applied to two opposite sides; (e) multiscale electron transport in the Au NWs/MWCNTs/Au NWs layered structure.

Transmittance measurements were performed using an integrated-sphere-combined UV/Vis spectrophotometer. Considering only the first layer of Au NWs, different Au NWs volumes were tested: 0.2 mL, 0.6 mL, 1.0 mL and 1.4 mL. All the volumes were spray-coated with nitrogen gas at a pressure of 0.5 bar. **Figure 2e** shows the transmittance in the visible range for the four tested sample: at a reference wavelength of 550 nm, the transmittances of 82.8%, 81.4%, 81.0% and 80.3% were obtained for volumes of 0.2 mL, 0.6 mL, 1.0 mL and 1.4 mL, respectively.

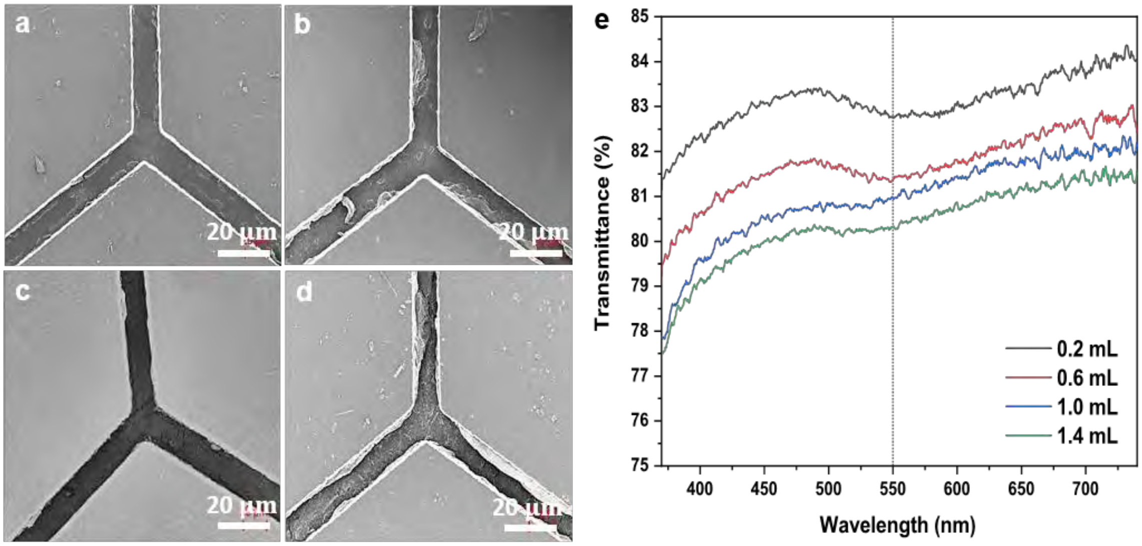

Figure 2. SEM images for different Au NWs spray-coated volumes: 0.2 mL (a), 0.6 mL (b), 1.0 mL (c) and 1.4 mL (d); (e) the transmittances for four Au NWs spray-coated volumes: 0.2 mL, 0.6 mL, 1.0 mL and 1.4 mL.

The total percent transmittance decreases with increasing Au NWs spray-coated volumes. Scanning electron microscope (SEM) images were used determine the minimum amount of Au NWs that guarantees a uniform coverage of the PDMS channels. The results are shown and compared in **Figures 2a**, **2b**, **2c** and **2d**. A homogeneous Au NWs layer in the PDMS channels is achieved for a volume of 1mL. For higher volumes (i.e. 1.4 mL), bulky Au-NWs-compounds have formed on the side walls of the channels; these aggregates are responsible for a major drop in the overall transmittance. At lower volumes, such as 0.2 mL and 0.6 mL, the coverage results incomplete, with several disjointed Au NWs islands on the PDMS substrate. As a successive step, the concentration of MWCNTs of the second layer had to be optimized. Three different concentrations (i.e. 1:6, 1:4 and 1:2 MWCNTs-ethanol) were tested and compared via the total transmittance of the so-obtained devices.

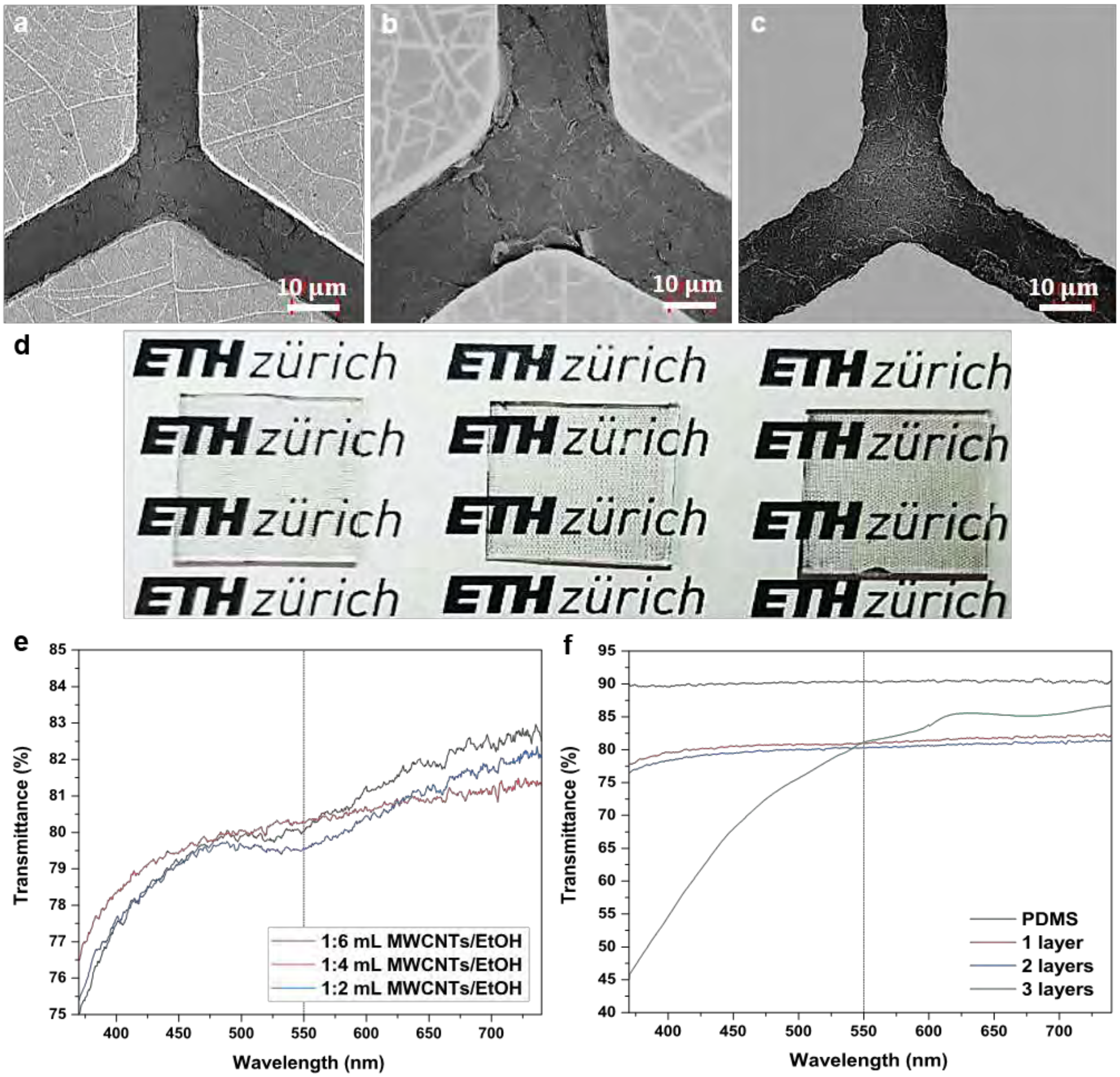

Figure 3. SEM images for different MWCNTs-Ethanol concentrations: 1:6 (a), 1:4 (b) and 1:2 (c); (d) digital pictures for 1-layer (left), 2-layer (middle) and 3-layer (right) current collectors; (e) the transmittances for three MWCNTs-ethanol concentrations: 1:6, 1:4 and 1:2; (f) transmittance in the visible range for current collectors with one, two and three spray-coated layers in the PDMS channels.

Figure 3e displays the total transmittance in the visible range: at a reference wavelength of 550 nm, the transmittances of 80.0%, 80.3% and 79.5% were measured for MWCNTs concentrations of 1:6, 1:4 and 1:2, respectively. **Figures 3a**, **3b** and **3c** show the SEM images for each MWCNTs concentration tested. As can be observed, the best coverage was obtained for a MWCNTs concentration in ethanol of 1:4, while for a lower CNT-ethanol ratio (i.e. 1:6) and a higher CNT-ethanol ratio (i.e. 1:2) the channels showed an incomplete coverage and an excess presence of MWCNTs bulky aggregates, respectively. The optimized devices were obtained by spray-coating 1 mL of Au NWs for the first and third layer, and 2 mL of 1:4 ethanol-diluted

MWCNTs for the intermediate layer. **Figure 3d** compares the current collecting nanocomposites with 1 layer, 2 layers and 3 layers of spray-coated materials inside the PDMS channels, respectively. As easily deduced from previous transparency measures, the more the spray-coated layers the less the devices transparency will be. This can be explained by assuming that the more the number of spray-coating stages the PDMS membrane undergoes, the more the number of bulky agglomerates that are formed on the channels side walls; these agglomerates are supposed to be responsible for the major transmittance drop that we observe while increasing the number of layers. A further evidence can be found in **Figure 3f**, where total transmittance in the visible range were collected for the three tested devices. The bare PDMS membrane's transmittance is also shown as a baseline. At a reference wavelength of 550 nm, percent transmittances of 90.4%, 81.0%, 80.3% and 81.1% were measured for a bare PDMS, 1-layer, 2-layer and 3-layer device, respectively. The current collector transmittance effectively decreases with the number of spray-coated layers.

In order to prove the multiscale nanocomposite to be highly stretchable and flexible, we tested it under two main mechanical deformation: stretching and bending. For the stretching tests, the spray-coated PDMS membranes were hooked with two binder clips on two opposite sides; then, they were manually stretched once up to a Δε%≈100% strain. Digital pictures of the PDMS membranes under stretching are shown in **Figures 4a** and **4b**. As can be seen, the PDMS membranes displayed structural integrity up to 100% strain, without fracturing or breaking phenomena. For the bending tests, the spray-coated PDMS membranes were hooked with two crocodile clips in the middle of two opposite sides; then, they were manually bent once up to an angle of 90°. A picture of the outcome of the bending test on a PDMS membrane is shown in **Figure 4c**. We used a curing agent-elastomer ratio of 1:20; by further increasing the amount of elastomer with respect to the curing agent, the elasticity of the PDMS membrane (and of the entire current collector) will improve. The devices were mounted on a SEM sample holder (**Figure 4h**) and stretched up to different strain levels: Δε% = 20%, 50% and 100%. As shown in **Figures 4d**, **4e** and **4f**, at a strain of 20%, the microstructure was still intact, without displaying fracturing nor cracking. At a strain of 50% some cracking appeared at the junction points of the PDMS channels; however, the top Au NWs layer still appeared quite homogeneous and compact. Instead, at a strain of 100%, some severe cracking could be observed at the junction points, suggesting a potential increase in overall electrical sheet resistance (see **Figure 4g**).

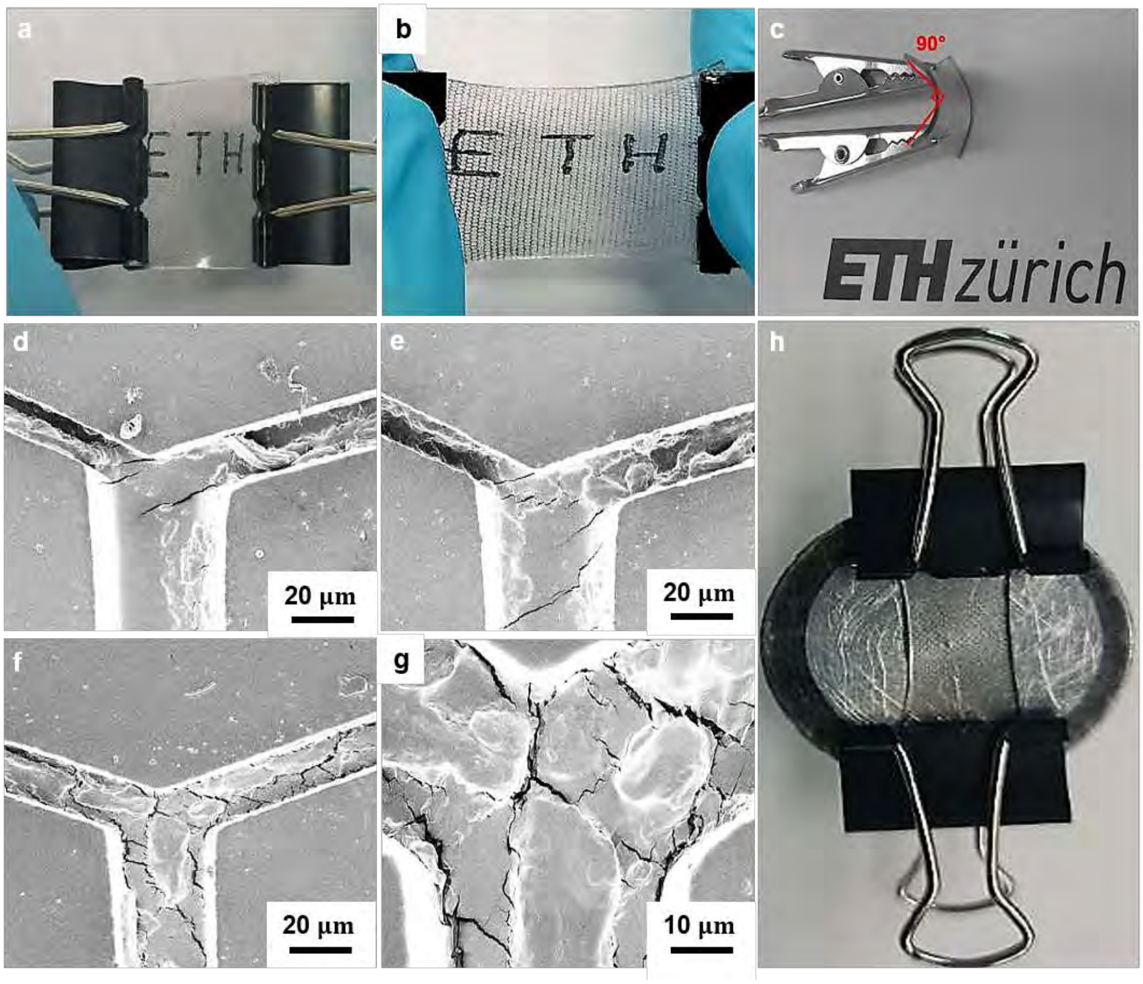

Figure 4. Digital pictures of the PDMS membranes under a Δε% ≈ 0% (a) and Δε% ≈ 100% (b) stretch; (c) digital picture of the PDMS membrane under θ=90° bending; SEM images of the current collectors' intra-channel microstructure during uniaxial stretching tests at 20% (d), 50% (e) and 100% (f) strain; (g) magnified detail of the multi-layered structure at the channels' junction points at Δε% ≈ 100%; (h) sample holder setup for under-stretch SEM imaging.

For the sheet resistance under uniaxial stretching, three identical samples were manually tested for 1000 stretching cycles at three different strain levels: Δε% ≈ 20%, 50%, 100%. The sheet resistance was measured with a multimeter (Fluke Digital Multimeter 15B+) after each cycle. **Figures 5a**, **5b** and **5c** show the experimental setup that was used during each measurement, together with the multimeter displays reporting the no-stretch sheet resistances for each device. The current collectors (2 cm x 2 cm squares with an average thickness of 1 mm) displayed initial sheet resistances of 37.0 ohm/sq, 47.8 ohm/sq and 52.5 ohm/sq. This may suggest a high reproducibility of the hybrid nanocomposites manufacturing process. Quantitative results of the normalized sheet resistances measurements with the number of uniaxial stretching cycles are plotted in **Figure 5f**. We observe an overall increase (up to 25%) in the current collectors sheet resistance as the number of stretching cycles increases. This result may be due to a progressive loss of contact between the Ag paste (see Experiments section) and the hybrid nanocomposite material in the PDMS channels. In addition, the increasingly severe wrinkling of the multilayered structure may provoke a breaking of the 3-layer structure and the multiscale percolation network, leading to a dramatic increase of the current collector sheet resistance with time and number of deformation cycles. For the sheet resistance under bending, three identical samples were manually tested for 1000 bending cycles at the same fixed bending angle: θ=90°. **Figure 5d** shows the experimental setup that was used during each measurement; a magnified detail of the under-bending membrane is also shown (**Figure 5e**).

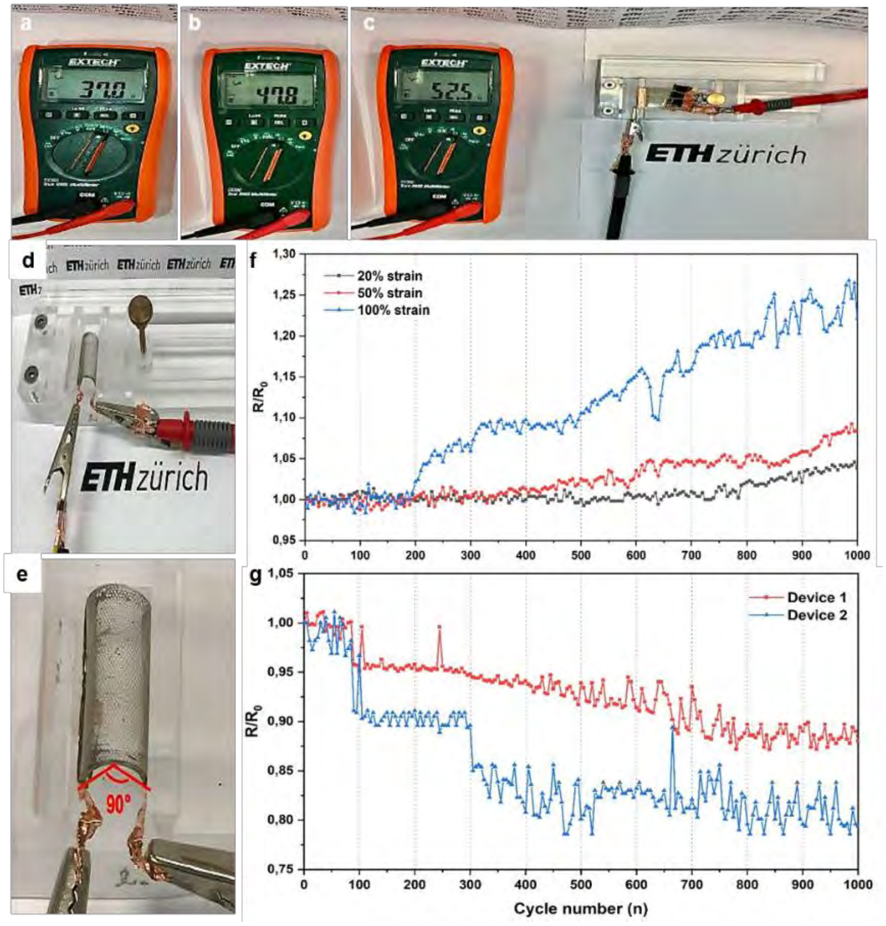

Figure 5. Experimental setup for sheet resistance measurements during 1000 uniaxial stretching cycles (a,b,c) and 1000 bending cycles (d); (e) magnified detail of the under-bending membrane; sheet resistance measurements for each of the 1000 uniaxial stretching cycles (f) and each of the 1000 bending cycles (g).

In **Figure 5g**, an overall decrease (up to 20%) in the sheet resistance is observed as the number of bending cycles increases. During bending, the PDMS membrane leads to normal compression of the Au NWs layer in the channels, as well as inducing an in-plane tension of the Au NWs percolation network. Secondly, bending could apply a further normal compression on the unwelded Ag NWs junction parts. It is very likely that the previous phenomena generate a slight decrease of the current collector sheet resistance with time and number of applied bending cycles.

Conclusion

We manufactured and optimized a hierarchical multiscale hybrid nanocomposite current collector for applications in Li-ion batteries. Highly stretchable, transparent and conductive devices films were realized by combining the enhanced mechanical compliance and optical transparency of small MWCNTs (Ø ≈ 11 nm, L ≈ 5-20 µm) and the enhanced electrical conductivity of relatively longer Au NWs (Ø ≈ 3 nm, L ≈ 50-100 µm) backbone. The structure can provide efficient multiscale electron transport paths with Au NWs as a main current backbone collector and MWCNTs a local elastic percolation network. Indeed, our devices showed much superior and robust mechanical compliance, electrical conductivity and optical transmittance over single component materials such as Au NWs only or MWCNTs only conductors. The Au NWs/MWCNTs/Au NWs hybrid current collector demonstrated to be

- conductive (average resistance of 40-50 ohms);
- transparent (T: 80-85%);
- highly stretchable (up to 100% strain);
- with remarkable mechanical reliability over long repeated bending-stretching cycles (1000 cycles).

Experiments

Synthesis of Au NWs: Gold nanowires (Au NWs) were utilized due to gold high electrical conductivity (EC ≈ $4.52 \cdot 10^5$ S/cm)[13]. Au nanowires are synthesized by successive multistep growth[17,18]. This method allows the production of high quality ultrathin Au NWs with uniform diameter of approximately 3 nm and length up to ≈ 4 µm. The actual procedure involves 4 chemicals ($HAuCl_4$, oleylamine, n-hexane and Triisopropylsilane (TIPS)) which were used throughout the entire synthetic process: n-hexane served as solvent, oleylamine as surface capping agent and TIPS as reducing agent. The Au NWs are synthesized at room temperature.

In a glove box, 0.1 g of $HAuCl_4 \cdot 3H_2O$ powder (99.99%, abcr GmbH) and 15.35 mL of n hexane (95%, Sigma-Aldrich) were mixed and stirred for 5 min. After that, 4.55 mL of oleylamine (≥ 70%, technical grade from Sigma-Aldrich) were added, followed by a 5 min stirring. At this stage of the process, the resulting solution was transparent yellowish red. 6.55 mL of Triisopropylsilane (TIPS) were finally added to the solution, again followed by stirring for 5 min. The final resulting yellowish solution was aged at room temperature (20-25°C) for 12 hours. During this aging process, purple suspension was formed. Separation of the Au NWs requires thorough washing with mixed solvents (1:4): 20 ml of ethanol and 5 mL of methanol. After that, the supernatant was removed and the remaining precipitate was re-dispersed in 12.6 mL of cyclohexane (≥ 99.5% purity, Sigma-Aldrich). The finally cyclohexane-dispersed Au-NWs were stored at 5°C with nitrogen gas (N_2). A simplified scheme of the overall synthesis procedure for the Au NWs is shown in **Figure S1a**.

MWCNTs preparation: High purity COOH-functionalized graphitized MWCNTs with an external diameter of approximately 30 nm (purity of 99%wt, Iljin Nanotech) produced by an arc-discharge method were dispersed in an ethanol solution, sonicated, and then centrifuged. A concentration of 4 mg/mL was chosen as the initial MWCNTs-COOH/ethanol concentration. **Figures S1b** and **S1c** show the Au NWs and MWCNTs suspensions obtained just after dispersion in cyclohexane and ethanol, respectively. These well dispersed suspensions make the batch suitable for many deposition techniques, such as spray-coating.

Current collector preparation: We fabricated stretchable transparent electrodes with regularly patterned channels carved in an elastomeric substrate, poly-dimethylsiloxane (PDMS). The fabrication process for the textured PDMS membrane includes two major steps: photolithography, and elastomer casting and curing. The hexagonal grid photoresist on silicon wafer was fabricated in cleanroom. In the second step, after cleaning the grid with ethanol, a layer of PDMS prepolymer (Sylgard 184 kit, 20:1 mixed ratio) is cast on the silicon wafer, and cured after degassing in an oven at 60°C for 20 min. The cured PDMS substrate is then peeled off from the silicon wafer with the hexagonal channel carved on one side. Finally, the cured PDMS substrate is cut with a blade into 2 cm x 2 cm squares.

In order to realize the multilayered structure inside the PDMS channels, spray-coating technique was exploited. After attaching each PDMS membrane to a Petri dish, a certain volume of Au NWs was spray-coated with a spray gun on the membranes at a pressure of circa 0.5 bar at room temperature. Subsequently, the devices were O_2 plasma-treated for 30 min in order to make the Au NWs carpet (first layer) in the channels hydrophilic. Hydrophilicity of each Au NWs layer is fundamental to guarantee the maximum adhesion with the intermediate layer of COOH-functionalized MWCNTs. After plasma treatment, the spray-coating process was repeated on a hot plate at 40°C with MWCNTs at a certain concentration: the second layer (i.e. intermediate carbon nanotubes carpet) is now realized. Spray-coating was iterated one last time at room temperature using Au NWs; in this way, all three layers have been deposited in the PDMS channels. Finally, the complete device underwent the O_2 plasma process again, so that the third Au NWs layer conductivity could be increased. It is important to underline that after each spray-coating stage, the membranes were cleaned multiple times using different adhesive tapes. The spray-coating equipment and the Petri-dish-membrane setup are shown in **Figure S2d**.

Stability of the electrical conductivity under stretching and bending is a critical issue for stretchable electrode. In order to measure the sheet resistance of the current collectors, it is necessary to ensure reliable contact between the electrodes and the multimeter probes. Liquid Ag ink was deposited on the contact regions; then, each device was heated for 20 min at 140°C in an oven to make the Ag ink dry. This entire process was repeated 5 times per device in order to achieve the maximum contact between the multi-layered structure inside the PDMS channels and the Ag ink. Secondly, ethanol-diluted Ag paste was applied once on the contact regions, followed by a 45 min drying process at 140°C in an oven. Finally, conductive copper tape was attached on the dried Ag paste on both sides of the PDMS membrane.

Material characterization: The morphologies of the synthesized Au NWs and the MWCNTs were analyzed by transmission electron microscopy (TEM, Hitachi HT 7700 EXALENS at an accelerating voltage of 100 kV and JEOL JEM-1400 Plus at an accelerating voltage of 150 kV) at low and high magnification (see **Figures S1d**, **S1e** and **S1f**). The morphology of electrodes was studied by scanning electron microscopy (SEM) on a LEO 1530 Gemini.

Optimization of the spray-coating pressure: We tested 2 different nitrogen pressures for the MWCNT-carpet deposition and compared the different results using a scanning electron microscope (SEM). As can be seen in **Figures S2b**, the best result in terms of deposition homogeneity was achieved for the lowest nitrogen pressure (i.e. 0.5 bar); this is also confirmed in the SEM image of **Figure S2c** where a dense, compact and relatively homogeneous MWCNTs carpet was achieved. A higher pressure (i.e. 1.5 bar) leads to an incomplete coverage of the PDMS channels (**Figure S2a**).

EDX mapping analysis: EDX mapping of a 3-layer hybrid current collector can be found in **Figure S2e**. We have the confirmation that the material inside the channels is predominantly gold; in this case, the gold EDX signal (in yellow) corresponds to the third spray-coated layer of Au NWs. In addition, we can further verify that the flexible transparent membrane is effectively made of polydimethylsiloxane (PDMS): in the regions around the channels, the EDX mapping shows a percent elemental composition of carbon, oxygen and silicon which is coherent with the expected polydimethylsiloxane.

References

1. J. Kim, M. Lee, H. J. Shim, R. Ghaari, H. R. Cho, D. Son, Y. H. Jung, M. Soh, C. Choi, S. Jung, et al., *Nature communications* **2014**.
2. W. Zeng, L. Shu, Q. Li, S. Chen, F. Wang, X.-M. Tao, *Advanced materials* **2014**, *26*, 5310-5336.
3. S. Ye, A. R. Rathmell, Z. Chen, I. E. Stewart, B. J. Wiley, *Advanced materials* **2014**, *26*, 6670-6687.
4. E. Artukovic, M. Kaempgen, D. Hecht, S. Roth, G. Gurner, *Nano letters* **2005**, *5*, 757-760.
5. M. Zhang, S. Fang, A. A. Zakhidov, S. B. Lee, A. E. Aliev, C. D. Williams, K. R. Atkinson, R. H. *Baughman, Science* **2005**, 309.
6. S. Bae, H. Kim, Y. Lee, X. Xu, J.-S. Park, Y. Zheng, J. Balakrishnan, T. Lei, H. R. Kim, Y. I. Song, et al., *Nature nanotechnology* **2010**, *5*, 574.
7. G. Eda, G. Fanchini, M. Chhowalla, *Nature nanotechnology* **2008**, *3*, 270-274.
8. J. Lee, P. Lee, H. Lee, D. Lee, S. S. Lee, S. H. Ko, *Nanoscale* **2012**, *4*, 6408-6414.
9. S. De, T. M. Higgins, P. E. Lyons, E. M. Doherty, P. N. Nirmalraj, W. J. Blau, J. J. Boland, J. N. Coleman, *ACS nano* **2009**, *3*, 1767-1774.
10. J.-Y. Lee, S. T. Connor, Y. Cui, P. Peumans, *Nano letters* **2008**, *8*.
11. P. Lee, J. Ham, J. Lee, S. Hong, S. Han, Y. D. Suh, S. E. Lee, J. Yeo, S. S. Lee, D. Lee, et al., *Advanced Functional Materials* **2014**, *24*, 5618.
12. Yun, Y. S. et al., *Synthetic Meterials* **2012**, *162*, 1364-1368.
13. H. Feng, Y. Yang, Y. You, G. Li, J. Guo, T. Yu, Z. Shen, T. Wu, B. Xing, *Chemical Communications* **2009**, 1984-1986.
14. Azadmanjiri, Jalal et al., *RSC advances* **2016**, *109*, 361-385.
15. Zhang, Shuai et al., *Nano letters* **2018**, 6030-6036.
16. R. A. Serway, Fort Worth, Texas; London: *Saunders College Pub*, tech. rep., **1998**.
17. Z. Huo, C.-k. Tsung, W. Huang, X. Zhang, P. Yang, *Nano letters* **2008**, *8*, 2041-2044.
18. A. Khan, S. Lee, T. Jang, Z. Xiong, C. Zhang, J. Tang, L. J. Guo, *Small* **2016**, *12*, 3021-3030.

Supporting information

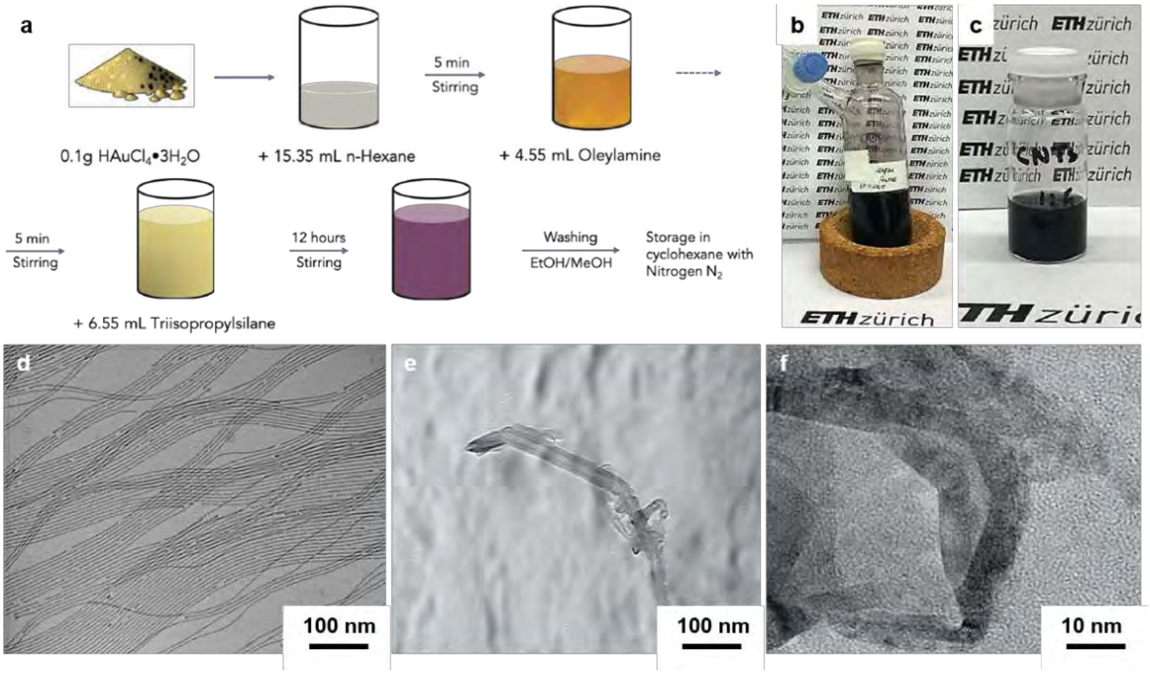

Figure S1. (a) Simplified scheme of the overall synthesis procedure for the Au NWs; (b) Au NWs-cyclohexane suspension; (c) MWCNTs-ethanol suspension; TEM pictures of Au NWs (d) and MWCNTs (e,f).

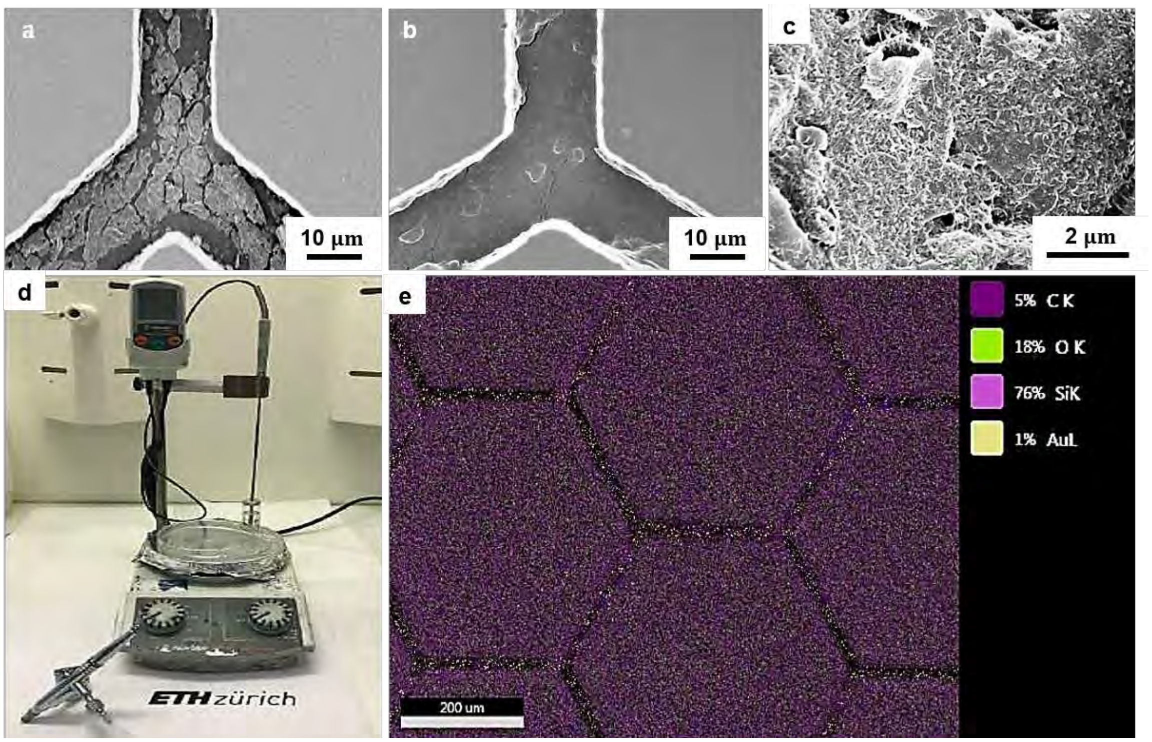

Figure S2. SEM pictures of MWCNT carpets inside the PDMS channels, spray-coated at a nitrogen pressure of 1.5 bar (a) and 0.5 bar (b); (c) magnified SEM detail of the MWCNT carpet obtained at a pressure of 0.5 bar; (d) spray-coating equipment setup; (e) EDX mapping of Au NWs/MWCNTs/Au NWs current collector.

Eidgenössische Technische Hochschule Zürich
Swiss Federal Institute of Technology Zurich

D MATL

CROSS-COUPLING EFFECTS FOR VISCOELASTIC INTERFACES IN THE PRESENCE OF E-FIELDS

Luca Mondonico

19-945-641

Supervisor:

Prof. Dr. Jan Vermant

September 2020

ETH Zürich

Acknowledgements

I thank...

PROF. DR. JAN VERMANT for having me as part of the Soft Materials group at ETH Zürich, as well as for the precious help and guidance during this research project.

Contents

1. Maxwell's equations and charge conservation

We can consider systems where flowing matter is formed by charges species, hence causing and experiencing electromagnetic fields. Specifically, we are able to define the charge per unit mass of species α

$$z_\alpha = n_\alpha \frac{\tilde{F}}{\tilde{M}_\alpha} \tag{1}$$

where $\tilde{F}$ is the Faraday constant, and n_α is the elementary integer charge of species α.

The balance equation for the electric charge (2) derives from the continuity equation for species mass density and can be written as

$$\frac{\partial \rho_{el}}{\partial t} = -\boldsymbol{\nabla} \cdot \boldsymbol{i} = -\boldsymbol{\nabla} \cdot \left(\rho_{el} \boldsymbol{v} + \boldsymbol{j}_{el}\right) \qquad \text{where} \qquad \sum_{\alpha=1}^{k} \tilde{M}_\alpha z_\alpha \tilde{\nu}_\alpha = 0 \tag{2}$$

where the electric charge conservation is guaranteed even for chemically reacting systems. The total electric charge density ρ_{el} and the total electric current flux $\boldsymbol{i}$ are given, respectively, by

$$\rho_{el} = \sum_{\alpha=1}^{k} z_\alpha \rho_\alpha \qquad\qquad \boldsymbol{i} = \sum_{\alpha=1}^{k} z_\alpha \rho_\alpha \boldsymbol{v}_\alpha \tag{3}$$

or, alternatively by

$$\boldsymbol{i} = \rho_{el} \boldsymbol{v} + \boldsymbol{j}_{el} \qquad \text{with} \qquad \boldsymbol{j}_{el} = \sum_{\alpha=1}^{k} z_\alpha \boldsymbol{j}_\alpha \tag{4}$$

where $\boldsymbol{j}_{el}$ is the flux relative to the mass-average velocity.

The total electric charge density ρ_{el} and the current density $\boldsymbol{i}$ are related to both electric $\boldsymbol{E}$ and magnetic $\boldsymbol{H}$ fields via the so-called *Maxwell's equations*. If we consider a polarizable and magnetizable medium, it is useful to express the Maxwell's equations in Lorentz-Heaviside units [1], as follows

$$\begin{aligned} \boldsymbol{\nabla} \times \boldsymbol{E} &= -\frac{1}{c}\frac{\partial}{\partial t}\boldsymbol{B} & \qquad \boldsymbol{\nabla} \cdot \boldsymbol{D} &= \rho_{el} \\ \boldsymbol{\nabla} \times \boldsymbol{H} &= \frac{1}{c}\frac{\partial}{\partial t}\boldsymbol{D} + \frac{\boldsymbol{i}}{c} & \qquad \boldsymbol{\nabla} \cdot \boldsymbol{B} &= 0 \end{aligned} \tag{5}$$

where $\boldsymbol{D}$ is the electric displacement field and $\boldsymbol{B}$ is the magnetic displacement field.

On the dividing surface, these equations give

$$\begin{aligned} \boldsymbol{\nabla} \times \boldsymbol{E}^s + \boldsymbol{n} \times \left(\boldsymbol{E}^{II} - \boldsymbol{E}^{I}\right) &= -\frac{1}{c}\frac{\partial}{\partial t}\boldsymbol{B}^s + \frac{1}{c} v_\perp^s \left(\boldsymbol{B}^{II} - \boldsymbol{B}^{I}\right) & \qquad \boldsymbol{\nabla} \cdot \boldsymbol{D}^s + \left(D_\perp^{II} - D_\perp^{I}\right) &= \rho_{el}^s \\ \boldsymbol{\nabla} \times \boldsymbol{H}^s + \boldsymbol{n} \times \left(\boldsymbol{H}^{II} - \boldsymbol{H}^{I}\right) &= \frac{1}{c}\frac{\partial}{\partial t}\boldsymbol{D}^s - \frac{1}{c} v_\perp^s \left(\boldsymbol{D}^{II} - \boldsymbol{D}^{I}\right) + \frac{1}{c}\boldsymbol{i}^s & \qquad \boldsymbol{\nabla} \cdot \boldsymbol{B}^s + \left(B_\perp^{II} - B_\perp^{I}\right) &= 0 \end{aligned} \tag{6}$$

Charge conservation on the interface is given by

$$\frac{\partial}{\partial t} q^s + \frac{1}{c} \boldsymbol{\nabla} \cdot \boldsymbol{i}^s + \boldsymbol{n} \cdot \left[\boldsymbol{i}^{II} - \boldsymbol{i}^{I} - \boldsymbol{v}^s \left(\rho_{el}^{II} - \rho_{el}^{I}\right)\right] = 0 \tag{7}$$

together with the interfacial electric current

$$i_\perp^s - v_\perp^s \rho_{el}^s = 0 \tag{8}$$

and the transversality conditions

$$\begin{aligned} &\boldsymbol{n} \times \boldsymbol{E}^s - \frac{1}{c} v_\perp^s \boldsymbol{B}^s = \boldsymbol{0} \qquad && \boldsymbol{n} \cdot \boldsymbol{D}^s = 0 \\ &\boldsymbol{n} \times \boldsymbol{H}^s + \frac{1}{c} v_\perp^s \boldsymbol{D}^s = \boldsymbol{0} \qquad && \boldsymbol{n} \cdot \boldsymbol{B}^s = 0 \end{aligned} \tag{9}$$

As to simplify future expressions, we can introduce the electromagnetic fields measured by an observer moving with *barycentric* velocity $\boldsymbol{v}$ in the nonrelativistic approximation. As proposed by Albano et al. [1],

$$\begin{aligned} &\boldsymbol{E}^* = \boldsymbol{E} + \frac{\boldsymbol{v}}{c} \times \boldsymbol{B} \qquad && \boldsymbol{H}^* = \boldsymbol{H} - \frac{\boldsymbol{v}}{c} \times \boldsymbol{D} \qquad && \boldsymbol{i}^* = \boldsymbol{i} - \boldsymbol{v}\rho_{el} \\ &\boldsymbol{D}^* = \boldsymbol{D} + \frac{\boldsymbol{v}}{c} \times \boldsymbol{H} \qquad && \boldsymbol{B}^* = \boldsymbol{B} - \frac{\boldsymbol{v}}{c} \times \boldsymbol{E} \qquad && \rho_{el}^* = \rho_{el} \end{aligned} \tag{10}$$

These relations are perfectly valid in the bulk regions; on the dividing interface, we will have the same expressions with $\boldsymbol{v} = \boldsymbol{v}^s$. By applying the relation (8) and the transversality conditions (9), we get the useful result for a dividing interface ”at rest” ($\boldsymbol{v}^s = 0$)

$$\boldsymbol{n} \times \boldsymbol{E}^{s*} = \boldsymbol{n} \cdot \boldsymbol{D}^{s*} = \boldsymbol{n} \times \boldsymbol{H}^{s*} = \boldsymbol{n} \cdot \boldsymbol{B}^{s*} = \boldsymbol{n} \cdot \boldsymbol{i}^{s*} = 0 \tag{11}$$

In a polarizable and magnetizable material, we can define fundamental quantities such as the polarization $\boldsymbol{P}$ and the magnetization $\boldsymbol{M}$. Recalling the expressions for $\boldsymbol{P}$ and $\boldsymbol{M}$ from theory [1], we write

$$\boldsymbol{P} \equiv \boldsymbol{D} - \boldsymbol{E} \qquad \text{and} \qquad \boldsymbol{M} \equiv \boldsymbol{B} - \boldsymbol{H} \tag{12}$$

similarly to (10), we obtain the barycenter-related (or surface-related if $\boldsymbol{v} = \boldsymbol{v}^s$) relations

$$\boldsymbol{P}^* = \boldsymbol{P} - \frac{\boldsymbol{v}}{c} \times \boldsymbol{M} \qquad \text{and} \qquad \boldsymbol{M}^* = \boldsymbol{M} + \frac{\boldsymbol{v}}{c} \times \boldsymbol{P} \tag{13}$$

with the relative transversality conditions

$$\boldsymbol{P}_\parallel^{s*} = \boldsymbol{D}_\parallel^{s*} \qquad \boldsymbol{M}_\parallel^{s*} = \boldsymbol{B}_\parallel^{s*} \qquad P_\perp^{s*} = -E_\perp^{s*} \qquad M_\perp^{s*} = -H_\perp^{s*} \tag{14}$$

If we refer to previous works [5, 16], we can recall the definition in Lorentz-Heaviside units of the bulk-phase electromagnetic energy density per unit volume g^i

$$g^i \equiv \frac{1}{2} \left|\boldsymbol{E}^i\right|^2 + \frac{1}{2} \left|\boldsymbol{B}^i\right|^2 - \boldsymbol{M}^i \cdot \boldsymbol{B}^i - \frac{\boldsymbol{v}^i}{c} \cdot \left(\boldsymbol{E}^i \times \boldsymbol{M}^i\right) \qquad \text{with} \qquad i = I, II \tag{15}$$

and the interfacial electromagnetic energy density per unit of surface area g^s

$$g^s \equiv \bar{\boldsymbol{D}} \cdot \boldsymbol{E}^{s*} + \bar{\boldsymbol{B}} \cdot \boldsymbol{H}^{s*} - \frac{\boldsymbol{v}^s}{c} \cdot \left(\bar{\boldsymbol{H}} \times \boldsymbol{E}^s + \boldsymbol{H}^s \times \bar{\boldsymbol{E}}\right) \tag{16}$$

The quantity $\frac{1}{c}\left(\boldsymbol{E}^i \times \boldsymbol{M}^i\right)$ represents the momentum density of the electromagnetic field and the superscript ”$-$” indicates a quantity averaged over the different bulk phases.

Finally, combining Maxwell's equations (5) we can derive the fundamental Poynting's theorem for the bulk

$$\boldsymbol{E} \cdot \frac{\partial}{\partial t} \boldsymbol{D} + \boldsymbol{H} \cdot \frac{\partial}{\partial t} \boldsymbol{B} = -\boldsymbol{\nabla} \cdot c \left(\boldsymbol{E} \times \boldsymbol{H}\right) - \boldsymbol{i} \cdot \boldsymbol{E} \tag{17}$$

From (17) it has been obtained [7] the evolution equation for the bulk total energy density (i.e. kinetic energy and electromagnetic energy) for a polarizable system (with $i = I, II$ the two bulk phases)

$$\begin{aligned} \frac{\partial}{\partial t} &\left\{ \frac{1}{2} \rho^i \left|\boldsymbol{v}^i\right|^2 + \frac{1}{2} \left|\boldsymbol{E}^i\right|^2 + \frac{1}{2} \left|\boldsymbol{B}^i\right|^2 - \boldsymbol{M}^{i*} \cdot \boldsymbol{B}^i - \frac{\boldsymbol{v}^i}{c} \cdot \left(\boldsymbol{E}^{i*} \times \boldsymbol{M}^i\right) \right\} \qquad \text{with} \qquad i = I, II \\ &= \frac{\partial}{\partial t} \left\{ \frac{1}{2} \rho^i \left|\boldsymbol{v}^i\right|^2 + g^i \right\} \\ &= -\boldsymbol{\nabla} \cdot \left\{ \frac{1}{2} \rho^i \left|\boldsymbol{v}^i\right|^2 \boldsymbol{v}^i + \boldsymbol{\pi}^i \cdot \boldsymbol{v}^i - \left(\boldsymbol{P}^{i*} \cdot \boldsymbol{E}^i + \boldsymbol{M}^{i*} \cdot \boldsymbol{B}^i\right) \boldsymbol{v}^i + c \left(\boldsymbol{E}^i \times \boldsymbol{H}^i\right) \right\} \\ &\qquad + \boldsymbol{\pi}^i : \boldsymbol{\nabla}_\parallel \boldsymbol{v}^i - \boldsymbol{i}^i \cdot \boldsymbol{E}^{i*} - \rho^i \boldsymbol{E}^{i*} \cdot \frac{d\boldsymbol{p}^{i*}}{dt} - \rho^i \boldsymbol{B}^{i*} \cdot \frac{d\boldsymbol{m}^{i*}}{dt} \end{aligned} \tag{18}$$

In the same way as in (17) and in (18), we now report [1] the Poynting's theorem for the interface (19)

$$\begin{aligned}
&\bar{\boldsymbol{E}} \cdot \frac{\partial}{\partial t}\boldsymbol{D}^s + \bar{\boldsymbol{H}} \cdot \frac{\partial}{\partial t}\boldsymbol{B}^s + \boldsymbol{E}^s \cdot \left(\frac{\partial}{\partial t}\bar{\boldsymbol{D}}\right) + \boldsymbol{H}^s \cdot \left(\frac{\partial}{\partial t}\bar{\boldsymbol{B}}\right) \\
&\qquad = -c\left[\boldsymbol{\nabla} \cdot \left(\bar{\boldsymbol{E}} \times \boldsymbol{H}^s + \boldsymbol{E}^s \times \bar{\boldsymbol{H}}\right)\right] + c\;\boldsymbol{n} \cdot \left(\boldsymbol{H}^{II} \times \boldsymbol{E}^{II} - \boldsymbol{H}^I \times \boldsymbol{E}^I\right) \\
&\qquad\quad + v_\perp^s\left[\bar{\boldsymbol{E}} \cdot \left(\boldsymbol{D}^{II} - \boldsymbol{D}^I\right) + \bar{\boldsymbol{H}} \cdot \left(\boldsymbol{B}^{II} - \boldsymbol{B}^I\right)\right] - \boldsymbol{i}^s \cdot \bar{\boldsymbol{E}} - \bar{\boldsymbol{i}} \cdot \boldsymbol{E}^s
\end{aligned} \tag{19}$$

and the evolution equation for the total energy density for a polarizable interface (20)

$$\begin{aligned}
&\frac{\partial}{\partial t}\left\{\frac{1}{2}\;\rho^s\left|\boldsymbol{v}^s\right|^2 + \bar{\boldsymbol{D}} \cdot \boldsymbol{E}^{s*} + \bar{\boldsymbol{B}} \cdot \boldsymbol{H}^{s*} - \frac{\boldsymbol{v}^s}{c} \cdot \left(\bar{\boldsymbol{H}} \times \boldsymbol{E}^s + \boldsymbol{H}^s \times \bar{\boldsymbol{E}}\right)\right\} = \frac{\partial}{\partial t}\left\{\frac{1}{2}\rho^s\left|\boldsymbol{v}^s\right|^2 + g^s\right\} \\
&= \quad -\boldsymbol{i}^{s*} \cdot \bar{\boldsymbol{E}}^* - \bar{\boldsymbol{i}}^* \cdot \boldsymbol{E}^{s*} + \boldsymbol{\pi}^s : \left(\boldsymbol{\nabla}\boldsymbol{v}^s\right)^T \\
&\qquad -\left\{\boldsymbol{\nabla} \cdot \left[\frac{1}{2}\rho^s\left|\boldsymbol{v}^s\right|^2\boldsymbol{v}^s + \boldsymbol{\pi}^s \cdot \boldsymbol{v}^s - \boldsymbol{v}^s\left(\bar{\boldsymbol{D}}^* \cdot \boldsymbol{P}_\perp^s + \bar{\boldsymbol{E}}^* \cdot \boldsymbol{P}_\parallel^s + \bar{\boldsymbol{B}}^* \cdot \boldsymbol{M}_\perp^s + \bar{\boldsymbol{H}}^* \cdot \boldsymbol{M}_\parallel^s\right)\right.\right. \\
&\qquad\qquad\qquad \left.\left. +c\left(\bar{\boldsymbol{E}} \times \boldsymbol{H}^s + \boldsymbol{E}^s \times \bar{\boldsymbol{H}}\right)\right]\right\} - \boldsymbol{n} \cdot \left(\boldsymbol{\pi}^{II} - \boldsymbol{\pi}^I\right) \cdot \boldsymbol{v}^s \\
&\qquad -\bar{\boldsymbol{D}}^* \cdot \left(\frac{\partial}{\partial t} + \boldsymbol{\nabla} \cdot \boldsymbol{v}^s\right)\boldsymbol{P}_\perp^{s*} - \bar{\boldsymbol{E}}^* \cdot \left(\frac{\partial}{\partial t} + \boldsymbol{\nabla} \cdot \boldsymbol{v}^s\right)\boldsymbol{P}_\parallel^{s*} \\
&\qquad -\bar{\boldsymbol{B}}^* \cdot \left(\frac{\partial}{\partial t} + \boldsymbol{\nabla} \cdot \boldsymbol{v}^s\right)\boldsymbol{M}_\perp^{s*} - \bar{\boldsymbol{H}}^* \cdot \left(\frac{\partial}{\partial t} + \boldsymbol{\nabla} \cdot \boldsymbol{v}^s\right)\boldsymbol{M}_\parallel^{s*} \\
&\qquad -\frac{1}{c}\bar{\boldsymbol{M}} \cdot \left[\boldsymbol{\nabla} \cdot \boldsymbol{v}^s\left(\boldsymbol{v}_\perp^s \times \boldsymbol{P}^s\right)\right] + \frac{1}{c}\bar{\boldsymbol{P}} \cdot \left[\boldsymbol{\nabla} \cdot \boldsymbol{v}^s\left(\boldsymbol{v}_\perp^s \times \boldsymbol{M}^s\right)\right] + c\;\boldsymbol{n} \cdot \left(\boldsymbol{H}^{II} \times \boldsymbol{E}^{II} - \boldsymbol{H}^I \times \boldsymbol{E}^I\right) \\
&\qquad +v_\perp^s\left[\frac{1}{2}\left|\boldsymbol{E}^{II}\right|^2 - \frac{1}{2}\left|\boldsymbol{E}^I\right|^2 + \frac{1}{2}\left|\boldsymbol{B}^{II}\right|^2 - \frac{1}{2}\left|\boldsymbol{B}^I\right|^2 + \boldsymbol{P}^{II} \cdot \boldsymbol{E}^{II} - \boldsymbol{P}^I \cdot \boldsymbol{E}^I\right] \\
&\qquad +\frac{1}{c}\boldsymbol{v}^s\left[\left(v_\perp^{II} - v_\perp^s\right)\left(\boldsymbol{P}^{II} \times \boldsymbol{B}^{II} + \boldsymbol{E}^{II} \times \boldsymbol{M}^{II}\right) - \left(v_\perp^I - v_\perp^s\right)\left(\boldsymbol{P}^I \times \boldsymbol{B}^I + \boldsymbol{E}^I \times \boldsymbol{M}^I\right)\right] \\
&\qquad -\frac{1}{2}\left[\rho^{II}\left(v_\perp^{II} - v_\perp^s\right)\left(\left|\boldsymbol{v}^{II}\right|^2 - \left|\boldsymbol{v}^{II} - \boldsymbol{v}^s\right|^2\right) - \rho^I\left(v_\perp^I - v_\perp^s\right)\left(\left|\boldsymbol{v}^I\right|^2 - \left|\boldsymbol{v}^I - \boldsymbol{v}^s\right|^2\right)\right]
\end{aligned} \tag{20}$$

2. Derivation of $\boldsymbol{\sigma}^s$ in the presence of electromagnetic fields

2.1 Balance equations

Here we derive the interfacial entropy production rate σ^s for a polarizable multicomponent system in the presence of electromagnetic fields. In our case, we make the assumption of local equilibrium in both the bulk phases as well as for the interface. This means

$$\begin{aligned} s^i &= s^i\left(u^i, \rho^i, N^i_\alpha, \boldsymbol{p}^{i*}, \boldsymbol{m}^{i*}\right) && \text{in the bulk regions with } i = I, II \\ s^s &= s^s\left(u^s, \rho^s, N^s_\alpha, \boldsymbol{p}^{s*}, \boldsymbol{m}^{s*}\right) && \text{at the interface} \end{aligned} \tag{21}$$

where the polarization $\boldsymbol{p}$ and the magnetization $\boldsymbol{m}$ are expressed per unit volume (for the bulk) and per unit area (for the interface).

Firstly, we recall Gibbs' thermodynamic fundamental form for a one-component system in the absence of electromagnetic fields:

$$dU = TdS - pdV + \mu dN + \gamma dA \tag{22}$$

which can be extended for an entire system at equilibrium in the form of the Euler (23) and the Gibbs-Duhem (24) equations :

$$U = TS - pV + \mu N + \gamma A \tag{23}$$

$$SdT - Vdp + Nd\mu + Ad\gamma = 0 \tag{24}$$

For each of the two equilibrium bulk phases (I and II) we then have

$$\begin{aligned} U^i &= TS^i - pV^i + \mu N^i \qquad \text{for} \qquad i = I, II \\ S^i dT &- V^i dp + N^i d\mu = 0 \end{aligned} \tag{25}$$

By defining the interfacial quantities $N^s = N - N^1 - N^2$, $U^s = U - U^1 - U^2$ and $S^s = S - S^1 - S^2$ (with $V = V^1 + V^2$) [16], we can re-write expressions (23) and (24) for interfacial systems in global equilibrium:

$$u^s = Ts^s + \gamma + \hat{\mu}\rho^s \tag{26}$$

$$s^s d^s T + d^s\gamma + \rho^s d^s\hat{\mu} = 0 \tag{27}$$

From now on, we will identify d^s as $\dfrac{d^s}{dt}$, which can be seen as an "interface total time derivative". Note that in (26) and (27) the purely intensive quantities T, $\hat{\mu}$ and γ are now closely related to the ambiguous gauge-variant excess densities u^s, s^s and ρ^s. As for other physical systems, according to the Gibbs phase rule, one independent physical variable is lost because of the coexistence of two phases.

We can now extend (26) and (27) for a polarizable and magnetizable system in the presence of an electromagnetic field.

$$u^s = Ts^s + \gamma + \hat{\mu}\rho^s + \left(\bar{\boldsymbol{E}}^*_\parallel\right)_{eq} \cdot \boldsymbol{p}^{s*}_\parallel + \left(\bar{D}^*_\perp\right)_{eq} p^{s*}_\perp + \left(\bar{\boldsymbol{H}}^*_\parallel\right)_{eq} \cdot \boldsymbol{m}^{s*}_\parallel + \left(\bar{B}^*_\perp\right)_{eq} m^{s*}_\perp \tag{28}$$

$$s^s d^s T + d^s\gamma + \rho^s d^s\hat{\mu} + \boldsymbol{p}^{s*}_\parallel \cdot d^s\left(\bar{\boldsymbol{E}}^*_\parallel\right)_{eq} + p^{s*}_\perp\ d^s\left(\bar{D}^*_\perp\right)_{eq} + \boldsymbol{m}^{s*}_\parallel \cdot d^s\left(\bar{\boldsymbol{H}}^*_\parallel\right)_{eq} + m^{s*}_\perp\ d^s\left(\bar{B}^*_\perp\right)_{eq} = 0 \tag{29}$$

Rewriting (28), (29) for a multi-component systems, given $\hat{\mu}_k = \hat{\mu}_k\left(T, \hat{\mu}_1, ..., \hat{\mu}_{k-1}\right)$ and $\gamma = \gamma\left(T, \hat{\mu}_1, ..., \hat{\mu}_{k-1}\right)$

$$u^s = Ts^s + \gamma + \sum_{\alpha=1}^{k-1} \hat{\mu}_\alpha\rho^s_\alpha + \hat{\mu}_k\rho^s_k + \left(\bar{\boldsymbol{E}}^*_\parallel\right)_{eq} \cdot \boldsymbol{p}^{s*}_\parallel + \left(\bar{D}^*_\perp\right)_{eq} p^{s*}_\perp + \left(\bar{\boldsymbol{H}}^*_\parallel\right)_{eq} \cdot \boldsymbol{m}^{s*}_\parallel + \left(\bar{B}^*_\perp\right)_{eq} m^{s*}_\perp \tag{30}$$

$$s^s d^s T + d^s\gamma + \sum_{\alpha=1}^{k-1} \rho^s_\alpha d^s \hat{\mu}_\alpha + \rho^s_k d^s \hat{\mu}_k + \boldsymbol{p}^{s*}_\parallel \cdot d^s \left(\bar{\boldsymbol{E}}^*_\parallel\right)_{eq} + p^{s*}_\perp \; d^s \left(\bar{D}^*_\perp\right)_{eq} + \boldsymbol{m}^{s*}_\parallel \cdot d^s \left(\bar{\boldsymbol{H}}^*_\parallel\right)_{eq} + m^{s*}_\perp \; d^s \left(\bar{B}^*_\perp\right)_{eq} = 0 \tag{31}$$

We can now obtain the expression for the total interfacial energy density e^s. To accomplish this, we simply add to (30) the kinetic energy density term $\frac{1}{2}\left|\boldsymbol{v}^s\right|^2$ to account for interface movements, i.e. $e^s = u^s + \frac{1}{2}\left|\boldsymbol{v}^s\right|^2$.

$$e^s = T^s s^s + \gamma + \sum_{\alpha=1}^{k} \left(\hat{\mu}^s_\alpha + \frac{1}{2}\left|\boldsymbol{v}^s\right|^2\right) \rho^s_\alpha + \left(\bar{\boldsymbol{E}}^*_\parallel\right)_{eq} \cdot \boldsymbol{p}^{s*}_\parallel + \left(\bar{D}^*_\perp\right)_{eq} p^{s*}_\perp + \left(\bar{\boldsymbol{H}}^*_\parallel\right)_{eq} \cdot \boldsymbol{m}^{s*}_\parallel + \left(\bar{B}^*_\perp\right)_{eq} m^{s*}_\perp \tag{32}$$

By differentiating the Euler equation (32) and using the Gibbs-Duhem equation (31), we get the expression

$$\begin{aligned} \frac{d^s}{dt} e^s = T^s \frac{d^s}{dt} s^s + \sum_{\alpha=1}^{k} \left(\hat{\mu}^s_\alpha - \frac{1}{2}\left|\boldsymbol{v}^s\right|^2\right) \frac{d^s}{dt}\rho^s_\alpha + \boldsymbol{v}^s \cdot \frac{d^s}{dt}\left(\rho^s \boldsymbol{v}^s\right) \\ + \left(\bar{\boldsymbol{E}}^*_\parallel\right)_{eq} \cdot \frac{d^s}{dt}\boldsymbol{p}^{s*}_\parallel + \left(\bar{D}^*_\perp\right)_{eq} \frac{d^s}{dt} p^{s*}_\perp + \left(\bar{\boldsymbol{H}}^*_\parallel\right)_{eq} \cdot \frac{d^s}{dt}\boldsymbol{m}^{s*}_\parallel + \left(\bar{B}^*_\perp\right)_{eq} \frac{d^s}{dt} m^{s*}_\perp \end{aligned} \tag{33}$$

where $\boldsymbol{v}^s \cdot \boldsymbol{v}^s d\rho^s_\alpha + \rho^s_\alpha \boldsymbol{v}^s \cdot d\boldsymbol{v}^s = \boldsymbol{v}^s \cdot d\left(\rho^s_\alpha \boldsymbol{v}^s\right)$; the third term in (33) is associated with the kinetic energy.

Let us call a the density of a generic conserved quantity and a^s its ambiguous excess density. For an inhomogeneous (i.e. non planar) moving interface, the interface normal velocity v^s_{na} may be affected by the transport processes occurring within the very same interface. If we consider as a reference the interface defined by the gauge $a^s = 0$, we can write the generalized expression

$$v^s_{na}\left(a^{II} - a^I\right) = \boldsymbol{n} \cdot \left(\boldsymbol{v}^{II} a^{II} + \boldsymbol{j}^{II}_a - \boldsymbol{v}^I a^I - \boldsymbol{j}^{II}_a\right) - \boldsymbol{\nabla}_\parallel \cdot \boldsymbol{j}^s_a + \mathcal{F} \tag{34}$$

where $\boldsymbol{j}^s_a$ is the interface analog of the bulk conductive fluxes $\boldsymbol{j}^I_a$ and $\boldsymbol{j}^{II}_a$, and the symbol $\mathcal{F}$ represents the electromagnetic source term.

In addition, we report the jump momentum balance,

$$-\left(\frac{1}{\rho^{II}} - \frac{1}{\rho^I}\right)^{-1} \boldsymbol{n} \cdot \left(\boldsymbol{v}^{II} - \boldsymbol{v}^I\right)\left(\boldsymbol{v}^{II} - \boldsymbol{v}^I\right) = \boldsymbol{n} \cdot \left(\boldsymbol{\pi}^{II} - \boldsymbol{\pi}^I\right) - \boldsymbol{\nabla}_\parallel \cdot \boldsymbol{\pi}^s \tag{35}$$

together with other jump relations [16] (36) and (37),

$$\rho^I\left(\boldsymbol{v}^I - \boldsymbol{v}^s\right) = \left(\frac{1}{\rho^{II}} - \frac{1}{\rho^I}\right)^{-1}\left(\boldsymbol{v}^{II} - \boldsymbol{v}^I\right) \tag{36}$$

$$\rho^{II}\left(\boldsymbol{v}^{II} - \boldsymbol{v}^s\right) = \left(\frac{1}{\rho^{II}} - \frac{1}{\rho^I}\right)^{-1}\left(\boldsymbol{v}^{II} - \boldsymbol{v}^I\right) \tag{37}$$

Let us now assume the gauge $\rho^s = 0$, we can then recall from previous works [16] the time evolution (i.e. rate of change) equation for a generic extensive interfacial density b^s

$$\frac{\partial^s b^s}{\partial t} = \left(v^s_{n\rho} - v^s_n\right)\left(b^{II} - b^I\right) - \boldsymbol{\nabla}_\parallel \cdot \left(\boldsymbol{v}^s_{def} b^s\right) - b^s \boldsymbol{\nabla}_\parallel \cdot \boldsymbol{v}^s_{tr} \tag{38}$$

In the equation above (see (38)), the "interface partial time derivative" has been introduced; for a surface moving with velocity $\boldsymbol{v}^s$, it can be formally expressed as

$$\boldsymbol{v}^s = \boldsymbol{v}^s_{\text{translational}} + \boldsymbol{v}^s_{\text{deformational}} \qquad \Rightarrow \qquad \frac{\partial^s}{\partial t} = \frac{\partial}{\partial t} + \boldsymbol{v}^s_{\text{tr}} \cdot \boldsymbol{\nabla} \tag{39}$$

By combining expressions (34), (38) and the evolution equation for the total energy density in a polarizable interface (see (20)), we derive the evolution equation for the excess total energy density e^s in the gauge $\rho^s = 0$

$$\begin{aligned}
\frac{\partial^s e^s}{\partial t} &= -\boldsymbol{\nabla}_\parallel \cdot \left(\boldsymbol{v}^s_{def} e^s + \boldsymbol{j}^s_q + \boldsymbol{\pi}^s \cdot \boldsymbol{v}^s\right) - e^s \boldsymbol{\nabla}_\parallel \cdot \boldsymbol{v}^s_{tr} \\
&+ \boldsymbol{n} \cdot \left[\left(\boldsymbol{v}^{II} - \boldsymbol{v}^s\right) e^{II} + \boldsymbol{j}^{II}_q + \boldsymbol{\pi}^{II} \cdot \boldsymbol{v}^{II} - \left(\boldsymbol{v}^I - \boldsymbol{v}^s\right) e^I - \boldsymbol{j}^I_q - \boldsymbol{\pi}^I \cdot \boldsymbol{v}^I\right] \\
&+ \boldsymbol{\nabla}_\parallel \left\{\boldsymbol{p}^{s*}_\parallel \cdot \left[\bar{\boldsymbol{E}}^*_\parallel - \left(\bar{\boldsymbol{E}}^*_\parallel\right)_{eq}\right] + p^{s*}_\perp \left[\bar{D}^*_\perp - \left(\bar{D}^*_\perp\right)_{eq}\right] + \boldsymbol{m}^{s*}_\parallel \cdot \left[\bar{\boldsymbol{H}}^*_\parallel - \left(\bar{\boldsymbol{H}}^*_\parallel\right)_{eq}\right] + m^{s*}_\perp \left[\bar{B}^*_\perp - \left(\bar{B}^*_\perp\right)_{eq}\right]\right\} \\
&+ \boldsymbol{i}^{s*} \cdot \bar{\boldsymbol{E}}^* + \bar{\boldsymbol{i}}^* \cdot \boldsymbol{E}^{s*} \\
&+ \bar{\boldsymbol{D}}^* \cdot \left(\frac{\partial}{\partial t} + \boldsymbol{\nabla} \cdot \boldsymbol{v}^s\right) \boldsymbol{p}^{s*}_\perp + \bar{\boldsymbol{E}}^* \cdot \left(\frac{\partial}{\partial t} + \boldsymbol{\nabla} \cdot \boldsymbol{v}^s\right) \boldsymbol{p}^{s*}_\parallel \\
&+ \bar{\boldsymbol{B}}^* \cdot \left(\frac{\partial}{\partial t} + \boldsymbol{\nabla} \cdot \boldsymbol{v}^s\right) \boldsymbol{m}^{s*}_\perp + \bar{\boldsymbol{H}}^* \cdot \left(\frac{\partial}{\partial t} + \boldsymbol{\nabla} \cdot \boldsymbol{v}^s\right) \boldsymbol{m}^{s*}_\parallel \\
&+ \frac{1}{c} \bar{\boldsymbol{m}} \cdot \left[\boldsymbol{\nabla} \cdot \boldsymbol{v}^s \left(\boldsymbol{v}^s_\perp \times \boldsymbol{p}^s\right)\right] - \frac{1}{c} \bar{\boldsymbol{p}} \cdot \left[\boldsymbol{\nabla} \cdot \boldsymbol{v}^s \left(\boldsymbol{v}^s_\perp \times \boldsymbol{m}^s\right)\right] \\
&+ \boldsymbol{n} \cdot \boldsymbol{v}^s_\perp \left[\frac{1}{2} \left|\boldsymbol{E}^{II}\right|^2 - \frac{1}{2} \left|\boldsymbol{E}^I\right|^2 + \frac{1}{2} \left|\boldsymbol{B}^{II}\right|^2 - \frac{1}{2} \left|\boldsymbol{B}^I\right|^2 + \boldsymbol{p}^{II} \cdot \boldsymbol{E}^{II} - \boldsymbol{p}^I \cdot \boldsymbol{E}^I\right] \\
&+ \boldsymbol{v}^s \left\{\boldsymbol{n} \cdot \left[\left(\boldsymbol{v}^{II} - \boldsymbol{v}^s\right) \left(\boldsymbol{p}^{II} \times \boldsymbol{B}^{II} + \boldsymbol{E}^{II} \times \boldsymbol{m}^{II}\right) - \left(\boldsymbol{v}^I - \boldsymbol{v}^s\right) \left(\boldsymbol{p}^I \times \boldsymbol{B}^I + \boldsymbol{E}^I \times \boldsymbol{m}^I\right)\right]\right\}
\end{aligned} \tag{40}$$

We set $e^s = u^s + \frac{1}{2} \left(\boldsymbol{v}^s \cdot \boldsymbol{v}^s\right)$ in (40), and recognize in (40) the definition of the Lorentz-Heaviside bulk-phase electromagnetic energy density per unit volume g^i as defined in (15). Then, we can start to derive the evolution equation for the excess internal energy density u^s

$$\begin{aligned}
\frac{\partial^s u^s}{\partial t} &= -\boldsymbol{\nabla}_\parallel \cdot \left(\boldsymbol{v}^s_{def} u^s + \boldsymbol{j}^s_q\right) - u^s \boldsymbol{\nabla}_\parallel \cdot \boldsymbol{v}^s_{tr} - \boldsymbol{\pi}^s : \boldsymbol{\nabla}_\parallel \boldsymbol{v}^s - \boldsymbol{v}^s \cdot \boldsymbol{\nabla}_\parallel \cdot \boldsymbol{\pi}^s \\
&+ \boldsymbol{n} \cdot \Bigg[\left(\boldsymbol{v}^{II} - \boldsymbol{v}^s\right) \left(u^{II} + \frac{1}{2} \rho^{II} \boldsymbol{v}^{II} \cdot \boldsymbol{v}^{II} + \boldsymbol{v}^s \left\{\boldsymbol{p}^{II} \times \boldsymbol{B}^{II} + \boldsymbol{E}^{II} \times \boldsymbol{m}^{II}\right\}\right) - g^{II} \boldsymbol{v}^s + \boldsymbol{\pi}^{II} \cdot \boldsymbol{v}^{II} + \boldsymbol{j}^{II}_q \\
&\qquad - \left(\boldsymbol{v}^I - \boldsymbol{v}^s\right) \left(u^I + \frac{1}{2} \rho^I \boldsymbol{v}^I \cdot \boldsymbol{v}^I + \boldsymbol{v}^s \left\{\boldsymbol{p}^I \times \boldsymbol{B}^I + \boldsymbol{E}^I \times \boldsymbol{m}^I\right\}\right) + g^I \boldsymbol{v}^s - \boldsymbol{\pi}^I \cdot \boldsymbol{v}^I - \boldsymbol{j}^I_q\Bigg] \\
&+ \boldsymbol{i}^{s*} \cdot \bar{\boldsymbol{E}}^* + \bar{\boldsymbol{i}}^* \cdot \boldsymbol{E}^{s*} \\
&+ \bar{\boldsymbol{D}}^* \cdot \left(\frac{\partial}{\partial t} + \boldsymbol{\nabla} \cdot \boldsymbol{v}^s\right) \boldsymbol{p}^{s*}_\perp + \bar{\boldsymbol{E}}^* \cdot \left(\frac{\partial}{\partial t} + \boldsymbol{\nabla} \cdot \boldsymbol{v}^s\right) \boldsymbol{p}^{s*}_\parallel \\
&+ \bar{\boldsymbol{B}}^* \cdot \left(\frac{\partial}{\partial t} + \boldsymbol{\nabla} \cdot \boldsymbol{v}^s\right) \boldsymbol{m}^{s*}_\perp + \bar{\boldsymbol{H}}^* \cdot \left(\frac{\partial}{\partial t} + \boldsymbol{\nabla} \cdot \boldsymbol{v}^s\right) \boldsymbol{m}^{s*}_\parallel \\
&+ \frac{1}{c} \bar{\boldsymbol{m}} \cdot \left[\boldsymbol{\nabla} \cdot \boldsymbol{v}^s \left(\boldsymbol{v}^s_\perp \times \boldsymbol{p}^s\right)\right] - \frac{1}{c} \bar{\boldsymbol{p}} \cdot \left[\boldsymbol{\nabla} \cdot \boldsymbol{v}^s \left(\boldsymbol{v}^s_\perp \times \boldsymbol{m}^s\right)\right]
\end{aligned} \tag{41}$$

Multiplication of (35) by $\boldsymbol{v}^s \cdot$ and substitution for the last term in the first line of (41) gives the following

$$
\begin{aligned}
\frac{\partial^s u^s}{\partial t} &= -\boldsymbol{\nabla}_{\parallel} \cdot \left(\boldsymbol{v}^s_{def} u^s + \boldsymbol{j}^s_q \right) - u^s \boldsymbol{\nabla}_{\parallel} \cdot \boldsymbol{v}^s_{tr} - \boldsymbol{\pi}^s : \boldsymbol{\nabla}_{\parallel} \boldsymbol{v}^s \\
&+ \boldsymbol{n} \cdot \Bigg\{ \left(\boldsymbol{v}^{II} - \boldsymbol{v}^s \right) \left[u^{II} + \frac{1}{2} \rho^{II} \boldsymbol{v}^{II} \cdot \boldsymbol{v}^{II} - \rho^{II} \boldsymbol{v}^{II} \cdot \boldsymbol{v}^s + \boldsymbol{v}^s \cdot \left(\boldsymbol{p}^{II} \times \boldsymbol{B}^{II} + \boldsymbol{E}^{II} \times \boldsymbol{m}^{II} \right) \right] - g^{II} \boldsymbol{v}^s \\
&\qquad - \left(\boldsymbol{v}^{I} - \boldsymbol{v}^s \right) \left[u^{I} + \frac{1}{2} \rho^{I} \boldsymbol{v}^{I} \cdot \boldsymbol{v}^{I} - \rho^{I} \boldsymbol{v}^{I} \cdot \boldsymbol{v}^s + \boldsymbol{v}^s \cdot \left(\boldsymbol{p}^{I} \times \boldsymbol{B}^{I} + \boldsymbol{E}^{I} \times \boldsymbol{m}^{I} \right) \right] + g^{I} \boldsymbol{v}^s \\
&\qquad + \boldsymbol{\pi}^{II} \cdot \left(\boldsymbol{v}^{II} - \boldsymbol{v}^s \right) + \boldsymbol{j}^{II}_q - \boldsymbol{\pi}^{I} \cdot \left(\boldsymbol{v}^{I} - \boldsymbol{v}^s \right) - \boldsymbol{j}^{I}_q \Bigg\} \\
&+ \boldsymbol{i}^{s*} \cdot \bar{\boldsymbol{E}}^* + \bar{\boldsymbol{i}}^* \cdot \boldsymbol{E}^{s*} \\
&+ \bar{\boldsymbol{D}}^* \cdot \left(\frac{\partial}{\partial t} + \boldsymbol{\nabla} \cdot \boldsymbol{v}^s \right) \boldsymbol{p}^{s*}_{\perp} + \bar{\boldsymbol{E}}^* \cdot \left(\frac{\partial}{\partial t} + \boldsymbol{\nabla} \cdot \boldsymbol{v}^s \right) \boldsymbol{p}^{s*}_{\parallel} \\
&+ \bar{\boldsymbol{B}}^* \cdot \left(\frac{\partial}{\partial t} + \boldsymbol{\nabla} \cdot \boldsymbol{v}^s \right) \boldsymbol{m}^{s*}_{\perp} + \bar{\boldsymbol{H}}^* \cdot \left(\frac{\partial}{\partial t} + \boldsymbol{\nabla} \cdot \boldsymbol{v}^s \right) \boldsymbol{m}^{s*}_{\parallel} \\
&+ \frac{1}{c} \bar{\boldsymbol{m}} \cdot \left[\boldsymbol{\nabla} \cdot \boldsymbol{v}^s \left(\boldsymbol{v}^s_{\perp} \times \boldsymbol{p}^s \right) \right] - \frac{1}{c} \bar{\boldsymbol{p}} \cdot \left[\boldsymbol{\nabla} \cdot \boldsymbol{v}^s \left(\boldsymbol{v}^s_{\perp} \times \boldsymbol{m}^s \right) \right]
\end{aligned}
\tag{42}
$$

recalling the bulk pressure tensor $\boldsymbol{\pi} = p\boldsymbol{\delta} + \boldsymbol{\tau}$ and the thermodynamic volume-normalized relation $h = u + p$, we can re-write

$$
\begin{aligned}
\frac{\partial^s u^s}{\partial t} &= -\boldsymbol{\nabla}_{\parallel} \cdot \left(\boldsymbol{v}^s_{def} u^s + \boldsymbol{j}^s_q \right) - u^s \boldsymbol{\nabla}_{\parallel} \cdot \boldsymbol{v}^s_{tr} - \boldsymbol{\pi}^s : \boldsymbol{\nabla}_{\parallel} \boldsymbol{v}^s \\
&+ \boldsymbol{n} \cdot \left[\left(\boldsymbol{v}^{II} - \boldsymbol{v}^s \right) h^{II} + \boldsymbol{j}^{II}_q - \left(\boldsymbol{v}^{I} - \boldsymbol{v}^s \right) h^{I} - \boldsymbol{j}^{I}_q + \boldsymbol{\tau}^{II} \cdot \left(\boldsymbol{v}^{II} - \boldsymbol{v}^s \right) - \boldsymbol{\tau}^{I} \cdot \left(\boldsymbol{v}^{I} - \boldsymbol{v}^s \right) \right] \\
&+ \rho^I \left(\boldsymbol{v}^{I} - \boldsymbol{v}^s \right) \cdot \boldsymbol{n} \left[\frac{1}{2} \left(\boldsymbol{v}^{II} \cdot \boldsymbol{v}^{II} - \boldsymbol{v}^{I} \cdot \boldsymbol{v}^{I} \right) - \boldsymbol{v}^s \cdot \left(\boldsymbol{v}^{II} - \boldsymbol{v}^{I} \right) \right] - v^s_{\perp} \left(g^{II} - g^{I} \right) \\
&+ \rho^I \left(\boldsymbol{v}^{I} - \boldsymbol{v}^s \right) \cdot \boldsymbol{n} \left[\boldsymbol{v}^s \cdot \left(\boldsymbol{p}^{II} \times \boldsymbol{B}^{II} - \boldsymbol{p}^{I} \times \boldsymbol{B}^{I} + \boldsymbol{E}^{II} \times \boldsymbol{m}^{II} - \boldsymbol{E}^{I} \times \boldsymbol{m}^{I} \right) \right] \\
&+ \boldsymbol{i}^{s*} \cdot \bar{\boldsymbol{E}}^* + \bar{\boldsymbol{i}}^* \cdot \boldsymbol{E}^{s*} \\
&+ \bar{\boldsymbol{D}}^* \cdot \left(\frac{\partial}{\partial t} + \boldsymbol{\nabla} \cdot \boldsymbol{v}^s \right) \boldsymbol{p}^{s*}_{\perp} + \bar{\boldsymbol{E}}^* \cdot \left(\frac{\partial}{\partial t} + \boldsymbol{\nabla} \cdot \boldsymbol{v}^s \right) \boldsymbol{p}^{s*}_{\parallel} \\
&+ \bar{\boldsymbol{B}}^* \cdot \left(\frac{\partial}{\partial t} + \boldsymbol{\nabla} \cdot \boldsymbol{v}^s \right) \boldsymbol{m}^{s*}_{\perp} + \bar{\boldsymbol{H}}^* \cdot \left(\frac{\partial}{\partial t} + \boldsymbol{\nabla} \cdot \boldsymbol{v}^s \right) \boldsymbol{m}^{s*}_{\parallel} \\
&+ \frac{1}{c} \bar{\boldsymbol{m}} \cdot \left[\boldsymbol{\nabla} \cdot \boldsymbol{v}^s \left(\boldsymbol{v}^s_{\perp} \times \boldsymbol{p}^s \right) \right] - \frac{1}{c} \bar{\boldsymbol{p}} \cdot \left[\boldsymbol{\nabla} \cdot \boldsymbol{v}^s \left(\boldsymbol{v}^s_{\perp} \times \boldsymbol{m}^s \right) \right]
\end{aligned}
\tag{43}
$$

where we have used the jump balance for mass at the dividing interface.

$$
\boldsymbol{n} \cdot \left(\boldsymbol{v}^{I} - \boldsymbol{v}^s \right) \rho^{I} = \boldsymbol{n} \cdot \left(\boldsymbol{v}^{II} - \boldsymbol{v}^s \right) \rho^{II}
\tag{44}
$$

By using (36), (37) and (35), we obtain the final evolution equation for the excess internal energy density u^s

$$\begin{aligned}
\frac{\partial^s u^s}{\partial t} &= -\boldsymbol{\nabla}_\parallel \cdot \left(\boldsymbol{v}^s_{def} u^s + \boldsymbol{j}^s_q\right) - u^s \boldsymbol{\nabla}_\parallel \cdot \boldsymbol{v}^s_{tr} - \boldsymbol{\pi}^s : \boldsymbol{\nabla}_\parallel \boldsymbol{v}^s \\
&+ \boldsymbol{n} \cdot \left[\left(\boldsymbol{v}^{II} - \boldsymbol{v}^s\right) h^{II} + \boldsymbol{j}^{II}_q - \left(\boldsymbol{v}^I - \boldsymbol{v}^s\right) h^I - \boldsymbol{j}^I_q\right] - v^s_\perp \left(g^{II} - g^I\right) \\
&+ \left(\frac{1}{\rho^{II}} - \frac{1}{\rho^I}\right)^{-1} \times \left\{ \left[\frac{1}{2}\frac{\rho^I + \rho^{II}}{\rho^I - \rho^{II}} \left(\boldsymbol{v}^{II} - \boldsymbol{v}^I\right)^2 + \boldsymbol{n} \cdot \left(\frac{\boldsymbol{\tau}^{II}}{\rho^{II}} - \frac{\boldsymbol{\tau}^I}{\rho^I}\right) \cdot \boldsymbol{n}\right] \boldsymbol{n} \cdot \left(\boldsymbol{v}^{II} - \boldsymbol{v}^I\right) \right. \\
&\qquad \left. + \boldsymbol{n} \cdot \left(\frac{\boldsymbol{\tau}^{II}}{\rho^{II}} - \frac{\boldsymbol{\tau}^I}{\rho^I}\right) \cdot \left(\boldsymbol{v}^{II} - \boldsymbol{v}^I\right)_\parallel \right\} \\
&+ \left(\frac{1}{\rho^{II}} - \frac{1}{\rho^I}\right)^{-1} \boldsymbol{n} \cdot \left(\boldsymbol{v}^{II} - \boldsymbol{v}^I\right) \left[\boldsymbol{v}^s \cdot \left(\boldsymbol{p}^{II} \times \boldsymbol{B}^{II} - \boldsymbol{p}^I \times \boldsymbol{B}^I + \boldsymbol{E}^{II} \times \boldsymbol{m}^{II} - \boldsymbol{E}^I \times \boldsymbol{m}^I\right)\right] \\
&+ \boldsymbol{i}^{s*} \cdot \bar{\boldsymbol{E}}^* + \bar{\boldsymbol{i}}^* \cdot \boldsymbol{E}^{s*} \\
&+ \bar{\boldsymbol{D}}^* \cdot \left(\frac{\partial}{\partial t} + \boldsymbol{\nabla} \cdot \boldsymbol{v}^s\right) \boldsymbol{p}^{s*}_\perp + \bar{\boldsymbol{E}}^* \cdot \left(\frac{\partial}{\partial t} + \boldsymbol{\nabla} \cdot \boldsymbol{v}^s\right) \boldsymbol{p}^{s*}_\parallel \\
&+ \bar{\boldsymbol{B}}^* \cdot \left(\frac{\partial}{\partial t} + \boldsymbol{\nabla} \cdot \boldsymbol{v}^s\right) \boldsymbol{m}^{s*}_\perp + \bar{\boldsymbol{H}}^* \cdot \left(\frac{\partial}{\partial t} + \boldsymbol{\nabla} \cdot \boldsymbol{v}^s\right) \boldsymbol{m}^{s*}_\parallel \\
&+ \frac{1}{c} \bar{\boldsymbol{m}} \cdot \left[\boldsymbol{\nabla} \cdot \boldsymbol{v}^s \left(\boldsymbol{v}^s_\perp \times \boldsymbol{p}^s\right)\right] - \frac{1}{c} \bar{\boldsymbol{p}} \cdot \left[\boldsymbol{\nabla} \cdot \boldsymbol{v}^s \left(\boldsymbol{v}^s_\perp \times \boldsymbol{m}^s\right)\right]
\end{aligned} \tag{45}$$

where the velocity difference between bulk phases was decomposed into normal and tangential components as

$$\boldsymbol{v}^{II} - \boldsymbol{v}^I = \left(\boldsymbol{v}^{II} - \boldsymbol{v}^I\right)_\parallel + \boldsymbol{n}\boldsymbol{n} \cdot \left(\boldsymbol{v}^{II} - \boldsymbol{v}^I\right) \tag{46}$$

Combining expressions (34) and (38), we obtain for $b = s$ the evolution equation for the excess entropy density e^s in the gauge $\rho^s = 0$

$$\frac{\partial^s s^s}{\partial t} = -\boldsymbol{\nabla}_\parallel \cdot \left(\boldsymbol{v}^s_{def} s^s + \boldsymbol{j}^s_s\right) - s^s \boldsymbol{\nabla}_\parallel \cdot \boldsymbol{v}^s_{tr} + \sigma^s + \boldsymbol{n} \cdot \left[\left(\boldsymbol{v}^{II} - \boldsymbol{v}^s\right) s^{II} + \boldsymbol{j}^{II}_s - \left(\boldsymbol{v}^I - \boldsymbol{v}^s\right) s^I - \boldsymbol{j}^I_s\right] \tag{47}$$

and the excess species mass density

$$\frac{\partial^s \rho^s_\alpha}{\partial t} = -\boldsymbol{\nabla}_\parallel \cdot \left(\boldsymbol{v}^s_{def} \rho^s_\alpha + \boldsymbol{j}^s_\alpha\right) - \rho^s_\alpha \boldsymbol{\nabla}_\parallel \cdot \boldsymbol{v}^s_{tr} + \nu^s_\alpha \Gamma^s + \boldsymbol{n} \cdot \left[\left(\boldsymbol{v}^{II} - \boldsymbol{v}^s\right) \rho^{II}_\alpha + \boldsymbol{j}^{II}_\alpha - \left(\boldsymbol{v}^I - \boldsymbol{v}^s\right) \rho^I_\alpha - \boldsymbol{j}^{II}_\alpha\right] \tag{48}$$

where $\Gamma^s = \frac{1}{A}\frac{d\xi^s}{dt}$ is the mass rate of reaction per unit area, and ν^s_α is related to the stoichiometric coefficient of species α.

2.2 Derivation of the interfacial entropy production rate $\boldsymbol{\sigma}^s$

For a multi-component system, expression (33) in the gauge $\rho^s = 0$ becomes

$$\frac{\partial^s e^s}{\partial t} = T^s \frac{\partial^s s^s}{\partial t} + \sum_{\alpha=1}^{k} \left(\hat{\mu}^s_\alpha - \frac{1}{2}\left|\boldsymbol{v}^s\right|^2\right) \frac{\partial^s \rho^s_\alpha}{\partial t} + \left(\bar{\boldsymbol{E}}^*_\parallel\right)_{eq} \cdot \frac{d^s}{dt} \boldsymbol{p}^{s*}_\parallel + \left(\bar{D}^*_\perp\right)_{eq} \frac{d^s}{dt} p^{s*}_\perp + \left(\bar{\boldsymbol{H}}^*_\parallel\right)_{eq} \cdot \frac{d^s}{dt} \boldsymbol{m}^{s*}_\parallel + \left(\bar{B}^*_\perp\right)_{eq} \frac{d^s}{dt} m^{s*}_\perp \tag{49}$$

Recalling the generalized irreversible contribution to the diffusive entropy flux $\boldsymbol{j}_s$

$$\boldsymbol{j}_s = \frac{1}{T}\left(\boldsymbol{j}_q - \sum_{\alpha=1}^{k} \hat{\mu}_\alpha \boldsymbol{j}_\alpha\right) \tag{50}$$

and its equivalent for the diffusive entropy flux within the surface $\boldsymbol{j}^s_s$

$$\boldsymbol{j}^s_s = \frac{1}{T^s}\left(\boldsymbol{j}^s_q - \sum_{\alpha=1}^{k} \hat{\mu}^s_\alpha \boldsymbol{j}^s_\alpha\right) \tag{51}$$

Substituting the expressions (40), (47) and (48) into (49), together with the definitions (50) and (51), we get

$$
\begin{aligned}
&-\boldsymbol{\nabla}_{\parallel}\cdot\left(\boldsymbol{v}^{s}_{def}e^{s}+\boldsymbol{j}^{s}_{q}+\boldsymbol{\pi}^{s}\cdot\boldsymbol{v}^{s}\right)-e^{s}\boldsymbol{\nabla}_{\parallel}\cdot\boldsymbol{v}^{s}_{tr}\\
&\qquad+\boldsymbol{\nabla}_{\parallel}\left\{\boldsymbol{p}^{s*}_{\parallel}\cdot\left[\bar{\boldsymbol{E}}^{*}_{\parallel}-\left(\bar{\boldsymbol{E}}^{*}_{\parallel}\right)_{eq}\right]+p^{s*}_{\perp}\left[\bar{D}^{*}_{\perp}-\left(\bar{D}^{*}_{\perp}\right)_{eq}\right]+\boldsymbol{m}^{s*}_{\parallel}\cdot\left[\bar{\boldsymbol{H}}^{*}_{\parallel}-\left(\bar{\boldsymbol{H}}^{*}_{\parallel}\right)_{eq}\right]+m^{s*}_{\perp}\left[\bar{B}^{*}_{\perp}-\left(\bar{B}^{*}_{\perp}\right)_{eq}\right]\right\}\\
&\qquad+\boldsymbol{n}\cdot\left[\left(\boldsymbol{v}^{II}-\boldsymbol{v}^{s}\right)e^{II}+\boldsymbol{j}^{II}_{q}+\boldsymbol{\pi}^{II}\cdot\boldsymbol{v}^{II}-\left(\boldsymbol{v}^{II}-\boldsymbol{v}^{s}\right)e^{I}-\boldsymbol{j}^{I}_{q}-\boldsymbol{\pi}^{I}\cdot\boldsymbol{v}^{I}\right]\\
=\quad& T^{s}\Bigg\{-\boldsymbol{\nabla}_{\parallel}\cdot\left[\boldsymbol{v}^{s}_{def}s^{s}+\frac{1}{T^{s}}\left(\boldsymbol{j}^{s}_{q}-\sum_{\alpha=1}^{k}\hat{\mu}^{s}_{\alpha}\boldsymbol{j}^{s}_{\alpha}\right)\right]-s^{s}\boldsymbol{\nabla}_{\parallel}\cdot\boldsymbol{v}^{s}_{tr}+\sigma^{s}\\
&\qquad+\boldsymbol{n}\cdot\Bigg[\left(\boldsymbol{v}^{II}-\boldsymbol{v}^{s}\right)\left(s^{II}+\frac{1}{T^{II}}\left\{\frac{1}{2}\left|\boldsymbol{E}^{II}\right|^{2}+\frac{1}{2}\left|\boldsymbol{B}^{II}\right|^{2}+\boldsymbol{p}^{II*}\cdot\left[\boldsymbol{E}^{II*}-\left(\boldsymbol{E}^{II*}\right)_{eq}\right]\right\}\right)\\
&\qquad\qquad-\left(\boldsymbol{v}^{I}-\boldsymbol{v}^{s}\right)\left(s^{I}+\frac{1}{T^{I}}\left\{\frac{1}{2}\left|\boldsymbol{E}^{I}\right|^{2}+\frac{1}{2}\left|\boldsymbol{B}^{I}\right|^{2}+\boldsymbol{p}^{I*}\cdot\left[\boldsymbol{E}^{I*}-\left(\boldsymbol{E}^{I*}\right)_{eq}\right]\right\}\right)\\
&\qquad\qquad+\frac{1}{T^{II}}\left(\boldsymbol{j}^{II}_{q}-\sum_{\alpha=1}^{k}\hat{\mu}^{II}_{\alpha}\boldsymbol{j}^{II}_{\alpha}\right)-\frac{1}{T^{I}}\left(\boldsymbol{j}^{I}_{q}-\sum_{\alpha=1}^{k}\hat{\mu}^{I}_{\alpha}\boldsymbol{j}^{I}_{\alpha}\right)\Bigg]\Bigg\}\\
&\quad+\sum_{\alpha=1}^{k}\left(\hat{\mu}^{s}_{\alpha}-\frac{1}{2}\left|\boldsymbol{v}^{s}\right|^{2}\right)\left\{-\boldsymbol{\nabla}_{\parallel}\cdot\left(\boldsymbol{v}^{s}_{def}\rho^{s}_{\alpha}+\boldsymbol{j}^{s}_{\alpha}\right)-\rho^{s}_{\alpha}\boldsymbol{\nabla}_{\parallel}\cdot\boldsymbol{v}^{s}_{tr}+\nu^{s}_{\alpha}\Gamma^{s}\right.\\
&\qquad\qquad\qquad\qquad\left.+\boldsymbol{n}\cdot\left[\left(\boldsymbol{v}^{II}-\boldsymbol{v}^{s}\right)\rho^{II}_{\alpha}+\boldsymbol{j}^{II}_{\alpha}-\left(\boldsymbol{v}^{I}-\boldsymbol{v}^{s}\right)\rho^{I}_{\alpha}-\boldsymbol{j}^{I}_{\alpha}\right]\right\}\\
&\quad-\frac{1}{2}\left[\boldsymbol{i}^{s*}_{\parallel}\cdot\left(\boldsymbol{E}^{I*}_{\parallel}+\boldsymbol{E}^{II*}_{\parallel}\right)+\left(i^{I*}_{\perp}+i^{II*}_{\perp}\right)E^{s*}_{\perp}\right]\\
&\quad-\frac{1}{2}\Bigg\{\left[\left(\boldsymbol{E}^{I*}_{\parallel}+\boldsymbol{E}^{II*}_{\parallel}\right)-\left(\boldsymbol{E}^{I*}_{\parallel}+\boldsymbol{E}^{II*}_{\parallel}\right)_{eq}\right]\cdot\frac{d^{s}}{dt}\boldsymbol{p}^{s*}_{\parallel}-\left[\left(D^{I*}_{\perp}+D^{II*}_{\perp}\right)-\left(D^{I*}_{\perp}+D^{II*}_{\perp}\right)_{eq}\right]\frac{d^{s}}{dt}p^{s*}_{\perp}\\
&\qquad-\left[\left(\boldsymbol{H}^{I*}_{\parallel}+\boldsymbol{H}^{II*}_{\parallel}\right)-\left(\boldsymbol{H}^{I*}_{\parallel}+\boldsymbol{H}^{II*}_{\parallel}\right)_{eq}\right]\cdot\frac{d^{s}}{dt}\boldsymbol{m}^{s*}_{\parallel}-\left[\left(B^{I*}_{\perp}+B^{II*}_{\perp}\right)-\left(B^{I*}_{\perp}+B^{II*}_{\perp}\right)_{eq}\right]\frac{d^{s}}{dt}m^{s*}_{\perp}\Bigg\}
\end{aligned}
\tag{52}
$$

We can define the following averages of the bulk fields at the dividing interface

$$
\begin{aligned}
\bar{\boldsymbol{E}}^{*}_{\parallel}&=\frac{1}{2}\left(\boldsymbol{E}^{I*}_{\parallel}+\boldsymbol{E}^{II*}_{\parallel}\right) &\qquad \bar{D}^{*}_{\perp}&=\frac{1}{2}\left(D^{I*}_{\perp}+D^{II*}_{\perp}\right) &\qquad \bar{i}^{*}_{\perp}&=\frac{1}{2}\left(i^{I*}_{\perp}+i^{II*}_{\perp}\right)\\
\bar{\boldsymbol{H}}^{*}_{\parallel}&=\frac{1}{2}\left(\boldsymbol{H}^{I*}_{\parallel}+\boldsymbol{H}^{II*}_{\parallel}\right) &\qquad \bar{B}^{*}_{\perp}&=\frac{1}{2}\left(B^{I*}_{\perp}+B^{II*}_{\perp}\right)
\end{aligned}
\tag{53}
$$

We add and subtract the terms $\boldsymbol{m}^{i*} \cdot \left[\boldsymbol{B}^{i*} - \left(\boldsymbol{B}^{i*}\right)_{eq}\right]$ in line five and six of (52), and we also substitute the expressions (53) in the last three lines of (52); we obtain

$$
\begin{aligned}
&-\boldsymbol{\nabla}_{\|} \cdot \left(\boldsymbol{v}^s_{def} e^s + \boldsymbol{j}^s_q + \boldsymbol{\pi}^s \cdot \boldsymbol{v}^s\right) - e^s \boldsymbol{\nabla}_{\|} \cdot \boldsymbol{v}^s_{tr} \\
&\qquad + \boldsymbol{\nabla}_{\|} \left\{ \boldsymbol{p}^{s*}_{\|} \cdot \left[\bar{\boldsymbol{E}}^*_{\|} - \left(\bar{\boldsymbol{E}}^*_{\|}\right)_{eq}\right] + p^{s*}_{\perp} \left[\bar{D}^*_{\perp} - \left(\bar{D}^*_{\perp}\right)_{eq}\right] + \boldsymbol{m}^{s*}_{\|} \cdot \left[\bar{\boldsymbol{H}}^*_{\|} - \left(\bar{\boldsymbol{H}}^*_{\|}\right)_{eq}\right] + m^{s*}_{\perp} \left[\bar{B}^*_{\perp} - \left(\bar{B}^*_{\perp}\right)_{eq}\right] \right\} \\
&\qquad + \boldsymbol{n} \cdot \left[\left(\boldsymbol{v}^{II} - \boldsymbol{v}^s\right) e^{II} + \boldsymbol{j}^{II}_q + \boldsymbol{\pi}^{II} \cdot \boldsymbol{v}^{II} - \left(\boldsymbol{v}^{II} - \boldsymbol{v}^s\right) e^{I} - \boldsymbol{j}^{I}_q - \boldsymbol{\pi}^{I} \cdot \boldsymbol{v}^{I}\right] \\
= \quad & T^s \Bigg\{ -\boldsymbol{\nabla}_{\|} \cdot \left[\boldsymbol{v}^s_{def} s^s + \frac{1}{T^s} \left(\boldsymbol{j}^s_q - \sum_{\alpha=1}^{k} \hat{\mu}^s_\alpha \boldsymbol{j}^s_\alpha\right)\right] - s^s \boldsymbol{\nabla}_{\|} \cdot \boldsymbol{v}^s_{tr} + \sigma^s \\
&\qquad + \boldsymbol{n} \cdot \Bigg[\left(\boldsymbol{v}^{II} - \boldsymbol{v}^s\right) \Bigg(s^{II} + \frac{1}{T^{II}} \left\{ \frac{1}{2} \left|\boldsymbol{E}^{II}\right|^2 + \frac{1}{2} \left|\boldsymbol{B}^{II}\right|^2 - \boldsymbol{m}^{II*} \cdot \left[\boldsymbol{B}^{II*} - \left(\boldsymbol{B}^{II*}\right)_{eq}\right] \right\} \\
&\qquad\qquad\qquad\qquad + \frac{1}{T^{II}} \left\{ \boldsymbol{p}^{II*} \cdot \left[\boldsymbol{E}^{II*} - \left(\boldsymbol{E}^{II*}\right)_{eq}\right] + \boldsymbol{m}^{II*} \cdot \left[\boldsymbol{B}^{II*} + \left(\boldsymbol{B}^{II*}\right)_{eq}\right] \right\} \Bigg) \\
&\qquad\qquad - \left(\boldsymbol{v}^{I} - \boldsymbol{v}^s\right) \Bigg(s^{I} + \frac{1}{T^{I}} \left\{ \frac{1}{2} \left|\boldsymbol{E}^{I}\right|^2 + \frac{1}{2} \left|\boldsymbol{B}^{I}\right|^2 - \boldsymbol{m}^{I*} \cdot \left[\boldsymbol{B}^{I*} - \left(\boldsymbol{B}^{I*}\right)_{eq}\right] \right\} \\
&\qquad\qquad\qquad\qquad + \frac{1}{T^{I}} \left\{ \boldsymbol{p}^{I*} \cdot \left[\boldsymbol{E}^{I*} - \left(\boldsymbol{E}^{I*}\right)_{eq}\right] + \boldsymbol{m}^{I*} \cdot \left[\boldsymbol{B}^{I*} + \left(\boldsymbol{B}^{I*}\right)_{eq}\right] \right\} \Bigg) \\
&\qquad\qquad + \frac{1}{T^{II}} \left(\boldsymbol{j}^{II}_q - \sum_{\alpha=1}^{k} \hat{\mu}^{II}_\alpha \boldsymbol{j}^{II}_\alpha\right) - \frac{1}{T^{I}} \left(\boldsymbol{j}^{I}_q - \sum_{\alpha=1}^{k} \hat{\mu}^{I}_\alpha \boldsymbol{j}^{I}_\alpha\right) \Bigg] \Bigg\} \\
&\quad + \sum_{\alpha=1}^{k} \left(\hat{\mu}^s_\alpha - \frac{1}{2} \left|\boldsymbol{v}^s\right|^2\right) \left\{ -\boldsymbol{\nabla}_{\|} \cdot \left(\boldsymbol{v}^s_{def} \rho^s_\alpha + \boldsymbol{j}^s_\alpha\right) - \rho^s_\alpha \boldsymbol{\nabla}_{\|} \cdot \boldsymbol{v}^s_{tr} + \nu^s_\alpha \Gamma^s \right. \\
&\qquad\qquad\qquad\qquad \left. + \boldsymbol{n} \cdot \left[\left(\boldsymbol{v}^{II} - \boldsymbol{v}^s\right) \rho^{II}_\alpha + \boldsymbol{j}^{II}_\alpha - \left(\boldsymbol{v}^{I} - \boldsymbol{v}^s\right) \rho^{I}_\alpha - \boldsymbol{j}^{I}_\alpha\right] \right\} \\
&\quad - \left(\boldsymbol{i}^{s*}_{\|} \cdot \bar{\boldsymbol{E}}^*_{\|} + \bar{i}^*_{\perp} E^{s*}_{\perp}\right) \\
&\quad - \left\{ \left[\bar{\boldsymbol{E}}^*_{\|} - \left(\bar{\boldsymbol{E}}^*_{\|}\right)_{eq}\right] \cdot \frac{d^s}{dt} \boldsymbol{p}^{s*}_{\|} + \left[\bar{D}^*_{\perp} - \left(\bar{D}^*_{\perp}\right)_{eq}\right] \frac{d^s}{dt} p^{s*}_{\perp} \right. \\
&\qquad \left. + \left[\bar{\boldsymbol{H}}^*_{\|} - \left(\bar{\boldsymbol{H}}^*_{\|}\right)_{eq}\right] \cdot \frac{d^s}{dt} \boldsymbol{m}^{s*}_{\|} + \left[\bar{B}^*_{\perp} - \left(\bar{B}^*_{\perp}\right)_{eq}\right] \frac{d^s}{dt} m^{s*}_{\perp} \right\}
\end{aligned}
\tag{54}
$$

In our gauge $\rho^s = 0$, we can neglect the term for the momentum density of the electromagnetic field $\frac{1}{c}\left(\boldsymbol{E}^i \times \boldsymbol{M}^i\right)$. We then notice that the expressions in curly brackets in lines 5 and 7 represent the Lorentz-Heaviside bulk-phase electromagnetic energy densities per unit volume g^i for the two phases I and II (see expression (15)). Therefore we can re-write (54) as

$$
\begin{aligned}
&-\boldsymbol{\nabla}_{\parallel}\cdot\left(\boldsymbol{v}^{s}_{def}e^{s}+\boldsymbol{j}^{s}_{q}+\boldsymbol{\pi}^{s}\cdot\boldsymbol{v}^{s}\right)-e^{s}\boldsymbol{\nabla}_{\parallel}\cdot\boldsymbol{v}^{s}_{tr}\\
&\quad+\boldsymbol{\nabla}_{\parallel}\left\{\boldsymbol{p}^{s*}_{\parallel}\cdot\left[\bar{\boldsymbol{E}}^{*}_{\parallel}-\left(\bar{\boldsymbol{E}}^{*}_{\parallel}\right)_{eq}\right]+p^{s*}_{\perp}\left[\bar{D}^{*}_{\perp}-\left(\bar{D}^{*}_{\perp}\right)_{eq}\right]+\boldsymbol{m}^{s*}_{\parallel}\cdot\left[\bar{\boldsymbol{H}}^{*}_{\parallel}-\left(\bar{\boldsymbol{H}}^{*}_{\parallel}\right)_{eq}\right]+m^{s*}_{\perp}\left[\bar{B}^{*}_{\perp}-\left(\bar{B}^{*}_{\perp}\right)_{eq}\right]\right\}\\
&\quad+\boldsymbol{n}\cdot\left[\left(\boldsymbol{v}^{II}-\boldsymbol{v}^{s}\right)e^{II}+\boldsymbol{j}^{II}_{q}+\boldsymbol{\pi}^{II}\cdot\boldsymbol{v}^{II}-\left(\boldsymbol{v}^{II}-\boldsymbol{v}^{s}\right)e^{I}-\boldsymbol{j}^{I}_{q}-\boldsymbol{\pi}^{I}\cdot\boldsymbol{v}^{I}\right]\\
=\;\; & T^{s}\left\{-\boldsymbol{\nabla}_{\parallel}\cdot\left[\boldsymbol{v}^{s}_{def}s^{s}+\frac{1}{T^{s}}\left(\boldsymbol{j}^{s}_{q}-\sum_{\alpha=1}^{k}\hat{\mu}^{s}_{\alpha}\boldsymbol{j}^{s}_{\alpha}\right)\right]-s^{s}\boldsymbol{\nabla}_{\parallel}\cdot\boldsymbol{v}^{s}_{tr}+\sigma^{s}\right.\\
&\quad+\boldsymbol{n}\cdot\left[\left(\boldsymbol{v}^{II}-\boldsymbol{v}^{s}\right)\left(s^{II}+\frac{1}{T^{II}}g^{II}+\frac{1}{T^{II}}\left\{\boldsymbol{p}^{II*}\cdot\left[\boldsymbol{E}^{II*}-\left(\boldsymbol{E}^{II*}\right)_{eq}\right]+\boldsymbol{m}^{II*}\cdot\left[\boldsymbol{B}^{II*}+\left(\boldsymbol{B}^{II*}\right)_{eq}\right]\right\}\right)\right.\\
&\qquad-\left(\boldsymbol{v}^{I}-\boldsymbol{v}^{s}\right)\left(s^{I}+\frac{1}{T^{I}}g^{I}+\frac{1}{T^{I}}\left\{\boldsymbol{p}^{I*}\cdot\left[\boldsymbol{E}^{I*}-\left(\boldsymbol{E}^{I*}\right)_{eq}\right]+\boldsymbol{m}^{I*}\cdot\left[\boldsymbol{B}^{I*}+\left(\boldsymbol{B}^{I*}\right)_{eq}\right]\right\}\right)\\
&\qquad\left.\left.+\frac{1}{T^{II}}\left(\boldsymbol{j}^{II}_{q}-\sum_{\alpha=1}^{k}\hat{\mu}^{II}_{\alpha}\boldsymbol{j}^{II}_{\alpha}\right)-\frac{1}{T^{I}}\left(\boldsymbol{j}^{I}_{q}-\sum_{\alpha=1}^{k}\hat{\mu}^{I}_{\alpha}\boldsymbol{j}^{I}_{\alpha}\right)\right]\right\}\\
&+\sum_{\alpha=1}^{k}\left(\hat{\mu}^{s}_{\alpha}-\frac{1}{2}\left|\boldsymbol{v}^{s}\right|^{2}\right)\left\{-\boldsymbol{\nabla}_{\parallel}\cdot\left(\boldsymbol{v}^{s}_{def}\rho^{s}_{\alpha}+\boldsymbol{j}^{s}_{\alpha}\right)-\rho^{s}_{\alpha}\boldsymbol{\nabla}_{\parallel}\cdot\boldsymbol{v}^{s}_{tr}+\nu^{s}_{\alpha}\Gamma^{s}\right.\\
&\qquad\qquad\qquad\left.+\boldsymbol{n}\cdot\left[\left(\boldsymbol{v}^{II}-\boldsymbol{v}^{s}\right)\rho^{II}_{\alpha}+\boldsymbol{j}^{II}_{\alpha}-\left(\boldsymbol{v}^{I}-\boldsymbol{v}^{s}\right)\rho^{I}_{\alpha}-\boldsymbol{j}^{I}_{\alpha}\right]\right\}\\
&-\left(\boldsymbol{i}^{s*}_{\parallel}\cdot\bar{\boldsymbol{E}}^{*}_{\parallel}+\bar{i}^{*}_{\perp}E^{s*}_{\perp}\right)\\
&-\left\{\left[\bar{\boldsymbol{E}}^{*}_{\parallel}-\left(\bar{\boldsymbol{E}}^{*}_{\parallel}\right)_{eq}\right]\cdot\frac{d^{s}}{dt}\boldsymbol{p}^{s*}_{\parallel}+\left[\bar{D}^{*}_{\perp}-\left(\bar{D}^{*}_{\perp}\right)_{eq}\right]\frac{d^{s}}{dt}p^{s*}_{\perp}\right.\\
&\quad\left.+\left[\bar{\boldsymbol{H}}^{*}_{\parallel}-\left(\bar{\boldsymbol{H}}^{*}_{\parallel}\right)_{eq}\right]\cdot\frac{d^{s}}{dt}\boldsymbol{m}^{s*}_{\parallel}+\left[\bar{B}^{*}_{\perp}-\left(\bar{B}^{*}_{\perp}\right)_{eq}\right]\frac{d^{s}}{dt}m^{s*}_{\perp}\right\}
\end{aligned}
\tag{55}
$$

We use the following definitions of the modified chemical potentials at the dividing interface [1]:

$$
\begin{aligned}
\tilde{\mu}^{i}_{\alpha}&\equiv\hat{\mu}^{i}_{\alpha}-\boldsymbol{p}^{i*}\cdot\left[\boldsymbol{E}^{i*}-\left(\boldsymbol{E}^{i*}\right)_{eq}\right]-\boldsymbol{m}^{i*}\cdot\left[\boldsymbol{B}^{i*}-\left(\boldsymbol{B}^{i*}\right)_{eq}\right]-\frac{1}{2}\left|\boldsymbol{v}^{i}\right|^{2}\qquad\text{with}\qquad i=I,II\\
\tilde{\mu}^{s}_{\alpha}&\equiv\hat{\mu}^{s}_{\alpha}-\boldsymbol{p}^{s*}_{\parallel}\cdot\left[\bar{\boldsymbol{E}}^{*}_{\parallel}-\left(\bar{\boldsymbol{E}}^{*}_{\parallel}\right)_{eq}\right]-p^{s*}_{\perp}\left[\bar{D}^{*}_{\perp}-\left(\bar{D}^{*}_{\perp}\right)_{eq}\right]\\
&\qquad-\boldsymbol{m}^{s*}_{\parallel}\cdot\left[\bar{\boldsymbol{H}}^{*}_{\parallel}-\left(\bar{\boldsymbol{H}}^{*}_{\parallel}\right)_{eq}\right]-m^{s*}_{\perp}\left[\bar{B}^{*}_{\perp}-\left(\bar{B}^{*}_{\perp}\right)_{eq}\right]-\frac{1}{2}\left|\boldsymbol{v}^{s}\right|^{2}
\end{aligned}
\tag{56}
$$

Solving expression (55) for σ^s and substituting (56), we obtain

$$\begin{aligned}
T^s\sigma^s = &-\boldsymbol{\nabla}_\parallel \cdot \left(\boldsymbol{v}^s_{def} e^s\right) + T^s \boldsymbol{\nabla}_\parallel \cdot \left(\boldsymbol{v}^s_{def} s^s\right) + \sum_{\alpha=1}^{k} \hat{\mu}^s_\alpha \boldsymbol{\nabla}_\parallel \cdot \left(\boldsymbol{v}^s_{def} \rho^s_\alpha\right) \\
&+ T^s \boldsymbol{j}^s_q \cdot \boldsymbol{\nabla}_\parallel \frac{1}{T^s} - T^s \sum_{\alpha=1}^{k} \boldsymbol{j}^s_\alpha \cdot \boldsymbol{\nabla}_\parallel \frac{\hat{\mu}^s_\alpha}{T^s} - \sum_{\alpha=1}^{k} \nu^s_\alpha \hat{\mu}^s_\alpha \Gamma^s \\
&- \boldsymbol{v}^s \cdot \left(\boldsymbol{\nabla}_\parallel \cdot \boldsymbol{\pi}^s\right) - \boldsymbol{\pi}^s : \boldsymbol{\nabla}_\parallel \boldsymbol{v}^s - \left(e^s - T^s s^s - \sum_{\alpha=1}^{k} \hat{\mu}^s_\alpha \rho^s_\alpha\right) \boldsymbol{\nabla}_\parallel \cdot \boldsymbol{v}^s_{tr} \\
&+ \boldsymbol{n} \cdot \left\{ \left(\boldsymbol{v}^{II} - \boldsymbol{v}^s\right) \left(e^{II} - T^s s^{II} - \sum_{\alpha=1}^{k} \hat{\mu}^s_\alpha \rho^{II}_\alpha\right) - \left(\boldsymbol{v}^I - \boldsymbol{v}^s\right) \left(e^I - T^s s^I - \sum_{\alpha=1}^{k} \hat{\mu}^s_\alpha \rho^I_\alpha\right) \right\} \\
&+ T^s \boldsymbol{n} \cdot \boldsymbol{j}^{II}_q \left(\frac{1}{T^s} - \frac{1}{T^{II}}\right) - T^s \boldsymbol{n} \cdot \boldsymbol{j}^I_q \left(\frac{1}{T^s} - \frac{1}{T^I}\right) \\
&- T^s \sum_{\alpha=1}^{k} \boldsymbol{n} \cdot \boldsymbol{j}^{II}_\alpha \left(\frac{\tilde{\mu}^s_\alpha}{T^s} - \frac{\tilde{\mu}^{II}_\alpha}{T^{II}}\right) + T^s \sum_{\alpha=1}^{k} \boldsymbol{n} \cdot \boldsymbol{j}^I_\alpha \left(\frac{\tilde{\mu}^s_\alpha}{T^s} - \frac{\tilde{\mu}^I_\alpha}{T^I}\right) \\
&+ \boldsymbol{n} \cdot \left[\boldsymbol{\pi}^{II} \cdot \left(\boldsymbol{v}^{II} - \boldsymbol{v}^s\right) - \boldsymbol{\pi}^I \cdot \left(\boldsymbol{v}^I - \boldsymbol{v}^s\right)\right] + \boldsymbol{n} \cdot \left(\boldsymbol{\pi}^{II} - \boldsymbol{\pi}^I\right) \cdot \boldsymbol{v}^s \\
&+ \left(\boldsymbol{i}^{s*}_\parallel \cdot \bar{\boldsymbol{E}}^*_\parallel + \bar{i}^*_\perp E^{s*}_\perp\right) \\
&+ \left\{ \left[\bar{\boldsymbol{E}}^*_\parallel - \left(\bar{\boldsymbol{E}}^*_\parallel\right)_{eq}\right] \cdot \frac{d^s}{dt} \boldsymbol{p}^{s*}_\parallel + \left[\bar{D}^*_\perp - \left(\bar{D}^*_\perp\right)_{eq}\right] \frac{d^s}{dt} p^{s*}_\perp \right. \\
&\qquad \left. + \left[\bar{\boldsymbol{H}}^*_\parallel - \left(\bar{\boldsymbol{H}}^*_\parallel\right)_{eq}\right] \cdot \frac{d^s}{dt} \boldsymbol{m}^{s*}_\parallel + \left[\bar{B}^*_\perp - \left(\bar{B}^*_\perp\right)_{eq}\right] \frac{d^s}{dt} m^{s*}_\perp \right\}
\end{aligned} \tag{57}$$

Let us now recall the surface pressure tensor decomposition $\boldsymbol{\pi}^s = -\gamma \boldsymbol{\delta}_\parallel + \boldsymbol{\tau}^s$, together with the Euler equation (30) and the fundamental thermodynamic form (33); let us also express energy and entropy densities in terms of bulk intensive variables.

Finally, we decompose the bulk pressure tensor $\boldsymbol{\pi}$ as $\boldsymbol{\pi} = p\boldsymbol{\delta} + \boldsymbol{\tau}$ and we recall the general expression for the conservation of the bulk energy density

$$e + p - Ts - \sum_{\alpha=1}^{k} \hat{\mu}_\alpha \rho_\alpha = \frac{1}{2} \rho \boldsymbol{v}^2 \tag{58}$$

We ultimately expand the expression (57)

$$
\begin{aligned}
\sigma^s = {} & \boldsymbol{j}_q^s \cdot \boldsymbol{\nabla}_\parallel \frac{1}{T^s} - \frac{1}{T^s} \boldsymbol{\tau}^s : \boldsymbol{\nabla}_\parallel \boldsymbol{v}^s - \sum_{\alpha=1}^{k} \boldsymbol{j}_\alpha^s \cdot \boldsymbol{\nabla}_\parallel \frac{\hat{\mu}_\alpha^s}{T^s} - \frac{1}{T^s} \sum_{\alpha=1}^{k} \nu_\alpha^s \hat{\mu}_\alpha^s \Gamma^s \\
& + \frac{1}{T^s} \left\{ \boldsymbol{n} \cdot \left[\rho^{II} \left(\boldsymbol{v}^{II} - \boldsymbol{v}^s \right) \frac{1}{2} {\boldsymbol{v}^{II}}^2 - \rho^I \left(\boldsymbol{v}^I - \boldsymbol{v}^s \right) \frac{1}{2} {\boldsymbol{v}^I}^2 \right] + \boldsymbol{n} \cdot \left[\boldsymbol{\tau}^{II} \cdot \left(\boldsymbol{v}^{II} - \boldsymbol{v}^s \right) - \boldsymbol{\tau}^I \cdot \left(\boldsymbol{v}^I - \boldsymbol{v}^s \right) \right] \right\} \\
& + \boldsymbol{n} \cdot \left[\left(\boldsymbol{v}^{II} - \boldsymbol{v}^s \right) \left(T^{II} s^{II} + g^{II} \right) + \boldsymbol{j}_q^{II} \right] \left(\frac{1}{T^s} - \frac{1}{T^{II}} \right) - \boldsymbol{n} \cdot \left[\left(\boldsymbol{v}^I - \boldsymbol{v}^s \right) \left(T^I s^I + g^I \right) + \boldsymbol{j}_q^I \right] \left(\frac{1}{T^s} - \frac{1}{T^I} \right) \\
& - \sum_{\alpha=1}^{k} \boldsymbol{n} \cdot \left[\left(\boldsymbol{v}^{II} - \boldsymbol{v}^s \right) \rho_\alpha^{II} \left(\frac{\hat{\mu}_\alpha^s}{T^s} - \frac{\hat{\mu}_\alpha^{II}}{T^s} \right) + \boldsymbol{j}_\alpha^{II} \left(\frac{\hat{\mu}_\alpha^s}{T^s} - \frac{\hat{\mu}_\alpha^{II}}{T^{II}} \right) \right] \\
& + \sum_{\alpha=1}^{k} \boldsymbol{n} \cdot \left[\left(\boldsymbol{v}^I - \boldsymbol{v}^s \right) \rho_\alpha^I \left(\frac{\hat{\mu}_\alpha^s}{T^s} - \frac{\hat{\mu}_\alpha^I}{T^s} \right) + \boldsymbol{j}_\alpha^I \left(\frac{\hat{\mu}_\alpha^s}{T^s} - \frac{\hat{\mu}_\alpha^I}{T^I} \right) \right] \\
& + \frac{1}{T^s} \left[\boldsymbol{n} \cdot \left(\boldsymbol{\pi}^{II} - \boldsymbol{\pi}^I \right) \cdot \boldsymbol{v}^s - \boldsymbol{v}^s \cdot \boldsymbol{\nabla}_\parallel \cdot \boldsymbol{\pi}^s \right] \\
& + \frac{1}{T^s} \left(\boldsymbol{i}_\parallel^{s*} \cdot \bar{\boldsymbol{E}}_\parallel^* + \bar{i}_\perp^* E_\perp^{s*} \right) \\
& + \frac{1}{T^s} \left\{ \left[\bar{\boldsymbol{E}}_\parallel^* - \left(\bar{\boldsymbol{E}}_\parallel^* \right)_{eq} \right] \cdot \frac{d^s}{dt} \boldsymbol{p}_\parallel^{s*} + \left[\bar{D}_\perp^* - \left(\bar{D}_\perp^* \right)_{eq} \right] \frac{d^s}{dt} p_\perp^{s*} \right. \\
& \qquad \left. + \left[\bar{\boldsymbol{H}}_\parallel^* - \left(\bar{\boldsymbol{H}}_\parallel^* \right)_{eq} \right] \cdot \frac{d^s}{dt} \boldsymbol{m}_\parallel^{s*} + \left[\bar{B}_\perp^* - \left(\bar{B}_\perp^* \right)_{eq} \right] \frac{d^s}{dt} m_\perp^{s*} \right\}
\end{aligned}
\tag{59}
$$

It is known the basic thermodynamic relation

$$
Ts = h - g - \sum_{\alpha=1}^{k} \hat{\mu}_\alpha \rho_\alpha \tag{60}
$$

Using the expressions (35), (36), (37) and (60) and decomposing the velocity difference into normal and tangential components, we can re-write Equation (59)

$$
\begin{aligned}
\sigma^s = {} & \boldsymbol{j}_q^s \cdot \boldsymbol{\nabla}_\parallel \frac{1}{T^s} - \frac{1}{T^s} \boldsymbol{\tau}^s : \boldsymbol{\nabla}_\parallel \boldsymbol{v}^s - \sum_{\alpha=1}^{k} \boldsymbol{j}_\alpha^s \cdot \boldsymbol{\nabla}_\parallel \frac{\hat{\mu}_\alpha^s}{T^s} - \frac{1}{T^s} \sum_{\alpha=1}^{k} \nu_\alpha^s \hat{\mu}_\alpha^s \Gamma^s \\
& + \boldsymbol{n} \cdot \left[\left(\boldsymbol{v}^{II} - \boldsymbol{v}^s \right) \left(h^{II} - g^{II} \right) + \boldsymbol{j}_q^{II} \right] \left(\frac{1}{T^s} - \frac{1}{T^{II}} \right) - \boldsymbol{n} \cdot \left[\left(\boldsymbol{v}^I - \boldsymbol{v}^s \right) \left(h^I - g^I \right) + \boldsymbol{j}_q^I \right] \left(\frac{1}{T^s} - \frac{1}{T^I} \right) \\
& + \frac{1}{T^s} \left(\frac{1}{\rho^{II}} - \frac{1}{\rho^I} \right)^{-1} \left\{ \frac{1}{2} \frac{\rho^I + \rho^{II}}{\rho^I - \rho^{II}} \left(\boldsymbol{v}^{II} - \boldsymbol{v}^I \right)^2 + \boldsymbol{n} \cdot \left(\frac{\boldsymbol{\tau}^{II}}{\rho^{II}} - \frac{\boldsymbol{\tau}^I}{\rho^I} \right) \cdot \boldsymbol{n} \right\} \boldsymbol{n} \cdot \left(\boldsymbol{v}^{II} - \boldsymbol{v}^I \right) \\
& + \frac{1}{T^s} \left(\frac{1}{\rho^{II}} - \frac{1}{\rho^I} \right)^{-1} \boldsymbol{n} \cdot \left(\frac{\boldsymbol{\tau}^{II}}{\rho^{II}} - \frac{\boldsymbol{\tau}^I}{\rho^I} \right) \cdot \left(\boldsymbol{v}^{II} - \boldsymbol{v}^I \right)_\parallel \\
& - \sum_{\alpha=1}^{k} \boldsymbol{n} \cdot \left[\left(\boldsymbol{v}^{II} - \boldsymbol{v}^s \right) \rho_\alpha^{II} + \boldsymbol{j}_\alpha^{II} \right] \left(\frac{\tilde{\mu}_\alpha^s}{T^s} - \frac{\tilde{\mu}_\alpha^{II}}{T^{II}} \right) + \sum_{\alpha=1}^{k} \boldsymbol{n} \cdot \left[\left(\boldsymbol{v}^I - \boldsymbol{v}^s \right) \rho_\alpha^I + \boldsymbol{j}_\alpha^I \right] \left(\frac{\tilde{\mu}_\alpha^s}{T^s} - \frac{\tilde{\mu}_\alpha^I}{T^I} \right) \\
& + \frac{1}{T^s} \left(\boldsymbol{i}_\parallel^{s*} \cdot \bar{\boldsymbol{E}}_\parallel^* + \bar{i}_\perp^* E_\perp^{s*} \right) \\
& + \frac{1}{T^s} \left\{ \left[\bar{\boldsymbol{E}}_\parallel^* - \left(\bar{\boldsymbol{E}}_\parallel^* \right)_{eq} \right] \cdot \frac{d^s}{dt} \boldsymbol{p}_\parallel^{s*} + \left[\bar{D}_\perp^* - \left(\bar{D}_\perp^* \right)_{eq} \right] \frac{d^s}{dt} p_\perp^{s*} \right. \\
& \qquad \left. + \left[\bar{\boldsymbol{H}}_\parallel^* - \left(\bar{\boldsymbol{H}}_\parallel^* \right)_{eq} \right] \cdot \frac{d^s}{dt} \boldsymbol{m}_\parallel^{s*} + \left[\bar{B}_\perp^* - \left(\bar{B}_\perp^* \right)_{eq} \right] \frac{d^s}{dt} m_\perp^{s*} \right\}
\end{aligned}
\tag{61}
$$

As done by other authors [16], the following *flat-average* chemical potentials are introduced

$$\tilde{\mu}^{I} = \frac{1}{k}\sum_{\alpha=1}^{k}\tilde{\mu}^{I}_{\alpha} \qquad \tilde{\mu}^{II} = \frac{1}{k}\sum_{\alpha=1}^{k}\tilde{\mu}^{II}_{\alpha} \qquad \tilde{\mu}^{s} = \frac{1}{k}\sum_{\alpha=1}^{k}\tilde{\mu}^{s}_{\alpha} \tag{62}$$

together with the expression for the momentum density

$$k\boldsymbol{m} = \left(\boldsymbol{v}^{I} - \boldsymbol{v}^{s}\right)\rho^{I} = \left(\boldsymbol{v}^{II} - \boldsymbol{v}^{s}\right)\rho^{II} \tag{63}$$

Substituting equations (62) and (63) into (61), we ultimately get

$$\begin{aligned}
\sigma^{s} = {} & \boldsymbol{j}^{s}_{q}\cdot\boldsymbol{\nabla}_{\parallel}\frac{1}{T^{s}} - \frac{1}{T^{s}}\boldsymbol{\tau}^{s} : \boldsymbol{\nabla}_{\parallel}\boldsymbol{v}^{s} - \sum_{\alpha=1}^{k}\boldsymbol{j}^{s}_{\alpha}\cdot\boldsymbol{\nabla}_{\parallel}\frac{\hat{\mu}^{s}_{\alpha} - \hat{\mu}^{s}}{T^{s}} - \frac{1}{T^{s}}\sum_{\alpha=1}^{k}\nu^{s}_{\alpha}\hat{\mu}^{s}_{\alpha}\Gamma^{s} \\
& + \boldsymbol{n}\cdot\left[\left(\boldsymbol{v}^{II} - \boldsymbol{v}^{s}\right)\left(h^{II} - g^{II}\right) + \boldsymbol{j}^{II}_{q}\right]\left(\frac{1}{T^{s}} - \frac{1}{T^{II}}\right) - \boldsymbol{n}\cdot\left[\left(\boldsymbol{v}^{I} - \boldsymbol{v}^{s}\right)\left(h^{I} - g^{I}\right) + \boldsymbol{j}^{I}_{q}\right]\left(\frac{1}{T^{s}} - \frac{1}{T^{I}}\right) \\
& + \frac{1}{T^{s}}\left(\frac{1}{\rho^{II}} - \frac{1}{\rho^{I}}\right)^{-1}\left\{T^{s}\left(\frac{\tilde{\mu}^{II}}{T^{II}} - \frac{\tilde{\mu}^{I}}{T^{I}}\right) + \frac{1}{2}\frac{\rho^{I} + \rho^{II}}{\rho^{I} - \rho^{II}}\left(\boldsymbol{v}^{II} - \boldsymbol{v}^{I}\right)^{2} + \boldsymbol{n}\cdot\left(\frac{\boldsymbol{\tau}^{II}}{\rho^{II}} - \frac{\boldsymbol{\tau}^{I}}{\rho^{I}}\right)\cdot\boldsymbol{n}\right\}\boldsymbol{n}\cdot\left(\boldsymbol{v}^{II} - \boldsymbol{v}^{I}\right) \\
& + \frac{1}{T^{s}}\left(\frac{1}{\rho^{II}} - \frac{1}{\rho^{I}}\right)^{-1}\boldsymbol{n}\cdot\left(\frac{\boldsymbol{\tau}^{II}}{\rho^{II}} - \frac{\boldsymbol{\tau}^{I}}{\rho^{I}}\right)\cdot\left(\boldsymbol{v}^{II} - \boldsymbol{v}^{I}\right)_{\parallel} \\
& - \sum_{\alpha=1}^{k}\boldsymbol{n}\cdot\left[\left(\boldsymbol{v}^{II} - \boldsymbol{v}^{s}\right)\rho^{II}_{\alpha} - \boldsymbol{m} + \boldsymbol{j}^{II}_{\alpha}\right]\left(\frac{\tilde{\mu}^{s}_{\alpha} - \tilde{\mu}^{s}}{T^{s}} - \frac{\tilde{\mu}^{II}_{\alpha} - \tilde{\mu}^{II}}{T^{II}}\right) \\
& + \sum_{\alpha=1}^{k}\boldsymbol{n}\cdot\left[\left(\boldsymbol{v}^{I} - \boldsymbol{v}^{s}\right)\rho^{I}_{\alpha} - \boldsymbol{m} + \boldsymbol{j}^{I}_{\alpha}\right]\left(\frac{\tilde{\mu}^{s}_{\alpha} - \tilde{\mu}^{s}}{T^{s}} - \frac{\tilde{\mu}^{I}_{\alpha} - \tilde{\mu}^{I}}{T^{I}}\right) \\
& + \frac{1}{T^{s}}\left(\boldsymbol{i}^{s*}_{\parallel}\cdot\bar{\boldsymbol{E}}^{*}_{\parallel} + \bar{i}^{*}_{\perp}E^{s*}_{\perp}\right) \\
& + \frac{1}{T^{s}}\left\{\left[\bar{\boldsymbol{E}}^{*}_{\parallel} - \left(\bar{\boldsymbol{E}}^{*}_{\parallel}\right)_{eq}\right]\cdot\frac{d^{s}}{dt}\boldsymbol{p}^{s*}_{\parallel} + \left[\bar{D}^{*}_{\perp} - \left(\bar{D}^{*}_{\perp}\right)_{eq}\right]\frac{d^{s}}{dt}p^{s*}_{\perp}\right. \\
& \qquad \left. + \left[\bar{\boldsymbol{H}}^{*}_{\parallel} - \left(\bar{\boldsymbol{H}}^{*}_{\parallel}\right)_{eq}\right]\cdot\frac{d^{s}}{dt}\boldsymbol{m}^{s*}_{\parallel} + \left[\bar{B}^{*}_{\perp} - \left(\bar{B}^{*}_{\perp}\right)_{eq}\right]\frac{d^{s}}{dt}m^{s*}_{\perp}\right\}
\end{aligned} \tag{64}$$

The expression (64) is the FINAL form of the entropy production rate for a polarizable chemically-active multicomponent system in the presence of electromagnetic fields.

It is important to note that the entropy production rate depends only on gauge-invariant surface properties and on the definition of the externally applied electromagnetic field.

3. Examples of Cross Effects via Force-Flux coupling at the interface

3.1 Heat and Mass transfer coupling

For simplicity, let us consider a non-isothermal two-component system with cross effects between the diffusive fluxes of mass and energy within an interface. We assume there are NO externally applied electromagnetic fields and there are NO chemical reactions occurring within the system.

We can rewrite the first line in equation (64) for the entropy production rate σ^s as:

$$\sigma^s = \boldsymbol{j}_q^s \cdot \boldsymbol{\nabla}_\| \frac{1}{T^s} - \boldsymbol{j}_1^s \cdot \boldsymbol{\nabla}_\| \frac{\hat{\mu}_1^s - \hat{\mu}^s}{T^s} - \boldsymbol{j}_2^s \cdot \boldsymbol{\nabla}_\| \frac{\hat{\mu}_2^s - \hat{\mu}^s}{T^s} \tag{65}$$

If we sum the momenta of each species in a generic k-component system, we have:

$$\begin{aligned} \sum_{\alpha=1}^{k} \boldsymbol{v}_\alpha \rho_\alpha &= \rho \sum_{\alpha=1}^{k} \boldsymbol{v}_\alpha w_\alpha \\ &= \sum_{\alpha=1}^{k} \boldsymbol{v}_\alpha \rho_\alpha + \sum_{\alpha=1}^{k} \boldsymbol{j}_\alpha = \boldsymbol{v}\rho + \sum_{\alpha=1}^{k} \boldsymbol{j}_\alpha \end{aligned} \tag{66}$$

where w_α is the mass fraction of species α. In a 2-component system this implies that:

$$\sum_{\alpha=1}^{k} \boldsymbol{j}_\alpha = 0 \quad \Longrightarrow \boldsymbol{j}_1 = -\boldsymbol{j}_2 \tag{67}$$

From Equation (67) we can rewrite (65) as

$$\sigma_s = \boldsymbol{j}_q^s \cdot \boldsymbol{\nabla}_\| \frac{1}{T^s} - \boldsymbol{j}_1^s \cdot \boldsymbol{\nabla}_\| \frac{\hat{\mu}_2^s - \hat{\mu}_1^s}{T^s} \tag{68}$$

We need to guarantee the non-negativity of the entropy production for the terms on the right-hand side of Equation (68)

$$\boldsymbol{j}_q^s = L_{qq}^s \cdot \boldsymbol{\nabla}_\| \frac{1}{T^s} - L_{1q}^s \cdot \boldsymbol{\nabla}_\| \frac{\hat{\mu}_2^s - \hat{\mu}_1^s}{T^s} \tag{69}$$

$$\boldsymbol{j}_1^s = L_{q1}^s \cdot \boldsymbol{\nabla}_\| \frac{1}{T^s} - L_{11}^s \cdot \boldsymbol{\nabla}_\| \frac{\hat{\mu}_2^s - \hat{\mu}_1^s}{T^s} \tag{70}$$

where $L_{q1}^s = L_{1q}^s$, L_{qq}^s and L_{11}^s are phenomenological transport coefficients defining a phenomenological symmetric matrix. We know from mass conservation that $\rho^s = \rho_1^s + \rho_2^s = 0$, so we can write

$$d\left(\frac{\hat{\mu}_2^s - \hat{\mu}_1^s}{T^s}\right) = \frac{1}{T_s} d\left(\hat{\mu}_2^s - \hat{\mu}_1^s\right) - \frac{\hat{\mu}_2^s - \hat{\mu}_1^s}{{T^s}^2} dT^s = \frac{1}{T_s \rho_1^s}\left(s^s dT^s + d\gamma\right) - \frac{\hat{\mu}_2^s - \hat{\mu}_1^s}{{T^s}^2} dT^s \tag{71}$$

Recalling the thermodynamic definition of the interfacial tension $\gamma = \gamma\left(T^s, \hat{\mu}_1^s\right)$, we can expand

$$d\gamma = \left(\frac{\partial \gamma}{\partial T_1^s}\right)_{\hat{\mu}_1^s} dT^s + \left(\frac{\partial \gamma}{\partial \hat{\mu}_1^s}\right)_{T_1^s} d\hat{\mu}_1^s \tag{72}$$

Recalling the thermodynamic gauge-invariant expressions ($\rho_k^s = 0$) for the surface excess entropy density s^s and the surface excess species mass density ρ_α^s

$$d\gamma = -s^s dT^s + \rho_1^s \left(\frac{\partial \hat{\mu}_2^s}{\partial T^s}\right)_{\hat{\mu}_1^s} dT^s - \rho_1^s \left[1 - \left(\frac{\partial \hat{\mu}_2^s}{\partial \hat{\mu}_1^s}\right)_{T^s}\right] d\hat{\mu}_1^s \tag{73}$$

Substituting Equation (73) into Equation (71) we obtain the expression

$$d\left(\frac{\hat{\mu}_2^s - \hat{\mu}_1^s}{T^s}\right) = -\frac{1}{{T^s}^2}\left[\hat{\mu}_2^s - \hat{\mu}_1^s - T^s\left(\frac{\partial \hat{\mu}_2^s}{\partial T^s}\right)_{\hat{\mu}_1^s}\right] dT^s - \frac{1}{T^s}\left[1 - \left(\frac{\partial \hat{\mu}_2^s}{\partial \hat{\mu}_1^s}\right)_{T^s}\right] d\hat{\mu}_1^s \tag{74}$$

Substituting (74) into (70) we get

$$\begin{aligned} \boldsymbol{j}_1^s &= -\frac{1}{{T^s}^2}\left\{L_{qq}^s + L_{11}^s\left[\hat{\mu}_2^s - \hat{\mu}_1^s - T^s\left(\frac{\partial \hat{\mu}_2^s}{\partial T^s}\right)_{\hat{\mu}_1^s}\right]\right\}\boldsymbol{\nabla}_{\parallel} T^s - \frac{L_{11}^s}{T^s}\left[1 - \left(\frac{\partial \hat{\mu}_2^s}{\partial \hat{\mu}_1^s}\right)_{T^s}\right]\boldsymbol{\nabla}_{\parallel}\hat{\mu}_1^s \\ &= -\rho_1^s \frac{D_{q1}^s}{T^s}\boldsymbol{\nabla}_{\parallel} T^s - D_{12}^s \boldsymbol{\nabla}_{\parallel}\hat{\mu}_1^s \end{aligned} \tag{75}$$

where we defined D_{12}^s, i.e. the surface diffusivity of species 1 relative to species 2, and D_{q1}^s, i.e. the surface thermal diffusion coefficient of species 1, as

$$D_{12}^s = \frac{L_{11}^s}{T^s}\left[1 - \left(\frac{\partial \hat{\mu}_2^s}{\partial \hat{\mu}_1^s}\right)_{T^s}\right]\left(\frac{\partial \hat{\mu}_1^s}{\partial \rho_1^s}\right)_{T^s} \tag{76}$$

$$D_{q1}^s = \frac{L_{qq}^s + L_{11}^s\left[\hat{\mu}_2^s - \hat{\mu}_1^s - T^s\left(\frac{\partial \hat{\mu}_2^s}{\partial T^s}\right)_{\hat{\mu}_1^s}\right]}{\rho_1^s T^s} \tag{77}$$

We can repeat the same process for the interfacial diffusive energy flux $\boldsymbol{j}_q^s$:

$$\boldsymbol{j}_q^s = -\frac{L_{qq}^s}{{T^s}^2}\boldsymbol{\nabla}_{\parallel} T^s - \frac{L_{q1}^s}{{T^s}^2}\left[\hat{\mu}_2^s - \hat{\mu}_1^s - T^s\left(\frac{\partial \hat{\mu}_2^s}{\partial T^s}\right)_{\hat{\mu}_1^s}\right]\boldsymbol{\nabla}_{\parallel} T^s - \frac{L_{q1}^s}{T^s}\left[1 - \left(\frac{\partial \hat{\mu}_2^s}{\partial \hat{\mu}_1^s}\right)_{T^s}\right]\left(\frac{\partial \hat{\mu}_1^s}{\partial \rho_1^s}\right)_{T^s}\boldsymbol{\nabla}_{\parallel}\rho_1^s \tag{78}$$

Having defined both $\boldsymbol{j}_q^s$ and $\boldsymbol{j}_1^s$, we are finally able to derive the expression for the interfacial modified diffusive energy flux $\boldsymbol{j}_q^{s\prime}$:

$$\begin{aligned} \boldsymbol{j}_q^{s\prime} &= \boldsymbol{j}_q^s - \left[\hat{\mu}_1^s - \hat{\mu}_2^s - T^s\left(\frac{\partial \hat{\mu}_2^s}{\partial T^s}\right)_{\hat{\mu}_1^s}\right]\boldsymbol{j}_1^s \\ &= -\frac{1}{{T^s}^2}\left\{L_{qq}^s + 2L_{q1}^s\left[\hat{\mu}_2^s - \hat{\mu}_1^s - T^s\left(\frac{\partial \hat{\mu}_2^s}{\partial T^s}\right)_{\hat{\mu}_1^s}\right] + L_{11}^s\left[\hat{\mu}_2^s - \hat{\mu}_1^s - T^s\left(\frac{\partial \hat{\mu}_2^s}{\partial T^s}\right)_{\hat{\mu}_1^s}\right]^2\right\}\boldsymbol{\nabla}_{\parallel} T^s \\ &\quad - \frac{1}{T^s}\left\{L_{q1}^s + 2L_{11}^s\left[\hat{\mu}_2^s - \hat{\mu}_1^s - T^s\left(\frac{\partial \hat{\mu}_2^s}{\partial T^s}\right)_{\hat{\mu}_1^s}\right]\right\}\left[1 - \left(\frac{\partial \hat{\mu}_2^s}{\partial \hat{\mu}_1^s}\right)_{T^s}\right]\left(\frac{\partial \hat{\mu}_1^s}{\partial \rho_1^s}\right)_{T^s}\boldsymbol{\nabla}_{\parallel}\rho_1^s \\ &= -\lambda^{s\prime}\boldsymbol{\nabla}_{\parallel} T^s - \rho_1^s\left[1 - \left(\frac{\partial \hat{\mu}_2^s}{\partial \hat{\mu}_1^s}\right)_{T^s}\right]\left(\frac{\partial \hat{\mu}_1^s}{\partial \rho_1^s}\right)_{T^s} D_{q1}^s \boldsymbol{\nabla}_{\parallel}\rho_1^s \end{aligned} \tag{79}$$

where we can define $\lambda^{s\prime}$, i.e. the interfacial modified thermal conductivity, as

$$\lambda^{s\prime} = \frac{L_{qq}^s + 2L_{q1}^s\left[\hat{\mu}_2^s - \hat{\mu}_1^s - T^s\left(\frac{\partial \hat{\mu}_2^s}{\partial T^s}\right)_{\hat{\mu}_1^s}\right] + L_{11}^s\left[\hat{\mu}_2^s - \hat{\mu}_1^s - T^s\left(\frac{\partial \hat{\mu}_2^s}{\partial T^s}\right)_{\hat{\mu}_1^s}\right]^2}{{T^s}^2} \tag{80}$$

3.2 Mass transfer and Chemical Reactions coupling

Active transport is the transport of mass from regions at low concentration to regions at high concentration [16]; this phenomenon is made possible by a coupling of diffusive mass transport and chemical reactions. In this section, we will examine an example of simplified active transport which can well model many processes occurring within biological cells [6, 12].

We assume there are NO externally applied electromagnetic fields and we NEGLECT both mechanical and thermal effects, i.e. $T^I = T^s = T^{II} = T$.

Let us consider the rate of entropy production σ^s at an interface where chemical reactions (with a surface reaction affinity $\mathcal{A}^s = \sum_{\alpha=1}^k \tilde{\nu}_\alpha^s \tilde{\mu}_\alpha^s$), and mass transfer can occur. Re-writing (64) we get

$$\begin{aligned} T\sigma^s = & \sum_{\alpha=1}^{k} \boldsymbol{n} \cdot \left[\left(\boldsymbol{v}^I - \boldsymbol{v}^s \right) \rho_\alpha^I - \boldsymbol{m} + \boldsymbol{j}_\alpha^I \right] \left[\left(\hat{\mu}_\alpha^s - \hat{\mu}^s \right) - \left(\hat{\mu}_\alpha^I - \hat{\mu}^I \right) \right] - \tilde{\Gamma}^s \mathcal{A}^s \\ & - \sum_{\alpha=1}^{k} \boldsymbol{n} \cdot \left[\left(\boldsymbol{v}^{II} - \boldsymbol{v}^s \right) \rho_\alpha^{II} - \boldsymbol{m} + \boldsymbol{j}_\alpha^{II} \right] \left[\left(\hat{\mu}_\alpha^s - \hat{\mu}^s \right) - \left(\hat{\mu}_\alpha^{II} - \hat{\mu}^{II} \right) \right] \end{aligned} \tag{81}$$

It can be noticed in (81) that coupling between species mass transfer and chemical reactions is possible as expression (81) only displays scalar force-flux pairs.

Limiting for simplicity our analysis to passive interfaces, we can now consider a steady-state system and assume that the interface between bulk phases is uniform. In this way, excess species mass densities are position and time-independent, thus allowing us to use the jump balances for species mass densities

$$\boldsymbol{n} \cdot \left[\left(\boldsymbol{v}^I - \boldsymbol{v}^s \right) \rho_\alpha^I + \boldsymbol{j}_\alpha^I \right] = \boldsymbol{n} \cdot \left[\left(\boldsymbol{v}^{II} - \boldsymbol{v}^s \right) \rho_\alpha^{II} + \boldsymbol{j}_\alpha^{II} \right] - \boldsymbol{\nabla}_\parallel \cdot \boldsymbol{j}_\alpha^s + \nu_\alpha^s \Gamma^s \tag{82}$$

We can then rewrite (81) as

$$T\sigma^s = \sum_{\alpha=1}^{k} \boldsymbol{n} \cdot \left[\left(\boldsymbol{v}^I - \boldsymbol{v}^s \right) \rho_\alpha^I - \boldsymbol{m} + \boldsymbol{j}_\alpha^I \right] \left[\left(\hat{\mu}_\alpha^{II} - \hat{\mu}^{II} \right) - \left(\hat{\mu}_\alpha^I - \hat{\mu}^I \right) \right] - \tilde{\Gamma}^s \sum_{\alpha=1}^{k} \tilde{\nu}_\alpha^s \tilde{\mu}_\alpha^{II} \tag{83}$$

which states that species mass transfer occurs directly between the bulk phases, and where the surface chemical potentials have disappeared. We can further assume that the interface is perfectly equilibrated with the bulk solution phase on the "incoming" side, i.e. $\hat{\mu}_\alpha^{II} = \tilde{\mu}_\alpha^s$. We can therefore express the reaction term in Equation (83) as $-\tilde{\Gamma}^s \tilde{\mathcal{A}}^s$. As proposed in previous works [16] for the bulk case, we have to ensure nonnegativity of the entropy production for the two force-flux pairs in (83); to achieve this, we can write

$$\tilde{\Gamma}^s = -L_{\mathcal{A}\mathcal{A}} \mathcal{A}^s - \sum_{\beta=1}^{k} L_{\mathcal{A}\beta} \left(\hat{\mu}_\beta^I - \hat{\mu}_\beta^{II} \right) \tag{84}$$

$$\boldsymbol{n} \cdot \left[\left(\boldsymbol{v}^I - \boldsymbol{v}^s \right) \rho_\alpha^I - \boldsymbol{m} + \boldsymbol{j}_\alpha^I \right] = -L_{\alpha\mathcal{A}} \mathcal{A}^s - \sum_{\beta=1}^{k} L_{\alpha\beta} \left(\hat{\mu}_\beta^I - \hat{\mu}_\beta^{II} \right) \tag{85}$$

where

$$L_{\alpha\beta} = \begin{bmatrix} L_{11} & L_{1k} & \dots \\ \vdots & \ddots & \\ L_{k1} & & L_{kk} \end{bmatrix} \qquad L_{\alpha\mathcal{A}} = \begin{bmatrix} L_{1\mathcal{A}} \\ \vdots \\ L_{k\mathcal{A}} \end{bmatrix} \qquad L_{\mathcal{A}\beta} = \begin{bmatrix} L_{\mathcal{A}1} & \dots & L_{\mathcal{A}k} \end{bmatrix} \tag{86}$$

Similarly to what already described in previous analysis [16], the terms $L_{\alpha,\beta}$ with $\alpha, \beta = 1, 2, ...k$ define a *(k-1)*-rank matrix of phenomenological coefficients under the constraints $\sum_{\alpha=1}^k L_{\alpha\beta} = \sum_{\alpha=1}^k L_{\beta\alpha} = 0$, while $L_{\alpha\mathcal{A}}$ and $L_{\mathcal{A}\beta}$ represent a column and a row vector, respectively, with $L_{\mathcal{A}\mathcal{A}}$ as the diagonal element and the property $\sum_{\alpha=1}^k L_{\alpha\mathcal{A}} = \sum_{\beta=1}^k L_{\mathcal{A}\beta} = 0$.

We now assume to consider a dilute, multicomponent system with species 1 as the only actively transported solute and species k as the solvent; specifically, this implies that [16]

$$L_{11} = -L_{1k} = -L_{k1} = L_{kk} \qquad \text{and} \qquad L_{1\mathcal{A}} = -L_{k\mathcal{A}} = -L_{\mathcal{A}k} = L_{\mathcal{A}1} \qquad \text{and} \qquad L_{\mathcal{A}\mathcal{A}} \tag{87}$$

are the only non-vanishing phenomenological coefficients. Thus we can rewrite expressions (84) and (85)

$$\tilde{\Gamma}^s = -L_{\mathcal{A}\mathcal{A}}\mathcal{A}^s - L_{\mathcal{A}1}\Delta\hat{\mu} \tag{88}$$

$$\boldsymbol{n}\cdot\left[\left(\boldsymbol{v}^I - \boldsymbol{v}^s\right)\rho^I_\alpha - \boldsymbol{m} + \boldsymbol{j}^I_\alpha\right] = -L_{1\mathcal{A}}\mathcal{A}^s - L_{11}\Delta\hat{\mu} \tag{89}$$

where $\Delta\hat{\mu} = \hat{\mu}^I_1 - \hat{\mu}^{II}_1 - \left(\hat{\mu}^I_k - \hat{\mu}^{II}_k\right)$ which becomes $\Delta\hat{\mu} = \hat{\mu}^I_1 - \hat{\mu}^{II}_1$ at equilibrium.

Finally, we may assume that the interface is at rest and the diffusive flux of species 1 is perfectly compensated by the diffusive solvent flux, i.e. $\boldsymbol{v}^I = \boldsymbol{v}^s = \boldsymbol{m} = \boldsymbol{0}$. In addition, we can recall the molar quantities

$$N^I_1 = \frac{1}{\tilde{M}_1}\boldsymbol{n}\cdot\boldsymbol{j}^I_1 \qquad \text{and} \qquad \Delta\hat{\mu}_1 = \frac{1}{\tilde{M}_1}\Delta\tilde{\mu}_1 = \frac{1}{\tilde{M}_1}\left(\tilde{\mu}^I_1 - \tilde{\mu}^{II}_1\right) \tag{90}$$

In such a way, expressions (88) and (89) can be rewritten as

$$\tilde{\Gamma}^s = -L_{\mathcal{A}\mathcal{A}}\mathcal{A}^s - \frac{L_{\mathcal{A}1}}{\tilde{M}_1}\Delta\tilde{\mu}_1 \tag{91}$$

$$N^I_1 = -\frac{L_{1\mathcal{A}}}{\tilde{M}_1}\mathcal{A}^s - \frac{L_{11}}{\tilde{M}^2_1}\Delta\tilde{\mu}_1 \tag{92}$$

By construction, both forms are consistent with a nonnegative rate of entropy production. As firstly proposed by Öttinger and Venerus [16], we can compute the transport process efficiency η defined as

$$\eta = -\frac{N^I_1\Delta\tilde{\mu}_1}{\tilde{\Gamma}\mathcal{A}^s} \tag{93}$$

which can be rearranged, according to (91) and (92), as

$$\eta = \frac{(q - Z)\,Z}{1 - qZ} \tag{94}$$

where

$$q = \frac{L_{\mathcal{A}1}}{\sqrt{L_{\mathcal{A}\mathcal{A}}L_{11}}} \qquad\qquad Z = -\sqrt{\frac{L_{11}}{L_{\mathcal{A}\mathcal{A}}\tilde{M}^2_1}}\,\frac{\Delta\tilde{\mu}_1}{\mathcal{A}^s} \tag{95}$$

We can easily spot in Equation (95) the transport coupling coefficient $q \leq 1$, which determines the strength of the cross effect, and the factor Z (where $Z < q$) relating the entropy generated from the species mass transport and the entropy resulting from chemical reactions.

3.3 Electrocoalescence: theory and examples

Electrocoalescence is a process by which an electric field is applied across a suspension of (usually) conducting fluid droplets dispersed in an insulating liquid in order to force the droplets to merge together [15]. The process has found applications in a number of technologies in which conducting water droplets are dispersed in insulating oils, such as lab-on-a-chip manufacturing [17], various biomedical diagnostic assays and water-in-crude-oil desalting operations in the oil refining industry [8].

Specifically, electrocoalescence is driven by the polarization of charge in conducting droplets, which is induced by an externally applied field and which generates electric dipoles out of the droplets. When such polarized droplets are oriented along the direction of the field, their induced dipoles create large attractive electrical stresses which drive coalescence. Finally, it is worth recalling another important phenomenon which can be described with electrocoalescence theory: the drainage of emulsion thin films stimulated by the application of an external electric field. As can be seen in figure 1, the drainage of liquid thin films in water (or air) can be approximated as the coalescence of 2 water drops (or air bubbles) whose radii are much greater than their

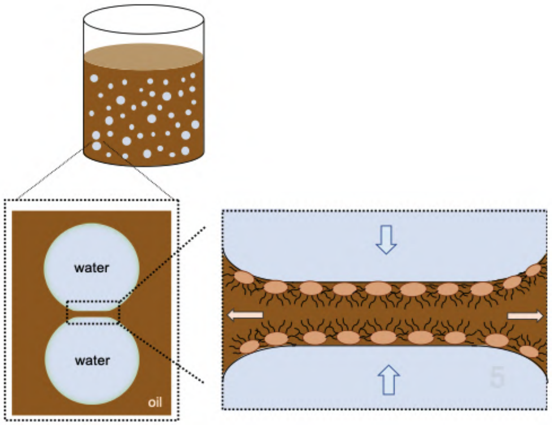

Figure 1: Drainage of liquid thin films can be approximated as the coalescence of 2 drops [2].

center-to-center separation. In this case, the additional presence of surface active agents (e.g. de-emulsifiers) has to be considered, since it greatly affects the behavior of the under-drainage thin film.

Of course, cross-coupling effects between mechanical and electrical stresses at the interfaces play a major role in both electrocoalescence and drainage phenomena. We start assuming there are NO externally applied magnetic fields, there are NO chemical reactions occurring and thermal effects can be neglected, i.e. $T^I = T^s = T^{II} = T$.

3.3.1 Interactions between droplets

Let us consider a single spherical drop A (of radius a) of conducting liquid and let us use subscripts d and m for *drop* and *medium* domains, respectively. If a uniform electric field E_0 is applied, the influence of the drop can be approximated by a dipolar moment p located at the sphere center. Outside the droplet, the electric potential V is simply given by:

$$V(r,\theta) = \frac{p\ cos\theta}{4\pi\epsilon_m r^2} - E_0 r cos\theta \tag{96}$$

where we have used spherical coordinates and defined $\epsilon_m = \epsilon_0\epsilon_r$ as the permittivity of the insulating liquid (e.g. oil) outside the droplet. By expressing the boundary conditions at the water/oil interface, we obtain the expression for p, V

$$p = 4\pi\epsilon_m E_0 a^3 \tag{97}$$

$$V(r,\theta) = E_0 r cos\theta \left(\frac{a^3}{r^3} - 1\right) \tag{98}$$

and the field components E_r (i.e. radial) and E_θ (i.e. angular)

$$\begin{aligned} E_r(r,\theta) &= E_0 cos\theta \left(1 + 2\frac{a^3}{r^3}\right) \\ E_\theta(r,\theta) &= E_0 sin\theta \left(\frac{a^3}{r^3} - 1\right) \end{aligned} \tag{99}$$

Let us now analyze the case of two drops A and B of radius a and b (with $b < a$ as initial reference), respectively. Calling s the center-to-center separation between the drops, where $s = a + b + d$ and d is the drops' surfaces separation in the undeformed state, the interaction force can be calculated as $\boldsymbol{F} = -\nabla U$ where U is the potential energy of the p_A-field-induced dipolar moment p_B on B:

$$p_B = \alpha_B E_0 = 4\pi\epsilon_m b^3 E_0 \tag{100}$$

Recalling equations (99) and (100), the force exerted on drop B by drop A will be (in spherical coordinates) equal to:

$$F_r = -12\pi\epsilon_m b^3 {E_0}^2 \frac{a^3}{s^4}\left(3cos^2\theta - 1\right)\frac{\epsilon_d - \epsilon_m}{\epsilon_d + 2\epsilon_d}\frac{R-1}{R+2} \qquad \text{where} \qquad s = a+b+d \tag{101}$$

and

$$F_\theta = -12\pi\epsilon_m b^3 {E_0}^2 \frac{a^3}{s^4} sin(2\theta)\frac{\epsilon_d - \epsilon_m}{\epsilon_d + 2\epsilon_d}\frac{R-1}{R+2} \tag{102}$$

Note that both expressions (101) and (102) display the end-term

$$\frac{\epsilon_d - \epsilon_m}{\epsilon_d + 2\epsilon_d}\frac{R-1}{R+2} \tag{103}$$

which is a correction used to describe the so called ”leaky-dielectric” systems [14]. In these systems, the droplets' dielectric properties are comparable to those of the dividing dielectric thin-film; in other words, as the droplets are weakly conducting and bring zero net charge, if an external electric field is applied the free charge accumulated on the droplets' interface modifies the local field.

Formulas derived in (101) and (102) are valid for spherical droplets at <u>large</u> center-to-center distances. However, in the study of thin-films drainage by electrocoalescence, these assumptions are no longer valid. As suggested by previous work [3], when the distance d ($d = s - a - b$) between spheres becomes lower than b (i.e. the smallest possible radius), the surface charge distributions on the spheres are heavily altered. Hence, corrective coefficients ξ and ψ have to be introduced; they will take into account eventual asymmetries of the two drops and can be expressed [14] as complicated higher-order series mainly depending on the ratio d/b:

$$\begin{aligned} \xi &= 1 + \frac{a^3 s^5}{\left(s^2 - b^2\right)^4} + \frac{b^3 s^5}{\left(s^2 - a^2\right)^4} + \frac{3a^3 b^3\left(3s^2 - a^2 - b^2\right)}{\left(s^2 - a^2 - b^2\right)^4} \\ \psi &= 1 + \frac{a^3 s^3}{2\left(s^2 - b^2\right)^3} + \frac{b^3 s^3}{2\left(s^2 - a^2\right)^3} + \frac{3a^3 b^3}{\left(s^2 - a^2 - b^2\right)^3} \end{aligned} \tag{104}$$

The corrected expression of equations (101) and (102) will then be

$$F_r = -12\pi\epsilon_m b^3 {E_0}^2 \frac{a^3}{s^4}\left(3\xi cos^2\theta - 1\right)\frac{\epsilon_d - \epsilon_m}{\epsilon_d + 2\epsilon_d}\frac{R-1}{R+2} \tag{105}$$

and

$$F_\theta = -12\pi\epsilon_m b^3 {E_0}^2 \frac{a^3}{s^4} \psi sin(2\theta)\frac{\epsilon_d - \epsilon_m}{\epsilon_d + 2\epsilon_d}\frac{R-1}{R+2} \tag{106}$$

As expected for a large center-to-center separation between the drops, i.e. $d/b >> 1$, the corrective coefficients in (104) tend to unity and the effective dipolar approximations above are recovered. On the other side, there exists a rather significant torque which tends to align two very close drops in the direction of the applied field.

Let us now assume our system to be identified by two drops of equal radius a aligned in the direction of the applied electric field (i.e. $\theta = 0$ and $s = 2a + d$). Equations (105) and (106) reduce to

$$\begin{aligned} &F_r = -12\pi\epsilon_m {E_0}^2 \frac{a^6}{s^4}\left(3\xi - 1\right)\frac{\epsilon_d - \epsilon_m}{\epsilon_d + 2\epsilon_d}\frac{R-1}{R+2} \qquad \text{where} \qquad s = 2a + d \\ &F_\theta = 0 \end{aligned} \tag{107}$$

where

$$\begin{aligned} \xi &= 1 + \frac{2a^3\left(2a+d\right)^5}{[\left(2a+d\right)^2 - a^2]^4} + \frac{3a^6[3\left(2a+d\right)^2 - 2a^2]}{[\left(2a+d\right)^2 - 2a^2]^4} = 1 + \frac{2a^3\left(2a+d\right)^5}{\left(3a^2 + 4ad + d^2\right)^4} + \frac{3a^6\left(10a^2 + 12ad + 3d^2\right)}{\left(2a^2 + 4ad + d^2\right)^4} \\ \psi &= 1 + \frac{a^3\left(2a+d\right)^3}{[\left(2a+d\right)^2 - a^2]^3} + \frac{3a^6}{[\left(2a+d\right)^2 - 2a^2]^3} = 1 + \frac{a^3\left(2a+d\right)^3}{\left(3a^2 + 4ad + d^2\right)^3} + \frac{3a^6}{\left(2a^2 + 4ad + d^2\right)^3} \end{aligned} \tag{108}$$

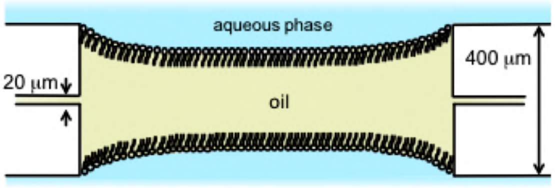

Figure 2: Example of system comprising of two droplets of saline water divided by a thin oil film [2].

We consider electrocoalescence in the scope of thin-film drainage phenomena; it is oftentimes experimental practice to analyze NOT-"leaky dielectric" systems. As shown in figure 2, studied systems usually comprise of two droplets of saline aqueous solution divided by a thin oil film. The aqueous phase can be considered a perfectly conducting medium (i.e. high ϵ_d and high conductivity σ_d), while the hydrocarbon phase can be seen as a perfectly dielectric film (i.e. low ϵ_m and low conductivity σ_m).

A practical example is offered in the work by Alexandra Alicke in Prof. Jan Vermant's group at ETH Zürich; values of ϵ and σ for each of the substance that have been used is reported in Table 1:

	Phase	Dielectric constant ϵ	Conducticity σ ($^{mS}/_{cm}$)
Aqueous solution (d)	0.5M NaCl in Mili-Q water	77.7	9.2
Hydrophobic core (m)	Hexadecane	2.1	0.03

Table 1: Parameters values for the model

As will be discussed later, it is possible to add surfactants (e.g. 1 wt% *Span80* nonionic surfactant) in the hydrophobic phase to tune the thin-film drainage behavior.

If we consider a system similar to that presented in Table 1, the following approximations can be made:

$$\epsilon_d \gg \epsilon_m \qquad \text{and} \qquad \sigma_m \gg \sigma_d \qquad \Rightarrow \qquad \epsilon_d - \epsilon_m \approx \epsilon_d \qquad \text{and} \qquad R = \frac{\sigma_m}{\sigma_d} \approx 0 \tag{109}$$

Hence, the end-term in (103) can be eliminated and expressions in (107) reduce to

$$\begin{aligned} F_r &= -12\pi\epsilon_m {E_0}^2 \frac{a^6}{s^4}\left(3\xi - 1\right) \\ F_\theta &= 0 \end{aligned} \tag{110}$$

3.3.2 Time of contact of 2 drops

Correctly estimating the time of contact of two initially-divided droplets under electrocoalescence represents a key issue in the study of foams and emulsions. Together with the external electric field, other major forces influence droplets' motion in the liquid medium, and their assessment is traditionally not trivial. For example, as suggested by previous research [14], a major drag resistive force acting on the drops (usually at a large separation) must be taken into account.

This force can be expressed via the Hadamard-Rybczynski [9] equation as

$$F_{Drag} = 4\pi\mu_m a v k \tag{111}$$

where μ_m is the viscosity of the low-dielectric medium, $v = \dfrac{ds}{dt}$ is the velocity of drop approach and k a viscosity parameter defined as

$$k = \frac{3\lambda + 2}{2\left(\lambda + 1\right)} \qquad \text{with} \qquad \lambda = \frac{\mu_d}{\mu_m} \tag{112}$$

Under the assumption of mutual induction of dipoles between the drops, the bipolar electrostatic force of attraction between uniform size drops aligned in the direction of an applied electric field will be given by (110).
To estimate the time of contact (t) of two drops from their initial surface-surface separation d_0, we combine equations (110) and (111) as to get a force balance resulting in

$$\begin{aligned} &F_{Bipolar} = 2F_r = -2 \cdot 12\pi\epsilon_m {E_0}^2 \frac{a^6}{s^4}(3\xi - 1) = F_{Drag} = 4\pi\mu_m a v k \\ &F_\theta = 0 \end{aligned} \tag{113}$$

rearranging

$$v(\mu_m a k) = -6\epsilon_m {E_0}^2 \frac{a^6}{s^4}(3\xi - 1); \qquad \frac{ds}{dt} = -\frac{6\epsilon_m E_0^2}{\mu_m k}\frac{a^5}{(2a+d)^4}(3\xi - 1) \tag{114}$$

We can assume that the drops' radii remain constant in time (a=const.)

$$\text{if} \qquad \frac{ds}{dt} = \frac{d(2a+d)}{dt} = \dot{d}(t) \qquad \Rightarrow \qquad \dot{d}(t) = -\frac{6\epsilon_m E_0^2}{\mu_m k}\frac{a^5}{(2a+d)^4}(3\xi - 1) \tag{115}$$

Recalling the expression for $\xi(d)$ and imposing the boundary conditions

$$\begin{aligned} d(t=0) &= d_0 && \text{initial state} \\ d(\bar{t}) &= 0 && \text{when contact occurs} \end{aligned} \tag{116}$$

we can solve the differential equation in (115):

$$\int_0^{\bar{t}} \mathrm{d}t = -\int_{d_0}^{0} \frac{\mu_m k}{6\epsilon_m E_0^2}\frac{(2a+d)^4}{a^5}\frac{1}{(3\xi(d) - 1)}\mathrm{d}d \tag{117}$$

Integration of the right-hand side term of (117) is neither trivial nor straightforward, so further assumptions are necessary.

- Firstly, we explore the case of droplets at large center-to-center separation:

$$d \gg a \qquad \Rightarrow \qquad \xi \approx 1 \qquad \Rightarrow \qquad \dot{d}(t) = -\frac{12\epsilon_m E_0^2}{\mu_m k}\frac{a^5}{(2a+d)^4} \tag{118}$$

$$\bar{t}_{\text{Large}} = \frac{8}{15}\frac{\mu_m k}{\epsilon_m E_0^2}\left[\left(\frac{d_0}{2a} + 1\right)^5 - 1\right] \tag{119}$$

- Secondly,the particular case of the drainage of an hydrophobic thin film in water will be explored. We assume our film to be FULLY PLANAR on both sides, i.e. drops' radii tend to infinity ($a \to +\infty$). We can then adjust the corrective factor ξ for extremely thin films:

$$\begin{aligned} \lim_{a\to+\infty} \xi(a) &= \lim_{a\to+\infty} 1 + \frac{2a^3(2a+d)^5}{(3a^2 + 4ad + d^2)^4} + \frac{3a^6(10a^2 + 12ad + 3d^2)}{(2a^2 + 4ad + d^2)^4} \\ &\sim 1 + \frac{64a^8}{81a^8} + \frac{30a^8}{16a^8} = \frac{2375}{648} \approx 3.67 \end{aligned} \tag{120}$$

hence

$$\dot{d}(t) = -\frac{60\epsilon_m E_0^2}{\mu_m k}\frac{a^5}{(2a+d)^4} \tag{121}$$

and

$$\bar{t}_{\text{Planar Film}} = \frac{8}{75}\frac{\mu_m k}{\epsilon_m E_0^2}\left[\left(\frac{d_0}{2a} + 1\right)^5 - 1\right] \tag{122}$$

In general, we can notice that the electrostatic interaction is proportional to $^1/_{s^4}$, while Stokes drag is independent of s for bulk drag and is proportional to $^1/_s$ in the lubrication limit. Thus, as the two drops get closer (or alternatively as the liquid film drainage proceeds) the electrical force heavily dominates the drag.

3.3.3 Thin films drainage

3.3.3.1 Cross-coupling effects, bilayers and the role of surface active agents

As suggested at the beginning of this discussion, cross-coupling effects between mechanical and electrical stresses at the interfaces play a major role electrocoalescence-driven drainage phenomena. In order to analyze such effects, we have to make the following assumptions:

- NO externally applied magnetic fields → we can use laws of electrostatics;
- NO chemical reactions occurring;
- thermal effects can be neglected → $T^I = T^s = T^{II} = T$;
- a fully planar film → uniform electric field across the film;
- the liquid inside the film is incompressible ($\boldsymbol{\nabla} \cdot \boldsymbol{v}$) and we ignore fluid inertia during the drainage → low Reynolds number;
- we have a perfectly dielectric film (i.e. hexadecane) in a perfectly conducting medium (i.e. water with high salt concentration).
- we neglect gravity effect to account for small drops size and small difference in density of the droplet-medium pair.

As already suggested [13], the propagation time of electromagnetic waves is traditionally very fast compared to the time scales characteristic of the electrohydrodynamics motions and thus, for times longer than the average charge relaxation time, any free charge experiences a confinement to the interfacial region. This phenomenon combined with the absence of an applied magnetic field in the system implies that the electric field in the two fluid phases is irrotational

$$\boldsymbol{\nabla} \times \boldsymbol{E} = \boldsymbol{0} \qquad \text{or} \qquad \boldsymbol{E} = -\boldsymbol{\nabla}\phi \tag{123}$$

and so according to the Gauss' law of electrostatics

$$\boldsymbol{\nabla} \cdot \boldsymbol{E} = 0 \qquad \text{or} \qquad \nabla^2\phi = 0 \tag{124}$$

We identify the drops liquid phase as I and the thin-film hydrophobic phase as II; in addition, let the two droplet-medium interfaces be called Λ_I and Λ_{II}, respectively. The boundary conditions at the fluid-fluid interface Λ_I and Λ_{II} in the most most general case are:

$$\begin{aligned}
&\boldsymbol{n} \cdot \boldsymbol{E}^I = R\boldsymbol{n} \cdot \boldsymbol{E}^{II} && \text{continuity of current}\\
&\boldsymbol{t} \cdot \boldsymbol{E}^I = \boldsymbol{t} \cdot \boldsymbol{E}^{II} && \text{continuity of tangential electric field}\\
&\boldsymbol{E}^{II} \to \boldsymbol{E}_0 && \text{as} \quad |\boldsymbol{x}| \to +\infty
\end{aligned} \tag{125}$$

The last condition indicates that far away from the drop, electric field is given by the external applied electric field $\boldsymbol{E}_0$. Note that the $\boldsymbol{n}$ and $\boldsymbol{t}$ are the outward unit normal and tangent vectors at the interface and $\boldsymbol{x}$ is the position vector.

The discontinuity in electric properties (e.g. refractive index, dielectric constants) at the drop-thin fluid interface causes a jump in the Maxwell stress tensor $\boldsymbol{T}_E$:

$$\boldsymbol{T}_E^i = \epsilon_0 \epsilon_i \left(\boldsymbol{E}\boldsymbol{E} - \frac{1}{2} E^2 \boldsymbol{\delta} \right) \qquad \text{where} \qquad i = I, II \tag{126}$$

the corresponding fluid-fluid interface electric stress jump being:

$$\boldsymbol{n} \cdot \left(\boldsymbol{T}_E^{II} - \boldsymbol{T}_E^{I} \right) = \frac{1}{2} \epsilon_0 \epsilon_I \left[{E_\perp^I}^2 \left(1 - \frac{1}{R^2} \frac{\epsilon_{II}}{\epsilon_I} \right) - {E_\parallel^I}^2 \left(1 - \frac{\epsilon_{II}}{\epsilon_I} \right) \right] \boldsymbol{n} + \epsilon_0 \epsilon_I E_\parallel^I E_\perp^I \left(1 - \frac{1}{R} \frac{\epsilon_{II}}{\epsilon_I} \right) \boldsymbol{t} \tag{127}$$

where we identify $E_\perp = \boldsymbol{n} \cdot \boldsymbol{E}^I$ and $E_\parallel = \boldsymbol{t} \cdot \boldsymbol{E}^I$ as the normal and tangential components of the electric field evaluated just inside the drop surface. Of course, if no flow fields are applied, the Maxwell stresses are sufficient to induce drops and fluid motion. In particular, we can notice that for a perfect dielectric medium (here the hydrophobic thin film) we can approximate [14]:

$$R \to \frac{\epsilon_{II}}{\epsilon_I} \qquad \Rightarrow \qquad \boldsymbol{n} \cdot \left(\boldsymbol{T}_E^{II} - \boldsymbol{T}_E^{I} \right)_{\text{Perfect}} = \frac{1}{2} \epsilon_0 \epsilon_I \left({E_\perp^I}^2 + \frac{\epsilon_{II}}{\epsilon_I} {E_\parallel^I}^2 \right) \left(1 - \frac{\epsilon_I}{\epsilon_{II}} \right) \boldsymbol{n} \tag{128}$$

Note that for a perfect dielectric, the interfacial stress jump is purely normal to the interface.

Given the jump relation above, we now have to determine the relationship between electrical stresses and the mechanical stresses in the fluid so as to make cross-coupling effects in this system evident.
As assumed at the beginning of the paragraph, absence of inertia and gravity as well as fluid incompressibility force the system to exist at low Reynolds numbers. For a non-compressible Newtonian fluid, the momentum balance equation can be simplified to give the Navier-Stokes equation:

$$\rho \left(\frac{\partial \boldsymbol{v}}{\partial t} + \boldsymbol{v} \cdot \boldsymbol{\nabla} \boldsymbol{v} \right) = \eta \nabla^2 \boldsymbol{v} - \boldsymbol{\nabla} P \tag{129}$$

where P is the modified pressure, which here coincides with the standard pressure p.
The balance equation for momentum is known

$$\frac{\partial \boldsymbol{m}}{\partial t} = -\boldsymbol{\nabla} \cdot (\boldsymbol{v}\boldsymbol{m} + \boldsymbol{\pi}) + \rho \boldsymbol{g} \qquad \xrightarrow{\text{NO Gravity}} \qquad \frac{\partial \boldsymbol{m}}{\partial t} = -\boldsymbol{\nabla} \cdot (\boldsymbol{v}\boldsymbol{m} + \boldsymbol{\pi}) \tag{130}$$

where $\boldsymbol{v}\boldsymbol{m}$ is the tensorial momentum flux (i.e. momentum transport by flow) and $\boldsymbol{\pi}$ is the second-rank hydrodynamic pressure-stress tensor. In other words, $\boldsymbol{\pi}$ represents the momentum flux associated with intermolecular interactions inside the fluid. Recalling the definition of material derivative and momentum $\boldsymbol{m} = \rho \boldsymbol{v}$, we re-write (130) as

$$\rho \frac{D\boldsymbol{v}}{Dt} = -\boldsymbol{\nabla} \cdot \boldsymbol{\pi} \tag{131}$$

We can notice that the terms on the left-hand side of both equations (129) and (131) are identical, thus allowing us to combine the two expressions

$$-\boldsymbol{\nabla} \cdot \boldsymbol{\pi} = \eta \nabla^2 \boldsymbol{v} - \boldsymbol{\nabla} p \tag{132}$$

Note that the "minus" sign on the left-hand side of equation (132) is coherent with our initial assumption on the orientation of the surface element unit vector. Let us now decompose the pressure tensor $\boldsymbol{\pi}$ as to discriminate the contribution coming from normal stresses p and viscous stresses $\boldsymbol{\tau}$:

$$\boldsymbol{\pi} = p\boldsymbol{\delta} + \boldsymbol{\tau} = p\boldsymbol{\delta} - \eta \left[\boldsymbol{\nabla} \boldsymbol{v} + (\boldsymbol{\nabla} \boldsymbol{v})^T - \frac{2}{3} (\boldsymbol{\nabla} \cdot \boldsymbol{v}) \boldsymbol{\delta} \right] - \eta_d (\boldsymbol{\nabla} \cdot \boldsymbol{v}) \boldsymbol{\delta} \tag{133}$$

where the nonnegative transport coefficient η_d is known as the dilatational or bulk viscosity leading to an additional contribution to viscous stresses. Under the assumption of fluid incompressibility ($\boldsymbol{\nabla} \cdot \boldsymbol{v}$), expression (133) becomes:

$$\boldsymbol{\pi} = p\boldsymbol{\delta} - \eta \left[\boldsymbol{\nabla} \boldsymbol{v} + (\boldsymbol{\nabla} \boldsymbol{v})^T \right] \tag{134}$$

Combining the previous relations, we are now able to write the balance equation at the interface for the stresses:

$$\boldsymbol{n} \cdot \left(\boldsymbol{\pi}^{II} - \boldsymbol{\pi}^{I}\right) + \boldsymbol{n} \cdot \left(\boldsymbol{T}_E^{II} - \boldsymbol{T}_E^{I}\right) = \gamma \kappa \boldsymbol{n} \qquad \text{with} \qquad \kappa = \boldsymbol{\nabla}_{\parallel} \cdot \boldsymbol{n} = \left[(\boldsymbol{\delta} - \boldsymbol{nn}) \cdot \boldsymbol{\nabla}\right] \cdot \boldsymbol{n} \tag{135}$$

where κ is the mean curvature of the interface and $\boldsymbol{\nabla}_{\parallel} \equiv (\boldsymbol{\delta} - \boldsymbol{nn}) \cdot \boldsymbol{\nabla}$ is the surface gradient operator. It is clear that at the interface the jump in the total stress, i.e. electric plus viscous, is balanced by the interfacial tension γ.

It is possible to make the following observations:

- Fundamental equation (135) clearly shows that electrocoalescence is heavily dependent on the value of the interfacial tension γ. The presence of **surface active agents**, such as (de-)emulsifiers, can thus facilitate or penalize the coalescence process;
- It is possible to stimulate electrocoalescence of two drops by increasing the jump in both mechanical $(\boldsymbol{\pi}^{II} - \boldsymbol{\pi}^{I})$ and electrical $(\boldsymbol{T}_E^{II} - \boldsymbol{T}_E^{I})$ stresses. For the electrical stresses jump, according to equation (128), it is sufficient to increase the normal $E_{\perp}$ or tangential $E_{\parallel}$ component of the electric field in the drops or in the thin film. To accomplish this the externally applied electric field E_0 have to be increased. In other words, the **higher** the modulus of the **external electric field**, the **easier** will be to have coalescence (or film drainage);
- In case of drainage a **perfectly planar** thin film of infinite extension (i.e. $\kappa = 0$), then the **electrocoalescence process is independent of the surface tension**.

  $$\kappa = 0 \qquad \Rightarrow \qquad \boldsymbol{n} \cdot \left(\boldsymbol{\pi}^{II} - \boldsymbol{\pi}^{I}\right) + \boldsymbol{n} \cdot \left(\boldsymbol{T}_E^{II} - \boldsymbol{T}_E^{I}\right) = 0 \tag{136}$$

  Hence, adding surface active agents with the purpose only to increase or decrease γ will not alter the final outcome nor increase the overall process. Of course, the added substances may also alter the mechanical stress jump at the interface as a collateral effect; in this case, modifications of the system dynamics are expected.
- **Bilayers** represent a particular scenario in the scope of thin-film drainage. Here, electrocoalescence of the two aqueous phases (i.e. the droplets) is prevented only by a double layer of surface active species, traditionally amphiphilic molecules. As we assumed that the phase in the film core is hydrophobic while the outer one is water-based, the double layer will display the hydrophilic "heads" in contact with water and the (conventionally polymeric) hydrophobic long chains on the inside (see figure 3). We can then assume that the thickness of the hydrophobic film (i.e. phase II) is approximately equal to double the length of an entire amphiphilic molecule (heads+tails). As also shown in figure 3, we can compute:

  $$\mathcal{P} = \frac{\mathcal{V}}{a_0 l_c} \tag{137}$$

  where $\mathcal{P}$ is the packing factor, $\mathcal{V}$ is the hydrodynamic volume of the hydrophobic part and a_0 is the area of the circular projection of an head-group on its hydrophobic chain. Let us compute the attraction forces between the two aqueous phases if an in-between bilayer is present; we consider the formula for the dipolar forces in the case of a perfectly planar film

  $$d \approx 2\left(l_c + \chi\right) = 2\left(\frac{\mathcal{V}}{a_0 \mathcal{P}} + \chi\right) \qquad \Rightarrow \qquad \begin{aligned} F_r &= -\frac{15}{2}\pi \epsilon_{II} {E_0}^2 \frac{a^6}{\left(a + \chi + \frac{\mathcal{V}}{a_0 \mathcal{P}}\right)^4} \\ F_\theta &= 0 \end{aligned} \tag{138}$$

  where χ is the average length of the hydrophilic head at the interface.

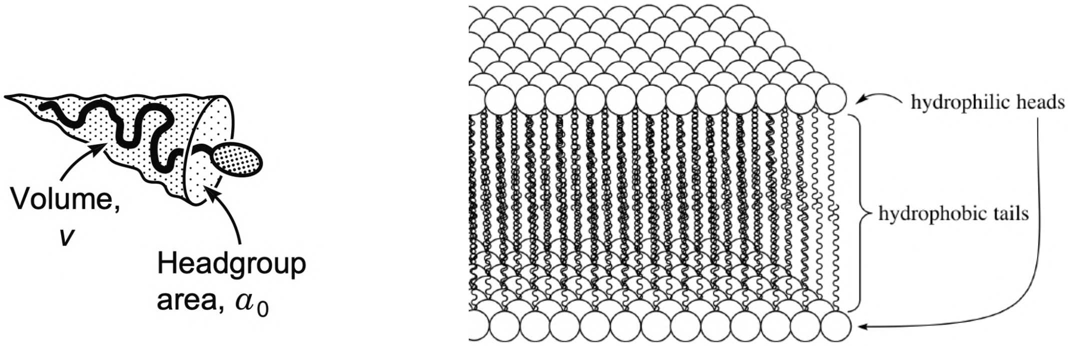

Figure 3: Structural parameters of an amphiphilic molecule (on the left) [11] and typical structure of a planar bilayer (on the right) [10].

- It is possible to connect the discontinuity of the electrical stresses at the droplets-film interface with properties of both bulk phase and of our gauge-identified dividing interface. Recalling equation (35)

$$\boldsymbol{n}\cdot\left(\boldsymbol{\pi}^{II}-\boldsymbol{\pi}^{I}\right)=\left(\frac{1}{\rho^{II}}-\frac{1}{\rho^{I}}\right)^{-1}\boldsymbol{n}\cdot\left(\boldsymbol{v}^{II}-\boldsymbol{v}^{I}\right)\left(\boldsymbol{v}^{II}-\boldsymbol{v}^{I}\right)-\boldsymbol{\nabla}_{\parallel}\cdot\boldsymbol{\pi}^{s} \tag{139}$$

  we can substitute it into (135)

$$\left(\frac{1}{\rho^{II}}-\frac{1}{\rho^{I}}\right)^{-1}\boldsymbol{n}\cdot\left(\boldsymbol{v}^{II}-\boldsymbol{v}^{I}\right)\left(\boldsymbol{v}^{II}-\boldsymbol{v}^{I}\right)+\boldsymbol{n}\cdot\left(\boldsymbol{T}_{E}^{II}-\boldsymbol{T}_{E}^{I}\right)=\gamma\kappa\boldsymbol{\nabla}_{\parallel}\cdot\boldsymbol{nn}+\boldsymbol{\nabla}_{\parallel}\cdot\boldsymbol{\pi}^{s} \tag{140}$$

  then substitute (128)

$$\begin{aligned}\left(\frac{1}{\rho^{II}}-\frac{1}{\rho^{I}}\right)^{-1}\boldsymbol{n}\cdot\left(\boldsymbol{v}^{II}-\boldsymbol{v}^{I}\right)\left(\boldsymbol{v}^{II}-\boldsymbol{v}^{I}\right)+\frac{1}{2}\epsilon_0\epsilon_I\left({E_{\perp}^{I}}^{2}+\frac{\epsilon_{II}}{\epsilon_I}{E_{\parallel}^{I}}^{2}\right)\left(1-\frac{\epsilon_I}{\epsilon_{II}}\right)\boldsymbol{n}=\\=\gamma\kappa\boldsymbol{\nabla}_{\parallel}\cdot\boldsymbol{nn}+\boldsymbol{\nabla}_{\parallel}\cdot\boldsymbol{\pi}^{s}\end{aligned} \tag{141}$$

  As can be seen in the expression above, it is possible to describe interfacial phenomena during electrocoalescence by knowing just the properties of the two bulk phases.
  Moreover, if we substituted equation (133) into (135), we could relate the jump in electrical stresses to the rheological properties of both droplets and hydrophobic dividing film.

3.3.3.2 Entropy production rate

As clearly displayed in (141), there is a strong coupling between mechanical and electrical properties at the interface. We now try to study the entropy production term σ in the specific case of planar thin-film drainage. We start recalling expression (110) of the interaction forces in a non leaky dielectric system (i.e. perfectly conducting aqueous phase in contact with a perfectly dielectric hydrophobic phase)

$$\begin{aligned}F_r&=-12\pi\epsilon_{II}{E_0}^{2}\frac{a^6}{s^4}\left(3\xi-1\right)\\F_\theta&=0\end{aligned} \tag{142}$$

We know from (120) that $\xi\approx 3.67$ for a fully planar film. We then substitute

$$\begin{aligned}F_r&=-120\pi\epsilon_{II}{E_0}^{2}\frac{a^6}{s^4}\\F_\theta&=0\end{aligned} \tag{143}$$

The expression for the jump in Maxwell's stress tensor has already been derived in (128); however, expressions for the normal ($E_\perp$) and tangential ($E_\parallel$) components of the electric field at the interface are still missing.In our analysis, we will look only at one droplet-film interfacial system, as the other one is perfectly identical. First, we report [4] the expression for the dimensionless electric fields external and internal to a single isolated spherical conducting drop

$$\begin{aligned} \boldsymbol{E}_{in}(\boldsymbol{r}) &= \boldsymbol{E}_0 + \frac{R-1}{R+2}\left(\frac{3\boldsymbol{E}_0 \cdot \boldsymbol{r}\boldsymbol{r}}{r^5} - \frac{\boldsymbol{E}_0}{r^3}\right) && \text{inside} \\ \boldsymbol{E}_{out}(\boldsymbol{r}) &= \frac{3}{R+2}\boldsymbol{E}_0 && \text{outside (uniform field)} \end{aligned} \tag{144}$$

where $\boldsymbol{r}$ is the position vector measured from the drop center.
The tangential component of the electric field is continuous at the interface, while the normal component undergoes a jump whenever the drop and suspending fluid have different electrical properties. This said, we can now combine equations (143) and (144), together with the governing conditions (125)

$$\boldsymbol{E}_0(\boldsymbol{x}) + \frac{R-1}{4\pi R}\int_{\Lambda_i}\frac{\boldsymbol{x}-\boldsymbol{y}}{|\boldsymbol{x}-\boldsymbol{y}|^3}E_\perp(\boldsymbol{y})d\Lambda_y = \begin{cases} \boldsymbol{E}^i(\boldsymbol{x}) & \boldsymbol{x} \in \text{bulk of } i = I, II \\ \frac{1}{2}\left[\boldsymbol{E}^I(\boldsymbol{x}) + \boldsymbol{E}^{II}(\boldsymbol{x})\right] & \boldsymbol{x_s} \in \bar{\Lambda} \text{ with surface } \bar{\Lambda} = \Lambda_1 + \Lambda_2 \end{cases} \tag{145}$$

where $\boldsymbol{E}_0$ is the external electric field and $\boldsymbol{x}_s$ is the position vector for a generic point on the interface. We can now solve the second-kind integral equation in (145) by computing the inner product of (145) and $\boldsymbol{n}(\boldsymbol{x_s})$ along the interface; the result is the expression for the normal component of the electric field $E_\perp$ along the interface

$$E_\perp^{II}(\boldsymbol{x}_s) = \frac{2}{1+R}\boldsymbol{n}(\boldsymbol{x}_s)\cdot\boldsymbol{E}_0(\boldsymbol{x}_s) + \frac{1-R}{2\pi(1+R)}\boldsymbol{n}(\boldsymbol{x}_s)\cdot\sum_{i=1}^{2}\int_{\Lambda_i}\frac{\boldsymbol{x}_s-\boldsymbol{y}}{|\boldsymbol{x}_s-\boldsymbol{y}|^3}E_\perp^i(\boldsymbol{y})\,\mathrm{d}\Lambda_y(\boldsymbol{x}) \tag{146}$$

The equation above determines the distribution of $E_\perp(\boldsymbol{x}_s)$ inside the hydrophobic thin film (i.e. phase II). Of course, the modulus of the electric field depends on the conductivity ratio R and the shape of the drops Λ_i; indeed, the complete planarity of the interface that we experience in the film drainage case is embedded here in the surface term Λ_i. Using the boundary condition (125), we can easily compute the interfacial normal component of E inside the droplet (i.e. phase I):

$$E_\perp^{I}(\boldsymbol{x}_s) = RE_\perp^{II}(\boldsymbol{x}_s) = \frac{2R}{1+R}\boldsymbol{n}(\boldsymbol{x}_s)\cdot\boldsymbol{E}_0(\boldsymbol{x}_s) + \frac{R(1-R)}{2\pi(1+R)}\boldsymbol{n}(\boldsymbol{x}_s)\cdot\sum_{i=1}^{2}\int_{\Lambda_i}\frac{\boldsymbol{x}_s-\boldsymbol{y}}{|\boldsymbol{x}_s-\boldsymbol{y}|^3}E_\perp^i(\boldsymbol{y})\,\mathrm{d}\Lambda_y(\boldsymbol{x}) \tag{147}$$

Note that the tangential component of the electric field $E_\parallel^i = \boldsymbol{t}\cdot\boldsymbol{E}^i$ can be analogously computed by integration of (145). Since we are in an electrostatic system and the normal electric field $E_\perp$ is known, we can apply equation (123) to calculate the electric potential ϕ^{II} across the hydrophobic thin-film

$$\phi^{II}(\boldsymbol{x}_0) = \phi_0(\boldsymbol{x}_0) - \frac{1-R}{4\pi}\sum_{i=1}^{2}\int_{\Lambda_i}\frac{E_\perp^i}{|\boldsymbol{x}_0-\boldsymbol{y}|}\,\mathrm{d}\Lambda_y(\boldsymbol{x}) \tag{148}$$

where ϕ_0 is the externally-applied electric potential.

It is important to notice that the closer the two water-oil interfaces get during the drainage (i.e. as the hydrophobic film gets thinner), the greater is the **locally-enhanced electric transport** at the interface. During real experiments, of course the non-zero mean curvature of the interface κ and the applied potential ϕ_0 exert a major influence on the electrocoalescence phenomenon.
In Prof. Jan Vermant's group at ETH Zürich it was also proved that the rupture of a stable film can be achieved by applying increasing DC electric fields up to a certain threshold value; when this value is reached, the enhanced electric forces greatly exceed the interfacial tension, and the thin film breaks. As to measure the thickness h of a film (of surface area A) up to its rupture, capacitance (C) measurements were performed and the modulus of the locally-enhanced electric field $|\boldsymbol{E}_{\text{Enhanced}}|$ was derived using the following relations:

$$|\boldsymbol{E}_{\text{Enhanced}}| \approx \frac{\Delta\phi}{h} \qquad \text{where} \qquad h = \frac{1}{\epsilon_0\epsilon_r}\frac{1}{A} \tag{149}$$

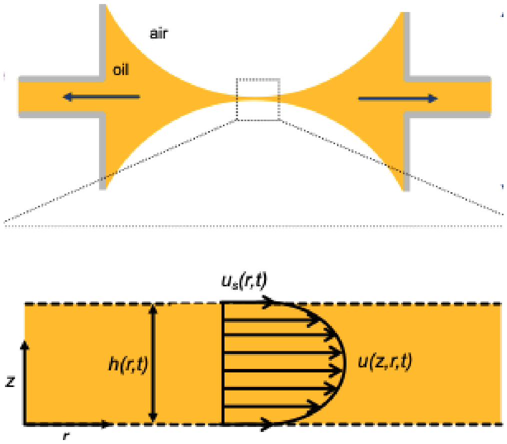

Figure 4: Oil in the hydrophobic film core is removed via pumping from multiple directions [2].

Finally, let us now analyze the entropy production rate σ in the case of the drainage of a thin film. All assumptions made at the beginning of the section are still valid. Moreover, we can further assume

- the droplet-film interface to be FULLY PLANAR and NON-DEFORMABLE;
- there are only 2 components in the system (aqueous solution and oil)
- the system comprises of two phases, one perfectly hydrophilic and the other perfectly hydrophobic $\Rightarrow$ NO mass transfer occurs within the interface.
  The absence of mass transfer can be experimentally achieved by removing the liquid from the hydrophobic film core via pumping from multiple directions (see figure 4 for reference).

We can know recall equation (59), which can be simplified according to the assumptions above:

$$\begin{aligned}\sigma^s_{\text{1st interf}} = &\frac{1}{T^s}\left\{\boldsymbol{n}\cdot\left[\rho^{II}\left(\boldsymbol{v}^{II}-\boldsymbol{v}^s\right)\frac{1}{2}\boldsymbol{v}^{II^2}-\rho^{I}\left(\boldsymbol{v}^{I}-\boldsymbol{v}^s\right)\frac{1}{2}\boldsymbol{v}^{I^2}\right]+\boldsymbol{n}\cdot\left[\boldsymbol{\tau}^{II}\cdot\left(\boldsymbol{v}^{II}-\boldsymbol{v}^s\right)-\boldsymbol{\tau}^{I}\cdot\left(\boldsymbol{v}^{I}-\boldsymbol{v}^s\right)\right]\right\}\\ &+\frac{1}{T^s}\left[\boldsymbol{n}\cdot\left(\boldsymbol{\pi}^{II}-\boldsymbol{\pi}^{I}\right)\cdot\boldsymbol{v}^s-\boldsymbol{v}^s\cdot\boldsymbol{\nabla}_{\parallel}\cdot\boldsymbol{\pi}^s\right]\\ &+\frac{1}{T^s}\left(\boldsymbol{i}^{s*}_{\parallel}\cdot\bar{\boldsymbol{E}}^*_{\parallel}+\bar{i}^*_{\perp}E^{s*}_{\perp}\right)\\ &+\frac{1}{T^s}\left\{\left[\bar{\boldsymbol{E}}^*_{\parallel}-\left(\bar{\boldsymbol{E}}^*_{\parallel}\right)_{eq}\right]\cdot\frac{d^s}{dt}\boldsymbol{p}^{s*}_{\parallel}+\left[\bar{D}^*_{\perp}-\left(\bar{D}^*_{\perp}\right)_{eq}\right]\frac{d^s}{dt}p^{s*}_{\perp}\right\}\end{aligned} \tag{150}$$

In the absence of mass transport across the interface, we know from the jump balance of mass that

$$\boldsymbol{v}^I\cdot\boldsymbol{n}=\boldsymbol{v}^s\cdot\boldsymbol{n}=\boldsymbol{v}^{II}\cdot\boldsymbol{n} \tag{151}$$

in the absence of a magnetic field, we know from the Poynting's theorem for the interface (19) that

$$\bar{\boldsymbol{E}}^*\cdot\frac{\partial}{\partial t}\boldsymbol{D}^{s*}+\boldsymbol{E}^{s*}\cdot\left(\frac{\partial}{\partial t}\bar{\boldsymbol{D}}^*\right)=v^s_{\perp}\bar{\boldsymbol{E}}^*\cdot\left(\boldsymbol{D}^{II}-\boldsymbol{D}^{I}\right)-\boldsymbol{i}^{s*}\cdot\bar{\boldsymbol{E}}^*-\bar{\boldsymbol{i}}^*\cdot\boldsymbol{E}^{s*} \tag{152}$$

from the definition of $\boldsymbol{D}^*$:

$$\boldsymbol{D}^*\equiv\boldsymbol{P}^*+\boldsymbol{E}^*=\epsilon_0\epsilon_r\boldsymbol{E}^*\qquad\xrightarrow[\text{Electrostatics}]{}\qquad\frac{\partial\boldsymbol{E}^*}{\partial t}=0\quad\Rightarrow\quad\frac{\partial\boldsymbol{D}^*}{\partial t}=0 \tag{153}$$

from expression (153), equation (152) further simplifies into

$$\boldsymbol{i}^{s*}\cdot\bar{\boldsymbol{E}}^{*}+\bar{\boldsymbol{i}}^{*}\cdot\boldsymbol{E}^{s*}=v^{s}_{\perp}\bar{\boldsymbol{E}}^{*}\cdot\left(\boldsymbol{D}^{II}-\boldsymbol{D}^{I}\right)\tag{154}$$

substituting (154) into (150)

$$\begin{aligned}\sigma^{s}_{\text{1st interface}}=&\frac{1}{T^{s}}\left[\boldsymbol{n}\cdot\left(\boldsymbol{\pi}^{II}-\boldsymbol{\pi}^{I}\right)\cdot\boldsymbol{v}^{s}-\boldsymbol{v}^{s}\cdot\boldsymbol{\nabla}_{\parallel}\cdot\boldsymbol{\pi}^{s}\right]\\&+\frac{1}{T^{s}}v^{s}_{\perp}\bar{\boldsymbol{E}}^{*}\cdot\left(\boldsymbol{D}^{II}-\boldsymbol{D}^{I}\right)\\&+\frac{1}{T^{s}}\left\{\left[\bar{\boldsymbol{E}}^{*}_{\parallel}-\left(\bar{\boldsymbol{E}}^{*}_{\parallel}\right)_{eq}\right]\cdot\frac{d^{s}}{dt}\boldsymbol{p}^{s*}_{\parallel}+\left[\bar{D}^{*}_{\perp}-\left(\bar{D}^{*}_{\perp}\right)_{eq}\right]\frac{d^{s}}{dt}p^{s*}_{\perp}\right\}\end{aligned}\tag{155}$$

Recalling equation (135)

$$\begin{aligned}\sigma^{s}_{\text{1st interface}}=&\frac{1}{T^{s}}\left[\gamma\kappa\boldsymbol{n}\cdot\boldsymbol{v}^{s}-\boldsymbol{v}^{s}\cdot\boldsymbol{\nabla}_{\parallel}\cdot\boldsymbol{\pi}^{s}\right]\\&+\frac{1}{T^{s}}\boldsymbol{v}^{s}\left[\bar{\boldsymbol{E}}^{*}\cdot\left(\boldsymbol{D}^{II}-\boldsymbol{D}^{I}\right)-\left(\boldsymbol{T}^{II}_{E}-\boldsymbol{T}^{I}_{E}\right)\right]\cdot\boldsymbol{n}\\&+\frac{1}{T^{s}}\left\{\left[\bar{\boldsymbol{E}}^{*}_{\parallel}-\left(\bar{\boldsymbol{E}}^{*}_{\parallel}\right)_{eq}\right]\cdot\frac{d^{s}}{dt}\boldsymbol{p}^{s*}_{\parallel}+\left[\bar{D}^{*}_{\perp}-\left(\bar{D}^{*}_{\perp}\right)_{eq}\right]\frac{d^{s}}{dt}p^{s*}_{\perp}\right\}\end{aligned}\tag{156}$$

As already done in the previous paragraphs, we can decompose the surface pressure tensor $\boldsymbol{\pi}^{s}=-\gamma\boldsymbol{\delta}_{\parallel}+\boldsymbol{\tau}^{s}$; recalling the definition of mean curvature $\kappa=\boldsymbol{\nabla}_{\parallel}\cdot\boldsymbol{n}$ we obtain

$$\begin{aligned}\sigma^{s}_{\text{1st interface}}=&\frac{1}{T^{s}}\boldsymbol{v}^{s}\cdot\left[\gamma\boldsymbol{\nabla}_{\parallel}\cdot\boldsymbol{n}\boldsymbol{n}-\boldsymbol{\nabla}_{\parallel}\cdot\left(-\gamma\boldsymbol{\delta}_{\parallel}+\boldsymbol{\tau}^{s}\right)\right]\\&+\frac{1}{T^{s}}\boldsymbol{v}^{s}\left[\bar{\boldsymbol{E}}^{*}\cdot\left(\boldsymbol{D}^{II}-\boldsymbol{D}^{I}\right)-\left(\boldsymbol{T}^{II}_{E}-\boldsymbol{T}^{I}_{E}\right)\right]\cdot\boldsymbol{n}\\&+\frac{1}{T^{s}}\left\{\left[\bar{\boldsymbol{E}}^{*}_{\parallel}-\left(\bar{\boldsymbol{E}}^{*}_{\parallel}\right)_{eq}\right]\cdot\frac{d^{s}}{dt}\boldsymbol{p}^{s*}_{\parallel}+\left[\bar{D}^{*}_{\perp}-\left(\bar{D}^{*}_{\perp}\right)_{eq}\right]\frac{d^{s}}{dt}p^{s*}_{\perp}\right\}\end{aligned}\tag{157}$$

Note that $\boldsymbol{\delta}_{\parallel}$ is the surface or tangential projector tensor defined as $\boldsymbol{\delta}_{\parallel}=\boldsymbol{\delta}-\boldsymbol{n}\boldsymbol{n}$. Substituting $\boldsymbol{\delta}_{\parallel}$ with is definition

$$\begin{aligned}\sigma^{s}_{\text{1st interface}}=&\frac{1}{T^{s}}\boldsymbol{v}^{s}\cdot\left[\gamma\boldsymbol{\nabla}_{\parallel}\cdot\boldsymbol{n}\boldsymbol{n}+\gamma\boldsymbol{\nabla}_{\parallel}\cdot\left(\boldsymbol{\delta}-\boldsymbol{n}\boldsymbol{n}\right)-\boldsymbol{\nabla}_{\parallel}\cdot\boldsymbol{\tau}^{s}\right]\\&+\frac{1}{T^{s}}\boldsymbol{v}^{s}\left[\bar{\boldsymbol{E}}^{*}\cdot\left(\boldsymbol{D}^{II}-\boldsymbol{D}^{I}\right)-\left(\boldsymbol{T}^{II}_{E}-\boldsymbol{T}^{I}_{E}\right)\right]\cdot\boldsymbol{n}\\&+\frac{1}{T^{s}}\left\{\left[\bar{\boldsymbol{E}}^{*}_{\parallel}-\left(\bar{\boldsymbol{E}}^{*}_{\parallel}\right)_{eq}\right]\cdot\frac{d^{s}}{dt}\boldsymbol{p}^{s*}_{\parallel}+\left[\bar{D}^{*}_{\perp}-\left(\bar{D}^{*}_{\perp}\right)_{eq}\right]\frac{d^{s}}{dt}p^{s*}_{\perp}\right\}\end{aligned}\tag{158}$$

Finally, we are now able to write the FINAL form of the interfacial entropy production rate σ for one of the two interfaces in the scope of thin films drainage.

$$\begin{aligned}\sigma^{s}_{\text{1st interface}}=&\frac{1}{T^{s}}\boldsymbol{v}^{s}\cdot\boldsymbol{\nabla}_{\parallel}\cdot\left(\gamma\boldsymbol{\delta}-\boldsymbol{\tau}^{s}\right)\\&+\frac{1}{T^{s}}\boldsymbol{v}^{s}\left[\bar{\boldsymbol{E}}^{*}\cdot\left(\boldsymbol{D}^{II}-\boldsymbol{D}^{I}\right)-\left(\boldsymbol{T}^{II}_{E}-\boldsymbol{T}^{I}_{E}\right)\right]\cdot\boldsymbol{n}\\&+\frac{1}{T^{s}}\left\{\left[\bar{\boldsymbol{E}}^{*}_{\parallel}-\left(\bar{\boldsymbol{E}}^{*}_{\parallel}\right)_{eq}\right]\cdot\frac{d^{s}}{dt}\boldsymbol{p}^{s*}_{\parallel}+\left[\bar{D}^{*}_{\perp}-\left(\bar{D}^{*}_{\perp}\right)_{eq}\right]\frac{d^{s}}{dt}p^{s*}_{\perp}\right\}\end{aligned}\tag{159}$$

with

$$\boldsymbol{n}\cdot\left(\boldsymbol{T}^{II}_{E}-\boldsymbol{T}^{I}_{E}\right)=\frac{1}{2}\epsilon_{0}\epsilon_{I}\left({E^{I}_{\perp}}^{2}+\frac{\epsilon_{II}}{\epsilon_{I}}{E^{I}_{\parallel}}^{2}\right)\left(1-\frac{\epsilon_{I}}{\epsilon_{II}}\right)\boldsymbol{n}\tag{160}$$

where $E^{I}_{\perp}$ and $E^{I}_{\parallel}$ are those previously derived in (147).
However, the real entropy generation rate must reflect the presence in the system of two identical interface

(i.e. top and bottom water-oil interfaces). To correct for this, it is sufficient to multiply by a factor 2 the entropy production rate for a single interface.

$$\sigma^{s}_{\mathrm{Total}} = 2\, \sigma^{s}_{\mathrm{1st\ interface}} \tag{161}$$

References

[1] AM Albano and Dick Bedeaux. "Non-equilibrium electro-thermodynamics of polarizable multicomponent fluids with an interface". In: *Physica A: Statistical Mechanics and its Applications* 147.1-2 (1987), pp. 407–435.

[2] Alexandra Alicke. *Soft Materials Group, ETH Zürich, Switzerland.*

[3] P Atten. "Electrocoalescence of water droplets in an insulating liquid". In: *Journal of Electrostatics* 30 (1993), pp. 259–269.

[4] James C Baygents, NJ Rivette, and Howard A Stone. "Electrohydrodynamic deformation and interaction of drop pairs". In: *Journal of Fluid Mechanics* 368 (1998), pp. 359–375.

[5] D Bedeaux. "Nonequilibrium thermodynamics and statistical physics of surfaces". In: *Adv. Chem. Phys* 64 (1986), pp. 47–109.

[6] S Roy Caplan and Alvin Essig. *Bioenergetics and linear nonequilibrium thermodynamics: the steady state.* Harvard University Press, 2013.

[7] Sybren Ruurds De Groot and Peter Mazur. *Non-equilibrium thermodynamics.* Courier Corporation, 2013.

[8] John S Eow et al. "Electrostatic enhancement of coalescence of water droplets in oil: a review of the current understanding". In: *Chemical engineering journal* 84.3 (2001), pp. 173–192.

[9] JS Hadamard. "Mouvement permanent lent d'une sphère liquid et visqueuse dans un liquide visqueux". In: *CR Hebd. Seances Acad. Sci. Paris* 152 (1911), pp. 1735–1738.

[10] S Hardinger. "Illustrated glossary of organic chemistry". In: *Retrieved July* 19 (2015), p. 2017.

[11] Jacob N Israelachvili. *Intermolecular and surface forces.* Academic press, 2011.

[12] Aharon Katchalsky and Peter F Curran. *Nonequilibrium thermodynamics in biophysics.* Harvard University Press, 2013.

[13] RL Melcher. "Linear contribution to spatial dispersion in the spin-wave spectrum of ferromagnets". In: *Physical Review Letters* 30.4 (1973), p. 125.

[14] Sameer Mhatre, Shivraj Deshmukh, and Rochish M Thaokar. "Electrocoalescence of a drop pair". In: *Physics of Fluids* 27.9 (2015), p. 092106.

[15] Herbert A Pohl. *Dielectrophoresis: The behavior of neutral matter in nonuniform electric fields (Cambridge Monographs on physics).* Cambridge/New York: Cambridge University Press, 1978.

[16] David C Venerus and Hans Christian Öttinger. *A modern course in transport phenomena.* Cambridge Univ. Press, 2018.

[17] Jun Zeng and Tom Korsmeyer. "Principles of droplet electrohydrodynamics for lab-on-a-chip". In: *Lab on a Chip* 4.4 (2004), pp. 265–277.

Eidgenössische Technische Hochschule Zürich
Swiss Federal Institute of Technology Zurich

D MATL

CASE STUDY

Life Cycle Assessment and Material Flow analysis of commercial lighting equipment

Luca Mondonico

19-945-641

December 2019

ETH Zürich

Contents

1 Introduction

1.1 A brief history of lighting

The presence of reliable and energy efficient lightings has played and continues playing a major role in modern society. The main advancements in lighting technology occurred in sequence more than two centuries ago with the advent and progress of the industrial revolution. Firstly, gas lamps were developed in England in 1790 and different types of gas, as methane, acetylene, butane, hydrogen or natural gas, were used over the years. Afterwards, on the other hand, the invention of electric light bulbs, attributed to Thomas Edison in 1879, entered the market and incandescent bulbs went on to dominate the world of lighting until the first light-source based on gas discharges was introduced commercially by Daniel McFarlan Moore in 1904. The 20th century was the century of high intensity discharge lamps (HID), among the most popular ones were fluorescent, mercury-vapor, high pressure sodium, and metal halide. All of these lamps used a similar type of technology and operated by sending an electrical current between two metal electrodes in a glass tube filled with inert gas that results in the emission of visible light. The lighting technology that significantly revolutionized the market was the one of Light Emitting Diodes (LEDs) that consisted in a solid-state lighting (SSL) that produced light by converting electrical current using a semiconductor material. The first practical LED emerged in 1962, and its invention was attributed to Nick Holonyak. Thenceforward, LEDs have been commercially available in many colors such as green, amber, and red, and this has contributed to their increasing popularity in signage and display applications. Moreover, the discovery of gallium nitride (GaN) LED revolutionized the lighting world making possible to get white light from a semiconductor and, this kind of LEDs established themselves in many fields including architectural lighting, indoor and outdoor lighting, and traffic and railway signaling. The excellent characteristics such as high luminous efficacy, robustness, long lifetime, high color rendering index (CRI), and high reliability, make LEDs good candidates for replacing completely traditional light sources in the short-term [1].

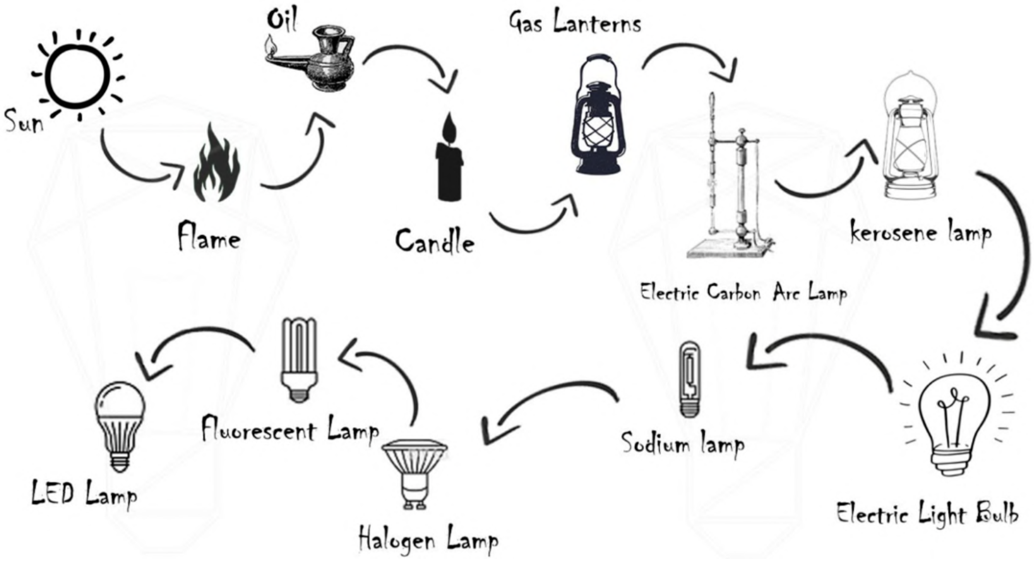

Figure 1: History of lighting [2].

2 The various types of lighting

2.1 Nowadays technologies

In Table 1 it is shown a comparison of the operating systems and properties of the major types of lighting commercially available for everyday use: incandescent lamps, halogen lamps, fluorescent lamps and LEDs.

Lighting efficiency has improved considerably since 2000. Incandescent bulbs have been recently banned in most countries and their phase-out prompted global technology shifts towards more efficient technologies such as fluorescent lamps or LEDs. In 2018, LEDs reached a critical milestone, achieving the same share of global residential sales as less-efficient fluorescent lamps (40%), and now appear to have overtaken fluorescent lamps with their sales that are expected to further increase in the next years. Even if many markets are still dominated by halogen and fluorescent lamps, LEDs need to become the global norm to remain in line with a Sustainable Development Scenario (SDS) in the global energy system. Current trends suggest that the market is on track to follow the SDS trajectory by 2030; however, to raise the share of LED sales to more than 65% of the residential market by 2025, countries need to update their regulatory policies, for instance extending the phase-out regulation also to halogen lamps, which are only slightly more efficient than incandescent ones.

LEDs are now massively produced in many markets, and competition among manufacturers is driving further innovation, wider product choices and lower prices. In particular, China has taken the lead in manufacturing, benefiting from strong financial subsidies and incentives from the government, and prices of LED lamps have fallen substantially to 3-5 $, making them more and more affordable [3].

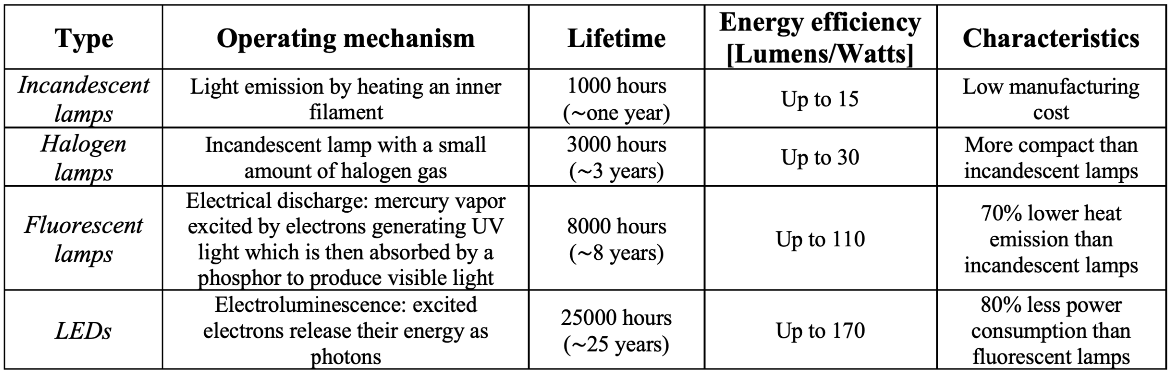

Type	**Operating mechanism**	**Lifetime**	**Energy efficiency [Lumens/Watts]**	**Characteristics**
Incandescent lamps	Light emission by heating an inner filament	1000 hours (~one year)	Up to 15	Low manufacturing cost
Halogen lamps	Incandescent lamp with a small amount of halogen gas	3000 hours (~3 years)	Up to 30	More compact than incandescent lamps
Fluorescent lamps	Electrical discharge: mercury vapor excited by electrons generating UV light which is then absorbed by a phosphor to produce visible light	8000 hours (~8 years)	Up to 110	70% lower heat emission than incandescent lamps
LEDs	Electroluminescence: excited electrons release their energy as photons	25000 hours (~25 years)	Up to 170	80% less power consumption than fluorescent lamps

Table 1: Comparison of lighting systems.

3 Life Cycle Assessment

A question arises: LEDs are the most efficient lighting technology, but what about their life cycle impact? Are they sustainable? To answer this question the following Life Cycle Assessment, where LEDs were compared with incandescent lamps (IND) and compact fluorescent lamps (CFL), was performed.

For each luminaire system, the impacts were separately calculated for the production of four raw material components (fixture, ballast, lamp and lens), the packaging, the transport (by road and by sea), the power consumed during use, and the end of life (recycling and disposal). Examples of the impact categories include resource depletion, land use and landfill, ecotoxicity (terrestrial and aquatic), and global warming. Fig 2 shows the flow diagram of an LCA evaluation of a generic lamp, including the component parts involved in the raw material phase, the manufacturing, transport, the in- use service and the end of life disposal [4].

Of all the possible LCA variations, this analysis used a "cradle-to-grave" approach: it examined the entire life cycle, from the extraction of the raw material (the "cradle") to the end of life ("grave"). The time period of analysis was calibrated on the longest-lived component to guarantee that the maximum life service is taken into account and the impacts associated with manufacturing are amortized over that time range.

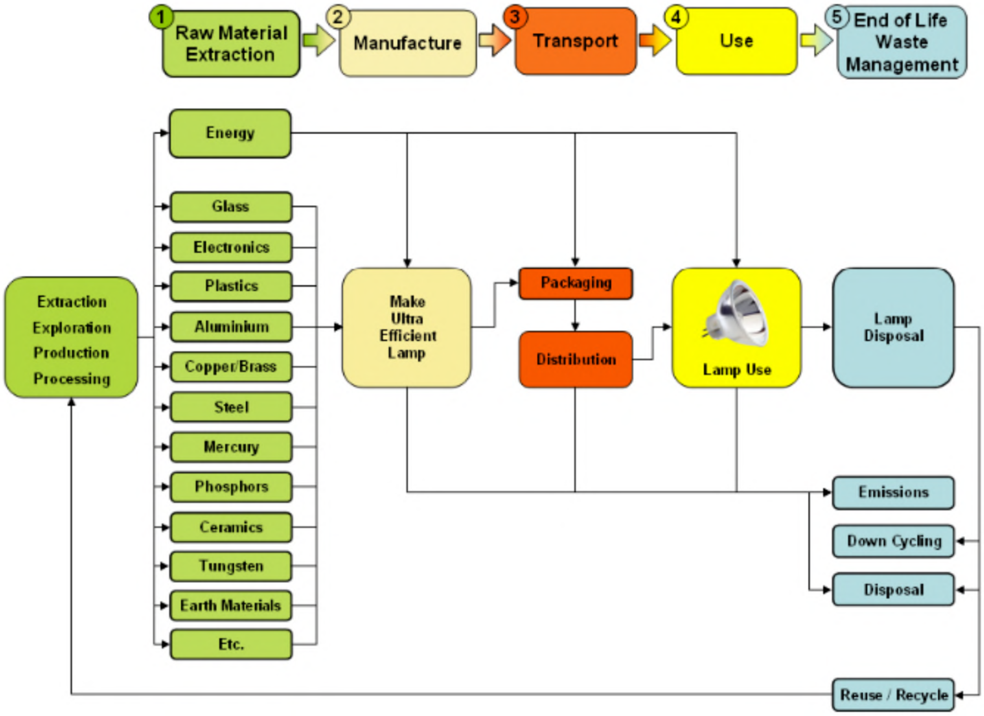

Figure 2: Life Cycle Assessment Flow Diagram for a Generic Lamp [4].

3.1 Lamp Performance and Functional Unit

As seen in the previous chapter, incandescent lamps, compact fluorescent bulbs and LED lamps have different performance characteristics. A functional unit of "20 million lumens-hour" was chosen to ensure the uniformity required for the energy life cycle analysis (see Table 2). This functional unit represents the lighting service provided by a single 12.5 W LED lamp over its lifetime (Fig. 3) [5].

Lamp type	**Watts**	**Lumens**	**Operating lifetime (hrs)**
Incandescent lamp	60	900	1000
CFL	15	900	8500
LED (2011)	12.5	800	25000
LED (2015)	5.8	800	40000

Table 2: Performance of conventional and LED lighting technologies [5].

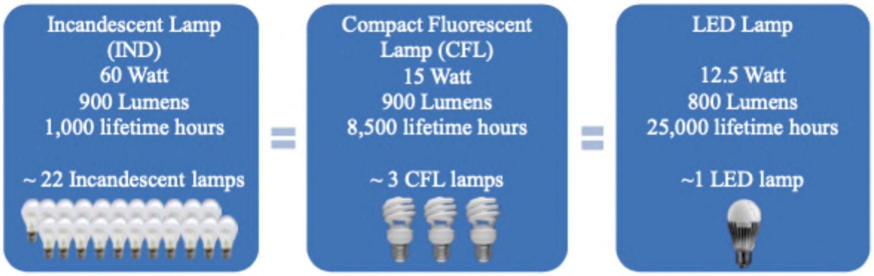

Figure 3: Number of lamps needed to supply 20 million Lumen-Hours [5].

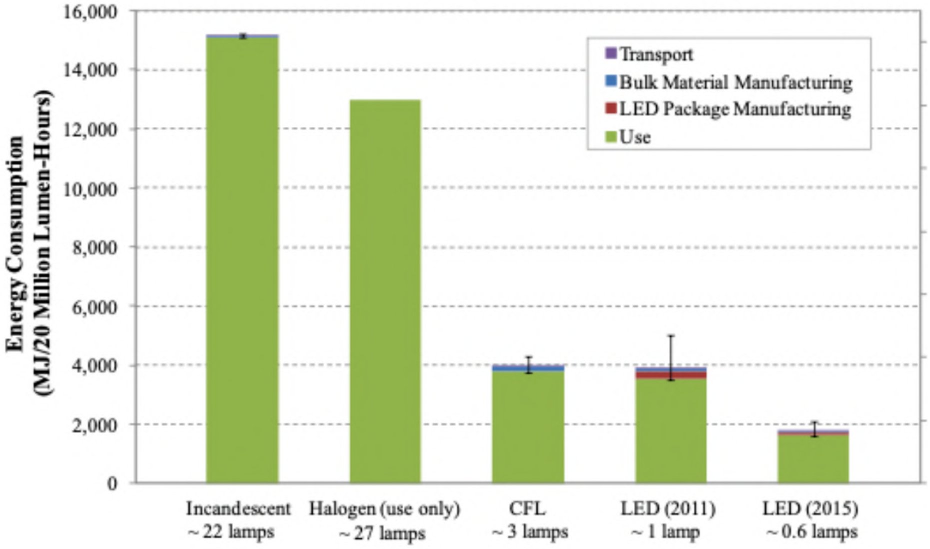

Figure 4: Life-Cycle Energy of incandescent lamps, CFLs and LED lamps [5].

The following discussion in based on a research made in 2012, so the data for 2015 are estimations that, however, are not far from the actual values [5,6]. Since incandescent lamps and CFLs have a lower efficiency than LEDs, the functional unit can be used to indicate how many incandescent lamps and compact fluorescent bulbs are required to achieve performance equivalence. Fig. 4 shows that the energy consumption of LEDs (2011) and compact fluorescent lamps during their life cycle is approximately the same: 3900 MJ per 20 million lumens per hour. This corresponds to approximately a quarter of the energy consumption of an incandescent lamp (15100 MJ per functional unit). The "use phase" contributes the most to the consumption of energy (approx. 90% of total energy consumption over a life cycle), followed by lamp production and finally transportation (less than 1% of the total). It is finally worth remembering that one pivotal issue that can be easily identified in literature is the high uncertainty of manufacturing-related energy consumption data, which range from 0.1% to 27% of the total life cycle [5,7].

3.2 LCA – Results

The first step is to identify which stages of the LCA are ecologically relevant and which are not. For each lamp type, the LCA impacts are calculated separately for the raw materials, the manufacturing, the transport (by sea and by road), the power consumed during the lamp's operating life and finally the end of life. The following series of tables and bar charts (Fig 5) present the LCA results for each lamp type, broken down by these LCA stages. These results clearly show that the factor that dominates the majority of the environmental indicators considered (Table 3) is "energy-in-use" which is depicted in each figure with yellow shading, followed by "raw materials" and "manufacturing". The remaining two LCA steps – disposal and transport – are almost insignificant although the packaged lamps have traveled over 10000 km from factory to home [6].

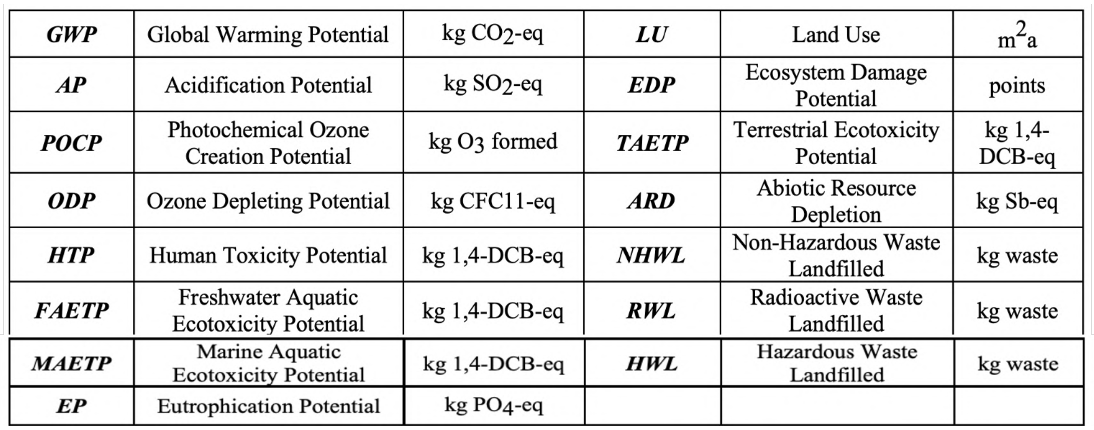

GWP	Global Warming Potential	kg CO_2-eq	***LU***	Land Use	m^2a
AP	Acidification Potential	kg SO_2-eq	***EDP***	Ecosystem Damage Potential	points
POCP	Photochemical Ozone Creation Potential	kg O_3 formed	***TAETP***	Terrestrial Ecotoxicity Potential	kg 1,4-DCB-eq
ODP	Ozone Depleting Potential	kg CFC11-eq	***ARD***	Abiotic Resource Depletion	kg Sb-eq
HTP	Human Toxicity Potential	kg 1,4-DCB-eq	***NHWL***	Non-Hazardous Waste Landfilled	kg waste
FAETP	Freshwater Aquatic Ecotoxicity Potential	kg 1,4-DCB-eq	***RWL***	Radioactive Waste Landfilled	kg waste
MAETP	Marine Aquatic Ecotoxicity Potential	kg 1,4-DCB-eq	***HWL***	Hazardous Waste Landfilled	kg waste
EP	Eutrophication Potential	kg PO_4-eq			

Table 3: Environmental impacts considered in the LCA with their units of measurement [6].

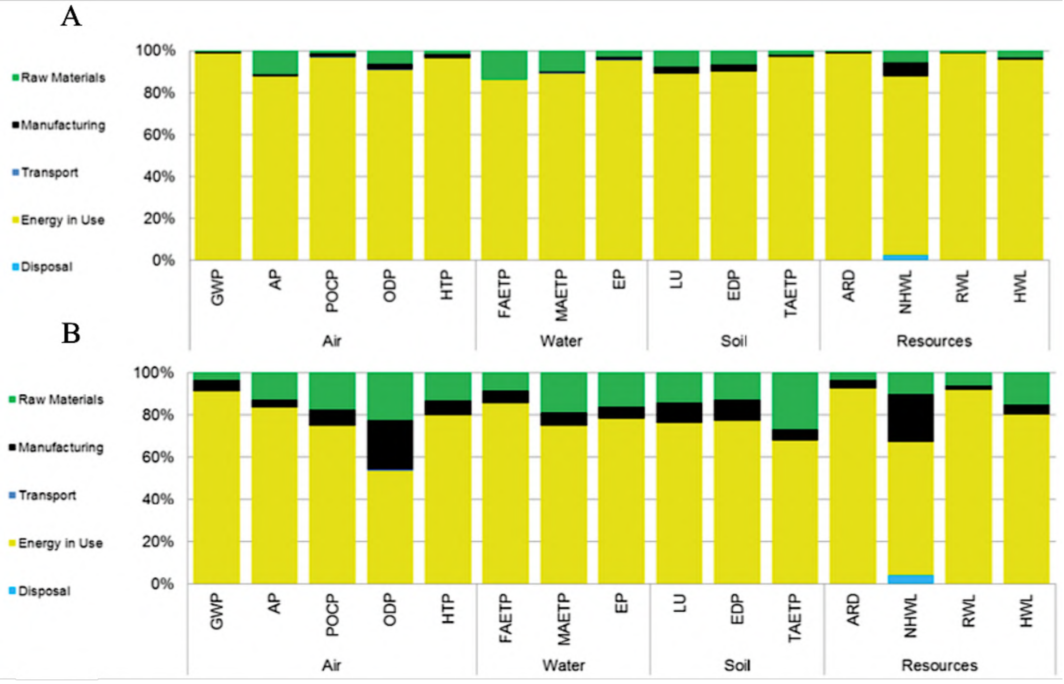

Figure 5: Proportions of the Life Cycle Impact of (A) 60 W incandescent lamp, (B) Compact Fluorescent Lamp, (C) 2012 LED lamp, and (D) 2017 LED lamp [6].

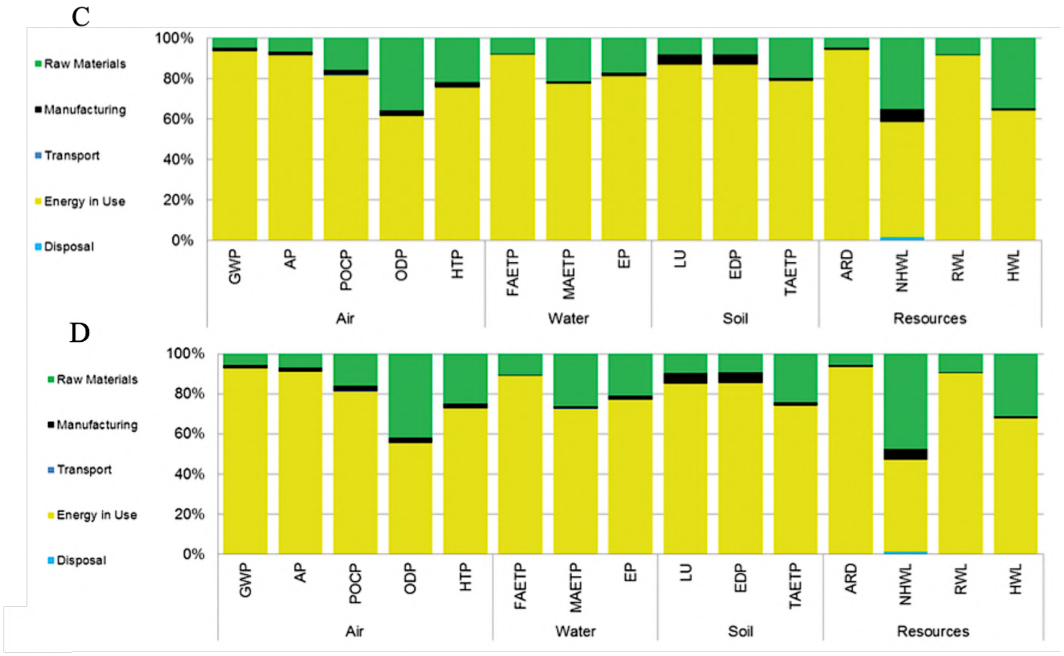

Figure 5: Proportions of the Life Cycle Impact of (A) 60 W incandescent lamp, (B) Compact Fluorescent Lamp, (C) 2012 LED lamp, and (D) 2017 LED lamp [6](*cont.*).

3.3 LCA – Environmental impact

To simplify the interpretation of the results for the four lamps and the 15 environmental indicators (Table 3), the results are also displayed in the form of two "spider graphs" (Fig.6-7). The 15 impacts are also here divided into four categories: soil (green), resources (yellow), air (orange) and water (blue). The radial lines in the diagram identify the different environmental indicators, and, for each of these, the technology with the greatest impact value is put to the outer circle while the remaining ones are then normalized respect to that value. In other words, those lamps with many impacts plotted close to the spider-graph center are the best environmental-friendly performers [6]. Fig. 6 clearly shows that, of all the sources considered, it is the incandescent lamp that has the greatest impact per lighting unit; this result is intuitive since it has the lowest efficiency (i.e. the highest energy consumption per lighting unit) among the four lamps. The next worst performer is the CFL ("hazardous waste landfill" indicator excluded), followed by the 2012 LED lamp and finally by the 2017 LEDs. It has been demonstrated that 2012 LEDs showed a slightly higher "hazardous waste landfill" indicator (0.4 grams) than that of CFLs because of one of their components - the aluminum heat sink - which counts for the 20% of this indicator. From a quantitative point of view, the impact of 2017 LED lamps is considerably lower than that of incandescent lamps, about 70% lower than that of compact fluorescent bulbs and about 50% lower than that of LEDs in 2012. Fig. 7 presents the same results of Fig. 6, but the graph has been adjusted to remove the incandescent lamp and provide the impacts relative mainly to the CFL. Therefore, out of these graphs, it can be noticed the remarkable reduction (up from 3 to 10 times) in environmental impacts that would result from replacing incandescent lamps and CFL with the new generation LEDs [7].

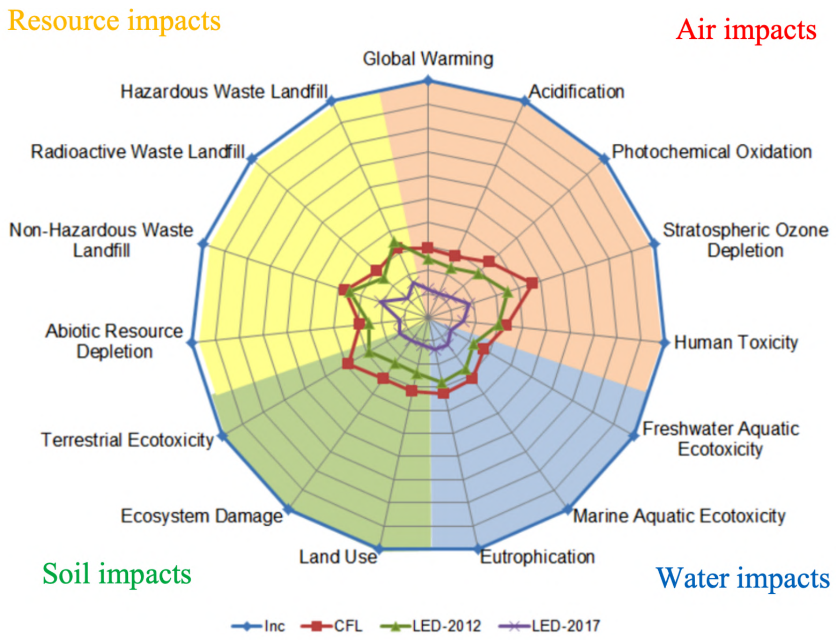

Figure 6: Life-Cycle Assessment Impacts of the lamps analysed relative to incandescent lamps [6].

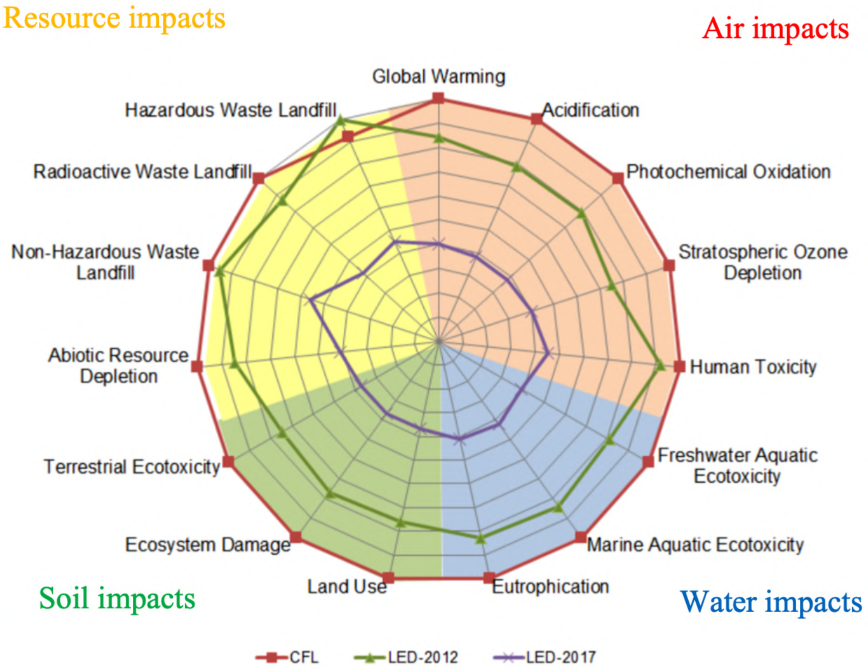

Figure 7: Life-Cycle Assessment Impacts of the lamps analysed relative mainly to CFLs [6].

Finally, it can be concluded that LEDs are the best technology on the market both concerning the performances and the sustainability of their life cycle. This is the reason why, following the Sustainable Development Scenario (SDS), LEDs will occupy up to the 80% of the market share of lighting equipment by 2030 (Fig. 8).

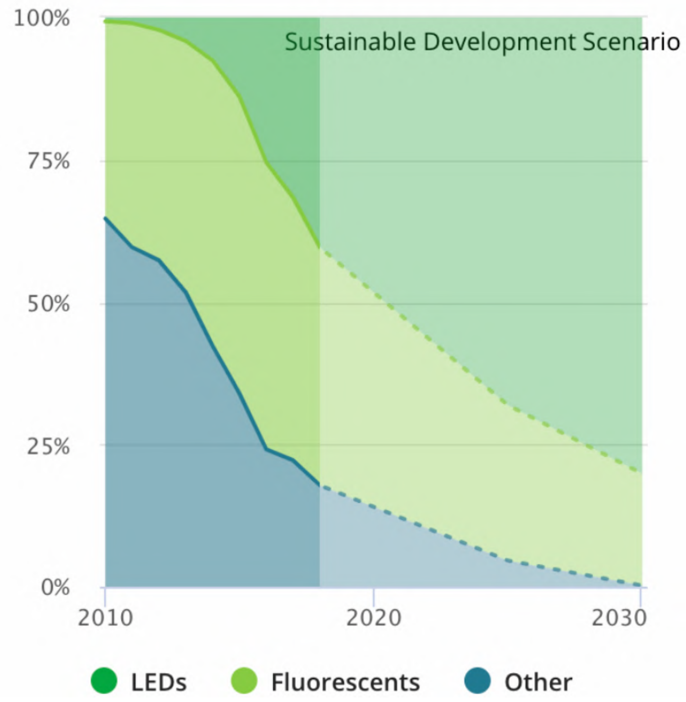

Figure 8: Lighting sales by type according to Sustainable Development Scenario [3].

4 Material flow analysis

According to the graph in Fig. 8, a simplified material flow analysis (MFA) was carried out to understand what kind of output the recycling system of lighting equipment will face in the next years.

The assumptions made are the following:

- the period under observation is from 2010 to 2060;
- the market stock in 2010 was considered equal to zero. This assumption introduces an error only in the first years, but not from the 2019 onwards;
- the value of output is normalized respect to the total amount of lighting system introduced every year in the market, that was assumed constant over all the period;
- as a simplification, only three different categories of lighting equipment were considered: LEDs, CFL and "other technologies";
- it was considered the model according to which the outflow is the inflow delayed and dispersed by a lifetime distribution function F(t);
- most of the data concerning the input were taken according to the graph in Fig. 8, while the others that are not displayed were assumed;
- regarding the lifetime, it was considered of 15-24 years for LEDs, 6-10 for CFL and 2-4 for "other technologies". Therefore, the failure probability was assumed higher in those years, but with a smaller percentage of failure also in the years before (Table 4).

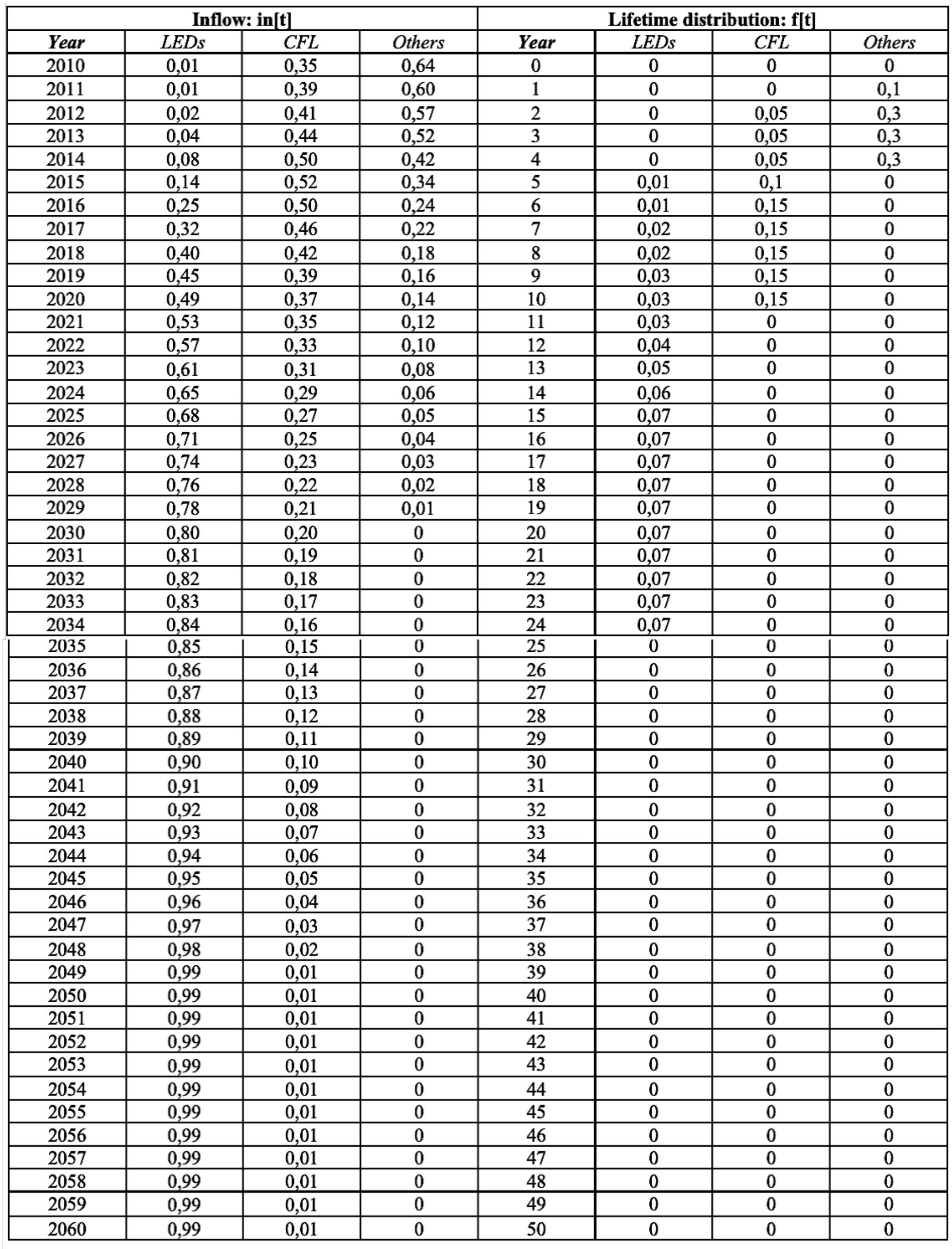

Inflow: in[t]				**Lifetime distribution: f[t]**			
Year	*LEDs*	*CFL*	*Others*	***Year***	*LEDs*	*CFL*	*Others*
2010	0,01	0,35	0,64	0	0	0	0
2011	0,01	0,39	0,60	1	0	0	0,1
2012	0,02	0,41	0,57	2	0	0,05	0,3
2013	0,04	0,44	0,52	3	0	0,05	0,3
2014	0,08	0,50	0,42	4	0	0,05	0,3
2015	0,14	0,52	0,34	5	0,01	0,1	0
2016	0,25	0,50	0,24	6	0,01	0,15	0
2017	0,32	0,46	0,22	7	0,02	0,15	0
2018	0,40	0,42	0,18	8	0,02	0,15	0
2019	0,45	0,39	0,16	9	0,03	0,15	0
2020	0,49	0,37	0,14	10	0,03	0,15	0
2021	0,53	0,35	0,12	11	0,03	0	0
2022	0,57	0,33	0,10	12	0,04	0	0
2023	0,61	0,31	0,08	13	0,05	0	0
2024	0,65	0,29	0,06	14	0,06	0	0
2025	0,68	0,27	0,05	15	0,07	0	0
2026	0,71	0,25	0,04	16	0,07	0	0
2027	0,74	0,23	0,03	17	0,07	0	0
2028	0,76	0,22	0,02	18	0,07	0	0
2029	0,78	0,21	0,01	19	0,07	0	0
2030	0,80	0,20	0	20	0,07	0	0
2031	0,81	0,19	0	21	0,07	0	0
2032	0,82	0,18	0	22	0,07	0	0
2033	0,83	0,17	0	23	0,07	0	0
2034	0,84	0,16	0	24	0,07	0	0
2035	0,85	0,15	0	25	0	0	0
2036	0,86	0,14	0	26	0	0	0
2037	0,87	0,13	0	27	0	0	0
2038	0,88	0,12	0	28	0	0	0
2039	0,89	0,11	0	29	0	0	0
2040	0,90	0,10	0	30	0	0	0
2041	0,91	0,09	0	31	0	0	0
2042	0,92	0,08	0	32	0	0	0
2043	0,93	0,07	0	33	0	0	0
2044	0,94	0,06	0	34	0	0	0
2045	0,95	0,05	0	35	0	0	0
2046	0,96	0,04	0	36	0	0	0
2047	0,97	0,03	0	37	0	0	0
2048	0,98	0,02	0	38	0	0	0
2049	0,99	0,01	0	39	0	0	0
2050	0,99	0,01	0	40	0	0	0
2051	0,99	0,01	0	41	0	0	0
2052	0,99	0,01	0	42	0	0	0
2053	0,99	0,01	0	43	0	0	0
2054	0,99	0,01	0	44	0	0	0
2055	0,99	0,01	0	45	0	0	0
2056	0,99	0,01	0	46	0	0	0
2057	0,99	0,01	0	47	0	0	0
2058	0,99	0,01	0	48	0	0	0
2059	0,99	0,01	0	49	0	0	0
2060	0,99	0,01	0	50	0	0	0

Table 4: Inflow and lifetime distribution used for plotting the graph in Fig.9.

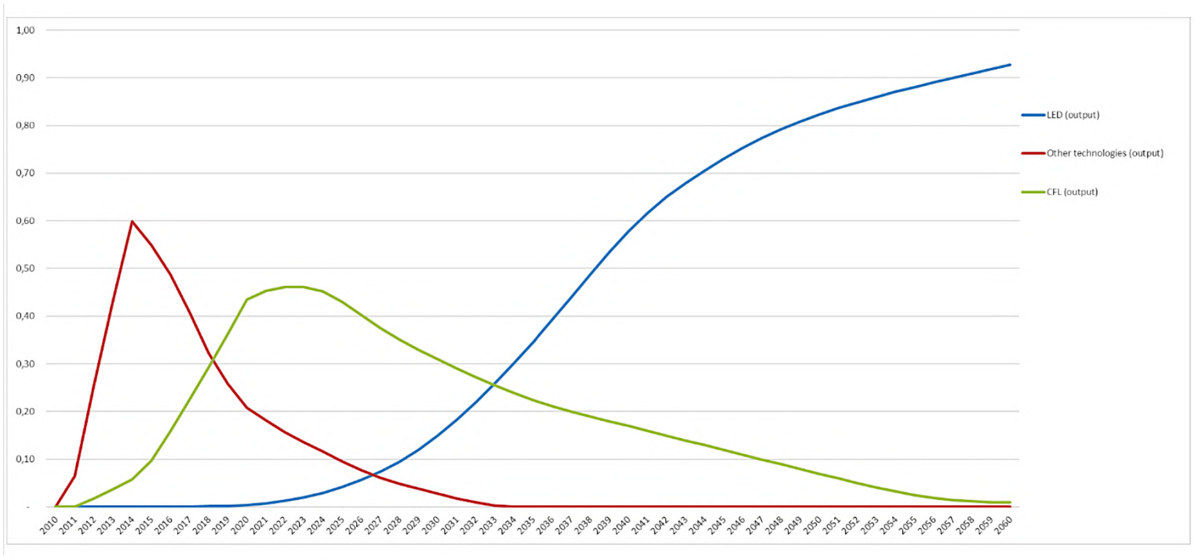

Figure 9: Material flow analysis.

From the graph it is possible to see the output trends for the different lighting sources. In the next 10 years the recycling system will mainly deal with fluorescent lamps (green line) and with the last amount of other technologies (red line). On the other hand, from 2025 onwards, the output of LEDs (blue line) will increase significantly and it will continue growing, first reaching the CFL output in approximately 2033, and then becoming almost the only one to take into account. For this reason, the importance to have a good recycling for LEDs is clear, since they will be, undoubtedly, the major technology employed in the following years.

5 Current recycling system and possible improvements

For the moment, the main unsolved challenge for LEDs and CFL recycling are rare earth elements, which are the materials thanks to which they can emit light. Recycling rare earth materials is not easy as glass or plastic, both because they are present in small amounts and because to separate these materials is often necessary to use aggressive solvents or very high temperatures during the process. Indeed, because of the nasty materials and large amount of energy needed, in some cases recycling would create greater environmental harm than mining them. When small amounts of rare earth are part of complex mixtures, separation can be too expansive to justify it for these elements [8].

However, in addition to the technical challenges of recycling rare earths elements, another issue is caused by the little incentives given to try to get these materials back. In fact, their price has remained almost constant over the last years and there are no laws that subsidy their recycle. For this reason, as of 2011, less than 1% of rare earths elements was recovered [8].

The existing recycling infrastructure for fluorescent bulbs makes them good candidates for rare earth recycling. Even if LEDs are getting popularity, there are plenty of fluorescent and compact fluorescent bulbs that will be disposed in next years and they remain the main target for short-term recycling. Fluorescent light bulbs, in fact, make use of a large quantity of rare earth elements to fill out the color spectrum: the red and green phosphors in the powder that lines the inside of the lights are the rare earth elements europium (Eu) and terbium (Tb). Recyclers collect the mercury, the glass and the metal parts of the bulbs, but they have traditionally dumped the rare-earth-containing white powder that lines the tubes. Some companies are now starting to recover it, but much effort should be put on that in order to have an efficient recycling system for rare earth elements. Also LEDs contain REE used as phosphors in them, but their smaller amount compared to CFL makes a possible economical recycle even more difficult [8].

In Switzerland, an example of company that recycles lighting equipment is SOVAG-VEOLIA which uses the so-called BLUBOX technology. Thanks to this technology, 95% of the supplied material is returned either as recycling metal and recycling glass back into the recycle cycle or, in case of plastics, it is used in the thermal utilization of fuel.

The BLUBOX enables to process of almost all kind of lamps (CFLs, LEDs, halogen, incandescent) in one machine. Concerning fluorescent tubes, that usually must be treated differently due to the amount of toxic mercury contained, they are broken down, crushed in smaller particles and the powder containing mercury is captured by the exhaust gas system and collected separately. The whole system is built-in a 40ft HC container, which is constantly working under negative pressure to ensure a clean environment and output products are free from mercury and can be sold on the market. The recycling capacity of lamps is up to 500 kg/h, which results in 1000 tonnes a year based on an 8-hour working shift. BLUBOX system is efficient, fast, and it reduces to minimum manual operations, but, unfortunately, it can only divide materials as metals, glass or plastics without separating completely rare earth elements that are collected in a powder that is sold as well because it contains almost 15% of these species. All the output powder with Hg inside goes lost and, for this reason, the first possible improvement that could be done to this process is to enhance the removal of mercury from the powder, in order to sell a higher percentage of products and result in an increased revenue for the recyclers [9,10]. The separation of mercury from the powdered mixture of elements can be done using iron nanoparticles. However, often mercury remains trapped in the white powder coating in the bulb's glass tubing and, in this case, it would be required additional heat to extract Hg and the operating costs for the recyclers might increase considerably [11].

Figure 10: Process flow of lamp recycling by BLUBOX [10].

Concerning REE, if losing them is such a concern, one solution could be to use phosphors that are free of these elements. Nitrides, such as BCNO materials, have recently emerged as promising environmentally friendly phosphor candidates that are REE free. They are environmentally friendly, but still more expensive than the phosphors containing rare earth elements and their quantum efficiency is slightly lower. For these reasons, further studies and improvements must be done in order to consider them as a valid alternative for the market of lighting equipment [12,13].

If the composition is kept the conventional one, an entirely different recycling approach is necessary to efficiently separate and recycle all the components of a LED or CFL lamp. In fact, if the entire device is shredded, it becomes much more difficult to divide the materials. A process called "electrohydraulic comminution" could be used to break the lamps into their different parts without destroying them. It consists in using shock waves created by electrical impulses in a water bath to separate the components at their predetermined break points. The only question mark is whether this process can be repeated until the desired materials have been separated. For this reason, maybe also a design innovation and a better predisposition of the devices to recycle can help to pursuit the goal [14].

However, all these methods are still at the research stage and their applicability on an industrial level is difficult because they remain quite expansive and they are not worthwhile for the energy effort. Therefore, first more incentives should be given to companies to improve the separate collection of REE in lighting equipment and the development of a more efficient recycling system in terms of energy consumption, and second laws and regulations should be adjusted and updated for the newest technologies such as LEDs. In Switzerland, in fact, the disposal of all kinds of illuminants is part of the 1998 decree VREG (*Verordnung über die Rückgabe, die Rücknahme und die Entsorgung elektrischer und elektronischer Geräte*), whose purpose is to prevent electric and electronic devices to get into normal waste or the environment and to ensure that they are disposed in an environmental-friendly way and according to the technical state of the art. This decree works quite well according to the take-back number of illuminants, but it does not include for the moment LEDs, and this is a serious lack especially since these devices are predicted to be the dominant technology in the close future and for many years to come [15].

References

[1] Vitor C Bender, Tiago B Marchesan, and J Marcos Alonso. "Solid-state lighting: A concise review of the state of the art on LED and OLED modeling". In: *IEEE Industrial Electronics Magazine* 9.2 (2015).

[2] *The Lighting Blog*. Available at `https://thelighting.blog/2018/10/10/history-of-lighting/`. Oct. 2018.

[3] John Dulac Thibaut Abergel. *Lighting*. Available at `https://www.iea.org/tcep/buildings/lighting/`. Nov. 2019.

[4] Navigant Consulting Europe et al. "Life cycle assessment of ultra-efficient lamps". In: *Department of the Environment and Energy* (2009).

[5] Michael Scholand and Heather E Dillon. *Life-cycle assessment of energy and environmental impacts of LED lighting products part 1: LED manufacturing and performance*. Tech. rep. Pacific Northwest National Lab.(PNNL), Richland, WA (United States), 2012.

[6] Michael Scholand and Heather E Dillon. *Life-cycle assessment of energy and environmental impacts of LED lighting products part 2: LED manufacturing and performance*. Tech. rep. Pacific Northwest National Lab.(PNNL), Richland, WA (United States), 2012.

[7] Osram Opto Semiconductors. "Life cycle assessment of illuminants—A comparison of light bulbs, compact fluorescent lamps and LED lamps". In: *OsramOpto Semiconductors GmbH* (2009).

[8] Jessica Marshall. "Why rare earth recycling is rare and what we can do about it". In: *Ensia Magazine* (2014).

[9] Veolia Sovag. Available at `https://www.iea.org/tcep/buildings/lighting/`. Nov. 2019.

[10] *Blu Box – Plug Recycle*. Available at `https://www.iea.org/tcep/buildings/lighting/`. 2017.

[11] J.Melissa Pandika. "New technique reclaims mercury from spent compact fluorescent light bulbs". In: (2016).

[12] Wei-Ning Wang et al. "Novel rare-earth-free tunable-color-emitting BCNO phosphors". In: *Journal of Materials Chemistry* 21.14 (2011), pp. 5183–5189.

[13] Xin Song, Moon-Hwan Chang, and Michael Pecht. "Rare-earth elements in lighting and optical applications and their recycling". In: *Jom* 65.10 (2013), pp. 1276–1282.

[14] Erika Machacek et al. "Recycling of rare earths from fluorescent lamps: Value analysis of closing-the-loop under demand and supply uncertainties". In: *Resources, Conservation and Recycling* 104 (2015), pp. 76–93.

[15] *SR 814.620 Verordnung vom 14. Januar 1998 über die Rückgabe, die Rücknahme und die Entsorgung elektrischer und elektronischer Geräte (VREG)*. Available at `https://www.admin.ch/opc/de/classified-compilation/19980114/index.html#id-1.`. 2019.

ETH
Eidgenössische Technische Hochschule Zürich
Swiss Federal Institute of Technology Zurich

D MTEC

ADVANCED SUSTAINABILITY ECONOMICS

Luca Mondonico

19-945-641

February 2020

ETH Zürich

Social optimum in the Basic Climate Economy (BCE) model

The Basic Climate Economy (BCE) model is a useful tool which is able to deal with climate economics and climate policy, incorporating non-renewable (fossil) stock depletion, pollution stock accumulation, endogenous growth and climate-induced capital depreciation. Specifically, the BCE model adds stock pollution to a two-sector capital-resource model; we have the manufacturing sector which produces goods immediately available to consumption, and the corporate sector that provides goods and services for investments which increase the physical capital stock.

Here we can make the following modeling assumptions: constant returns to capital in capital sector, natural resource use for final goods, emissions (caused by resource use) add to pollution stock, and capital depreciation is increased by pollution stock.

.1 Assumptions

For the *production*, the final output Y_t is produced by capital K_t and natural resources R_t according to the Cobb-Douglas form:

$$Y_t = A\left(\epsilon_t K_t\right)^{\alpha} R_t^{1-\alpha} \tag{1}$$

where $\epsilon_t \equiv \frac{K_{Y_t}}{K_t} \in [0,1]$ is the aggregate fraction of capital devoted to the consumption good.

For the *resources*, let R be a natural resource which is extracted from resource stock S and regenerated by nature at a rate ζ . We have the following motion equation:

$$\dot{S}_t = \zeta S_t - R_t \tag{2}$$

Here we assume the resource R to be exhaustible, $\zeta = 0$. Hence,

$$\dot{S}_t = -R_t \quad s.t. \quad \int_0^{\infty} R_t dt \leq S_0 \tag{3}$$

For the *capital*, capital K_t is assumed to be the only input, so that investment good I_t can be written as:

$$I_t = B\left(1-\epsilon_t\right) K_t \quad with \quad B > 0 \tag{4}$$

Investment leads to capital accumulation according to

$$\dot{K}_t = I_t - D_t\left(P_t\right) K_t = \; = B\left(1-\epsilon_t\right) K_t - D_t\left(P_t\right) K_t \tag{5}$$

where $D_t\left(P_t\right)$ is the damage function. Given an endogenous rate of capital depreciation, $D_t\left(P_t\right) \in [0,1]$ denotes the share of capital loss.

For the *pollution*, pollution stock P increases with the use of natural resources and could decay at a rate ω:

$$\dot{P}_t = \phi R_t - \omega P_t \quad with \quad \phi > 0, \omega \in [0,1] \tag{6}$$

where ϕ represents the carbon intensity of the polluting resource. Here we assume no decay of pollution stock, i.e. $\omega = 0$. Hence,

$$\dot{P}_t = \phi R_t = -\phi \dot{S}_t \tag{7}$$

Moreover, we assume there is no emission mitigation technology available. Finally, we can suppose that the stock of exhaustible resources and the state of the atmosphere influence individual utility, together with (negatively) affecting the production and the capital stock.

.2 Social optimum

Given all the assumptions above, the social planner chooses the share ϵ_t, and resource extraction R_t in order to maximize the utility function, which will have Equations 1,4,5,3 as constraints. The utility function $U\left(C_t\right)$ is given by a CRRA-type function:

$$\max_{C_t,\epsilon_t} \int_0^\infty U\left(C_t\right) e^{-\rho t} dt = \max_{C_t,\epsilon_t} \int_0^\infty \frac{C_t^{1-\sigma}-1}{1-\sigma} e^{-\rho t} dt \tag{8}$$

with with $\sigma > 0$, the inverse of the elasticity of intertemporal substitution.

We assume to have an equilibrium condition on consumer goods market, which ensures $Y_t = C_t$ and the no-arbitrage condition on the prices $p_Y = p_C$ (and on the shadow prices $\lambda_{C_t} = \lambda_{Y_t}$). Hence,

$$C_t = Y_t = A\left(\epsilon_t K_t\right)^\alpha R_t^{1-\alpha} \tag{9}$$

In order to optimize the problem, we need to write the expression for the current-value Hamiltonian H_t, taking into account the CRRA utility function and all the constraints.

$$H_t = \frac{C_t^{1-\sigma}-1}{1-\sigma} + \lambda_{C_t}\left[A\left(\epsilon_t K_t\right)^\alpha R_t^{1-\alpha} - C_t\right] + \lambda_{K_t} K_t \left[B\left(1-\epsilon_t\right) - D\left(P_t\right)\right] - \lambda_{S_t} R_t + \lambda_{P_t}\phi R_t \tag{10}$$

where λ_{C_t},λ_{K_t},λ_{S_t}, λ_{C_t}, λ_{P_t} are the shadow prices of the consumption good, C_t, capital stock, K_t, stock of non-renewable resources, S_t, and stock of pollution, λ_{P_t}. Assuming an internal solution, we are able to write the first order conditions $\left(\frac{\partial H_t}{\partial(\cdot)} = 0\right)$ with reference to C_t, ϵ_t and R_t:

$$\frac{\partial H_t}{\partial C_t} = 0 \quad \Rightarrow \quad \frac{1-\sigma}{1-\sigma} C^{-\sigma} - \lambda_{C_t} = 0; \quad C_t^{-\sigma} - \lambda_{C_t} = 0 \tag{11}$$

$$\frac{\partial H_t}{\partial \epsilon_t} = 0 \quad \Rightarrow \quad \lambda_{C_t} \alpha A K_t^\alpha R_t^{1-\alpha} \epsilon_t^{\alpha-1} - \lambda_{K_t} B K_t = 0 \tag{12}$$

$$\frac{\partial H_t}{\partial R_t} = 0 \quad \Rightarrow \quad \lambda_{C_t}\left(1-\alpha\right) A\left(\epsilon_t K_t\right)^\alpha R_t^{-\alpha} - \lambda_{S_t} + \lambda_{P_t}\phi = 0 \tag{13}$$

Rearranging Equations 11,12,13, we obtain:

$$C_t^{-\sigma} = \lambda_{C_t} \tag{14}$$

$$\lambda_{C_t} \alpha A(\epsilon_t K_t)^\alpha R_t^{1-\alpha} = \lambda_{K_t} B K_t \epsilon_t \quad \xrightarrow{Eqn.9} \quad \lambda_{C_t} \alpha C_t = \lambda_{K_t} B K_t \epsilon_t \quad \rightarrow \quad \alpha \frac{C_t}{K_t} = \frac{\lambda_{K_t}}{\lambda_{C_t}} B \epsilon_t \tag{15}$$

$$\lambda_{C_t}\left(1-\alpha\right) A\left(\epsilon_t K_t\right)^\alpha R_t^{-\alpha} \frac{R_t}{R_t} = \lambda_{S_t} - \lambda_{P_t}\phi \quad \xrightarrow{Eqn.9} \quad \lambda_{C_t}\left(1-\alpha\right) C_t \frac{1}{R_t} = \lambda_{S_t} - \lambda_{P_t}\phi \quad \xrightarrow{continues} \tag{16}$$

$$\xrightarrow{continues} \quad \left(1-\alpha\right)\frac{C_t}{R_t} = \frac{\lambda_{S_t}}{\lambda_{C_t}} - \frac{\lambda_{P_t}}{\lambda_{C_t}}\phi; \quad \left(1-\alpha\right)\frac{C_t}{R_t} = \frac{1}{\lambda_{C_t}}\left(\lambda_{S_t} - \phi\lambda_{P_t}\right) \tag{17}$$

Moreover, we know that $\frac{\partial H_t}{\partial(*)} = \rho\lambda_{*_t} - \dot{\lambda}_{*_t}$ for every state variable, here K_t, S_t and P_t, with its shadow price λ_{*_t}. Therefore, we can write:

$$\frac{\partial H_t}{\partial K_t} = \rho\lambda_{K_t} - \dot{\lambda}_{K_t} \quad \Rightarrow \quad \lambda_{C_t}\alpha A \epsilon^\alpha K_t^{\alpha-1} R_t^{1-\alpha} + \lambda_{K_t}\left[B\left(1-\epsilon_t\right) - D\left(P_t\right)\right] = \rho\lambda_{K_t} - \dot{\lambda}_{K_t} \tag{18}$$

$$\frac{\partial H_t}{\partial S_t} = \rho\lambda_{S_t} - \dot{\lambda}_{S_t} \quad \Rightarrow \quad 0 = \rho\lambda_{S_t} - \dot{\lambda}_{S_t} \tag{19}$$

$$\frac{\partial H_t}{\partial P_t} = \rho\lambda_{P_t} - \dot{\lambda}_{P_t} \quad \Rightarrow \quad -\lambda_{K_t} K_t \dot{D}(P_t) = \rho\lambda_{P_t} - \dot{\lambda}_{P_t} \tag{20}$$

Rewriting Equations 18 we obtain:

$$\lambda_{C_t} \alpha A \epsilon^{\alpha} K_t^{\alpha} R_t^{1-\alpha} \frac{1}{K_t} + \lambda_{K_t} \left[B\left(1-\epsilon_t\right) - D\left(P_t\right)\right] \frac{K_t}{K_t} = \rho \lambda_{K_t} - \dot{\lambda}_{K_t} \tag{21}$$

$$\xrightarrow{Equations\ 5\ and\ 9} \quad \lambda_{C_t} \alpha C_t \frac{1}{K_t} + \lambda_{K_t} \frac{\dot{K}_t}{K_t} = \rho \lambda_{K_t} - \dot{\lambda}_{K_t} \tag{22}$$

$$\xrightarrow{Dividing\ by\ \lambda_{K_t}} \quad \alpha \frac{\lambda_{C_t} C_t}{\lambda_{K_t} K_t} + \frac{\dot{K}_t}{K_t} = \rho - \frac{\dot{\lambda}_{K_t}}{\lambda_{K_t}} \tag{23}$$

$$\xrightarrow{Rearranging} \quad \frac{\dot{\lambda}_{K_t}}{\lambda_{K_t}} + \frac{\dot{K}_t}{K_t} = -\alpha \frac{\lambda_{C_t} C_t}{\lambda_{K_t} K_t} + \rho; \quad \frac{\dot{\lambda}_{K_t} K_t + \dot{K}_t \lambda_{K_t}}{\lambda_{K_t} K_t} = -\alpha \frac{\lambda_{C_t} C_t}{\lambda_{K_t} K_t} + \rho \tag{24}$$

$$\xrightarrow{We\ identify\ the\ growth\ rates\ \frac{\dot{\circ}}{\circ} = \hat{\circ}} \quad \widehat{\lambda_{K_t} K_t} = -\alpha \frac{\lambda_{C_t} C_t}{\lambda_{K_t} K_t} + \rho \tag{25}$$

Rewriting Equations 19 we obtain:

$$\hat{\lambda}_{S_t} = \rho \tag{26}$$

Rewriting Equations 20 we obtain:

$$\dot{\lambda}_{P_t} = \lambda_{K_t} K_t \dot{D}(P_t) + \rho \lambda_{P_t} \tag{27}$$

$$\xrightarrow{Dividing\ by\ \lambda_{P_t}} \quad \hat{\lambda}_{P_t} = \dot{D}(P_t) K_t \frac{\lambda_{K_t}}{\lambda_{P_t}} + \rho \tag{28}$$

The optimization must also include appropriate transversality conditions:

$$\lim_{t \to \infty} \lambda_{S_t} S_t e^{-\rho t} = 0 \tag{29}$$

$$\lim_{t \to \infty} \lambda_{K_t} K_t e^{-\rho t} = 0 \tag{30}$$

$$\lim_{t \to \infty} \lambda_{P_t} P_t e^{-\rho t} = 0 \tag{31}$$

We can notice in Equation 26 the **Hotelling rule** for the extraction of the non-renewable resource.

Moreover, Equation 15 suggests that it is indifferent allocating capital between the two activities of the BCE model: producing the investment good and the consumption good. If we had $\sigma = 1$ (i.e logarithmic utility), we would have from Equation 14:

$$\lambda_{C_t} C_t = 1 \quad \xrightarrow{Eqn.15} \quad \lambda_{K_t} K_t = \frac{\alpha}{B \epsilon_t} \quad \xrightarrow{Eqn.25} \quad \frac{d\left(\lambda_{K_t} K_t\right)}{\lambda_{K_t} K_t} = -B\epsilon + \rho; \quad \dot{\epsilon}_t = B{\epsilon_t}^2 - \rho \epsilon_t \tag{32}$$

$$\xrightarrow{Solving\ the\ differential\ equation} \quad \epsilon_t = \frac{\rho C_1 e^{-\rho t}}{B C_1 e^{-\rho t} + B \rho C_2} \tag{33}$$

Using the transversality condition (30):

$$\lim_{t \to \infty} \frac{\alpha}{B \epsilon_t} e^{-\rho t} = 0 \quad \xrightarrow{Eqn.33} \quad \lim_{t \to \infty} \frac{\alpha}{\rho C_1} \left(C_1 e^{-\rho t} + \rho C_2\right) = 0 \quad \Rightarrow \quad C_2 = 0 \tag{34}$$

Therefore we derive that:

$$\epsilon = \frac{\rho}{B} \equiv \bar{\epsilon} \tag{35}$$

Equation 35 indicates that the share of capital used in the final goods sector instantaneously jumps to its *steady-state value.*

In order to find the Keynes-Ramsey rule (KRR) for the optimal growth rate of consumption $\hat{C}_t$, we consider Equation 9:

$$C_t = A\left(\epsilon_t K_t\right)^{\alpha} R_t^{1-\alpha} \quad \xrightarrow{\textit{Natural logarithm}} \quad \ln C_t = \ln A + \alpha \ln \epsilon_t + \alpha \ln K_t + (1-\alpha)\ln R_t \tag{36}$$

$$\xrightarrow[\textit{Recalling the growth rates } \frac{\dot{\circ}}{\circ}=\hat{\circ}]{\textit{Taking the derivative}} \quad \hat{C}_t = \alpha\hat{\epsilon}_t + \alpha\hat{K}_t + (1-\alpha)\hat{R}_t \tag{37}$$

Recalling Equation 5:

$$\dot{K}_t = B\left(1-\epsilon_t\right)K_t - D_t\left(P_t\right)K_t \quad \xrightarrow{\textit{Dividing by } K_t} \quad \hat{K}_t = B\left(1-\epsilon_t\right) - D_t\left(P_t\right) \tag{38}$$

Recalling Equation 14:

$$C_t^{-\sigma} = \lambda_{C_t} \quad \xrightarrow{\textit{Natural logarithm}} \quad -\sigma \ln C_t = \ln \lambda_{C_t} \quad \xrightarrow{\textit{Derivative}} \quad \hat{\lambda}_{C_t} = -\sigma\hat{C}_t \tag{39}$$

From Equation 15:

$$(1-\alpha)\frac{C_t}{R_t} = \frac{1}{\lambda_{C_t}}\left(\lambda_{S_t} - \lambda_{P_t}\right)\phi \quad \xrightarrow{\textit{Nat. log.}} \quad \ln(1-\alpha) + \ln C_t - \ln R_t = -\ln\lambda_{C_t} + \ln\left(\lambda_{S_t} - \lambda_{P_t}\right) + \ln\phi \tag{40}$$

$$\xrightarrow{\textit{Deriv.}} \hat{C}_t - \hat{R}_t = -\hat{\lambda}_{C_t} + \frac{\dot{\lambda}_{S_t} - \dot{\lambda}_{P_t}}{\lambda_{S_t} - \lambda_{P_t}};\ \hat{R}_t = \hat{C}_t + \hat{\lambda}_{C_t} - \frac{\dot{\lambda}_{S_t}}{\lambda_{S_t}}\left(\frac{1-\frac{\dot{\lambda}_{P_t}}{\dot{\lambda}_{S_t}}}{1-\frac{\lambda_{P_t}}{\lambda_{S_t}}}\right);\ \hat{R}_t = \hat{C}_t + \hat{\lambda}_{C_t} - \hat{\lambda}_{S_t}\left(\frac{1-\frac{\dot{\lambda}_{P_t}}{\dot{\lambda}_{S_t}}}{1-\frac{\lambda_{P_t}}{\lambda_{S_t}}}\right) \tag{41}$$

$$\xrightarrow{\textit{Equations 26 and 38}} \quad \hat{R}_t = \hat{C}_t - \sigma\hat{C}_t - \rho\left(\frac{1-\frac{\dot{\lambda}_{P_t}}{\dot{\lambda}_{S_t}}}{1-\frac{\lambda_{P_t}}{\lambda_{S_t}}}\right); \quad \hat{R}_t = (1-\sigma)\hat{C}_t - \rho\left(\frac{1-\frac{\dot{\lambda}_{P_t}}{\dot{\lambda}_{S_t}}}{1-\frac{\lambda_{P_t}}{\lambda_{S_t}}}\right) \tag{42}$$

From Equation 17:

$$\alpha\frac{C_t}{K_t} = \frac{\lambda_{K_t}}{\lambda_{C_t}}B\epsilon_t \quad \xrightarrow{\textit{Nat. log.}} \quad \ln(\alpha) + \ln C_t - \ln K_t = \ln\lambda_{K_t} - \ln\lambda_{C_t} + \ln B + \ln\epsilon_t \tag{43}$$

$$\xrightarrow{\textit{Deriv.}} \hat{C}_t - \hat{K}_t = \hat{\lambda}_{K_t} - \hat{\lambda}_{C_t} + \hat{\epsilon}_t \xrightarrow[\textit{Equations 38 and 39}]{\textit{Rearranging}} \quad \hat{\epsilon}_t = \hat{C}_t - \left(B\left(1-\epsilon_t\right) - D_t\left(P_t\right)\right) - \hat{\lambda}_{K_t} - \sigma\hat{C}_t \tag{44}$$

From Equation 25:

$$\hat{\lambda}_{K_t} + \hat{K}_t = -\alpha\frac{\lambda_{C_t}C_t}{\lambda_{K_t}K_t} + \rho \xrightarrow{\textit{Eq 15}} \hat{\lambda}_{K_t} + \hat{K}_t = -B\epsilon_t + \rho; \xrightarrow{\textit{Eq 38}} \hat{\lambda}_{K_t} = -B\epsilon_t + \rho - \left(B\left(1-\epsilon_t\right) - D_t\left(P_t\right)\right) \tag{45}$$

Substituting Equation 45 into Equation 44:

$$\hat{\epsilon}_t = \hat{C}_t - \left(B\left(1-\epsilon_t\right) - D_t\left(P_t\right)\right) - \left(-B\epsilon_t + \rho - \left(B\left(1-\epsilon_t\right) - D_t\left(P_t\right)\right)\right) - \sigma\hat{C}_t \tag{46}$$

$$\hat{\epsilon}_t = B\epsilon_t + (1-\sigma)\hat{C}_t - \rho \tag{47}$$

Finally, we can substitute Equation 38, 42, 47 into Equation 37:

$$\hat{C}_t = \alpha\left[B\epsilon_t + (1-\sigma)\hat{C}_t - \rho\right] + \alpha\left[B\left(1-\epsilon_t\right) - D_t\left(P_t\right)\right] + (1-\alpha)\left[(1-\sigma)\hat{C}_t - \rho\left(\frac{1-\frac{\dot{\lambda}_{P_t}}{\dot{\lambda}_{S_t}}}{1-\frac{\lambda_{P_t}}{\lambda_{S_t}}}\right)\right] \tag{48}$$

$$\hat{C}_t = \alpha B\epsilon_t + \alpha(1-\sigma)\hat{C}_t - \alpha\rho + \alpha B - \alpha B\epsilon_t - \alpha D_t\left(P_t\right) + (1-\sigma)\hat{C}_t - \alpha(1-\sigma)\hat{C}_t - (1-\alpha)\rho\left(\frac{1-\frac{\dot{\lambda}_{P_t}}{\dot{\lambda}_{S_t}}}{1-\frac{\lambda_{P_t}}{\lambda_{S_t}}}\right) \tag{49}$$

$$\sigma\hat{C}_t = -\alpha\rho + \alpha B - \alpha D_t\left(P_t\right) - (1-\alpha)\,\rho\left(\frac{1-\frac{\dot{\lambda}_{P_t}}{\dot{\lambda}_{S_t}}}{1-\frac{\lambda_{P_t}}{\lambda_{S_t}}}\right) \tag{50}$$

$$\hat{C}_t = \frac{1}{\sigma}\left[\alpha B - \alpha D_t\left(P_t\right) - \alpha\rho - \rho\left(\alpha + \alpha\left(\frac{1-\frac{\dot{\lambda}_{P_t}}{\dot{\lambda}_{S_t}}}{1-\frac{\lambda_{P_t}}{\lambda_{S_t}}}\right) + \left(\frac{1-\frac{\dot{\lambda}_{P_t}}{\dot{\lambda}_{S_t}}}{1-\frac{\lambda_{P_t}}{\lambda_{S_t}}}\right)\right)\right] \tag{51}$$

We can notice that Equation 51 is the **Keynes-Ramsey rule** for the optimal growth rate of consumption.

In particular, if we can assume that the stock of exhaustible resources and the state of the atmosphere do NOT primarily affect individual utility, we will have the shadow price for the stock of pollution equal to zero:

$$\lambda_{P_t} = 0 \quad therefore \quad \dot{\lambda}_{P_t} = 0 \tag{52}$$

and the Keynes-Ramsey rule as written in Equation 51 is reduced to

$$\hat{C}_t = \frac{\alpha B}{\sigma} - \frac{\alpha D\left(P_t\right)}{\sigma} - \frac{\rho}{\sigma} \tag{53}$$

Equation 53 coincide with the KRR obtained with the decentralized equilibrium in the BCE model paper [Bretschger, L., Karydas, C.,(2018)]. We can notice in Equation 53 the different aspects of productivity, depreciation, and discounting on the growth rate of consumption in time.

In particular, for any given damage function $D\left(P_t\right)$, the dynamic system expressed by Equations 47 and 53, along with the resource and climate dynamics (3), (7), and the transversality conditions (29), (30), (31), are sufficient to completely characterize the social optimum model.

The **steady-state values** that we can immediately derive from the above results are:

$$S_\infty \overset{Exhaustible}{=} 0 \tag{54}$$

$$P_\infty = P_{\max} = P_0 + \phi S_0 \tag{55}$$

$$\hat{C}_\infty = \frac{\alpha B}{\sigma} - \frac{\alpha D\left(P_\infty\right)}{\sigma} - \frac{\rho}{\sigma} \tag{56}$$

For the final steady-state condition, we recall the transversality condition 30:

$$\lim_{t\to\infty} \lambda_{K_t} K_t e^{-\rho t} = 0 \tag{57}$$

The above expression implies that

$$\widehat{\lambda_{K_t} K_t} - \rho < 0 \tag{58}$$

Moreover, we know from Equation 45 that:

$$\widehat{\lambda_{K_t} K_t} = -B\epsilon_t + \rho \tag{59}$$

We combine the above conditions 58, 59 to get that:

$$\lim_{t\to\infty} \epsilon_t > 0 \tag{60}$$

As we know from Equation 5 that $\hat{K}_t$ is asymptotically constant for $t \to \infty$, we have that $\lim_{t\to\infty} \hat{\epsilon}_t \leq 0$. However, we know from (60) that $\hat{\epsilon}_t$ is strictly positive; hence it must be

$$\lim_{t\to\infty} \hat{\epsilon}_t = 0 \tag{61}$$

The final steady-state condition can be directly obtained from Equation 47:

$$\epsilon_\infty = \frac{1}{B}\left[(1-\sigma)\hat{C}_t - \rho\right] \tag{62}$$

As a final part of our model solution for the social optimum, we will try to derive the social cost of carbon (SCC). The SCC basically reflects total damages from releasing greenhouse gas emissions to the atmosphere at every point in time. Labeling the SCC as χ_t, that is the marginal externality damage from burning an additional unit of polluting non-renewable resource, we can define it as:

$$\chi_t = -\phi\frac{\lambda_{P_t}}{\lambda_{C_t}} \tag{63}$$

Let $(\nu - t)$ the time interval between a generic period of emission ν and the reference period of emission t. We suppose the pollution stock increases over time. Since we took ν such that $\nu > t$, we have

$$P_\nu \geq P_t \quad for\ all \quad \nu \geq t \tag{64}$$

It is then possible to rewrite the transversality condition for the stock pollution (31):

$$0 = \lim_{\nu\to\infty} \lambda_{P_\nu} P_\nu e^{-\rho\nu} \geq \lim_{\nu\to\infty} \lambda_{P_\nu} P_t e^{-\rho\nu} \tag{65}$$

which implies

$$\lim_{\nu\to\infty} \lambda_{P_\nu} e^{-\rho(\nu-t)} = 0 \quad for\ all \quad \nu \geq t \tag{66}$$

We recall Equation 28 in terms of ν:

$$\hat{\lambda}_{P_\nu} = \dot{D}(P_\nu)K_\nu\frac{\lambda_{K_\nu}}{\lambda_{P_\nu}} + \rho \xrightarrow[e^{-\rho(\nu-t)}]{Multiplying\ both\ sides\ with} \hat{\lambda}_{P_\nu} e^{-\rho(\nu-t)} = \dot{D}(P_\nu)K_\nu\frac{\lambda_{K_\nu}}{\lambda_{P_\nu}}e^{-\rho(\nu-t)} + \rho e^{-\rho(\nu-t)}; \tag{67}$$

$$\xrightarrow{Multiplying\ both\ sides\ with\ \lambda_{P_\nu}} \quad \dot{\lambda}_{P_\nu} e^{-\rho(\nu-t)} - \rho\lambda_{P_\nu} e^{-\rho(\nu-t)} = \dot{D}\left(P_\nu\right)\lambda_{K_\nu} K_\nu e^{-\rho(\nu-t)}; \tag{68}$$

$$\frac{d\left(\lambda_{P_\nu} e^{-\rho(\nu-t)}\right)}{d\nu} = \dot{D}\left(P_\nu\right)\lambda_{K_\nu} K_\nu e^{-\rho(\nu-t)}; \tag{69}$$

Using the transversality implication (66), we can calculate the indefinite integral from $\nu = t$ to $\nu \to \infty$ as

$$-\lambda_{P_t} = \int_t^\infty \dot{D}\left(P_\nu\right)\lambda_{K_\nu} K_\nu e^{-\rho(\nu-t)} d\nu \tag{70}$$

Substituting $-\lambda_{P_t}$ from (70) into (63) we get that

$$\chi_t = -\phi\frac{\lambda_{P_t}}{\lambda_{C_t}} = \frac{\phi}{\lambda_{C_t}}\int_t^\infty \dot{D}\left(P_\nu\right)\lambda_{K_\nu} K_\nu e^{-\rho(\nu-t)} d\nu \tag{71}$$

Substituting λ_{C_t} from (14) and $(\lambda_{K_\nu} K_\nu)$ from (15) we get that

$$\chi_t = \frac{\phi}{C_t^{-\sigma}}\int_t^\infty \dot{D}\left(P_\nu\right)\frac{\alpha C_\nu \lambda_{C_\nu}}{B\epsilon_\nu} e^{-\rho(\nu-t)} d\nu \tag{72}$$

We multiply and divide the right-hand side of Equation 72 with C_t and ρ:

$$\chi_t = C_t\frac{\alpha\phi}{\rho}\int_t^\infty \dot{D}\left(P_\nu\right)\left(\frac{\rho}{B\epsilon_\nu}\right)\frac{(C_\nu\lambda_{C_\nu})}{C_t^{1-\sigma}} e^{-\rho(\nu-t)} d\nu \tag{73}$$

We substitute $\frac{\rho}{B}$ and λ_{C_ν} according to Equations 35 and 14, respectively.

$$SCC = \chi_t = C_t\frac{\alpha\phi}{\rho}\int_t^\infty \dot{D}\left(P_\nu\right)\left(\frac{\bar{\epsilon}}{\epsilon_\nu}\right)\left(\frac{C_t}{C_\nu}\right)^{\sigma-1} e^{-\rho(\nu-t)} d\nu \tag{74}$$

We can notice that Equation 74 is the **Social Cost of Carbon (SCC)** for the BCE model we are studying.

The first term inside the integral is the marginal damage of pollution on capital accumulation,i.e. $\dot{D}(P_t)$, the second term comes from shadow prices of capital and is responsible for allocating capital between the consumption and the investment sector, while the third term reflects preferences of agents regarding intertemporal consumption.

.3 Comparison with the decentralized case and the role of policy

In Section 2 we characterized the socially optimal solution and derived the general expression for the social cost of carbon, χ_t (see Equation 74).
Here we compare the results obtained in the model above with those for the decentralized equilibrium case. For the decentralized case, we make reference to the work done by Bretschger L. and Karydas C. in "Economics of climate change: Introducing the Basic Climate Economic (BCE) model" [2018].

After a careful look at the two models we can notice that, if expressed per units of output, the social cost of carbon (SCC) for the social planner case equals the Pigouvian carbon tax, i.e. the tax needed to optimally correct for the environmental pollution externality in the decentralized equilibrium case.
Indeed, under general conditions, we have that:

$$\widetilde{SCC} = \tilde{\chi_t} \equiv \frac{\chi_t}{Y_t} \ = \ Social\ cost\ of\ carbon\ per\ unit\ of\ output \tag{75}$$

Substituting χ_t according to Equation 74:

$$\tilde{\chi_t} \equiv -\frac{\phi\lambda_{P_t}}{\lambda_{C_t}Y_t} \quad \xrightarrow[Eqn.9]{Y_t=C_T} \quad \tilde{\chi_t} = \frac{\alpha\phi}{\rho}\int_t^{\infty} \dot{D}\left(P_\nu\right)\left(\frac{\bar{\epsilon}}{\epsilon_\nu}\right)\left(\frac{C_t}{C_\nu}\right)^{\sigma-1} e^{-\rho(\nu-t)}d\nu \tag{76}$$

and if we assume $\sigma = 1$, i.e. logarithmic utility function, we have from (32) that

$$\lambda_{C_t}C_t = 1 \Rightarrow \tilde{\chi_t} \equiv -\phi\lambda_{P_t} \quad which\ implies \quad \hat{\tilde{\chi_t}} \equiv -\phi\hat{\lambda}_{P_t} \tag{77}$$

It can be shown that in the decentralized case, given $\sigma = 1$, the capital share ϵ_t immediately jumps to its optimal steady state value $\bar{\epsilon} \equiv \rho/B$. This is the same result that we obtained with the social planner in Equation 35. We can compare the social planner's optimality condition in Equation 17 with its equivalent from the market case[1]:

Social Planner	Decentralized Equilibrium
$(1-\alpha)\frac{C_t}{R_t} = \frac{\lambda_{S_t}}{\lambda_{C_t}} - \phi\frac{\lambda_{P_t}}{\lambda_{C_t}}$	$(1-\alpha)\frac{Y_t}{R_t} = p_{R_t} + \tau_t$

Assuming the equilibrium condition on consumer goods market, i.e. $C_t = Y_t$, it is immediate to notice that the resource extraction will follow its optimal path ONLY if the producer's price for the non-renewable resource p_{R_t} equals its scarcity rent ($p_{R_t} = \lambda_{S_t}/\lambda_{C_t}$), and if the carbon tax τ_t per-unit in the decentralized case equals the marginal externality damage of emissions $-\phi\frac{\lambda_{P_t}}{\lambda_{C_t}}$ in the social planner case.
Recalling the definition of the social cost of carbon χ_t, we have

$$\tau_t = -\phi\frac{\lambda_{P_t}}{\lambda_{C_t}} = \chi_t \quad \xrightarrow[Y_t=C_t]{\widetilde{\chi_t}Y_t\equiv\chi_t} \quad \boldsymbol{\tau_t = \widetilde{\chi_t}\mathbf{C_t}} \tag{78}$$

We have verified in Equation 78 that the social cost of carbon (SCC), derived from the social optimum model, equals the optimal per-unit carbon tax, here τ_t^0.

As long as we are considering only polluting non-renewable resources, we can see from (78) that the optimal carbon tax τ_t is proportional to the good consumption C_t for $\sigma = 1$, or it asymptotically becomes so in the long run for $\sigma \neq 1$. [1,2]
Hence a carbon tax as τ_t affects the starting point and the transition of all the control variables, but not the long-run steady state of the economy. Resource taxation delays extraction and stretches the depletion of the resource stock to the future. Comparing the baseline no-tax model with the taxation model, we can therefore suppose that during the transition phase we will have

---

[1] Lucas Bretschger and Christos Karydas. "Optimum growth and carbon policies with lags in the climate system". In: Environmental and Resource Economics 70.4 (2018-08), pp. 781–806. ISSN: 0924-6460. DOI: `10.1007/s10640-017-0153-4`.

[2] Lucas Bretschger and Christos Karydas. "Economics of Climate Change: Introducing the Basic Climate Economic (BCE) Model". In: Environment and development economics 24.6 (2019-12), pp. 560–582. ISSN: 1355-770X. DOI: `10.3929/ethz-b-000394747`.

No-Tax		Tax
$S_{baseline}$	$<$	S_{tax}
$D_{baseline}$	$>$	D_{tax}
$P_{baseline}$	$>$	P_{tax}
$\hat{C}_{baseline}$	$<$	$\hat{C}_{tax}$

Moreover, it is also logical to think that the per-unit tax that should in theory postpone extraction has to grow at a slower rate than the price of the non-renewable resource. In this way, the unit-price paid for the resource by consumers increases less rapidly than the price received by producers (which will grow at the market's interest rate ρ), encouraging them to postpone extraction.
This hypothesis is confirmed by looking at the results (79), (80) of the households optimization problem, as reported by Bretschger and Karydas (2019)^2:

$$\hat{C}_t = \frac{1}{\sigma}\left(r_t - \rho\right) \tag{79}$$

$$\hat{p}_{R_t} = r_t \tag{80}$$

if we assume $\sigma = 1$, the price received by producers p_{R_t} grows at a rate r_t, while the optimal carbon tax τ_t^0 grows at $r_t - \rho$, (i.e. with consumption).

We can finally conclude the models comparison by stating that, given an economy in the social optimum, the economy can still have positive growth with climate change. For the decentralized equilibrium, positive growth is feasible provided that efficient climate policies, such as carbon taxes, replicating the social optimum are implemented.

Social Planner	Decentralized Equilibrium
Less consumption	A TAX is needed to increase the price of polluting activities
⇒ Less pollution	⇒ Decrease in the number of polluting activities

If there are no externalities, the results of the two models will coincide.

	Value	
σ	1.8	
ρ	0.015	
α	0.9	
δ_0	0.05	
δ_1	0.04	
δ_2	5×10^{-9}	
η	2.35	
P_0	830	GtC
S_0	6000	GtC
ϕ	1	
B	0.106	

Table 1: Parameters values for the model

.4 Baseline model simulation

Here we will try to show graphically the outcome of the simulation for the BCE social optimum baseline model. In particular, we will try to plot via MATLAB the trend with respect to time of the *Resource stock* S_t, the *Capital depreciation* D_t and the *Consumption growth rate* $\hat{C}_t$.

For the calibration of the BCE baseline model, we will use the parameters suggested by Bretschger and Karydas (2019)[3]. Despite being 2010 the initial time ($t = 0$) considered in the previous study, we will choose parameters on the damage function such that the growth rate of consumption starts at about 2 percent per annum converging to about 0.5 percent per annum in the long run. The parameters values are reported in Table 1.

As suggested in this study, we will assume that pollution feeds back in the economy through a sigmoidal damage function $D(P_t)$, according to:

$$D\left(P_t\right) = \delta_0 + \delta_1 \left(1 - \frac{1}{1 + \delta_2 \left(P_t - P_0\right)^{\eta}}\right) \tag{81}$$

For the consumption growth rate $\hat{C}_t$, we make reference to the Keynes-Ramsey rule as expressed in Equation 53:

$$\hat{C}_t = \frac{\alpha B}{\sigma} - \frac{\alpha D\left(P_t\right)}{\sigma} - \frac{\rho}{\sigma} \tag{82}$$

For the resource stock, we recall the basic Equations 3 and 7:

$$\dot{S}_t = -R_t \quad s.t. \quad \int_0^{\infty} R_t dt \leq S_0 \qquad and \qquad \dot{P}_t = \phi R_t = -\phi \dot{S}_t \tag{83}$$

which combined lead to the model equation for the resource stock S_t:

$$P_t = P_0 + \phi\left(S_0 - S_t\right) \quad \xrightarrow{Rearranging} \quad S_t = S_0 + \frac{1}{\phi}\left(P_0 - P_t\right) \tag{84}$$

In order now to simulate the model, we will use the standard linearization technique via the jacobian matrix. To do this we can introduce the auxiliary variable ψ_t, i.e. the relative shadow price of the resource stock, such that:

$$\psi_t \equiv \frac{\lambda_{S_t}}{\lambda_{S_t} - \phi \lambda_{P_t}} \quad where \quad 0 < \psi_t < 1 \tag{85}$$

Recalling Equation 28:

$$\hat{\lambda}_{P_t} = \dot{D}(P_t) K_t \frac{\lambda_{K_t}}{\lambda_{P_t}} + \rho \tag{86}$$

---

[3] Bretschger and Karydas, "Economics of Climate Change: Introducing the Basic Climate Economic (BCE) Model".

We can rewrite Equation 17 using Equation 26, 28 and 85 in order to get

$$\hat{\psi}_t = \left(1-\psi_t\right)\frac{\alpha\dot{D}\left(P_t\right)}{B\epsilon_t\tilde{\chi}_t} \tag{87}$$

as well as

$$\xrightarrow[\textit{Equations 47 and 75}]{\textit{Recalling}} \quad \hat{R}_t = -B\epsilon_t + \hat{\epsilon}_t - \left(1-\psi_t\right)\frac{\alpha\dot{D}\left(P_t\right)}{B\epsilon_t\tilde{\chi}_t} \tag{88}$$

We now define the resource depletion rate u_t as

$$u_t = \frac{R_t}{S_t} \tag{89}$$

which allows us to rewrite Equation 3 and 7 as

$$\hat{P}_t = \phi u_t \frac{S_t}{P_t} \quad \textit{and} \quad \hat{S}_t = -u_t \tag{90}$$

If we recall Equations 37, 47, 75, 87, 89, 90, and express them in terms of $u_t, \epsilon_t, \psi_t, \tilde{\chi}_t, P_t$ and S_t we are finally able to represent the model dynamics by the following system of six variables.

$$\dot{u}_t = u_t\left(-B\epsilon_t + \frac{\dot{\epsilon}_t}{\epsilon_t} - \left(1-\psi_t\right)\frac{\alpha\dot{D}\left(P_t\right)}{B\epsilon_t\tilde{\chi}_t} + u_t\right) \tag{91}$$

$$\dot{\epsilon}_t = \epsilon_t\left(-\rho + B\epsilon_t - \left(\sigma-1\right)\hat{Y}_t\right) \tag{92}$$

$$\dot{\psi}_t = \psi_t\left(\left(1-\psi_t\right)\frac{\alpha\dot{D}\left(P_t\right)}{B\epsilon_t\tilde{\chi}_t}\right) \tag{93}$$

$$\dot{\tilde{\chi}}_t = \tilde{\chi}_t\left(B\epsilon_t - \frac{\dot{\epsilon}_t}{\epsilon_t} - \frac{\alpha\dot{D}\left(P_t\right)}{B\epsilon_t\tilde{\chi}_t}\right) \tag{94}$$

$$\dot{P}_t = P_t\left(\phi u_t\frac{S_t}{P_t}\right) \tag{95}$$

$$\dot{S}_t = S_t\left(-u_t\right) \tag{96}$$

where

$$\hat{Y}_t = \alpha\left(\frac{\dot{\epsilon}_t}{\epsilon_t} + B\left(1-\epsilon_t\right) - D\left(P_t\right)\right) + \left(1-\alpha\right)\left(\frac{\dot{u}_t}{u_t} - u_t\right) \tag{97}$$

Recalling (54), (92) and (62), we write the long-run steady state values of variables $u_t, \epsilon_t, \psi_t, \tilde{\chi}_t, P_t$ and S_t:

$$u_\infty = B\epsilon_\infty \tag{98}$$

$$\epsilon_\infty = \frac{\rho + \alpha\left(\sigma-1\right)\left(B - D\left(P_\infty\right)\right)}{B\sigma} \tag{99}$$

$$\psi_\infty = 1 \tag{100}$$

$$\widetilde{\chi_\infty} = \frac{\alpha\dot{D}\left(P_\infty\right)}{\left(B\epsilon_\infty\right)^2} \tag{101}$$

$$P_\infty = P_0 + \phi S_0 \tag{102}$$

$$S_\infty = 0 \tag{103}$$

The linearized version of our dynamic system in $\boldsymbol{x_t} = \{u_t, \epsilon_t, \psi_t, \tilde{\chi_t}, P_t, S_t\}^T$ can be obtained by using the jacobian matrix $\boldsymbol{J}$ evaluated at the steady states $\boldsymbol{x_\infty} = \{u_\infty, \epsilon_\infty, \psi_\infty, \tilde{\chi_\infty}, P_\infty, S_\infty\}^T$ according to the relation:

$$\frac{d\left(\boldsymbol{x_t} - \boldsymbol{x_\infty}\right)}{dt} \approx \boldsymbol{J}\left(\boldsymbol{x_t} - \boldsymbol{x_\infty}\right) \tag{104}$$

If we compute the jacobian matrix for the steady states we obtain the eigenvalues:

$$\begin{vmatrix} 0 & 0 & 0 & 0 & 0 & 0 \\ 0 & -\xi & 0 & 0 & 0 & 0 \\ 0 & 0 & -\xi & 0 & 0 & 0 \\ 0 & 0 & 0 & \xi & 0 & 0 \\ 0 & 0 & 0 & 0 & \xi & 0 \\ 0 & 0 & 0 & 0 & 0 & \xi \end{vmatrix} \tag{105}$$

where

$$\xi = \frac{\rho + \alpha\left(\sigma - 1\right)\left(B - \eta D\left(P_\infty\right)\right)}{\sigma} \tag{106}$$

We can now exploit the approximated relation expressed in Equation 104 and the jacobian matrix 105 to derive the model equation for the resource stock S_t:

$$\frac{d\left(S_t - S_\infty\right)}{dt} \approx J_{S_tS_t}\left(S_t - S_\infty\right) \quad \xrightarrow[J_{S_tS_t}=-\xi]{Eqn.103} \quad \frac{d\left(S_t\right)}{dt} \approx -\xi S_t \tag{107}$$

$$\dot{S_t} \approx -\xi S_t \tag{108}$$

Equation 108 can be solved both analytically and numerically. Here we propose the analytical approach first:

$$\xrightarrow{Solving\ the\ ODE} \quad S_t \approx C_1 e^{-\xi t} \quad \textit{we know that } S(t=0) = S_0 \quad \Rightarrow \quad C_1 = S_0 \tag{109}$$

therefore

$$S_t \approx S_0 e^{-\xi t} \quad \rightarrow \quad S_t \approx S_0 e^{-\frac{\rho + \alpha\left(\sigma - 1\right)\left(B - \eta D\left(P_\infty\right)\right)}{\sigma}t}; \tag{110}$$

$$S_t \approx S_0 e^{-\frac{\rho + \alpha\left(\sigma - 1\right)\left(B - \eta\left(\delta_0 + \delta_1\left(1 - \frac{1}{1 + \delta_2\left(\left(P_0 + \phi S_o\right) - P_0\right)^\eta}\right)\right)\right)}{\sigma}t} \tag{111}$$

We have found the expression for the time evolution of the resource stock S_t, which will be a function of time exclusively, since all the parameters in Equation 111 are known.

However, we will plot the time-trends of the *Resource stock* S_t, the *Capital depreciation* D_t and the *Consumption growth rate* $\hat{C}_t$ numerically using MATLAB.
In order to solve numerically the equation 108, we will use the Runge-Kutta method for numerical differentiation. We will assume a time period of interest of 200 years. Hereunder follows the MATLAB script for the numerical analysis.

.5 MATLAB Code

```
clc; clear all; close all;
%% PARAMETERS SETUP %%%%%%%%%%%%%%%%%%%%%%%%%%%%%%%%%%%%%%%%%%%%%%%%%%%%%%%%%%%%%%%%%%
%  Parameters values from Table 1

sigma = 1;
rho = 0.015;
alpha = 0.9;
delta_0 = 0.05;
delta_1 = 0.04;
delta_2 = 5*10^(-9);
eta = 2.35;
P_0 = 830;
S_0 = 6000;
phi = 1;
B = 0.106;

P_t=0; S_t=0;    %Random initial values
% Sigmoidal damage function D[t]
D=delta_0+delta_1*(1-(1)/(1+delta_2*(P_t-P_0)^(eta)));
% Long-run steady state value for the stock Pollution P_t
P_inf=P_0+phi*S_0;

% We derived in Equation 108 the ODE for the stock resource S_t:
S_t_prime = -((rho+alpha*(sigma-1)*(B-eta*D))/(sigma))*S_t;

%% 4th-order RUNGE-KUTTA NUMERICAL DIFFERENTIATION %%%%%%%%%%%%%%%%%%%%%%%%%%%%%%%%%%
% We will solve the ODE relative to S_t using the Runge-Kutta 4th-order method.
% Here we assume for simplicity y=S_t

% Equation to solve: Y'=-((rho+alpha*(sigma-1)*(B-eta*D(P_inf)))/(sigma))*Y;
%                    Y(0)=S_0; t=[0,200];

fid=fopen('Runge-Kutta_increments.m','w');  % Write results on an external file

h=0.1; a=0; b=200;           % h is the step size, t=[a,b] t-range
t = a:h:b;                   % Computes t-array
y = zeros(1,numel(t));       % Memory preallocation

P_t=P_inf;
y(1) = S_0;                         % initial condition; in MATLAB indices start at 1
Fyt = @(t,y) -((rho+alpha*(sigma-1)*(B-eta*D))/(sigma))*y;   % The function is the
                                                             % expression after (t,y)

% Table title
fprintf(fid,'%7s %7s %7s %7s %7s %7s %7s \n','i','t(i)','k1','k2','k3', 'k4','y(i)');
for ii=1:1:numel(t)
    k1 = Fyt(t(ii),y(ii));
    k2 = Fyt(t(ii)+0.5*h,y(ii)+0.5*h*k1);
    k3 = Fyt((t(ii)+0.5*h),(y(ii)+0.5*h*k2)); k4 = Fyt((t(ii)+h),(y(ii)+h*k3));
    y(ii+1) = y(ii) + (h/6)*(k1+2*k2+2*k3+k4);      % Main equation
```

```
    % Table data
    fprintf(fid,'%7d %7.2f %7.3f %7.3f',ii, t(ii), k1, k2);
    fprintf(fid,' %7.3f %7.3f %7.3f \n', k3, k4, y(ii));
end
y(numel(t))=[ ];          % Erase the last computation of y(n+1)

% Solution PLOT:
figure(1);
f1=plot(t,y,'DisplayName','S_t','MarkerSize',3,'Marker','o','LineStyle','none','Color',
   [0 0 0]); hold all;
title('Time evolution of the Resource Stock S_t','FontSize',14);
ylabel('Resource stock S_t'); xlabel('Time [years]');
box('on'); set(gca,'XMinorTick','on','YMinorTick','on');

S_t=get(f1,'YData');     % YData extrapolation from 'figure 1'
fclose(fid);

%% Derivation and plot for the POLLUTION STOCK P_t  %%%%%%%%%%%%%%%%%%%%%%%%%%%%%%%%%
% We recall Equation 84

P_t = P_0+phi*(S_0-S_t);

% Solution PLOT:
figure(2);
f2=plot(t,P_t,'DisplayName','P_t','MarkerSize',3,'Marker','o','LineStyle','none',
   'Color',[0 0 0]); hold all;
title('Time evolution of the Pollution Stock P_t','FontSize',14);
ylabel('Pollution stock P_t'); xlabel('Time [years]');
box('on'); set(gca,'XMinorTick','on','YMinorTick','on');

P_t=get(f2,'YData');     % YData extrapolation from 'figure 2'

%% Derivation and plot for the sigmoid DAMAGE FUNCTION D(P_t)  %%%%%%%%%%%%%%%%%%%%%%%
% We recall Equation 81

D_t=delta_0+delta_1*(1-(1)./(1+delta_2*(P_t-P_0).^(eta)));

% Solution PLOT:
figure(3);
f3=plot(t,D_t,'DisplayName','D_t)','MarkerSize',3,'Marker','o','LineStyle','none',
   'Color',[0 0 0]); hold all;
title('Time evolution of the Capital Depreciation D(P_t)','FontSize',14);
ylabel('Damage Function D(P_t)'); xlabel('Time [years]');
box('on'); set(gca,'XMinorTick','on','YMinorTick','on');

D_t=get(f3,'YData');     % YData extrapolation from 'figure 3'

%% Derivation and plot for the CONSUMPTION GROWTH RATE C^_t  %%%%%%%%%%%%%%%%%%%%%%%%
% We recall Equation 82

C_t = (1/sigma )*(alpha*B-alpha.*D_t-rho);

% Solution PLOT:
```

```
figure(4);
f4=plot(t,C_t,'DisplayName','C_t)','MarkerSize',3,'Marker','o','LineStyle','none',
   'Color',[0 0 0]); hold all;
title('Time evolution of the Consumption Growth Rate C_t','FontSize',14);
ylabel('Consumption Growth Rate C_t'); xlabel('Time [years]');
box('on'); set(gca,'XMinorTick','on','YMinorTick','on');

C_t=get(f4,'YData');      % YData extrapolation from 'figure 4'
```

.6 Graphical results

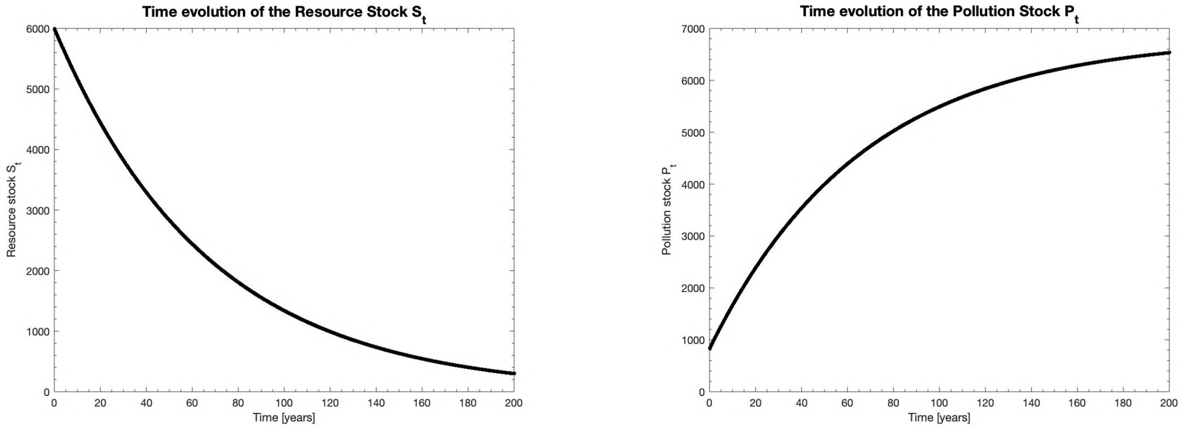
Time evolution of the Resource Stock S_t

Time evolution of the Pollution Stock P_t

Figure 1: Resource stock S_t (on the left) and Pollution stock P_t (on the right) as a function of time t.

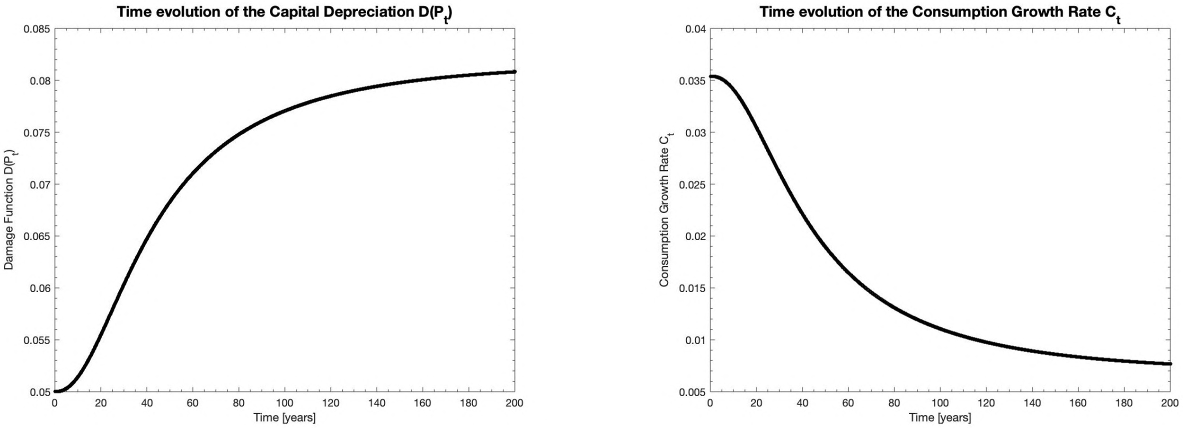
Time evolution of the Capital Depreciation $D(P_t)$

Time evolution of the Consumption Growth Rate C_t

Figure 2: Capital depreciation $D\left(P_t\right)$ (on the left) and Consumption growth rate $\hat{C}_t$ (on the right) as a function of time t.

The role of population growth in global sustainable development

Population growth is often seen as a threat to sustainable development...is it true?

World population is currently growing at the highest rate ever attained in history. Thomas Malthus in the late 18th century first introduced the "Malthusian trap", suggesting that there is a limit to population size and growth due to a finite natural resource base[4]. In a similar way, Paul Ehrlich (1994)[5] also claimed that "sustainable development cannot continue without limits to population growth", referring to capital accumulation and technical progress as the principal factors that could help overcome resource scarcity and food shortages. However, the pessimistic Malthusian notion of future "misery and vice" may not be fully appropriate. Despite the evident scarcity of energy resources, raw materials deposits and the atmospheric capacity to absorb polluting emissions, the total use of natural resources and energies will ultimately have to shrink in future centuries. The question therefore remains whether policy should actively limit population growth, even in the name of sustainable development.

From a mechanistic point of view, if we look at the so-called "IPAT" formula, per capita use of natural resources and limiting population are interchangeable. Given that affluence (A) is measured by income per capita (Y/P) and technology (T) is measured by resource use per income (R/Y), human impact on nature I equals resource use R, since income Y and population P cancel in the IPAT equation. This result, despite being always true, does not contribute to our understanding of the relation between population and sustainability. Indeed, the IPAT formula is based on the assumption that population, affluence, and technology are independent of one other. In reality, these variables are highly interdependent in many ways: we can have effects such as John Hicks' "induced" innovation and the so-called "demographic transition"[6], which deals with the impact of income and wealth on fertility. On average, wealthier countries tend to have smaller families than less developed countries; this means that both public social security and the increasing costs of child parenting are among the drivers of the transition.

The relationship between the impact of population growth and the capital accumulation is also a main issue. In the traditional neoclassical view, population growth is not favorable for development. By taking into account physical capital (i.e. machines and infrastructures) only, different stocks have to be shared among a rising number of people. In other words, the use of the capital by one person affects the use by another person, consequently reducing the capital per workplace, together with labor productivity and growth. To be realistic, however, basic parts of capital come also in the form of knowledge capital, which can be shared by everybody, as well as by an increasing workforce. If new ideas arise, everyone can use them without harming the knowledge of somebody else. If we consider knowledge capital, then population growth will not decrease labor productivity. In addition, as suggested by D. Gale Johnson (2001)[7], people specialized in the creation of knowledge work in research institutes and universities, which are clearly labor-intensive. These institutions can discover and promote substitutes, including clean goods and green technologies, which will reduce the overall natural resource consumption. As Julian Simon wrote in 1981[8], population could be the "ultimate solution" to resource scarcities and environmental problems, since people can innovate. More people generate more ideas, making the education and the size of the labor force augment the intensity of knowledge creation and consequently the economic growth rate.

However, it is now worth asking if these new elements are influential enough to change the general opinion of population growth and resource scarcity. A possible answer can be found in the paper "Population Growth and Natural Resource Scarcity: Long-Run Development under Seemingly Unfavorable Conditions"[9], where it was proofed under very restrictive assumptions (i.e. poor input substitution, increasing resource prices

---

[4] Thomas Robert Malthus. "An essay on the principle of population. 1798". In: *The Works of Thomas Robert Malthus, London, Pickering & Chatto Publishers* 1 (1986), pp. 1–139.

[5] Joseph H. Vogel. "The Population Explosion by Paul R. Ehrlich and Anne H. Ehrlich (Simon and Schuster, NewYork, 1990), pp. 320, $US18.95, ISBN 0-671-68984-3". In: *Prometheus* 9.2 (1991), pp. 396–397. DOI: `10.1080/08109029108631961`. eprint: `https://doi.org/10.1080/08109029108631961`. URL: `https://doi.org/10.1080/08109029108631961`.

[6] John R Hicks. "TheTheoryofWages". In: *London: Macmiilan* (1932).

[7] D Gale Johnson. "On population and resources: a comment". In: *Population and Development Review* 27.4 (2001), pp. 739–747.

[8] Simon JL. *The Ultimate Resource*. 1981.

[9] Lucas Bretschger. "Population Growth and Natural-Resource Scarcity: Long-Run Development under Seemingly Unfavorable Conditions". In: *The Scandinavian Journal of Economics* 115.3 (2013), pp. 722–755.

and the decision of families to have children) that population growth is not only positive, but even needed to ensure sufficient innovation. This is because it may help the economy during the transition phase by increasing the chances of developing efficient technologies. The above conclusion is also in conformity with Esther Boserup's research[10] on poor agrarian societies, where it is claimed that "necessity is the mother of invention". As she said in the book "The Conditions of Agricultural Growth: The Economics of Agrarian Change under Population Pressure", only in times of pressure people find out ways to increase the productivity by fundamentally innovating.

Moreover, in contrast to the idea that population size is a global concern, one can show that a growing labor force can be compatible with the natural environment, provided that the increasing resource scarcity is fully reflected in resource prices. To express the concept into the right perspective, the current per capita use of global resources is comparatively low in countries with high population growth, while it is much higher in rich countries. Instead of restricting population in developing countries, it could be proposed the population size to be restricted in richer countries. In many cases, however, the so-called "population problem" is actually a problem strongly related to the attitude of the individuals: to ensure sustainability, we need to constantly reduce the use of natural resource and to provide sufficiently high technical change. A transition to a long-run steady state with constant population, sustainable resource use, and positive consumption growth may be reached via a demographic transition which relies on individual behavior.

Finally, instead of a population policy which may result counterproductive, encouraging innovation, raising the prices of natural resources, and increasing living standards may induce the demographic transition and simultaneously promote sustainable consumption. As long as we don't have a shrinking population problem, just like in Japan, raising resource prices together with facilitating labor reallocation from knowledge-extensive to knowledge-intensive sectors, which can develop and exploit green technologies, are the best means to support sustainable development. Indeed, as shown in the paper "Population Growth and Natural Resource Scarcity"[11] adjusting resource process via continuous small steps to a sustainable equilibrium will help the economy. As soon as all the countries have achieved an average decent living standard, population growth is expected to stop.

---

[10] David Grigg. "Ester Boserup's theory of agrarian change: a critical review". In: *Progress in Geography* 3.1 (1979), pp. 64–84.

[11] Bretschger, "Population Growth and Natural-Resource Scarcity: Long-Run Development under Seemingly Unfavorable Conditions".

References

Bretschger, Lucas. “Population Growth and Natural-Resource Scarcity: Long-Run Development under Seemingly Unfavorable Conditions”. In: *The Scandinavian Journal of Economics* 115.3 (2013), pp. 722–755.

Bretschger, Lucas and Christos Karydas. “Economics of Climate Change: Introducing the Basic Climate Economic (BCE) Model”. In: Environment and development economics 24.6 (2019-12), pp. 560–582. ISSN: 1355-770X. DOI: `10.3929/ethz-b-000394747`.

— “Optimum growth and carbon policies with lags in the climate system”. In: Environmental and Resource Economics 70.4 (2018-08), pp. 781–806. ISSN: 0924-6460. DOI: `10.1007/s10640-017-0153-4`.

Grigg, David. “Ester Boserup’s theory of agrarian change: a critical review”. In: *Progress in Geography* 3.1 (1979), pp. 64–84.

Hicks, John R. “TheTheoryofWages”. In: *London: Macmiilan* (1932).

JL, Simon. *The Ultimate Resource*. 1981.

Johnson, D Gale. “On population and resources: a comment”. In: *Population and Development Review* 27.4 (2001), pp. 739–747.

Malthus, Thomas Robert. “An essay on the principle of population. 1798”. In: *The Works of Thomas Robert Malthus, London, Pickering & Chatto Publishers* 1 (1986), pp. 1–139.

Vogel, Joseph H. “The Population Explosion by Paul R. Ehrlich and Anne H. Ehrlich (Simon and Schuster, NewYork, 1990), pp. 320, $US18.95, ISBN 0-671-68984-3”. In: *Prometheus* 9.2 (1991), pp. 396–397. DOI: `10.1080/08109029108631961`. eprint: `https://doi.org/10.1080/08109029108631961`. URL: `https://doi.org/10.1080/08109029108631961`.

+1 (650) 507-9027
lu.mondonico@gmail.com